Civil Engineering Infrastructures Journal (CEIJ)

Civil Engineering Infrastructures Journal

CEIJ

Volume 57, Number 2, December 2024

Available online at
www.ceijournal.com

Civil Engineering Infrastructures Journal (CEIJ)
Semiannual Publication

CONTENTS
Volume 57, Number 2, December 2024

Feasibility of Using Electric Induction Furnace Steel Slag and Copper Slag in the Production of Hot Mix Asphalt

Chaubey, N.K.[1] and Mishra, A.K.[2]*

[1] Ph.D. Candidate, Research Scholar, Department of Civil Engineering, Madan Mohan Malaviya University of Technology Gorakhpur, Uttar Pradesh, India.
[2] Professor, Department of Civil Engineering, Madan Mohan Malaviya University of Technology Gorakhpur, Uttar Pradesh, India.

ABSTRACT: Industries produce large amounts of electric induction furnace steel slag (EIF) and copper slag (CuS) as waste, and their disposal poses serious economic and environmental issues. The use of these slags in pavement could ease environmental concerns and promote the conservation of non-renewable resources. This paper is based on an experimental investigation into the potential for employing EIF and CuS at 0, 5, 10, 15, 20, and 25% as a partial replacement of fine Natural Granite Aggregate (NGA), whose size ranges from 4.75 mm to 0.075 mm, in producing dense Hot Mix Asphalt (HMA) mixes. The physical, chemical, morphological, and expansive properties of EIF and CuS were investigated. The Marshall method of mix design was adopted to produce HMA mixes. The results showed that for EIF-based HMA mixes, stability, Indirect Tensile Strength (ITS), and rutting resistance increased, whereas for CuS-based HMA mixes, these properties decreased but satisfied their required permissible criteria. The Tensile Strength Ratio (TSR) of EIF and CuS-based HMA mixes was found to be increased. The findings of this study indicated a high possibility for using EIF and CuS as aggregates, and a replacement level of 20% of these slags in HMA mixes was suggested as optimal.

1. Introduction

Rapid growth is taking place in the transportation sector in India due to an increased emphasis on infrastructure development. This is generating a huge demand for pavement materials, which is putting pressure on natural resources. On the other hand, industrial waste products such as steel slag, copper slag, blast furnace slag, fly ash, and other waste are found abundantly in India, which is resulting in a shortage of disposal areas and creating a tremendous threat to public health and ecology. India has the world's second-largest road network, with around 6.2 million kilometers, and it is growing at a rate of 37 kilometers per day to keep up with economic growth. Asphalt is used in the construction of nearly all major Indian highways, and this trend is projected to continue. The most extensively used method for building asphalt pavement is the Hot Mix Asphalt (HMA) process. Natural aggregates make up about 90% of the total weight of the asphalt mixture. According to

---

* Corresponding author E-mail: akmce@mmmut.ac.in

Chaubey and Mishra (2020), one km pavement requires approximately 30000 metric tons of aggregate. The environment and ecosystem are rapidly deteriorating because of excessive quarrying of natural aggregate resources. Therefore, new alternate materials as a substitute for natural aggregate must be discovered and developed to protect natural resources.

Substituting industrial by-products and wastes for natural aggregates is one of the easiest tactics for achieving sustainable pavements since it provides two benefits: One, the rate of depletion of natural resources can be reduced, and another, the deposition of waste in landfills can be avoided, resulting in environmental benefits. In addition to having a favorable impact on the environment, using these discarded materials in asphalt mixes can help to achieve the goals of sustainable construction as per Ipekyol et al. (2022).

Some studies have suggested that it is feasible to produce asphalt mixtures with recycled concrete aggregate (Xu et al., 2022), reclaimed asphalt pavement (Naser et al., 2022), steel slag (Zhao et al., 2022), waste ceramic (Rochlani et al., 2021), and glass powder (Ming et al., 2022). India's copper, iron, and steel industries, on the other hand, have grown fast in line with the country's rapid economic boom. The slag coming out of these industries is considered a strong construction material. Patel and Shahu (2018) suggested that it is possible to use it profitably in the construction of base and subbase courses instead of natural aggregates. Steel slag and copper slag are common waste materials that have been utilized in the road construction sector as aggregate.

India is estimated to produce 12 million tons of steel slag each year. Steel production in India is mainly done through oxygen and electric routes. The oxygen route comprises a Basic Oxygen Furnace (BOF), while the electric route includes an Electric Arc Furnace (EAF) and an Electric Induction Furnace (EIF). According to Ghanbari and Bayat (2022), steel slag is a solid waste that

is generated during the steelmaking process, and its utilization could be advantageous for environmentally friendly construction practices. For every ton of steel produced, a steel plant generates 2-4 tons of waste, which includes solids, liquids, and gases. It was stated by Xu et al. (2020) that the steel slag produced by proper crushing and processing resembles natural aggregate in shape and has shown improved mechanical properties, moisture susceptibility, skid resistance performances, and crack resistance behavior. Asi et al. (2007) investigated several samples of asphalt mixes produced by substituting 0%, 25%, 75%, and 100% coarse limestone aggregate with steel slag. They observed better indirect tensile strength, rutting resistance, resilient modulus, fatigue, stripping resistance, and creep modulus. Except for creep performance, improved mechanical properties of asphalt concrete mixes were discovered when 100% of the coarse limestone particles were replaced with steel slag. Steel slag replacement of coarse limestone aggregates was adequate at 75%, while 25% replacement was optimal.

Ahmedzade and Sengoz (2009) examined the effects of using 100% steel slag in HMA. They discovered that steel slag mixed with asphalt mixtures demonstrated higher fatigue resistance, indirect tensile strength, and modulus values. To test the skid resistance of a thin asphalt surface, Kehagia (2009) carried out a site investigation on four different sections of a high-traffic PATHE motorway in Greece. It was observed that after one year of service, the EAF mixed asphalt mix outperformed the natural aggregate mixed asphalt. The mixture with the highest EAF content provided the most significant skid resistance. Steel slag was found to improve the roadway conditions in the study.

Kandhal and Hoffman (1997) investigated the performance of asphalt mixes incorporating fine steel slag as aggregate in Pennsylvania. The steel slags in the asphalt mix, both cured and uncured, were discovered to be non-expanding.

It was discovered that the expansion of untreated steel slag mixes was constrained by the presence of a bitumen layer on the steel slag. The Pennsylvania Department of Transportation permits the incorporation of fine and coarse steel slag aggregates with natural aggregates in producing asphalt mixes. Though steel slag mixtures with a higher asphalt content may minimize expansion, they also reduce skid resistance.

Despite having numerous advantages, there is literature available that explains the disadvantages of employing these slags in the production of asphalt mixes. It was reported by Rohde et al. (2003) that the steel slag expands when it meets moisture due to the existence of free lime. Because when free lime reacts with water, it produces $Ca(OH)_2$, which causes an increase in volume.

Consequently, volumetric instability can affect the performance of asphalt mixes. The use of steel slag in asphalt mixes must be restricted to replacing fine or coarse fractions of aggregates, but not both the sizes at the same time. Because of the angular shape of the steel slag, 100% steel slag mixed HMA mixes are more likely to develop a high percentage of air voids and expansion issues. Asi et al. (2007) reported that a high proportion of air voids consumes more asphalt content and will be prone to flushing because of traffic load. Moreover, it was also suggested that slags in asphalt mixes should be kept limited to avoid excessive density increases, which could result in higher mixing and transportation costs.

Copper Slag (CuS) is a waste material that has shown high potential for its application in the asphalt mix. CuS is a waste obtained from the copper industry during the matte smelting, converting, and refining of copper. According to Chaubey and Mishra (2020), approximately 2.2 tons of CuS are generated for every ton of copper produced. As per Modarres and Bengar (2019), slag that has a copper content of less than 0.8 percent is often dumped as waste in slag dump yards. Deposition of copper slag causes various environmental issues, including pollutant seepage into groundwater, air pollution from dust dispersal, landscape effects, and land use restrictions. It is generally stored near copper mining and smelting premises. According to Ziari et al. (2017), granular CuS has many properties suitable for its use as aggregates, such as its angular and irregular morphology, better abrasion resistance, soundness, and low water absorption characteristics.

In a study conducted by Modarres and Bengar (2019), they investigated the usage of CuS powder as a filler in HMA mixtures. It was discovered that adding more CuS powder improved the mechanical characteristics of HMA. The average values of the ITS, indirect tensile toughness index, fatigue life, and resilient modulus of HMA containing the same proportion of CuS powder were 10.2, 8.5, 7.5, and 21.6% greater than those of the control mix, which contains 6% limestone filler. The parameters of the fatigue life indirect tensile toughness index and fatigue life resilient modulus were found to be significantly correlated. For all strain levels, the indirect tensile toughness index correlation coefficients were more important than the resilient modulus. All the samples were determined to meet the necessary requirements, and the presence of toxic components in the leachates obtained from the CuS powder and, in particular, the CuS powder based HMA was found to be less than the maximum allowable levels. Pundhir et al. (2005) investigated the mechanical properties of various types of bituminous mixtures, which contained up to 30% of fine CuS particles. Based on the results of stability and ITS, they concluded that CuS improves interlocking, which enhances the mechanical and volumetric properties of bituminous macadam, dense bituminous macadam, bituminous concrete, and semi-dense bituminous concrete. Hassan and Al-Jabri (2011) explored the feasibility of using granulated CuS as a fine portion of aggregate in HMA mixtures.

Various aggregate mixtures containing up to 40 percent CuS were subjected to the Marshall mix design process. Master curves were established for the control and CuS-containing mixtures after executing the dynamic modulus testing at various frequencies ranging from 0.1 to 16 Hz and temperatures ranging from 25 to 60 °C. The modulus value was found to decrease with an increase in the slag content as well as the temperature. The obtained TSR was better than that of the control mix with limestone aggregates, even though the Indirect Tensile Strength (ITS) findings for moisture resistance tests showed a loss. The findings suggest that using CuS as fine aggregate in HMA has enormous potential. To enhance performance and reduce industrial waste, Zalnezhad et al. (2022) carried out a laboratory investigation in order to explore the potential use of CuS at 0, 10, 20, 30, and 40% as a partial substitute for aggregate in producing micro surfacing mixtures. Their findings indicated that the use of CuS in micro surfacing treatment appeared to be quite promising. Due to its angularity and high fraction of Fe_2O_3 and SiO_2, CuS, especially at 30%, enhanced the performance of asphalt mixes with respect to abrasion resistance, curing time, and vertical and lateral displacement. The findings of the Analysis of Variance (ANOVA) also demonstrated that the cure time and deformations brought on by traffic loads were more significantly influenced by the CuS than by residual bitumen. Hu et al. (2022) conducted experimental work investigating the microwave absorption characteristics of HMA containing CuS.

The specimen's interior temperature and heating rate were tested in the mixture cylinder at various heights using a fiber-optic thermometer. The infrared thermometer also captured the surface temperature. The effects of the mixture's age, heating capacity, and CuS content on its healing capacity were examined through semicircular three-point bending tests.

According to reports, CuS has superior microwave absorption qualities compared to conventional aggregate. Compared to standard mixtures, the mixture with CuS has a more pronounced healing effect. The heating speed and healing effectiveness are significantly influenced by microwave heating power.

As per Indian Mineral Yearbook (2019), in India, there are approximately 18 BOF units, 50 EAF-based steel units, and 999 electric induction furnace units in operation.

The standard integrated BOF approach produces about 44.6% of steel, and the electric route produces roughly 55.4% of steel, with the EIF and EAF routes accounting for 29.7% and 25.7% of production, respectively. To the best of the authors' knowledge, no research has been done on including EIF in the production of asphalt mixes, even though this approach produces far more steel than the EAF route.

Moreover, limited research has been done on the inclusion of granulated CuS as a fine aggregate that passes 4.75 mm and is retained on a 0.075 mm sieve in producing HMA mixes. Therefore, the research presented in this paper aims to study the feasibility of using EIF and CuS as fine aggregate in producing HMA mixtures and to minimize the consumption of mineral aggregates.

2. Materials and Methods

To ensure that the qualities of the materials to be used in the asphalt mixes are within the bounds specified in pertinent standards and guidelines, these were first examined using standard testing methods. The chemical, morphological, and volumetric expansion behaviors of EIF and CuS aggregates were determined to assess their suitability and feasibility for producing HMA mixtures. After testing the materials, the laboratory investigation was done on the HMA mixture produced by substituting NGA with EIF and CuS in fractions of 0, 5, 10, 15, 20, and 25%. The usefulness of replacing the fine NGA with both slags was concluded by evaluating the Marshall parameters for mechanical performance, the

ITS test for cracking behavior, and the TSR test for determining moisture susceptibility and rutting resistance for assessing the deformation behavior of the HMA mixes. The data are statistically examined using analysis of variance (ANOVA) at a level of significance of 0.05. The methodology of this research is illustrated in Figure 1. Each of these procedures is discussed in detail in the following subsections:

2.1. Aggregates

The NGA were obtained from the mines located in Kabrai city, Uttar Pradesh, India (25.42°N, 80.02°E), while the crushed EIF was procured from Gallant Ispat Limited, Sahjanwa, located in the district of Gorakhpur, Uttar Pradesh, India (26° 45′ N, 83° 13′ E), and the CuS was procured from the Indian Copper Complex, located in the district of East Singhbhum, Jharkhand, India (22.5950° N, 86.4515° E). Table 1 presents their physical characteristics. The general appearance of NGA, EIF, and CuS is shown in Figure 2. The middle gradation limit of dense bituminous macadam (DBM) grade-II was chosen as per MoRTH (2013). Figure 3 shows the gradation curve used in this study.
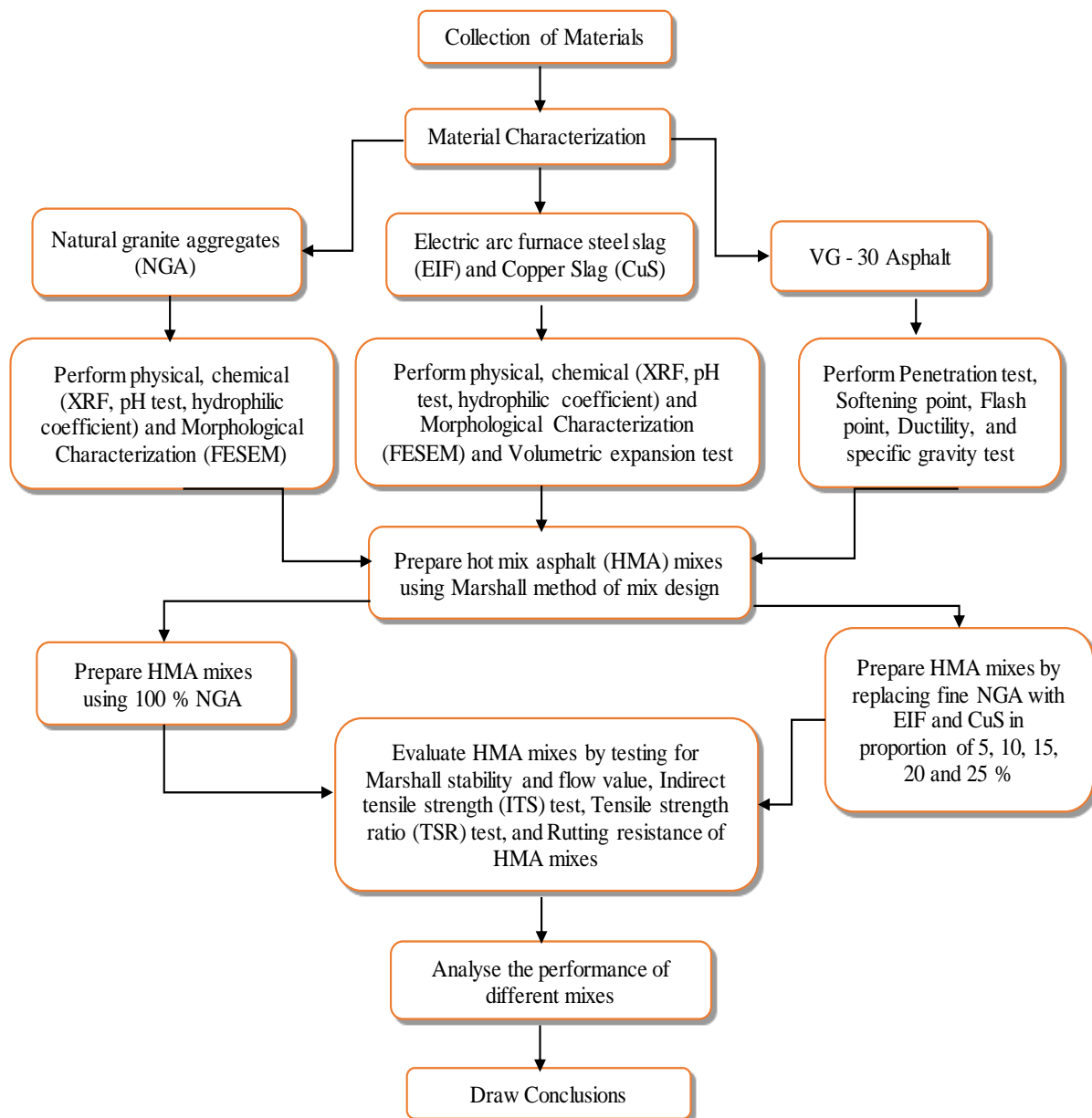
Fig. 1. Flowchart showing methodology

Table 1. Physical and mechanical properties of NGA, EIF and CuS

Properties	NGA	EIF	CuS	Requirements for DBM (MoRTH 2013)	Test method
Los Angeles abrasion value, %	23.22	21.43	18.35	≤ 35	IS 2386-4
Aggregate impact value, %	12.35	11.88	-	≤ 27	IS 2386-4
Combined flakiness and elongation indices, %	31.34	29.54	-	≤ 35	IS 2386-1
Water absorption of coarse aggregate, %	0.20	0.50	-	≤ 2	IS 2386-3
Water absorption of fine aggregate, %	1.40	2.10	1.87	≤ 2	IS 2386-3
Specific gravity of coarse aggregate	2.723	2.786	-	2.5-3.0	IS 2386-3
Specific gravity of fine aggregate	2.647	2.928	3.807	2.5-3.0	IS 2386-3
Stripping, %	> 95	> 95	-	≥ 95	IS 6241

| (a) | (b) | (c) |
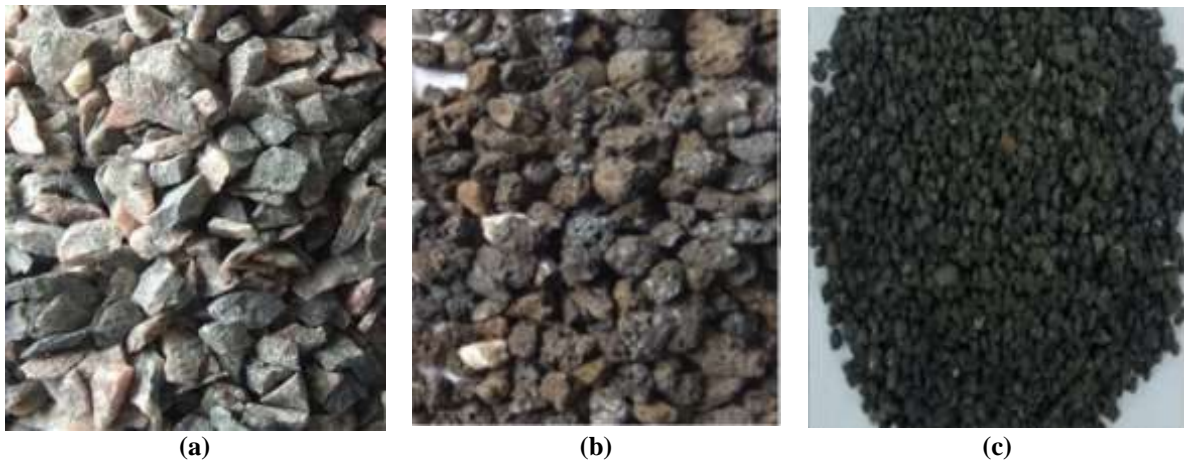
Fig. 2. General appearance of: a) NGA; b) EIFS; and c) CuS
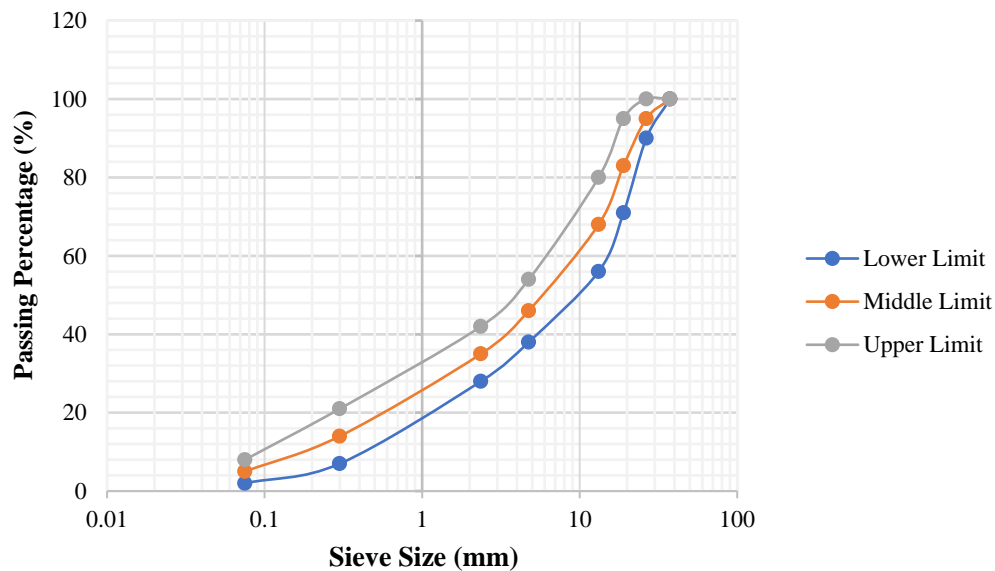
Fig. 3. DBM- II gradation curve

2.2. Asphalt

This study used asphalt with viscosity grade 30 (VG-30) produced by Hindustan Petroleum Corporation Limited. The results of the various tests conducted in accordance with Indian standard test procedures to assess the engineering features of the asphalt are shown in Table 2. All the properties of selected asphalt conform to the requirements as specified by IS 73 (2013) guidelines.

Table 2. Properties of asphalt

Characteristics	Result	Specifications	Test method
Penetration at 25 °C, 100 g, 5 s, 0.1 mm	66	≥ 45	IS 1203-1978
Softening point (R&B), °C	55	≥ 47	IS 1205-1978
Flash point	265	≥ 220	IS 1209-1978
Ductility at 25 °C, cm	84.5	≥ 40	IS 1208-1978
Specific gravity	1.03	-	IS 1202-1978

2.3. Experimental Program

The schematic representation of the experimental program conducted in this investigation is shown in Figure 1. The work was divided into two phases. The first phase included the characterization of NGA, EIF, and CuS, and in the second phase, the performance of slags incorporating HMA mixtures in terms of stability, cracking, moisture, and rutting was studied.

2.3.1. XRF Analysis and pH Test

The XRF test was executed to obtain the chemical components of these aggregates. The experimental setup for XRF is depicted in Figure 4. The pressed pellets of NGA, EIF, and CuS were prepared to trace the chemical composition through an XRF test.

The alkalinity level of these aggregates was accessed by executing a pH test on them. A higher pH in aggregates is expected to increase their binding capacity with asphalt. Because of the acidic nature of asphalt, alkaline materials establish stronger bonds with it, providing higher resistance to stripping and thereby improving the resistance to moisture damage of asphalt mixes. Figure 5 shows the setup for the determination of pH. A specimen solution for each material was made by mixing it with distilled water in a 1:9 weight ratio and then setting it aside for two hours before testing.
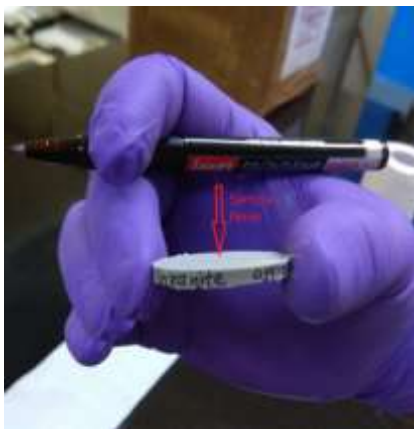
Fig. 4. XRF test setup

Fig. 5. Setup for the determination of pH value test

2.3.2. Hydrophilic Coefficient

Some materials have a stronger affinity for water than asphalt. These materials are known as hydrophilic materials. Asphalt absorption on the surface of hydrophilic materials is substantially lower than that of hydrophobic materials when they are dry. Materials with hydrophobic characteristics stick to asphalt extremely well. Because hydrophilic elements do not have a reciprocal connection with asphalt, the quality of the asphalt mixes gets inferior, resulting in lower impermeability, strength, and temperature resistance. Hydrophobic materials must be chosen for making durable asphalt mixes. There is a procedure for choosing these materials. It is based on the hydrophilic coefficient of the materials being determined. During the research, the ability of the materials to absorb kerosene was compared with their ability to absorb water. The set-up for determining the hydrophilic coefficient is shown in Figure 6. Asphalt and kerosene are liquids that are covalently bonded. However, kerosene was utilized instead of asphalt during the test since kerosene has a lower density than asphalt, allowing for faster sedimentation. Because the sedimentation of materials was measured, quick sedimentation is extremely crucial. The hydrophilic coefficient is the ratio of volumes after 72 hours of material sedimentation in water to kerosene. The hydrophilic coefficient can be obtained from the following equation:

$$C = \frac{V_{water}}{V_{kerosene}} \qquad (1)$$

where C: is the coefficient of hydrophilic, V_{water}: is the volume of material in water after 72 hours of sedimentation, and $V_{kerosene}$: is the volume of material in kerosene after 72 hours of sedimentation.

2.3.3. Morphological Characteristics

The Field Emission Scanning Electron Mmicroscope (FESEM) was used to obtain microscopic images of NGA, EIF, and CuS to study the morphological behaviors of aggregate surfaces.

2.3.4. Volumetric Expansion

Because of the high CaO and MgO content, the slags may expand and disintegrate when exposed to moisture. The volumetric expansions of EIF and CuS were determined as per ASTM D4792 (2013).

2.3.5. Marshall Test

Three types of HMA mixtures were produced with six different asphalt concentrations of 4.2, 4.5, 4.8, 5.1, 5.4, and 5.7% by weight of the total aggregates, in accordance with AASTHO T245 (2022). First, a control mix (CM) with 100% NGA was produced. Further, EIF and CuS-incorporated HMA mixes were prepared, respectively, by replacing 5, 10, 15, 20, and 25% of the fine fraction of NGA that passes through a sieve size of 4.75 mm and is retained at 0.075 mm. The specifications of each HMA mixture are represented in Table 3. The OAC of each asphalt mixture was calculated to correspond to a 4% air void as per MS-2 (2014).

Table 3. Types of HMA mixtures

Mixture name	HMA combinations
CM	Control mix having 100% NGA
EIF-5	5% EIF and 95% NGA
EIF -10	10% EIF and 90% NGA
EIF -15	15% EIF and 85% NGA
EIF -20	20% EIF and 80% NGA
EIF -25	25% EIF and 75% NGA
CuS-5	5% CuS and 95% NGA
CuS-10	10% CuS and 90% NGA
CuS-15	15% CuS and 85% NGA
CuS-20	20% CuS and 80% NGA
CuS-25	25 % CuS and 75 % NGA
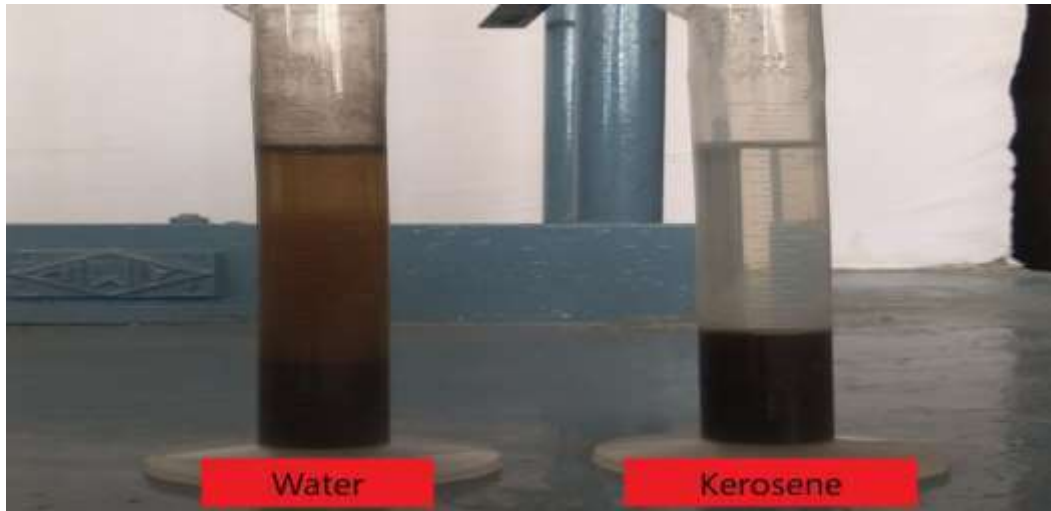
Fig. 6. Setup for the determination of hydrophilic coefficient value test

2.3.6. ITS

The cracking performance of pavements is directly affected by their tensile strength. Cracking usually leads to more serious damage, such as potholes. The adhesion efficiency of the aggregate and asphalt mixture, which is a key aspect of its cracking behavior, determines the tensile strength of the asphalt mixture. Therefore, precisely measuring the tensile strength of asphalt mixtures is very important to the design and analysis of asphalt pavement. Ziaee and Behnia (2020) stated that it is challenging to measure the tensile strength of asphalt mixtures directly, the ITS test is commonly performed for this purpose. The ITS test was performed following ASTM D6931 (2012) guidelines. According to Gautam et al. (2018), the greater the value of ITS, the better the crack resistance.

2.3.7. TSR

The presence of moisture in asphalt mixes can weaken the bond between the asphalt and aggregates, causing the asphalt mixture to deteriorate and consequently reducing the load-bearing capacity of the asphalt pavement. Therefore, the damage caused by moisture in the asphalt mix was investigated. The tensile strength ratio (TSR) was determined in line with AASTHO T283 (2014) to measure the moisture sensitivity of asphalt mixes. TSR values were obtained as a percentage by dividing the indirect tensile strength of the conditioned samples (ITS wet) by the indirect tensile strength of the unconditioned samples (ITS dry). A TSR value below 80% is undesirable. Benavides et al. (2023) suggested that the greater the TSR ratio, the more resistant the mixture will be to moisture-induced damage.

2.3.8. Rutting

The rutting resistance of all HMA mixes was evaluated by measuring their MQ and performing wheel tracking tests on them. The MQ measures the stiffness and rutting resistance of the asphalt mixtures (Chaudhary et al., 2018). It was calculated by dividing the Marshall stability results by the flow value of the HMA mixes. A higher MQ provides better stiffness and improved capacity to distribute the imposed load while resisting creep deformation (Muniandy et al., 2018).

The rutting resistance was also measured by conducting wheel track tests on all the HMA mixes. This test was conducted following the EN 12697-22 test procedure, in which the apparatus moves a steel wheel with a 203.2 mm diameter and a 47 mm width across the surface of the test sample. The wheel traverses the sample 52 times per minute. This test was conducted on all the HMA samples having a size of $300 \times 300 \times 50$ mm at a temperature of $40°C$ with a loading of 705N over a course of 10,000 cycles. The Wheel tracking test assembly is shown in Figure 7.

Fig. 7. Wheel tracking test device

3. Results and Discussion

3.1. XRF and pH Test

The XRF investigation revealed the existence of calcium oxide (CaO), magnesium oxide (MgO), manganese oxide (MnO), aluminum oxide (Al_2O_3), silica oxide (SiO_2), iron oxide (Fe_2O_3), potassium oxide (K_2O), sodium oxide (Na_2O), phosphorus pentoxide (P_2O_5), titanium (TiO_2), and nickel oxide (NiO) as their fundamental chemical compositions. Due to their higher iron oxide content, EIF and CuS have a higher specific gravity than NGA. The XRF outcomes of these aggregates are presented in Table 4.

According to the results of the pH test, both the slag materials had pH values greater than 7, indicating that they were alkaline. Since aggregates with a higher alkalinity level have a greater ability to form bonds with acidic asphalt, a higher pH for EIF and CuS is anticipated to increase their ability to bind to asphalt compared to NGA, improving the resistance to moisture

damage of asphalt mixes. EIF was discovered to have a higher pH value than NGA and CuS. The results of the pH value test are shown in Table 5.

3.2. Hydrophilic Coefficient

Hydrophilic compounds absorb more water than kerosene. Therefore, they have a higher volume in water than in kerosene, resulting in a high hydrophilic coefficient, whereas hydrophobic compounds have a larger volume in kerosene than in water, hence their hydrophilic coefficient will be low. If the coefficient value is more than 1, the compound is hydrophilic, and it is hydrophobic if the value is less than 1. As per Chaudhary et al. (2018), the hydrophilic coefficient for asphalt-suitable materials should be between 0.7 and 0.85. According to the test results shown in Table 6, all of the materials exhibited hydrophobic properties, but EIF outperformed NGA and CuS. Therefore, its inclusion in asphalt may bestow durable asphalt mixes.

Table 4. XRF results of NGA, EIF, and CuS

Materials	Al_2O_3	CaO	Fe_2O_3	K_2O	MgO	Na_2O	P_2O_5	SiO_2	TiO_2	NiO	MnO
NGA	12.78	0.44	2.62	3.89	1.14	0.27	0.05	65.42	0.57	0	0.03
EIF	9.95	2.96	25.27	0.73	1.11	0.51	0.1	45.8	0.78	0	0
CuS	3.08	1.93	52.56	0.74	0.46	0.14	0.08	29.46	0.27	0.05	0.03

Table 5. pH value of materials

Materials	pH value
NGA	8.83
EIF	9.63
CuS	9.52

Table 6. Coefficient of hydrophilic of materials

Materials	Coefficient of hydrophilic
NGA	0.94
EIF	0.75
CuS	0.91

3.3. FESEM Analysis

Yu et al. (2023) have suggested that the mechanical characteristics, rutting behavior, and moisture susceptibility of asphalt mixes are influenced by the surface morphology of the aggregates. Microscopic images of EIF, CuS, and NGA were acquired at different magnifications using FESEM and are shown in Figure 8. The EIF was found to have thicker, longer, and deeper surface pores and voids than those of the CuS and NGA, as seen in the obtained images. The surface characteristics of EIF were found to be similar to those found by Oluwasola et al. (2016). In their study, the EAF steel slag was discovered to be more porous and irregular than granite aggregate, which enhanced its bonding ability with asphalt. In addition, their mineralogical properties enhanced their alkalinity further, demonstrating their improved bond with asphalt. The rougher and more porous surfaces of EIF and CuS suggest that they will create a stronger bond with asphalt, but this may also require more asphalt in the mix. Therefore, this increase in asphalt will increase the cost of the project, but this can be compensated for as the waste is being utilized, which has environmental and technical benefits as per Noureldin et al. (1990).

3.4. Volumetric Expansion

Because of the high CaO and MgO content, the slags may expand and disintegrate when exposed to moisture. To avoid volumetric expansion, Tozsin et al. (2023) suggested that the slags can be weathered in the open air. It was found that the expansion rates of both slags for one week were much below the acceptable limits, which are 0.5% as per ASTM D4792 (2013) specification. The graph was plotted with respect to the obtained observation between duration in hours and expansion rate in percentage, as shown in Figure 9. Moreover, increased particle-to-asphalt adhesion can be aided by the high CaO component, which has a higher affinity for oil than for water as per Shen et al. (2009). Furthermore, due to the infiltration of adequate amounts of asphalt into the voids, the surfaces of EIF and CuS may get filled and well coated with asphalt, preventing moisture from contacting the CaO and MgO components of slag. As a result, moisture-induced slag volume expansion in HMA can be avoided.

(a)   (b)   (c)
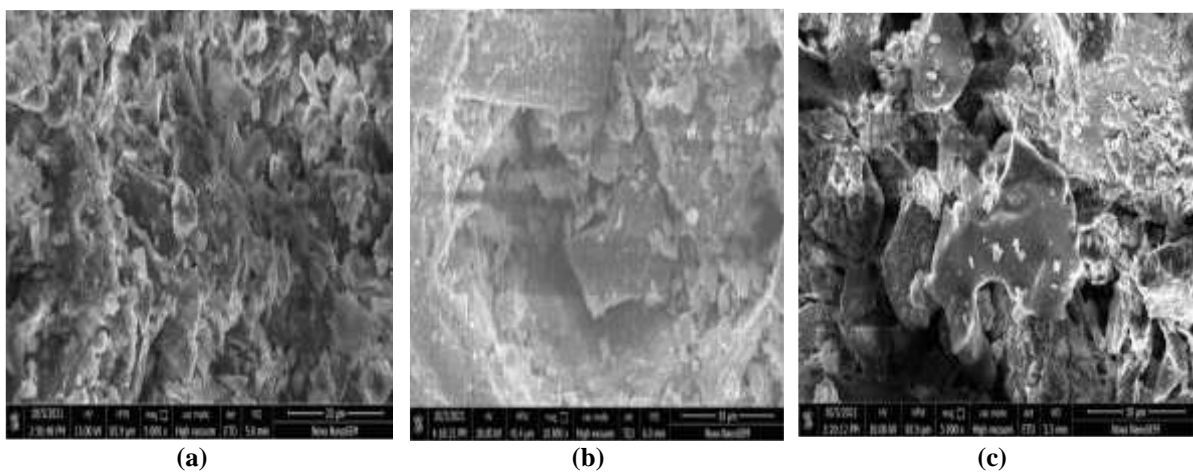
Fig. 8. FESEM image: a) NGA; b) CuS; and c) EIF
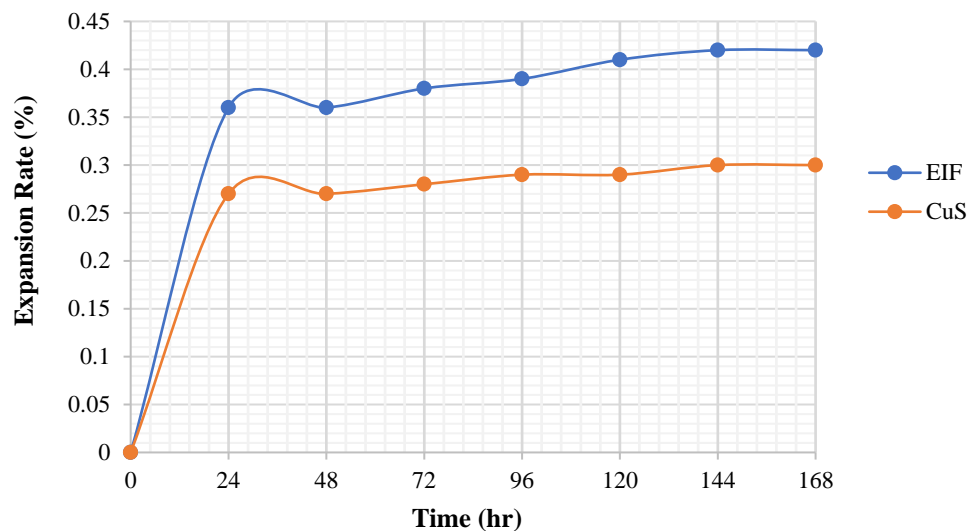
Fig. 9. Volumetric expansion curve of EIF and CuS

3.5. Marshall Test Result

The outcomes of Marshall parameters such as stability, flow, Optimum Asphalt Content (OAC), Voids in Mineral Aggregates (VMA), and Voids Filled with Asphalt (VFA) are presented in Table 7. These results show that the OAC of EIF and CuS-incorporated HMA mixtures is higher than that of the control mix, and it increases as the replacement percentage increases. This increase was primarily brought on by the high surface porosity and irregularity of EIF and CuS, as determined through FESEM analysis, which cause increased voids in the HMA mixes. As a result, more asphalt is needed to meet the higher air-void requirement and completely coat the aggregate surface. Past research has also shown that the slag content enhances the OAC (Ziaee and Behnia, 2020) because of its high specific surface area (Ameri et al., 2013), surface porosity, and air voids (Asi et al., 2007).

The effect of increased air voids due to slag content can be seen in the results of the VMA and VFA values of these mixes. The asphalt mixes with EIF and CuS presented higher values than the control mix, and it was observed that these increased with an increase in slag fraction. The VMA significantly impacts the performance of asphalt mixtures because mixtures with a high and low VMA may have stability and durability issues, respectively. On the other

hand, to avoid defects in the asphalt mixes, the limits of VFA must be maintained according to the required specification. MoRTH (2013) specifies the range of VFA between 65 and 75, and it was observed that by replacing 20-25% of fine NGA with both types of slag, one exceeded the permissible limits. Moreover, Hasita et al. (2020) suggested that less than 80% of VFA indicates high rutting resistance.

As for the results for stability, it was found that the Marshall stability for EIF-incorporated HMA mixes increased while it decreased for CuS incorporated HMA mixtures with their increasing proportions. As compared to the control mix, the stability of HMA mixes having 5, 10, 15, 20, and 25% of EIF and CuS increased by 4.46, 14.10, 17.10, 20.03, and 21.50% and was reduced by 1.21, 8.80, 15.82, 23.22, and 33.75%, respectively. The increased Marshall stability of the EIF-incorporated HMA mixture was attributed to the higher angularity, bulk specific gravity, and angle of internal friction of the EIF content, and the reason behind the significant decrease in Marshall stability of CuS-incorporated HMA mixes can be attributed to two reasons. One is due to the increased asphalt content, and the second is due to the higher specific gravity of CuS aggregate than NGA. The higher asphalt content was available to fill most of the voids, and therefore, the load is transmitted via

hydrostatic pressure through the asphalt rather than the contact point of the aggregates, which weakens the mix and accounts for the decrease in stability with higher optimum asphalt content. As a result, when the amount of asphalt in the HMA mixes exceeds a particular level, their Marshall stability begins to decline. On the other hand, replacing the fine portion of NGA with CuS, which has a higher specific gravity, reduced the amount of fine particles in HMA mixes since gradation was based on weight batching. Fewer fine particles adversely impacted packing friction. As a result, stability declined. Abdelfattah et al. (2018) and Hassan and Al-Jabri (2011) obtained similar results for Marshall parameters for CuS-incorporated HMA mixes. However, the Marshall stability and flow value results of all mixes met the requirements specified as per MoRTH (2013).

3.6. ITS

The cracking resistance of the produced mixes was assessed by conducting the ITS test. These results were found to be in line with the trend observed in the outcomes of Marshall stability studied earlier. The average value of three test samples was reported as the ITS value.

It was found that, compared with the control mixture, all the mixtures containing EIF had higher tensile strength values, which were found to increase with the incorporation percentage of EIF. Figure 10 depicts the ITS for EIF-based HMA mixes. The influence of surface roughness and angularity on EIF is greater than that of NGA. As a result, asphalt and EIF particles can develop a stronger interlock, leading to a higher ITS of the HMA mixes. This consequence can be seen in the fact that the ITS of the EIF-25 mix is 8.82% higher than that of the CM. The maximum increase in the ITS value was found for mix EIF-20, which is 9.48% higher than the CM. Following that, it was reduced to 0.60% from mix EIF-20 to mix EIF-25. This reduction was attributed to the higher stiffness of mix S-25, which was anticipated based on its higher MQ.

In contrast, the addition of the CuS fraction to HMA mixes lowers the ITS values, as shown in Figure 11. The ITS values for CuS-5, CuS-10, CuS-15, CuS-20, and CuS-25 mixes were found to be 2.24, 9.41, 10.08, 10.76, and 22.93% lower than the control mix, respectively. The maximum decrease in ITS was observed for mixes containing CuS-25 when the amount of CuS exceeded 20 percent in HMA mixes. This result is consistent with Hassan and Al-Jabri (2011) findings. They observed a reduction in the ITS as the slag content increased. Despite the decrease in ITS, all HMA mixes had ITS values higher than 0.44 MPa, which was the minimum required value that was suggested for pavement design by Hasita et al. (2020). However, a study carried out by Modarres and Bengar (2019) showed increased ITS value when copper slag is incorporated as filler in producing HMA concrete. This increase was due to the finer gradation of CuS than the limestone powder.

Table 7. Marshall mix design results

Mixes	OAC	Marshall stability	Flow value	VMA	VFA	MQ
CM	4.74	15.67	3.87	14.60	72.64	4.04
EIF-5	4.91	16.37	3.84	14.94	73.24	4.26
EIF-10	5.02	17.88	3.78	15.21	73.71	4.73
EIF-15	5.21	18.46	3.74	15.56	74.31	4.93
EIF-20	5.56	18.81	3.71	16.28	75.46	5.07
EIF-25	5.67	19.04	3.68	16.47	75.71	5.17
CuS-5	4.91	15.48	3.76	14.98	73.29	4.11
CuS-10	5.07	14.29	3.52	15.38	74.00	4.05
CuS-15	5.35	13.19	3.62	15.99	75.00	3.64
CuS-20	5.58	12.03	3.34	16.51	75.85	3.60
CuS-25	5.69	10.38	3.28	16.80	76.20	3.16
MoRTH requirements	Min. 4.5	Min. 9-12	2-4	Min. 12	65-75	2-5
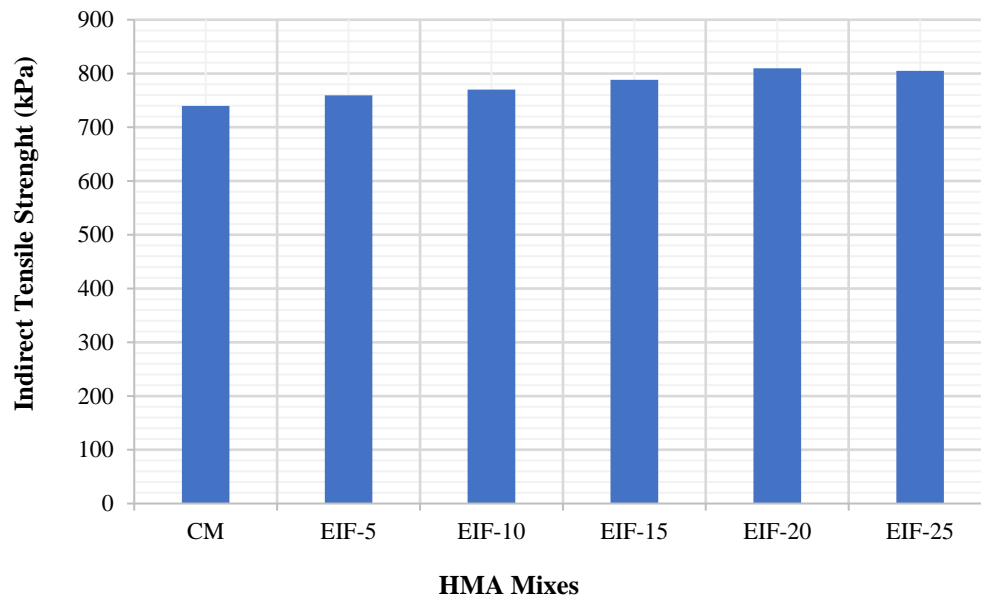
Fig. 10. Indirect tensile strength of EIF-based HMA mixes
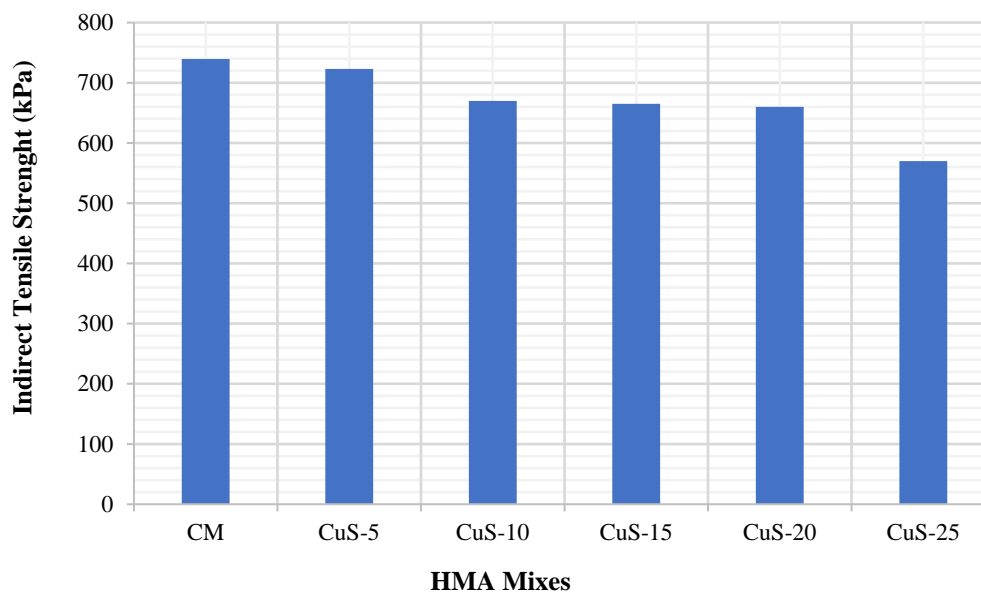
Fig. 11. Indirect tensile strength of CuS-based HMA mixes

3.7. TSR

Moisture susceptibility was assessed by examining the TSR of the asphalt mixes, and their outcomes are shown in Figures 12 and 13, respectively. Deterioration of asphalt pavement due to moisture is one of the major concerns for the pavement industry because moisture affects adhesion properties, resulting in weak bonding between aggregate and asphalt, which leads to premature pavement failure. It was observed that the TSR for the EIF and CuS-incorporated HMA mixtures was increased as compared to the control mix. Ziari et al.

(2017) discovered that the morphological, chemical, and physical properties of aggregate have a direct impact on moisture resistance. They also stated that the chemical composition and characteristics of the aggregates play a significant role in forming a bond with asphalt. Therefore, this result was attributed to two reasons. One was due to chemical characteristics, and the second was the surface morphology of EIF and CuS.

The chemical explanation for enhanced TSR was due to the higher alkaline nature of EIF and CuS. The CaO/SiO_2 ratio is an

indicator used to evaluate the level of alkalinity of the aggregate. Compared to NGA, EIF and CuS exhibited higher alkalinity. A larger proportion of this ratio increases the adhesion between the aggregate and the asphalt, promoting moisture resistance. This phenomenon can be explained by the fact that when asphalt meets an alkaline aggregate, the carboxylic acid component of the asphalt is adsorbed on the surface and the hydrocarbon portion points outward. This changed the overall surface characteristics of the aggregate sufficiently for the asphalt to cling to it (Xie et al., 2013). Further, pH testing also confirms that the EIF and CuS were more

alkaline than the NGA, which improves the adhesive bond. As a result, the TSR for the EIF and CuS-containing HMA mixes was improved. Additionally, EIF and CuS have more pores and cavities than NGA, as seen in Figure 8. The physical cling of asphalt to the cavities presents on the surface of this slag content resulted in improved adhesion between them. However, if an aggregate is entirely coated with asphalt, moisture cannot access its surface, and stripping potential can be considerably reduced. According to MoRTH (2013), all the HMA mixes produced met the minimum requirement of 80% TSR.
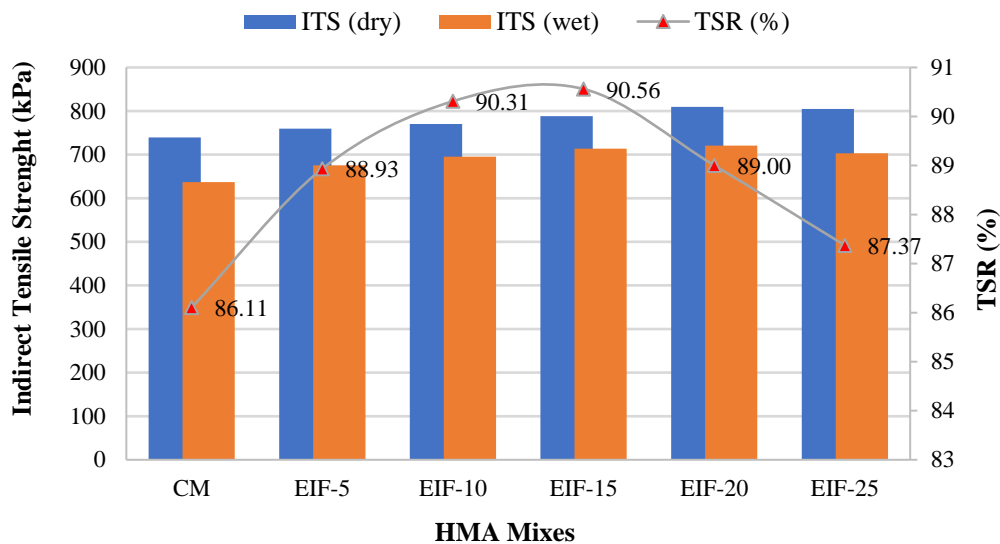
Fig. 12. Tensile strength ratio of EIF-based HMA mixes
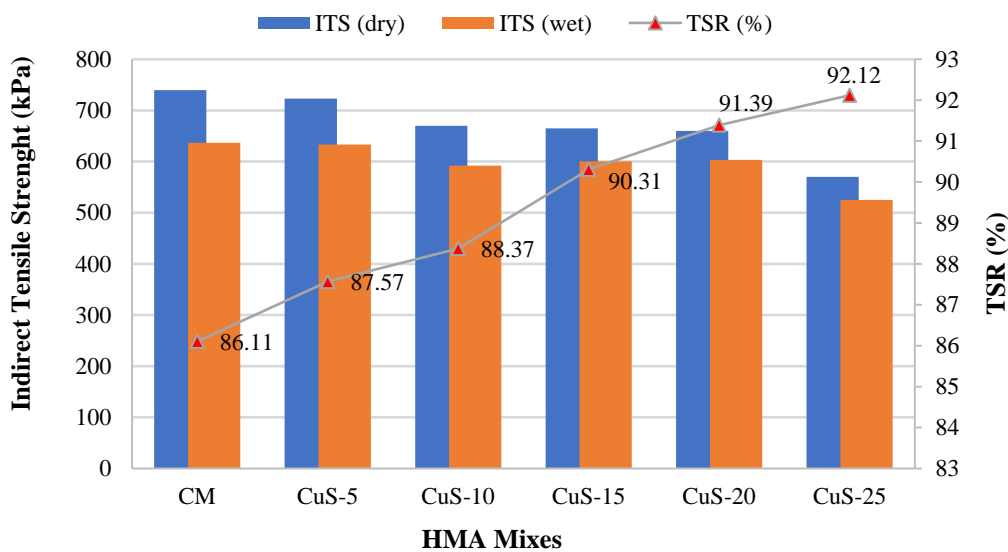
Fig. 13. Tensile strength ratio of CuS-based HMA mixes

3.8. Rutting Resistance

The MQ measures the resistance of the asphalt mixture to shear stress, rutting, and permanent deformation. As per Muniandy et al. (2018), the higher value of MQ suggests that the asphalt mixture will have a high degree of stiffness, increasing its ability to distribute loads and resist creep deformation. The MQ for EIF mixes was found to be higher than the CuS-incorporated HMA mixtures. It was found that the MQ increased for EIF mixes and declined for CuS mixes with their increasing proportions. Figures 14 and 15 illustrate the MQ results of EIF and CuS-incorporated HMA mixes, respectively. The MQ for the EIF-25 mix was found to be slightly higher than the maximum required criteria, and for the CuS-25 mix, it was slightly higher than the minimum requirement. Therefore, it can be stated that including more than 25 percent EIF and CuS content in the HMA mixes may significantly decrease the rutting resistance.

Additionally, the rutting resistance was evaluated by conducting wheel track tests, and the outcomes for the HMA mixes with EIF and CuS incorporation are shown in Figures 16 and 17, respectively. Lower rut depth indicated higher rutting resistance. It was observed that the rutting resistance increases as EIF content increases, while the addition of CuS exhibited a lower rutting resistance as compared to the control mix.
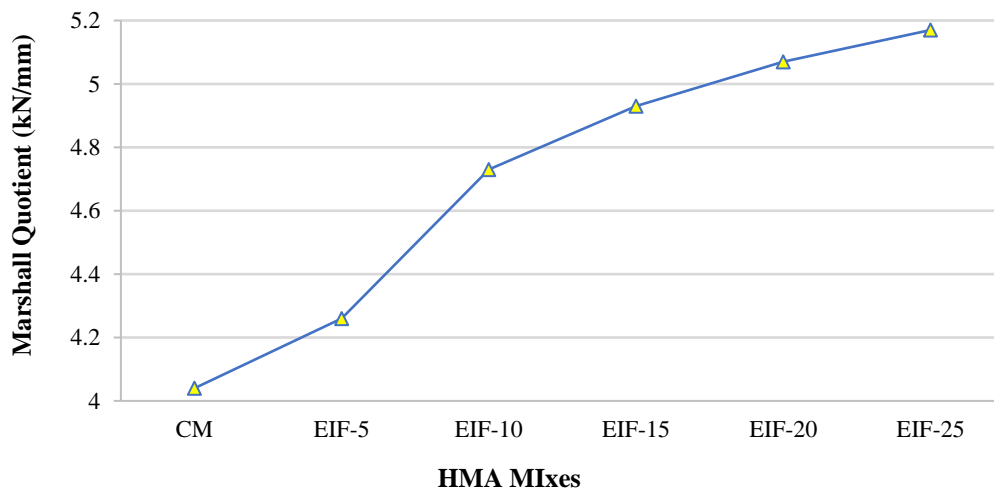
Fig. 14. Marshall quotient of EIF-based HMA mixes
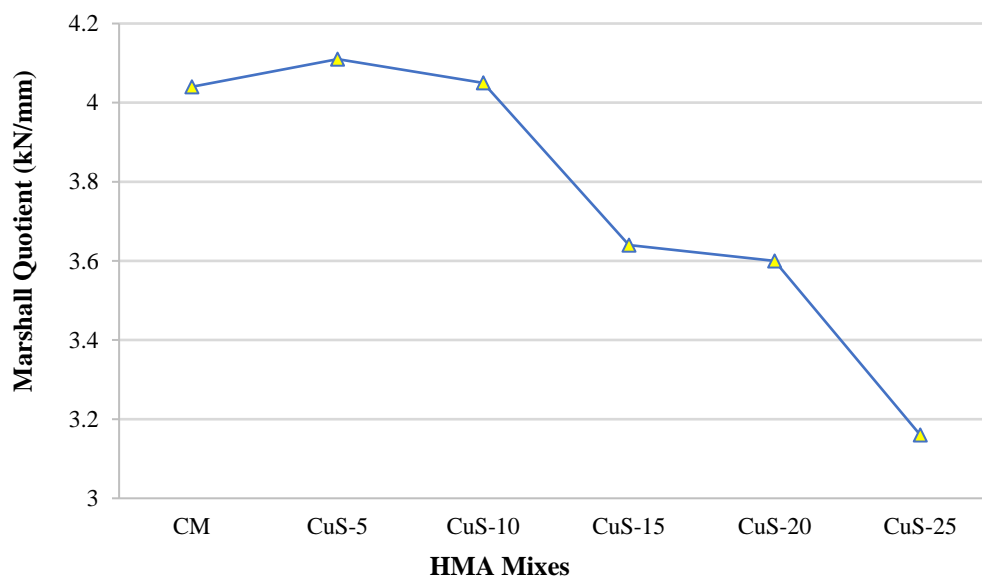
Fig. 15. Marshall quotient of CuS-based HMA mixes

The rutting resistance for the mix EIF-25 was increased by 36.01% as compared to the mix CM. This result was attributed to the high strength and rough surface texture of EIF that allowed for effective interlocking of the aggregates, which resulted in a reduction in rut depth for the EIF-incorporated HMA mixes. In contrast, the CuS-incorporated HMA mixes had an increase in rut depth due to the lack of fine CuS particles, which resulted in a reduction in rutting resistance. The rutting resistance of the CuS-25 mix was found to be reduced by 19.94%. The rut depth for the CuS-25 mix was found to be 4.63 mm and according to Fwa et al. (2012), several highway agencies classify rut depths under 12 mm as low-severe. Therefore, it can be concluded that adding up to 25% of CuS does not result in severe rutting problems on the asphalt pavement.
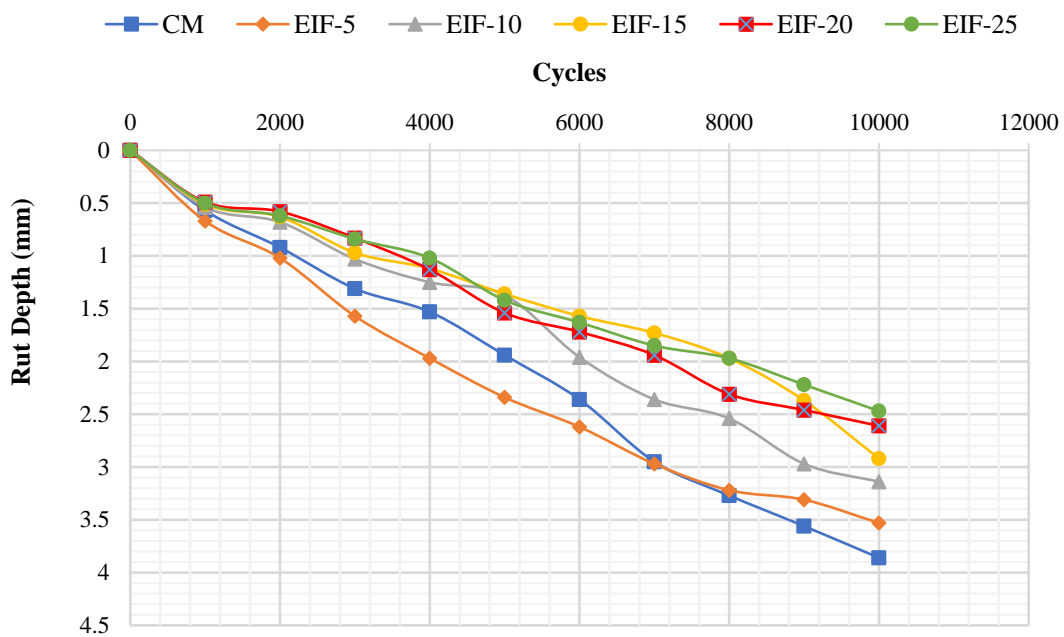
Fig. 16. Rut depth of EIF-based HMA Mixes
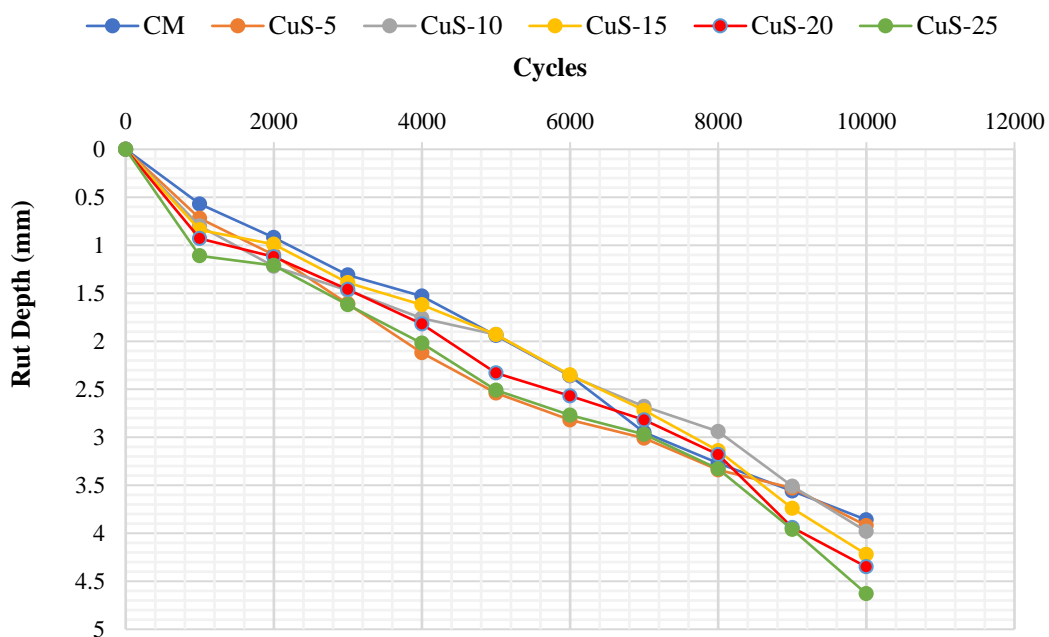
Fig. 17. Rut depth of CuS-based HMA mixes

3.9. Statistical Analysis

To ascertain whether the incorporation of slags in place of fine NGA significantly altered the properties of the HMA mixtures, the experimental findings were subjected to an analysis of variance (ANOVA) at a 95% confidence level. In this case, when the P value is lower than the specified Significance Level (SL), which is 5%, the results are statistically significant (Sig). Sig equal to Y and N indicates that the difference between the means is significant and not significant, respectively. Tables 8 and 9 show the one-way ANOVA outcomes for the EIF and CuS-incorporated HMA mixtures, respectively. The data confirmed that at 5% SL, the difference between the means of the Marshall parameters, ITS, TSR, and rut depth values was significant, indicating that the difference was caused by the addition of EIF and CuS content.

4. Conclusions

In this study, the performance assessment of HMA mixtures containing fine EIF and CuS was examined. The strength, cracking resistance, moisture resistance, and rutting characteristics of the HMA mixtures were evaluated after natural granite aggregates were replaced by weight with 0, 5, 10, 15, 20, and 25% of fine EIF and CuS. From the test results, the following conclusions can be made:

Table 8. Results of one-way ANOVA for EIF-incorporated HMA mixes

Properties	Source of variation	Sum of squares	Degree of freedom	Mean square	F value	P value	Sig
Marshall Parameters	Between group	22362.18	6	3727.03	285.63	<0.0001	Y
	Within group	456.69	35	13.04			
	Total	22818.87	41				
ITS	Between group	1761041.75	1	1761041.75	4246.66	<0.0001	Y
	Within group	4146.89	10	414.69			
	Total	1765188.63	11				
TSR	Between group	2849193.97	3	949731.32	2131.83	<0.0001	Y
	Within group	8909.99	20	445.50			
	Total	2858103.96	23				
Rut depth	Between group	265.73	1	265.73	6.05	0.03365	Y
	Within group	438.93	10	43.89			
	Total	704.67	11				

Table 9. Results of one-way ANOVA for CuS-incorporated HMA mixes

Properties	Source of variation	Sum of squares	Degree of freedom	Mean square	F value	P value	Sig
Marshall parameters	Between group	459.60	3	153.20	6.66	0.00267	Y
	Within group	459.61	20	22.98			
	Total	919.22	23				
ITS	Between group	1301927.15	1	1301927.15	715.04	<0.0001	Y
	Within group	18207.59	10	1820.76			
	Total	1320134.74	11				
TSR	Between group	2079693.27	3	693231.09	525.948	<0.0001	Y
	Within group	26361.16	20	1318.06			
	Total	2106054.43	23				
Rut depth	Between group	208.66	1	208.66	4.76	0.0539	Y
	Within group	437.94	10	43.79			
	Total	646.60	11				

- EIF and CuS outperformed NGA in terms of physical and mechanical properties. XRF results revealed that the materials' major components were CaO, SiO_2, Al_2O_3, FeO, and MgO. The EIF and CuS were found to be more alkaline and hydrophobic in nature than the NGA. This signifies the better binding efficiency of materials with asphalt. Since no potential for volume expansion was found in either of the slags when tested for 7 days, their inclusion in asphalt mixtures can be recommended to minimize the damages related to volumetric expansion. The FESEM image analysis revealed the rough, porous, and irregular surface characteristics of EIF and CuS rather than those of NGA. The rough and porous surface enables the improved binding ability of aggregate with asphalt. Therefore, using EIF and CuS in HMA mixtures can be suggested to have better mechanical strength.
- With the increase in EIF content in HMA mixtures, there was an increase in OAC, Marshall stability, and MQ values. At the same time, flow values were found to be decreasing. The volumetric parameters, such as VMA and VFA, were also increased but remained within the permissible limits. This outcome was attributed to the fact that the EIF content had higher angularity, surface porosity, bulk specific gravity, and angle of internal friction than the NGA. On the other hand, the OAC, VMA, and VFA, also increased with the increasing percentage of CuS content in HMA mixes. Based on the Marshall stability results, replacing fine NGA with CuS decreased the strength of HMA mixes. The HMA mix containing 25% CuS experienced the most significant decline, measuring 33.75% as compared to the control mix.
- The resistance to cracking of all mixtures was evaluated by conducting the ITS test. The asphalt mixture containing a higher percentage of EIF showed higher ITS values for the HMA mixtures, while the inclusion of CuS reduced the ITS. However, all the mixtures were found to be within the required range for ITS. Therefore, the use of an optimum amount of EIF and CuS in HMA mixes can be suggested as a solution to enhance the anti-cracking behavior.
- The TSR of all HMA mixtures was studied to determine moisture sensitivity. It was found that the TSR increased as the replacement percentage of fine NGA with EIF and CuS increased. However, all the HMA mixtures met the value of 80%, which is the minimum requirement. The favorable chemical and morphological attributes of these slags were the reason behind this result.
- The Marshall quotient of the HMA mix was found to be adequate up to 20% EIF content and 25% CuS concentration. The wheel tracking test results show that the rutting resistance of the HMA mixtures comprising EIF increased by 36.01%, while for CuS-based HMA mixtures, it declined by 19.94% for the 25% of their substitution.
- When EIF increased from 15 to 20%, HMA mixtures showed the greatest improvements in Marshall parameters, resistance to cracking, and moisture damage. Thus, this quantity of EIF can be considered the optimum replacement content. The HMA mixes showed the greatest decline in Marshall stability, ITS, and MQ values when the CuS content increased to 20–25%. However, it was discovered that the TSR for the 25% CuS mix was 6.99% greater than the control mix. Thus, the substitution of fine NGA with CuS up to 20% can be considered the optimum replacement content in HMA mixes.

In summary, it can be stated that the application of EIF and CuS as fine aggregates can reduce the consumption of conventional aggregates and offer a viable

waste disposal option. These slags were procured for free from waste yards and did not require any modification before their usage. They could therefore be used effectively where they are abundant. However, the selection of any suitable waste should be performed cautiously after a rigorous analysis of its physical and chemical compositions. For slag-based HMA mixtures, the optimum asphalt content and specific gravity of the HMA mix increased; as a result, it is critical to conduct a cost-benefit analysis to determine the requirements and appropriate amount of their use in each project.

5. Acknowledgement

6. References

AASHTO T245. (2022). *Standard method of test for resistance to plastic flow of asphalt mixtures using Marshall apparatus*, American Association of State Highway and Transportation Officials, Washington.

AASHTO T283. (2014). *Resistance of compacted bituminous mixture to moisture-induced damage*, American Association of State Highway and Transportation Officials, Washington.

Abdelfattah, H.F.H., Al-Shamsi, K. and Al-Jabri, K. (2018). "Evaluation of rutting potential for asphalt concrete mixes containing copper slag", *International Journal of Pavement Engineering*, 19(7), 630-640, https://doi.org/10.1080/10298436.2016.119987 5.

Ahmedzade, P. and Sengoz, B. (2009). "Evaluation of steel slag coarse aggregate in hot mix asphalt concrete", *Journal of hazardous materials*, 165(1-3), 300-305, https://doi.org/10.1016/j.jhazmat.2008.09.105.

Ameri M., Hesami S. and Goli, H. (2013). "Laboratory evaluation of warm mix asphalt mixtures containing electric arc furnace (EAF) steel slag", *Construction and Building materials*, 49, 611-617, https://doi.org/10.1016/j.conbuildmat.2013.08.0

34.

Asi, I.M., Qasrawi, H.Y. and Shalabi, F.I. (2007). "Use of steel slag aggregate in asphalt concrete mixes", *Canadian Journal of Civil Engineering*, 34(8), 902-911, https://doi.org/10.1139/L07-025.

ASTM D4792. (2013). *Standard test method for potential expansion of aggregates from hydration reactions*, West Conshohocken, PA, USA.

ASTM D6931. (2012). *Standard test method for Indirect tensile (IDT) strength of Bituminous mixtures*, West Conshohocken, PA, USA, https://doi.org/10.1520/D6931-12.2.

Benavides, D., Bizinotto, M.B., López, T. and Aponte, D. (2023). "Study of adhesion between steel slag aggregates and bitumen taking into consideration internal factors influencing moisture damage", *Construction and Building Materials*, 367, 130369, https://doi.org/10.1016/j.conbuildmat.2023.130 369.

Chaubey, N.K. and Mishra, A.K. (2020). "Copper slag utilization in paving sustainable asphalt roads", *I-Manager's Journal on Civil Engineering*, 10(4), 46-53, https://doi.org/10.26634/jce.10.4.17469.

Choudhary, J., Kumar, B. and Gupta, A. (2018). "Application of waste materials as fillers in bituminous mixes", *Waste Management*, 78, 417-425, https://doi.org/10.1016/j.wasman.2018.06.009.

EN 12697-22. (2020). *Bituminous mixtures- Test methods- Part 22: Wheel tracking*, European Committee for Standardization (CEN), Brussels.

Fwa, T.F., Pasindu, H.R. and Ong, G.P. (2012). "Critical rut depth for pavement maintenance based on vehicle skidding and hydroplaning consideration", *Journal of Transportation Engineering*, 138(4), 423-429, https://doi.org/10.1061/(ASCE)TE.1943-5436.0000336.

Gautam, P.K., Kalla, P., Nagar, R., Agrawal, R. and Jethoo, A.S. (2018). "Laboratory investigations on hot mix asphalt containing mining waste as aggregates", *Construction and Building Materials*, 168, 143-152, https://doi.org/10.1016/j.conbuildmat.2018.02.1 15.

Ghanbari, M. and Bayat, M. (2022). "Effectiveness of reusing steel slag powder and polypropylene fiber on the enhanced mechanical characteristics of cement-stabilized sand", *Civil Engineering Infrastructures Journal*, 55(2), 241-257, https://doi.org/10.22059/CEIJ.2021.319310.174 2.

Hasita, S., Rachan, R., Suddeepong, A., Horpibulsuk, S., Arulrajah, A., Mohammadinia, A. and Nazir, R. (2020). "Performance improvement of asphalt concretes using steel

slag as a replacement material", *Journal of Materials in Civil Engineering*, 32(8), 04020227, https://doi.org/10.1061/(asce)mt.1943-5533.0003306.

Hasita, S., Suddeepong, A., Horpibulsuk, S., Samingthong, W., Arulrajah, A. and Chinkulkijniwat, A. (2020). "Properties of asphalt concrete using aggregates composed of limestone and steel slag blends", *Journal of Materials in Civil Engineering*, 32(7), 06020007, https://doi.org/10.1061/(ASCE)MT.1943-5533.000314.

Hassan, H.F. and Al-jabri, K. (2011). "Laboratory evaluation of hot-mix asphalt concrete containing copper slag aggregate", *Journal of Materials in Civil Engineering*, 23(6), 879-885, https://doi.org/10.1061/(ASCE)MT.19435533.0000246.

Hu, C., Li, P., Zhu, Y., Zhao, Q. and Zhang, H. (2022). "Experimental study on microwave absorption properties of HMA containing copper slag", *Construction and Building Materials*, 341, 127850, https://doi.org/10.1016/j.conbuildmat.2022.127850.

Indian Mineral Yearbook Part-2. (2019). *Iron, steel and scrape and slag*, 58th Edition, Government of India, Ministry of mines, New Delhi, India.

Ipekyol, A., Tortum, A., Rasouli, R. and Yazdani, M. (2022). "Evaluating fatigue and crack resistance of asphalt mixture containing zinc tailing aggregates", *Case Studies in Construction Materials*, 17, e01384, https://doi.org/10.1016/j.cscm.2022.e01384.

IS-73. (2013). *Indian standard paving bitumen-specification*, 4th Revision, Bureau of Indian Standards. New Delhi, India.

Kandhal, P.S. and Hoffman, G.L. (1997). "Evaluation of steel slag fine aggregate in hot-mix asphalt mixtures", *Transportation Research Record*, 1583(1), 28-36, https://doi.org/10.3141/1583-04.

Kehagia, F. (2009). "Skid resistance performance of asphalt wearing courses with electric arc furnace slag aggregates", *Waste Management and Research*, 27(3), 288-294, https://doi.org/10.1177/0734242X08092025

Ming, N.C., Jaya, R.P., Awang, H., Ing, N.L.S., Hasan, M.RM. and Al-Saffar, Z.H. (2022). "Performance of glass powder as bitumen modifier in hot mix asphalt", *Physics and Chemistry of the Earth Parts A/B/C*, 128, 103263, https://doi.org/10.1016/j.pce.2022.103263.

Modarres, A. and Alinia Bengar, P. (2019). "Investigating the indirect tensile stiffness, toughness and fatigue life of hot mix asphalt containing copper slag powder", *International Journal of Pavement Engineering*, 20(8), 977-985,

https://doi.org/10.1080/10298436.2017.1373390.

MoRTH. (2013). *Specifications for road and bridge works*, Ministry of Road Transport and Highways, 5th Revision, Indian Road Congress. New Delhi, India.

MS-2. (2014). *Mix design methods for asphalt*, Asphalt Institute, 7th Edition.

Muniandy, R., Ismail, D.H. and Hassim, S. (2018). "Performance of recycled ceramic waste as aggregates in Hot Mix Asphalt (HMA)", *Journal of Material Cycles and Waste Management*, 20(2), 844-849, https://doi.org/10.1007/s10163-17-0645-x.

Naser, M., Abdel-Jaber, M.T., Al-shamayleh, R., Louzi, N. and Ibrahim, R. (2022). "Evaluating the effects of using reclaimed asphalt pavement and recycled concrete aggregate on the behavior of hot mix asphalts", Transportation *Engineering*, 10, 100140, https://doi.org/10.1016/j.treng.2022.100140.

Noureldin, A.S. and McDaniel, R.S. (1990). "Evaluation of surface mixtures of steel slag and asphalt", *Transportation Research Record*, 1269(1269), 133-149, http://onlinepubs.trb.org/Onlinepubs/trr/1990/1269/1269-015.pdf.

Oluwasola, E.A., Hainin, M.R., Aziz, M.M.A. and Warid, M.N.M. (2016). "Volumetric properties and leaching effect of asphalt mixes with electric arc furnace steel slag and copper mine tailings", *Sains Malaysiana*, 45(2), 279-287, http://www.ukm.my/jsm/english_journals/vol45num2_2.

Patel, S. and Shahu, J.T. (2018). "Comparison of industrial waste mixtures for use in subbase course of flexible pavements", *Journal of Materials in Civil Engineering*, 30(7), 04018124, https://doi.org/10.1061/(ASCE)MT.1943-5533.000232.

Pundhir, N.K.S., Kamaraj, C. and Nanda, P.K. (2005). "Use of copper slag as construction material in bituminous pavements", *Journal of Scientific and Industrial Research*, 64(12), 997-1002, http://nopr.niscpr.res.in/handle/123456789/5383.

Rochlani, M., Canon Falla, G., Wellner, F., Wang, D., Fan, Z. and Leischner, S. (2021). "Feasibility study of waste ceramic powder as a filler alternative for asphalt mastics using the DSR", *Road Materials and Pavement Design*, 22(11), 2591-2603, https://doi.org/10.1080/14680629.2020.1778508.

Rohde, L., Peres Núñez, W. and Augusto Pereira Ceratti, J. (2003). "Electric arc furnace steel slag: base material for low-volume roads", *Transportation Research Record*, 1819(1), 201-

207, https://doi.org/10.3141/1819b-26.

Shen, D.H., Wu, C.M. and Du, J.C. (2009). "Laboratory investigation of basic oxygen furnace slag for substitution of aggregate in porous asphalt mixture", *Construction and Building Materials*, 23(1), 453-461, https://doi.org/10.1016/j.conbuildmat.2007.11.001.

Tozsin, G., Yonar, F., Yucel, O. and Dikbas, A. (2023). "Utilization possibilities of steel slag as backfill material in coastal structures", *Scientific Reports*, 13(1), 4318, https://doi.org/10.1038/s41598-023-31156-z.

Xie, J., Chen, J., Wu, S., Lin, J. and Wei, W. (2013). "Performance characteristics of asphalt mixture with basic oxygen furnace slag", *Construction and Building Materials*, 38, 796-803, https://doi.org/10.1016/j.conbuildmat.2012.09.056.

Xu, H., Wu, S., Li, H., Zhao, Y. and Lv, Y. (2020). "Study on recycling of steel slags used as coarse and fine aggregates in induction healing asphalt concretes", *Materials*, 13(4), 889, https://doi.org/10.3390/ma13040889.

Xu, X., Luo, Y., Sreeram, A., Wu, Q., Chen, G., Cheng, S., Chen, Z. and Chen, X. (2022). "Potential use of recycled concrete aggregate (RCA) for sustainable asphalt pavements of the future: A state-of-the-art review", *Journal of Cleaner Production*, 344, 130893, https://doi.org/10.1016/j.jclepro.2022.130893.

Yu, H., Zhang, C., Qian, G., Ge, J., Zhu, X., Yao, D. and Shi, C. (2023). "Characterization and evaluation of coarse aggregate wearing morphology on mechanical properties of asphalt mixture", *Construction and Building Materials*, 388, 131299, https://doi.org/10.1016/j.conbuildmat.2023.131299.

Zalnezhad, A., Hosseini, S.A., Shirinabadi, R. and Korandeh, M.E. (2022). "Feasibility of using copper slag as natural aggregate replacement in microsurfacing for quality enhancement: Microscopic and mechanical analysis", *Construction and Building Materials*, 354, 129175. https://doi.org/10.1016/j.conbuildmat.2022.129175.

Zhao, X., Sheng, Y., Lv, H., Jia, H., Liu, Q., Ji, X., Xiong, R. and Meng, J. (2022). "Laboratory investigation on road performances of asphalt mixtures using steel slag and granite as aggregate", *Construction and Building Materials*, 315, 125655, https://doi.org/10.1016/j.conbuildmat.2021.125655.

Ziaee, S.A. and Behnia, K. (2020). "Evaluating the effect of electric arc furnace steel slag on dynamic and static mechanical behavior of warm mix asphalt mixtures", *Journal of Cleaner Production*, 274, 123092, https://doi.org/10.1016/j.jclepro.2020.123092.

Ziari, H., Moniri, A., Imaninasab, R. and Nakhaei, M. (2017). "Effect of copper slag on performance of warm mix asphalt", *International Journal of Pavement Engineering*, 20(7), 775-781, https://doi.org/10.1080/10298436.2017.1339884.

Machine Learning-Based Estimation of Concrete Compressive Strength: A Multi-Model and Multi-Dataset Study

Hoang, N.D.[1*] and Tran, D.V.[1]

[1] Ph.D. Instructor, Faculty of Civil Engineering, Duy Tan University, Da Nang, Vietnam.

ABSTRACT: Concrete is a commonly used construction material due to its favourable engineering properties, such as high compressive strength, good durability, and resistance to corrosion. Accurate predictions of the compressive strength of this material significantly reduce the time and effort required by laboratory tests. The current paper aims to compare the performance of prominent machine learning-based approaches used for predicting the compressive strength of concrete. In addition, 11 historical datasets, collected from the literature, are used. The diversity of the input features, the data dimensionality, and the number of instances can be helpful to evaluate the generalization capability of the employed machine learning models. Repetitive data sampling processes, consisting of 20 independent runs, are carried out to obtain the machine learning models' performances. Through experiments, it can be shown that the gradient boosting machines attain the best performance. Notably, the extreme gradient boosting machine has achieved the best outcome in five historical datasets.

Keywords: Concrete Compressive Strength, Gradient-Boosting Machine, Machine Learning, Regression Models, Comparative Study.

1. Introduction

Concrete has been commonly used in construction due to it is favorable engineering properties such as high compressive strength, good durability, resistance to corrosion, etc. (Chung et al., 2021). Basically, a concrete mix consists of four primary constituents: fine aggregate, coarse aggregate, cement, and water. These constituents can be easily accessed in the local market. These advantages allow concrete to be widely used in various forms of construction projects around the globe.

Moreover, in recent years, many studies have found that supplementary materials like Fly Ash (FA) (Gomaa et al., 2021), Ground Granulated Blast-furnace Slag (GGBS) (Kandiri et al., 2020), silica fume (Kang et al., 2021), and many other industrial/agricultural waste or by-products can be blended into concrete to meliorate its mechanical properties. Han et al. (2020), pointed out that the inclusion of those supplementary materials into concrete offers significant environmental benefits and also enhances the longevity and resiliency of concrete structures. Among various concrete properties, the Compressive Strength (CS) is apparently the most critical since this index directly governs the structural safety and must be

---

* Corresponding author E-mail: hoangnhatduc@duytan.edu.vn

specified to determine the performance of concrete structures throughout their lifecycles (Zhao et al., 2022).

When designing concrete mixes, one significant challenge is to select appropriate materials to achieve a targeted compressive strength. Therefore, it is of immense advantage to possess reliable predictive models that can yield accurate estimation of the CS based on the amount or proportion of the concrete components. These models can help to come up with meaningful predictions that can help to reduce the time and cost required for making and testing samples. Historical data plays a crucial role in constructing robust prediction models.

Recent studies with extensive data collection and model performance comparison have demonstrated the advantages of advanced Machine Learning (ML) models over conventional statistical regression analysis-based models (Ben Chaabene et al., 2020). Accordingly, various ML-based models have been proposed in the literature. Artificial Neural Network (ANN) and Genetic Programming (GP) was used in Chopra et al. (2016) to predict the CS at 28, 56, and 91 days. One advantage of the GP is its capability of constructing predictive formulas used for the CS prediction. However, using the collected dataset, the authors found that ANN is preferable to the GP with respect to predictive accuracy.

ANN was also utilized by Hocine (2018) to estimate the CS of limestone filler concrete and High-Performance Concrete (HPC), respectively. Although ANN-based models are capable nonlinear regressors, their performance substantially depends on the training algorithms. Current training methods of ANNs rely on stochastic gradient descent-based algorithms that are susceptible to being trapped in sub-optimal solutions. Gene expression programming was used by Shahmansouri et al. (2020) to estimate ground granulated blast-furnace slag blended concrete. Using a dataset consisting of 351 specimens, the authors successfully constructed predictive

formulas with high degrees of data fitting. Zhang and Aslani (2021) proposed a data-driven approach based on a back-propagation neural network incorporating ultrasonic pulse velocity for estimating the CS of lightweight aggregate concretes.

Nguyen et al. (2021) developed predictive models based on Support Vector Machine regressor (SVM), ANN, Gradient Boosting Machine (GBM), and Extreme Gradient Boosting (XGBoost) for estimating the CS of HPC. The authors found that GBR and XGBoost perform better than SVM and ANN. Nevertheless, this paper did not explore the capability of XGBoost in predicting the CS of other widely-used concretes (e.g., self-compacting concrete and class F fly ash-blended concrete). An intelligent approach that hybridizes a genetic algorithm and a backpropagation neural network was proposed by Zhang et al. (2021) for predicting the CS of rubberized concrete. GBM was also used by Rathakrishnan et al. (2022) to model the CS of concrete mixes blended with ground granulated blast-furnace slag.

Ensemble learning models based on adaptive boosting machine, GBM, XGBoost, and random forest were proposed by Li and Song (2022). The mixtures included admixtures such as fly ash and silica fume. The authors observed good performance of GBM that achieved a coefficient of determination (R^2) up to 0.96. Naser et al. (2022) applied Multivariate Adaptive Regression Splines (MARS) for estimating the CS of green concrete; MARS obtained the most desired performance (with $R^2 = 0.89$) which is better than that of SVM and random forest.

Hoang (2022) reported superior performances of neural computing models and XGBoost over other data-driven approaches for predicting the CS of self-consolidating concrete; however, the predictive capabilities of MARS and piecewise linear regression models were not investigated. In general, recent reviews and comparative works (Ben Chaabene et al.,

2020; Khambra and Shukla, 2021; Mirrashid and Naderpour, 2020) pointed out an increasing trend of using advanced data-driven tools in estimating this crucial mechanical property of concrete. However, the inclusion of various mineral additions, supplementary materials, and admixtures increases the complexity of the concrete. Thus, it is beneficial for the research community and practitioners to obtain information regarding the predictive capability of prominent ML models in estimating the CS of samples stored in various historical databases.

The current paper aims to compare the capabilities of prominent ML models, including XGBoost, GBM, SVM, MARS, GP, ANN and Sequential Piecewise Linear Regression (SPLR). The selections of the first six models are based on reviewing recent works on ML-based CS prediction (Naser et al., 2022; Nguyen et al., 2021; Tanyildizi and Çevik, 2010; Ullah et al., 2022; Zhang and Aslani, 2021). In addition, the SPLR model has been shown to be a capable nonlinear regressor (Hoang, 2019); however, its performance in modeling the CS has not yet been investigated.

Furthermore, 11 historical datasets, gathered from previous experimental works, are employed to train and test the ML models. Repeated data sampling processes, consisting of 20 runs, are performed to obtain statistical criteria that express the performance of the models. The current study aims to report the prediction results of the employed ML models in estimating the CS of concretes in multiple datasets.

The outcomes of this paper may serve as initial guidance for researchers in selecting appropriate ML models for the task of interest. Since data samples are crucial for constructing reliable ML models, the scope of the paper is limited to the datasets that are openly accessed via data repositories or reported in reliable sources such as academic journal articles. Accordingly, the current work contributes to the body of knowledge in the following aspects:

i) This study investigates the performances of a wide range of ML models, including the powerful methods of gradient boosting machines, for predicting the CS of concretes.

ii) Although XGBoost has shown outstanding performances in modeling the mechanical properties of HPC, its capability in estimating the CS of other concretes (e.g., self-compacting concrete, class F fly ash-blended concrete, rubberized concrete) has not been fully explored.

iii) Datasets representing diverse types of concrete are gathered from previous works to construct and test the ML approaches.

iv) Through experiments, it can be shown that the gradient boosting machines cannot attain the best performance in all datasets. Nevertheless, SVM, MARS, and GP may outperform the gradient-boosting-based models in predicting the CS of certain types of concrete.

2. The Employed Machine Learning Models

2.1. Extreme Gradient Boosting Machine (XGBoost)

The XGBoost (Chen and Guestrin, 2016) is an improved version of the standard the gradient boosting algorithm. This method is essentially an ensemble of boosted regression trees. the model training phase of the ML method is fast since it can be executed in parallel (Zhang et al., 2019).

Let D = {(x_i, y_i)} be a collected dataset including n samples and d predictor variables. The XGBoost employs Z additive functions for estimating the target variable of the CS as follows:

$$\hat{y} = \phi(x_i) = \sum_{z=0}^{Z-1} f_z(x_i) \qquad (1)$$

where $f_z \in F$: is the space of classification trees and $\hat{y}$: is the estimated CS value.

The objective function used in the model training phase is given by Eq. (2).

$$L^t = \sum_{i=0}^{n-1} l(y_i, \hat{y}_i^{t-1} + f_t(x_i)) + \Omega(f_t) \qquad (2)$$

where l: is a loss function which calculates the difference between the predicted (y_i) and the actual variable ($\hat{y}_i$) of the concrete CS at an iteration t. $\Omega(f)$: denotes a function that regularizes the model complexity. The regularization function $\Omega(f)$ is stated as follows:

$$\Omega(f) = \gamma T + \frac{1}{2}\lambda \sum_{j=0}^{T-1} w_j^2 \qquad (3)$$

where γ: is the minimum reduction coefficient, λ: denotes the regularization parameter, T: represents the number of leaves in a classification tree and w: is the weights associated with the leaves.

2.2. Gradient Boosting Machine (GBM)

The GBM iteratively combines a set of weak learners (e.g. trees) to attain a robust learner with enhanced fitting accuracy. This ML method can be viewed as a numerical optimization approach that establishes an additive model that minimizes a loss function (Friedman, 2001). For regression problems, the commonly used loss function is the mean squared error.

Hence, the GBM iteratively adds a new regression tree iteratively that helps reduce the used loss function. Via the process of fitting decision trees to the residuals, the overall ensemble model is enhanced in the regions where it did not well fit the data. The GBM operates by fitting a decision tree f^k at k^{th} iteration using the residual of the previous iteration r_{k-1}.

Accordingly, the updated model $f(x)$ is computed as follows:

$$f(x) = f(x) + \alpha f^k(x) \qquad (4)$$

subsequently, the residual r_k is updated as follows:

$$r_k = r_{k-1} - \alpha f^k(x) \qquad (5)$$

2.3. Support Vector Machine (SVM)

The SVM (Drucker et al., 1996) utilizes a margin of tolerance (ε) for fitting a nonlinear function that describes the mapping relationship between the CS and the concrete mix's constituents. This ML model minimizes the training error and concurrently searches for a hyper-plane that has a maximal margin. Additionally, the kernel function is used to cope with nonlinearity.

In detail, the kernel function has the role of mapping the data from its original input space to a high-dimensional space. In such high-dimensional space, a linear regression model can be established.

The training phase of a SVM model constructs a linear model $f(x)$ that minimizes the structural risk in the feature space:

$$f(x) = w^T \varphi(x) + b \qquad (6)$$

where $\phi(x)$: denotes to a nonlinear mapping from the input space to the high-dimensional feature space; w and b: are the model parameters which are used to specify a SVM model. To compute them, the following constrained optimization problem needs to be solved:

$$\text{Min. } \frac{1}{2}\|w\|^2 + C\sum_{i=1}^{N}(\xi_i + \xi_i^*)$$

subjected to:

$$\begin{cases} y_i - (\langle w, \varphi(x_i)\rangle + b) \le \varepsilon + \xi_i \\ (\langle w, \varphi(x_i)\rangle + b) - y_i \le \varepsilon + \xi_i^* \\ \xi_i, \xi_i^* \ge 0 \end{cases} \qquad (7)$$

where C: denotes the complexity coefficient; ξ_i and ξ_i^*: are the slack variables (Drucker et al., 1996); $i = 1, 2, \ldots, N$ and N is the number of data samples.

2.4. Multivariate Adaptive Regression Splines (MARS)

MARS (Friedman, 1991) constructs a nonlinear mapping relationship by dividing the high-dimensional learning space into sub-ranges of prediction variables. In

addition, this ML model employs piecewise linear functions and an adaptive training approach for model construction. A MARS model can be understood as a set of simple basis functions which describe the relationship between predictor variables and the CS.

A basis function can be expressed as follows:

$$b_m(x) = max(0, C - x)$$
$$\text{or} \qquad (8)$$
$$b_m(x) = max(0, x - C)$$

where b_m: is a basis function; x: denotes an input variable; C: is a threshold parameter used to divide the original range of x into sub-ranges.

Using the concept of the basis function, the general model can be expressed as follows:

$$f(x) = \alpha_0 + \sum_{m=1}^{M} \alpha_m b_m(x) \qquad (9)$$

where $\alpha_0, \alpha_1, ..., \alpha_M$: denote weighting coefficients of the model, $f(x)$: yields the output of the CS and M: represents the number of weighting coefficients.

2.5. Genetic Programming (GP)

The GP (Koza, 1994) is a ML approach inspired by real-world biological systems. This ML method is capable of generating mathematical equations (also called programs) to describe the behaviors of nonlinear systems. Thus, this method can be used to construct predictive equations used for estimating the CS without any assumptions about the prior form of the mapping relationships. GP is able to evolve both the model structure and its parameters according to the collected dataset.

The basic operations of a GP model are described as follows (Koza, 1994; Searson 2015): 1) The generation of a random population of programs; 2) The evaluation of programs with a specified fitness function; 3) The generation of new programs based on the processes of reproduction, mutation, and crossover; 4) The process of self-tuning and comparison of fitness; and 5) the selection of best program through evolutionary competition.

2.6. Artificial Neural Network (ANN)

The ANN is essentially an interconnected network of individual neurons (Haykin, 2008). This ML method is capable of simulating the information processing and knowledge generalization in the human brain. Each neuron uses a nonlinear activation function to process its input signal. To construct an ANN-based CS prediction model, a historical dataset is first collected. Subsequently, the back-propagation framework (Rumelhart et al., 1986) coupled with an optimizer is employed to fit the model's parameters including the weight matrix of the hidden layer (W_1), the weight matrix of the output layer (W_2), the bias vector of the hidden layer (b_1), and the bias vector of the output layer (b_2). The ANN model used for estimating the CS can be stated as follows:

$$f(x) = b_2 + W_2 \times \sigma(b_1 + W_1 \times x) \qquad (10)$$

where x: is the matrix of input variables; σ: denotes the activation function.

In the case of nonlinear function approximation, the Mean Square Error (MSE) loss function is often employed. Additionally, the sigmoid activation function can be used. The adaptive moment estimation (Adam) (Kingma and Ba, 2015) is the state-of-the-art optimizer employed for training the ANN model.

The Adam is an effective first-order gradient-based optimization of stochastic objective functions. This algorithm harnesses the information obtained from the average of the second moments of the gradients to enhance the performance of the optimization process.

A Piecewise Linear Regression Model (PLRM) is a data modeling method that uses Individual linear models to fit a subset of the training data. The transition location

between separated domains of input features is often called a breakpoint or a knot (Breiman, 1993).

The appropriate value of a knot is estimated from the training dataset. SPLR, described by Hoang (2019), employs a sequential algorithm to compute the knots of a PLRM. The model training phase of the SPLR relies on a set of hinge hydrophobic characteristics functions (Breiman, 1993).

This function basically separates the training data into separate domains in which individual linear models can be used to fit the dataset locally. A SPLR model with one predictor variable X and one break point or knot b is given by:

$$
\begin{aligned}
Y = &\beta_0 + \beta_{11}\max(0, \text{sign}(X - b)) + \\
&\beta_{12}\max(0, \text{sign}(b - X)) + \\
&\beta_{21}\max(0, X - b) + \\
&\beta_{22}\max(0, b - X)
\end{aligned}
\tag{11}
$$

where β_0, β_{11} and β_{12}: denote the bias parameters, β_{21} and β_{22}: represent the slope parameters of the two linear models separated by a knot. A general SPLR model used for estimating the CS values is expressed as follows:

$$
Y = \sum_{d=1}^{D}\sum_{v=1}^{V_d} LF_{d,v}(X_d)
\tag{12}
$$

where d: is the index of predictor variables (e.g. the components of a concrete mix), D:

is number of predictor variables, v: denotes the index of the hinge function of the dth predictor variable, V_d: represents the number of hinge functions of the dth explanatory variable.

3. The Collected Datasets

To assess the capability of the employed ML models, this study has selected 11 historical datasets compiled by the previous works. In these datasets, the number of features ranges from 4 to 10. The number of data samples is from 70 to 1030. The selected datasets include normal concrete (Al-Jamimi et al., 2022), high-strength concrete (Al-Shamiri et al., 2019), self-compacting concrete (Kovacevic et al., 2022), lightweight concrete (Tanyildizi and Çevik 2010; Ullah et al., 2022), and high-performance concrete (Videla and Gaedicke 2004; Yeh 1998). In addition, concrete with the alternative binder of GGBS (Shahmansouri et al., 2020) and the alternative aggregate of rubber (Gesoglu et al., 2009) are also considered. The diversity of the features and the number of data instances can be helpful to reveal the overall predictive capability of the ML approaches. The compiled datasets are summarized in Table 1 that provides information regarding the number of features, number of samples, descriptions, and the sources of the data.

Table 1. The employed datasets

Dataset	Number of input features	Number of samples	Description	Reference
1	7	108	Plain and blended cement concretes	Al-Jamimi et al. (2022)
2	5	324	High-strength concrete	Al-Shamiri et al. (2019)
3	8	70	Rubberized concretes	Gesoglu et al. (2009)
4	7	262	Self-Compacting Concrete with class F fly ash	Kovačević et al. (2022)
5	8	144	Concrete containing fly ash and silica fume	Pala et al. (2007)
6	5	117	Concrete containing GGBS	Shahmansouri et al. (2020)
7	6	96	Lightweight concrete containing silica fume	Tanyildizi and Cevik (2010)
8	4	191	Lightweight foamed concrete	Ullah et al. (2022)
9	10	195	Portland blast-furnace slag cement high-performance concrete	Videla and Gaedicke (2004)
10	8	1030	High performance concrete	Yeh (1998)
11	10	323	Concrete with manufactured sand	Zhao et al. (2017)

Table 2 provides an overview of the CS is influencing factors used in each dataset. Furthermore, the frequency of the predictor variables is demonstrated in Figure 1. It is noted that to standardize the range of the variables, this study relied on the Z-score normalization method. The Z-score normalization equation is given by:

$$X_Z = \frac{X_O - \mu_x}{\sigma_x} \tag{13}$$

where d: is the index of predictor variables (e.g. the components of a concrete mix), D: is number of predictor variables, v: denotes the index of the hinge function of the dth predictor variable, V_d: represents the number of hinge functions of the dth explanatory variable.

Table 2. The employed datasets

Input variables	Note	Dataset 1	2	3	4	5	6	7	8	9	10	11
Water content	X_1	x	x	x	x	x	o	o	o	x	x	x
Cement content	X_2	x	x	x	x	x	o	x	x	x	x	o
Water to cement ratio	X_3	o	o	o	o	o	o	x	x	o	o	x
Water to binder ratio	X_4	o	o	o	o	o	o	o	o	o	o	x
Silica fume content	X_5	x	o	x	o	x	x	x	o	x	o	o
Fly ash content	X_6	x	o	o	x	x	o	o	o	o	x	o
Coarse aggregate content	X_7	x	x	x	x	x	o	o	o	x	x	o
Fine aggregate content	X_8	x	x	x	x	x	o	o	x	x	x	o
Superplasticizer content	X_9	o	x	x	x	o	o	x	o	x	x	o
Crump rubber content	X_{10}	o	o	x	o	o	o	o	o	o	o	o
Tire chips content	X_{11}	o	o	x	o	o	o	o	o	o	o	o
High-rate water reducing agent content	X_{12}	o	o	o	o	x	o	o	o	x	o	o
NAOH concentration	X_{13}	o	o	o	o	o	x	o	o	o	o	o
Natural zeolite content	X_{14}	o	o	o	o	o	x	o	o	o	o	o
Ground granulated blast-furnace slag content	X_{15}	o	o	o	o	o	x	o	o	o	o	o
Temperature	X_{16}	o	o	o	o	o	o	x	o	o	o	o
Pumice aggregate	X_{17}	o	o	o	o	o	o	x	o	o	o	o
Foam	X_{18}	o	o	o	o	o	o	o	x	o	o	o
Entrapped air content	X_{19}	o	o	o	o	o	o	o	o	x	o	o
Blast furnace slag	X_{20}	o	o	o	o	o	o	o	o	o	x	o
Compressive strength of cement	X_{21}	o	o	o	o	o	o	o	o	o	o	x
Tensile strength of cement	X_{22}	o	o	o	o	o	o	o	o	o	o	x
D_{max} of crushed stone	X_{23}	o	o	o	o	o	o	o	o	o	o	x
Stone powder content in sand	X_{24}	o	o	o	o	o	o	o	o	o	o	x
Fineness modulus of sand	X_{25}	o	o	o	o	o	o	o	o	o	o	x
Sand ratio	X_{26}	o	o	o	o	o	o	o	o	o	o	x
Slump	X_{27}	o	o	o	o	o	o	o	o	x	o	o
Concrete age	X_{28}	x	o	o	x	x	x	o	o	x	x	x

4. Experimental Results and Discussion

The performance of the ML models with respect to the datasets of concrete strength samples is reported in this section of the article. For each dataset, 90% of the samples are used for training the prediction models; 10% of the dataset is used for testing the models predictive capability. To evaluate the ML models, the Root Mean Square Error (RMSE), Mean Absolute Percentage Error (MAPE) and coefficient of determination (R^2) are computed. The equations used to calculate those indices are presented in the following manner:

$$RMSE = \sqrt{\frac{1}{N}\sum_{i=1}^{N}(y_i - t_i)^2} \tag{14}$$

$$MAPE = \frac{100}{N} \times \sum_{i=1}^{N}\frac{|y_i - t_i|}{y_i} \tag{15}$$

$$R^2 = 1 - \frac{\sum_{i=1}^{N}(t_i - y_i)^2}{\sum_{i=1}^{N}(t_i - \bar{t})^2} \tag{16}$$

where t_i and y_i: are the experimental and estimated CS of the ith sample, respectively, N: denotes the number of samples, $\bar{t}$: is the mean of the actual CS. the RMSE measures the deviations between the experimental and estimated CS values.

It is actually the square root of the second sample moment of the deviations between estimated and actual values. This index aims to aggregate the magnitudes of the residuals in predictions for various data points into a single measurement, indicating the prediction error of a CS prediction model. The RSME is always non-negative and a RMSE of 0 implies a perfect fit to the collected data. Generally, the lower the RMSE is, the better the ML model is.

However, since the RMSE is scale-dependent, it is only valid to compare models fitting one dataset. The MAPE expresses the relative error of the model prediction. Similar to the RMSE, a small value of the MAPE indicates a good ML model. In addition, the R^2 represents the proportion of the variation in the CS of concrete that can be captured by the ML models (Mendenhall and Sincich, 2011).

A $R^2=1$ demonstrates a perfect regression model. Generally, the higher the R^2 is, the better the ML model is. In this study, the XGBoost model is constructed with the built-in functions provided in (XGBoost, 2021). The GBM, SVM, and ANN models are built with the Scikit-Learn library (Pedregosa et al., 2011). The MARS and GP are developed using the MATLAB toolboxes provided by Jekabsons (2016) and Searson (2015), respectively. The SPLR model is constructed in MATLAB by the author. It is noted that the five-fold cross validation processes (Wong and Yeh, 2020) were employed to set the free parameters of the ML models. The performances of the employed ML models in each dataset are presented in Tables 3 and 4. In Table 3, the model accuracy is presented in terms of the average RMSE obtained from the testing phase.

As can be observed from the experimental results the XGBoost model has achieved the best performances in 5 out of 11 datasets. The GBM model is the second best model with 5 times being the 1st rank.

The SVM model has been ranked as the best model twice. Meanwhile, each of the MARS and GP models attains the best outcome in one dataset. The model ranking is further demonstrated by Figure 2. Table 3 reports the average computation time of each model with respect to different datasets. It can be seen that the XGBoost's training phases are fast, with the average training time ranging from 0.03 to 0.06 s.
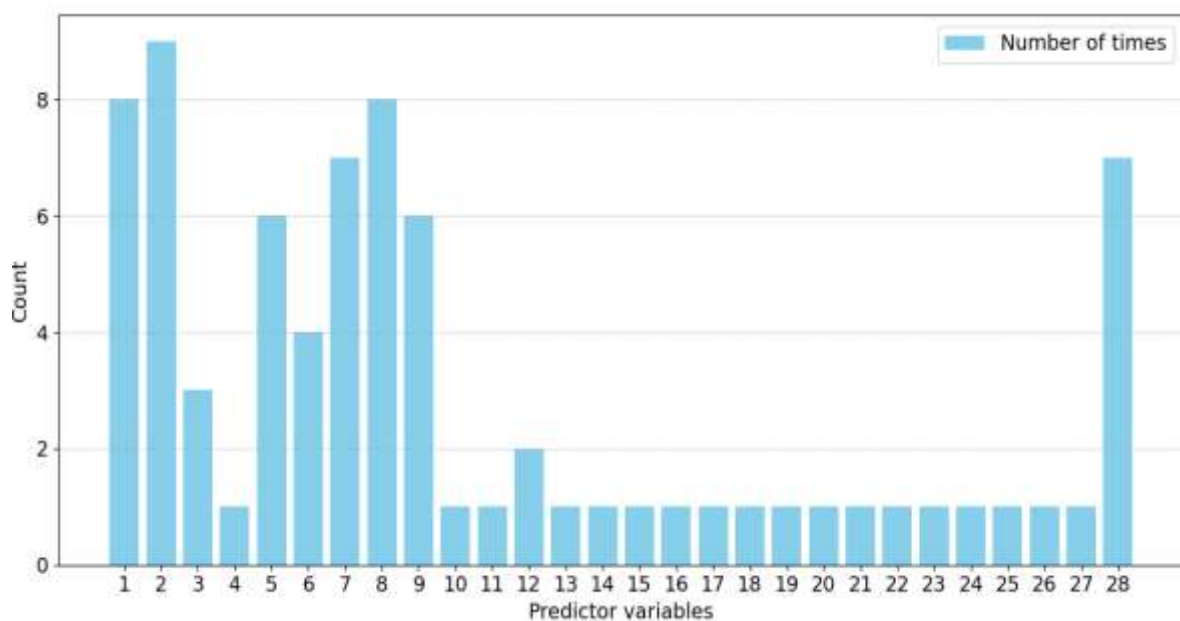

Fig. 1. The frequency of the predictor variables

Table 3. Prediction performance of the models in terms of RMSE

Data	Models						
	XGBoost	GBM	SVM	MARS	GP	ANN	SPLR
1	1.57	1.78	1.33	1.58	1.24	1.97	2.45
2	0.31	0.47	0.92	0.93	1.55	1.62	2.02
3	2.61	2.34	1.2	1.36	1.92	1.96	2.27
4	5.74	5.21	7.11	7.52	8.09	8.15	6.35
5	2.78	2.91	6.02	3.07	3.9	6.01	5.6
6	2.85	2.72	2.24	3.08	3.09	3.67	3.45
7	2.33	2.24	2.43	2.15	2.24	2.85	2.5
8	3.54	3.14	4.51	5.28	5.77	4.52	5.04
9	3.6	3.6	12.02	4.12	4.27	6.72	4.23
10	4.14	4.19	5.26	6.21	6.48	5.93	6.33
11	2.58	2.63	4.74	2.99	5.44	5.47	4.96

Table 4. Computational time (s)

Data	Concrete strength prediction models						
	XGBoost	GBM	SVM	MARS	GP	ANN	SPLR
1	0.03	0.03	0.01	0.12	96.38	0.04	0.05
2	0.03	0.08	0.14	11.33	222.92	0.08	0.05
3	0.03	0.04	0.01	0.10	1.70	0.05	0.06
4	0.04	0.13	0.04	21.15	227.53	0.14	0.70
5	0.03	0.04	0.01	3.80	101.20	0.04	0.03
6	0.03	0.02	0.02	1.50	103.18	0.21	0.06
7	0.03	0.01	0.01	0.06	101.44	0.07	0.08
8	0.04	0.02	0.01	0.13	103.64	0.11	0.03
9	0.03	0.03	0.01	0.66	100.40	0.15	0.75
10	0.06	0.20	0.15	7.30	968.45	0.40	0.29
11	0.03	0.10	0.02	10.87	19.00	0.17	0.14
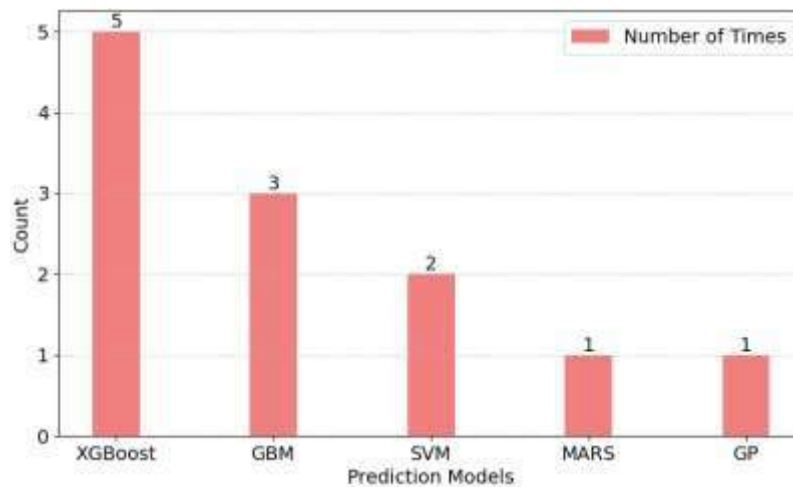
Fig. 2. The number of times that the model achieves the 1st rank

On the contrary, the GP requires much longer computational cost for model training; its training time can go up to 968 s in the Dataset 10. It is understandable because the training phase of the XGBoost model can be carried out in parallel. Meanwhile, the evolutionary operations performed by the GP's populations require much higher computational cost to accomplish. In addition, the detailed performance of the best model as sociated with each dataset is presented in Tables 5 and 6. As can be seen from the experimental results, the ML models are able to fit the datasets to a high degree. These results clearly demonstrate the capability of the ML models in CS prediction of various types of concrete. In general, the MAPE of the CS estimations can be as low as 2.48% in the case of the XGBoost used for

predicting the high-strength concrete samples provided in the Dataset 2 (Al-Shamiri et al., 2019). The R^2 values in all datasets are higher than 0.90 which indicates a sufficient degree of variance explanation. Additionally, in 8 out of 11 datasets, the R^2 is greater than or equal to 0.95. The SVM model used for predicting the CS of rubberized concrete achieves the R^2 of roughly 1 which indicates a nearly perfect fit. Herein, the red straight line represents a perfect fit. The scatter plots providing the overview of the data fitting results are presented in Figure 3.

The nearer the data points (denoted as black circles) to the red line, the better they are fitted by the ML models. The lines of ±10% and ± 20% bounds are also added to inspect the magnitude of the models' residuals. Most of the prediction errors lie within the ±20% bound. The Dataset 4 (self-compacting concrete blended with class F fly ash), the Dataset 8 (lightweight foamed concrete), and the Dataset 10 (high-performance concrete) have high proportions of data beyond the ±20% bound. One possible reason for this phenomenon is that the complexity of the mapping functions between the CS and its influencing factors hidden in those data is high.

Table 5. Performances of the best models (from Dataset 1 to Dataset 6)

Dataset	The best model	Performance indices	Mean	Std.
1	GP	RSME	1.24	0.36
		MAPE (%)	3.25	1.02
		R^2	0.97	0.03
2	XGBoost	RSME	1.55	0.16
		MAPE (%)	2.48	0.35
		R^2	0.97	0.01
3	SVM	RSME	1.20	0.34
		MAPE (%)	2.93	1.47
		R^2	1.00	0.00
4	GBM	RSME	5.21	0.88
		MAPE (%)	12.34	2.45
		R^2	0.91	0.03
5	XGBoost	RSME	2.78	0.62
		MAPE (%)	5.13	1.33
		R^2	0.98	0.01
6	SVM	RSME	2.24	0.67
		MAPE (%)	2.72	0.78
		R^2	0.93	0.05

Table 6. Performances of the best models (from Dataset 7 to Dataset 11)

Dataset	The best model	Performance indices	Mean	Std.
7	MARS	RSME	2.15	0.39
		MAPE (%)	8.28	2.85
		R^2	0.95	0.03
8	GBM	RSME	3.14	0.95
		MAPE (%)	19.20	10.30
		R^2	0.94	0.05
9	XGBoost	RSME	3.60	0.63
		MAPE (%)	4.90	1.03
		R^2	0.97	0.01
9	GBM	RSME	3.60	0.69
		MAPE (%)	4.87	1.12
		R^2	0.97	0.01
10	XGBoost	RSME	4.14	0.44
		MAPE (%)	9.97	1.14
		R^2	0.94	0.02
11	XGBoost	RSME	2.58	0.85
		MAPE (%)	5.10	5.00
		R^2	0.97	0.02
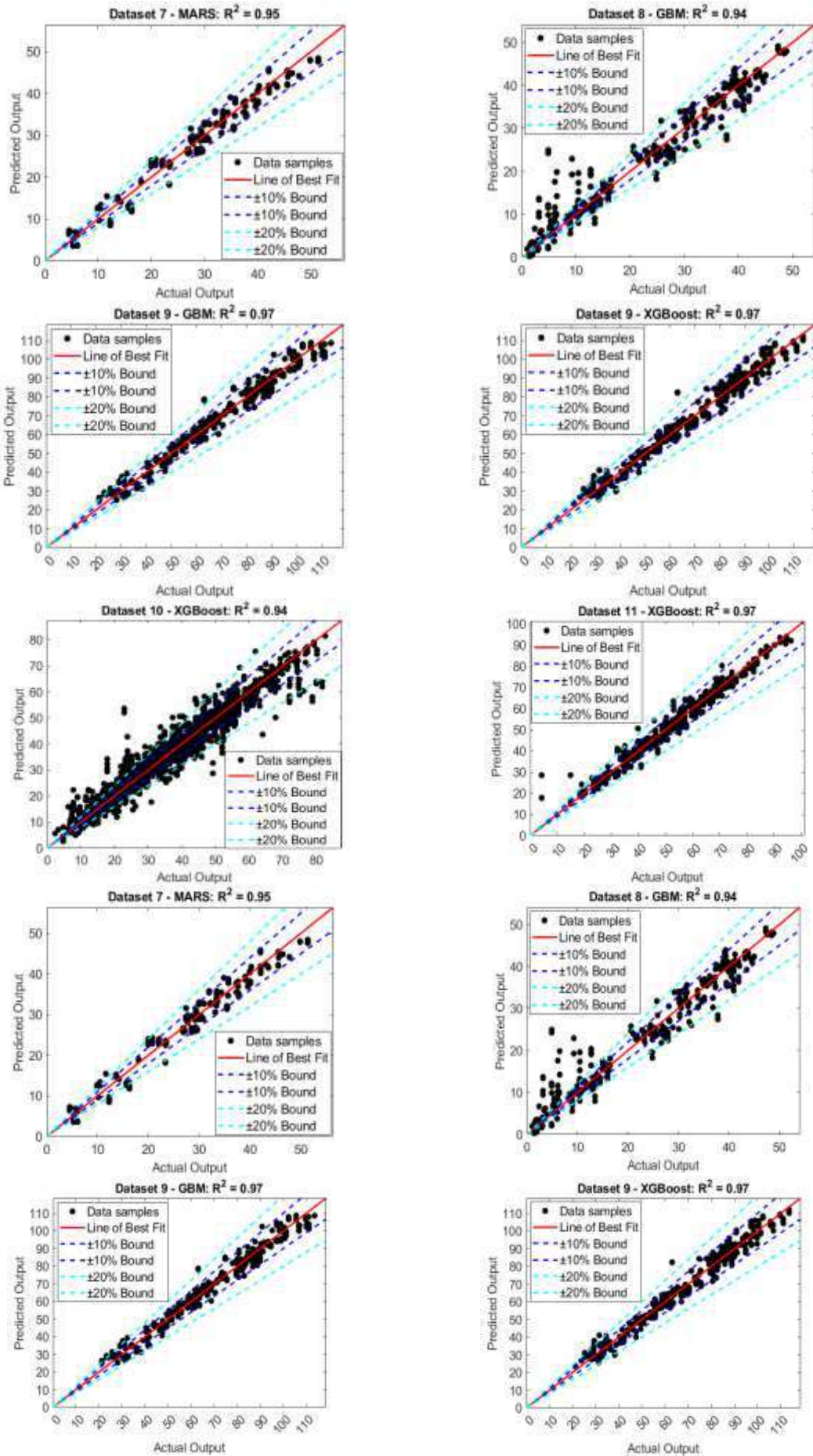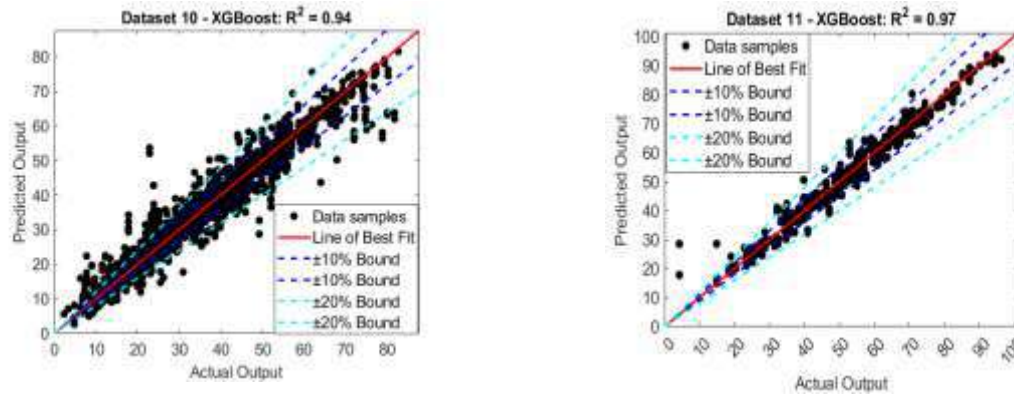
Fig. 3. Line of best fit plots

Table 7. Summary of the models' rank

Models	Dataset										
	1	2	3	4	5	6	7	8	9	10	11
XGBoost	3	1	7	2	1	3	4	2	1	1	1
GBM	5	2	6	1	2	2	2	1	1	2	2
SVM	2	3	1	4	7	1	5	3	7	3	4
MARS	4	4	2	5	3	4	1	6	3	5	3
GP	1	5	3	6	4	5	3	7	5	7	6
ANN	6	6	4	7	6	7	7	4	6	4	7
SPLR	7	7	5	3	5	6	6	5	4	6	5

Notably, the number of influencing factors used by the Dataset 8 is 4 which is quiet limited. It is possible that the CS values of the lightweight foamed concrete samples are affected by other explanatory factors that are not yet covered by the current work. Datasets 1, 2, 3, 5, 6, and 9 have the major proportion of the samples lying within the ±10% bound. This fact indicates a strong correlation between the estimated and the observed CS values.

Table 7 and Figure 4 summarize the ranks of the ML models with respect to different datasets. Apparently, the XGBoost is the best model with five 1st ranks, two 2nd ranks and two 3rd ranks. The GBM model is the second best one with three 1st ranks and six 2nd ranks. The SVM model succeeds the GBM model with two 1st ranks, one 2nd ranks, and three 3rd ranks. Each of the GP and MARS models achieves one 1st rank. However, MARS achieves the 2nd rank in one dataset. In addition, the highest rank of SPLR is the 3rd; the rank of the ANN model never goes higher than the 4th.

Thus, the outcomes of this study are in line with the previous works of Nguyen et

al. (2021) and Kang et al. (2021) which points out the advantage of the XGBoost and GBM models. However, the SVM, MARS and GP models can also be the models of choice in the tasks of predicting the CS of the rubberized concrete, concrete containing GGBS and lightweight concrete containing silica fume. More details regarding the performances of the ML models are reported in Appendix 1 (boxplots of the model performance) and Appendix 2 (detailed model ranking).

5. Concluding Remarks

CS is considered the most important mechanical property of concrete. This index serves as a crucial indicator of the concrete quality. This study carried out a large-scale comparative study which investigates the performance of the prominent ML models used in estimating the CS of 11 historical datasets. The number of explanatory variables in these datasets ranged from 4 to 10. The number of samples ranged from 70 to 1030.
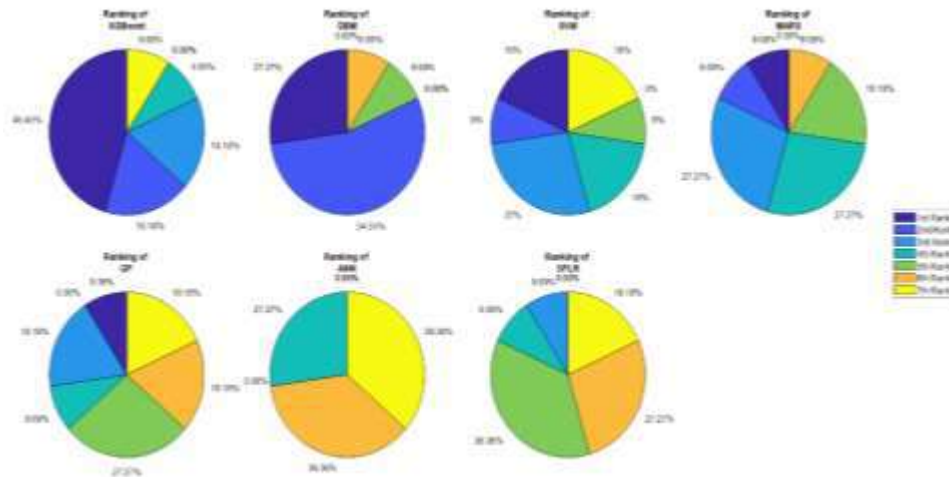
Fig. 4. Percentages of the model rankings

XGBoost, GBM, SVM, MARS, GP, ANN and SPLR were employed and their performances were benchmarked with the indices of RMSE, MAPE and R^2. Repetitive data sampling processes, consisting of 20 independent runs, were used for reliably assessing the model predictive capability.

Experimental results pointed out that the XGBoost model was achieved the most desired outcomes with 5 times of 1st rank. Its performance was followed by the GBM, SVM, MARS and GP. The highest rank that the SPRL achieves was 3rd and its performance was slightly better than that of ANN.

In general, XGBoost and GBM are the models of choice when dealing with the task of CS estimation. However, SVM, MARS, and GP should also be attempted for estimating the CS of the rubberized concrete, concrete containing GGBS, and lightweight concrete containing silica fume.

The prediction of the CS of diverse concrete types is a highly active research topic. Therefore, there are various datasets of concrete strength that are documented in the literature. In addition, researchers continuously compile, analyze, and report the testing records of the CS of concrete.

Hence, due to the limited time frame of the current study, the selected datasets in the current work cannot be comprehensive and cover all relevant datasets. In addition to the selected ML models, many other advanced methods (e.g., sophisticated ensembles of decision trees, light gradient boosting machines, neural networks trained by novel metaheuristic algorithms, etc.) also have potential for the task of interest.

Accordingly, the current work can be extended in multiple ways such as:

i) The investigation of other advanced ML methods such as deep learning regression (Zeng et al., 2022), hybrid ensemble learning (Cao et al., 2022), metaheuristic-trained ANN (Zhang et al., 2021) and ensemble deep neural networks (Barkhordari and Massone, 2022),

ii) The collection of more experimental datasets used for model validation.

iii) The applications of advanced feature selection for enhancing the model performance.

6. Supplementary Material

The datasets used to support the findings of this study are deposited in GitHub repository as follows: https://github.com/nhddtuedu/cs ml.

7. References

Al-Jamimi, H.A., Al-Kutti, W.A., Alwahaishi, S. and Alotaibi, K.S. (2022). "Prediction of compressive strength in plain and blended cement concretes using a hybrid artificial intelligence model", *Case Studies in Construction Materials*, 17, e01238, https://doi.org/10.1016/j.cscm.2022.e01238.

Al-Shamiri, A.K., Kim, J.H., Yuan, T.F. and Yoon,

Y.S. (2019). "Modeling the compressive strength of high-strength concrete: An extreme learning approach", *Construction and Building Materials*, 208, 204-219, https://doi.org/10.1016/j.conbuildmat.2019.02.165.

Barkhordari, M.S. and Massone, L.M. (2022). "Failure mode detection of reinforced concrete shear walls using ensemble deep Neural Networks, *International Journal of Concrete Structures and Materials"*, 16, 33, https://doi:10.1186/s40069-022-00522-y.

Ben Chaabene, W., Flah, M. and Nehdi, M.L. (2020). "Machine learning prediction of mechanical properties of concrete: *Critical review, construction and Building Materials*, 260, 119889, https://doi.org/10.1016/j.conbuildmat.2020.119889.

Bishop, CM. (2011). *Pattern recognition and machine learning (Information science and statistics)*, Springer, ISBN-10: 0387310738.

Breiman, L. (1993). "Hinging hyperplanes for regression, classification and function approximation", *IEEE Transactions on Information Theory*, 39, 999-1013, https://doi:10.110 9/18.256506.

Cao, M.T., Nguyen, N.M. and Wang, W.C. (2022). "Using an evolutionary heterogeneous ensemble of artificial neural network and multivariate adaptive regression splines to predict bearing capacity in axial piles, *Engineering Structures*, 268, 114769, https://doi.org/10.1016/j.engstruct.2022.114769.

Chen, T. and Guestrin, C. (2016). "XGBoost: A scalable tree boosting system*", Proceedings of the 22nd ACM SIGKDD International Conference on Knowledge Discovery and Data Mining,* San Francisco, California*, USA,* 785-794, https://doi.org/10.1145/2939672.29385.

Chopra, P., Sharma, R.K. and Kumar, M. (2016). "Prediction of compressive strength of concrete using Artificial Neural Network and Genetic Programming", *Advances in Materials Science and Engineering*, 2016, 7648467, https://doi.org/10.1155/2016/7648467.

Chung, K.L., Wang, L., Ghannam, M., Guan, M. and Luo, J. (2021). "Prediction of concrete compressive strength based on early-age effective conductivity measurement", *Journal of Building Engineering,* 35, 101998, https://doi.org/10 .1 016/j.jobe.2020.101998.

Drucker, H., Burges, CJC., Kaufman, L., Smola, A. and Vapnik, V. (1996). "Support vector regression machines", *Proceedings of the 9th International Conference on Neural Information Processing Systems,* Denver, Colorado.

Friedman, JH. (1991). "Multivariate adaptive regression spline*s", The Annals of Statistics,* 19(1), 1-67, https://doi.org/10.1214/aos/1176347963.

Friedman, JH. (2001). "Greedy function approximation: A Gradient Boosting Machine", *The Annals of Statistics,* 29(5), 1189-1232.

Friedman, J.H. (2002). "Stochastic gradient boosting", *Computational Statistics and Data Analysis*, 38(4), 367-378, https://doi.org/10.1016/S0167-9473(01)00065-2.

Gesoglu, M., Güneyisi, E., Özturan, T. and Özbay, E. (2009). "Modeling the mechanical properties of rubberized concretes by neural network and genetic programming", *Materials and Structures*, 43, 31, https://doi:10.1617/s11527-009-9468-0.

Gomaa, E., Han, T., ElGawady, M., Huang, J. and Kumar, A. (2021). "Machine learning to predict properties of fresh and hardened alkali-activated concrete", *Cement and Concrete Composites,* 115, 103863, https://doi.org/10.1016/j.cemconcomp.2020.103863.

Han, T., Siddique, A., Khayat, K., Huang, J. and Kumar, A. (2020). "An ensemble machine learning approach for prediction and optimization of modulus of elasticity of recycled aggregate concrete", *Construction and Building Materials,* 244, 118271, https://doi.org/10.1016/j.conb   uildmat.2020.118271.

Haykin, SO. (2008). *Neural Networks and Learning Machines*, Pearson, London, United Kingdom.

Hoang, N.D. (2019). "Estimating punching shear capacity of steel fibre reinforced concrete slabs using sequential piecewise multiple linear regression and Artificial Neural Network", *Measurement*, 137, 58-70, https://doi.org/10.1016/j.measurement.2019.01.035.

Hoang, N.D. (2022). "Machine learning-based estimation of the compressive strength of self-compacting concrete", *A Multi-Dataset Study Mathematics*, 10, 3771.

Hocine, A. (2018). "Compressive strength prediction of limestone filler concrete using artificial neural networks", *Advances in Computational Design*, 3(3), 289-302, https://doi.org/10.12989/acd.2018.3.3.289.

Jekabsons, G. (2016). ARESLab: *Adaptive regression splines toolbox for Matlab/Octave,* Technical Report, Riga Technical University, available at http://wwwcsrtulv/jekabsons/.

Kandiri, A., Mohammadi Golafshani, E. and Behnood, A. (2020). "Estimation of the compressive strength of concretes containing ground granulated blast furnace slag using hybridized multi-objective ANN and salp swarm algorithm", *Construction and Building Materials*, 248, 118676, https://doi.org/10.1016/j.conbuildmat.2020.118

676.

Kang, M.C., Yoo, D.Y., Gupta, R. (2021). "Machine learning-based prediction for compressive and flexural strengths of steel fiber-reinforced concrete", *Construction and Building Materials*, 266, 121117. https://doi.org/10.1016/j.conb uildmat.2020.121117.

Khambra, G. and Shukla, P. (2021). "Novel machine learning applications on fly ash based concrete", *An Overview Materials Today: Proceedings,* https://doi.org/10.1016/j.matpr.2021.07.262.

Kingma, D.P. and Ba, J. (2015). "Adam: *A method for stochastic optimization*, arXiv:14126980 [csLG], https://doi.org/10.48550/arXiv.1412.6980.

Kovacevic, M., Lozancic, S., Nyarko, E.K. and Hadzima-Nyarko, M. (2022). "Application of artificial intelligence methods for predicting the compressive strength of self-compacting concrete with class f, Fly Ash", *Materials*, 15, 4191.

Koza, J.R. (1994). "Genetic programming as a means for programming computers by natural selection", *Statistics and Computing,* 4, 87-112, https://doi:10.1007/BF00175355.

Li, Q.F. and Song, Z.M. (2022). "High-performance concrete strength prediction based on ensemble learning", *Construction and Building Materials,* 324, 126694, https://doi.org/10.1016/j.conb uildmat.2022.126694.

Mendenhall, W. and Sincich, T.T. (2011). *A second course in statistics: Regression analysis,* 7th Edition, Pearson, ISSN 978-0321691699.

Mirrashid, M., Naderpour, H. (2020). "Recent trends in prediction of concrete elements behavior using soft computing (2010-2020)", *Archives of Computational Methods in Engineering,* https://doi:10.1007/s11831-020-09500-7.

Naser, A.H., Badr, A.H., Henedy, S.N., Ostrowski, K.A. and Imran, H. (2022). "Application of Multivariate Adaptive Regression Splines (MARS) approach in prediction of compressive strength of eco-friendly concrete", *Case Studies in Construction Materials*, 17, e01262, https://doi.org /10.101 6/j.cscm.2022.e01262.

Nguyen, H., Vu, T., Vo, T.P. and Thai, H.T. (2021). "Efficient machine learning models for prediction of concrete strengths", *Construction and Building Material*s, 266, 120950, https://doi.org/10.1016/j.conbuildmat.2020.120 950.

Pala, M., Ozbay, E., Oztas, A. and Yuce, MI. (2007). Appraisal of long-term effects of fly ash and silica fume on compressive strength of concrete by neural networks", *Construction and Building Materials,* 21, 384-394, https://doi.org/10.1016/j.conbuildmat.2005.08.0 09.

Pedregosa, F. et al. (2011). "Scikit-learn: Machine learning in Python", *Journal of Machine Learning Research,* 12, 2825-2830.

Rathakrishnan, V.Bt., Beddu, S., Ahmed, A.N. (2022). "Predicting compressive strength of high-performance concrete with high volume ground granulated blast-furnace slag replacement using boosting machine learning algorithms", *Scientific Reports*, 12, 9539, https://doi:10.1038/s41598-02212890-2.

Rumelhart, D.E., Hinton, G.E. and Williams, R.J. (1986). "Learning representations by back-propagating errors", *Nature*, 323, 533-536, https://doi:10.1038/323533a0.

Ryan, S.E. and Porth, L.S. (2007). "A tutorial on the piecewise regression approach applied to bedload transport data", General Technical Report RMRS-GTR-189, Fort Collins, CO: US Department of Agriculture, Forest Service, Rocky Mountain Research Station, 41p, https://doi.org/10.2737/RMRS-GTR-189.

Searson, D.P. (2015), GPTIPS 2: An open-source software platform for symbolic data mining", In: Gandomi, A.H., Alavi, A.H., Ryan, C. (Eds.), *Handbook of Genetic Programming Applications*, Springer International Publishing, Cham, 22 p., 551-573, https://doi:10.1007/978-3-319-20883-1.

Shahmansouri, A.A., Akbarzadeh Bengar, H. and Ghanbari, S. (2020), "Compressive strength prediction of eco-efficient GGBS-based geopolymer concrete using GEP method", *Journal of Building Engineering,* 31, 101326, https://doi.org/10.1016/j.jobe.2020.101326.

Tanyildizi, H. and Çevik, A. (2010). "Modeling mechanical performance of lightweight concrete containing silica fume exposed to high temperature using genetic programming", *Construction and Building Materials*, 24, 2612-2618, https://doi.org/10.1016/j.conbuildmat.201005.0 01.

Touzani, S., Granderson, J. and Fernandes, S. (2018). "Gradient boosting machine for modeling the energy consumption of commercial buildings", *Energy and Buildings*, 158, 1533-1543, https://doi.org/10.1016/j.enbuild.2017.11.039.

Ullah, HS., Khushnood, R.A., Ahmad, J. and Farooq, F. (2022). "Predictive modelling of sustainable lightweight foamed concrete using machine learning novel approach", *Journal of Building Engineering,* 56, 104746. https://doi.org/1 0.1016/j.jobe.2022.104746.

Videla, C. and Gaedicke, C. (2004). "Modeling portland blast-furnace slag cement high-performance concrete", ACI, *Materials Journal*, 101, 365-375.

Wong, T. and Yeh, P. (2020). "Reliable accuracy estimates from k-fold cross validation", *IEEE Transactions on Knowledge and Data Engineering,* 32, 1586-1594,
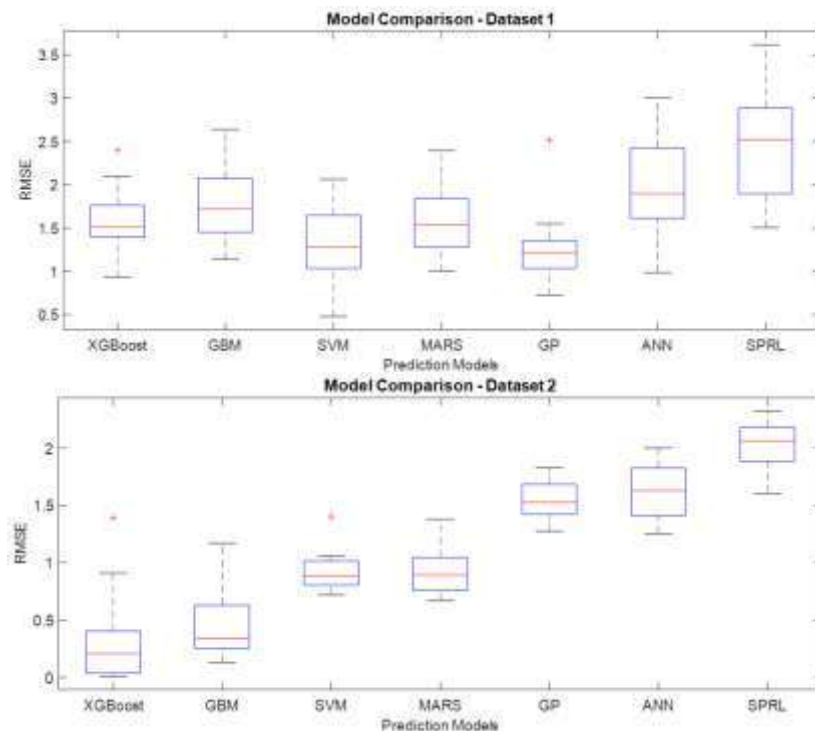
https://doi:10.1109/TKDE.2019.2912815.

XGBoost, (2021). "XGBoost documentation", https://xgboostreadthedocsio/en/stable/indexhtml" (Last access: 12/30/2021).

Yeh, I.C. (1998). Modeling concrete strength with Augment-Neuron Networks", *Journal of Materials in Civil Engineering*, 10, 263-268, https://doi:10.1061/(ASCE)08991561(1998)10:4(263).

Zeng, Z., Zhu, Z., Yao, W., Wang, Z., Wang, C., Wei, Y., Wei, Z. and Guan, X. (2022). "Accurate prediction of concrete compressive strength based on explainable features using deep learning", *Construction and Building Materials*, 329, 127082, https://doi.org/10.1016/j.conbuildmat.2022127082.

Zhang, X., Nguyen, H., Bui, X.N., Tran, Q.H., Nguyen, D.A., Bui, D.T. and Moayedi, H. (2019). "Novel soft computing model for predicting blast-induced ground vibration in open-pit mines based on Particle Swarm Optimization and XGBoost", *Natural Resources Research*, https://doi:10.1007/s11053-019-9492-7.

Zhang, Y. and Aslani, F. (2021). "Compressive strength prediction models of lightweight aggregate concretes using ultrasonic pulse velocity", *Construction and Building Materials*, 292, 123419, https://doi.org/10.1016/j.conbuildmat.2021.123419.

Zhang, Y., Aslani, F. and Lehane, B. (2021). "Compressive strength of rubberized concrete: Regression and GA-BPNN approaches using ultrasonic pulse velocity", *Construction and Building Materials,* 307, 124951, https://doi.org/10.1016/j.conbuildmat.2021.124951.

Zhao, S., Hu, F., Ding, X., Zhao, M., Li, C. and Pei, S. (2017). "Dataset of tensile strength development of concrete with manufactured sand" Data in Brief*, 11, 469-472, https://doi.org/10.1016/j.dib.2 017.02.043.

Zhao, Y., Hu, H., Song, C. and Wang, Z. (2022). "Predicting compressive strength of manufactured-sand concrete using conventional and metaheuristic-tuned Artificial Neural Network", *Measurement*, 194, 110993, https://doi.org/10.1016/j.measurement.2022.110993.

Appendix 1

Boxplots of the Model Performance

Model Comparison - Dataset 3

Model Comparison - Dataset 4

Model Comparison - Dataset 5

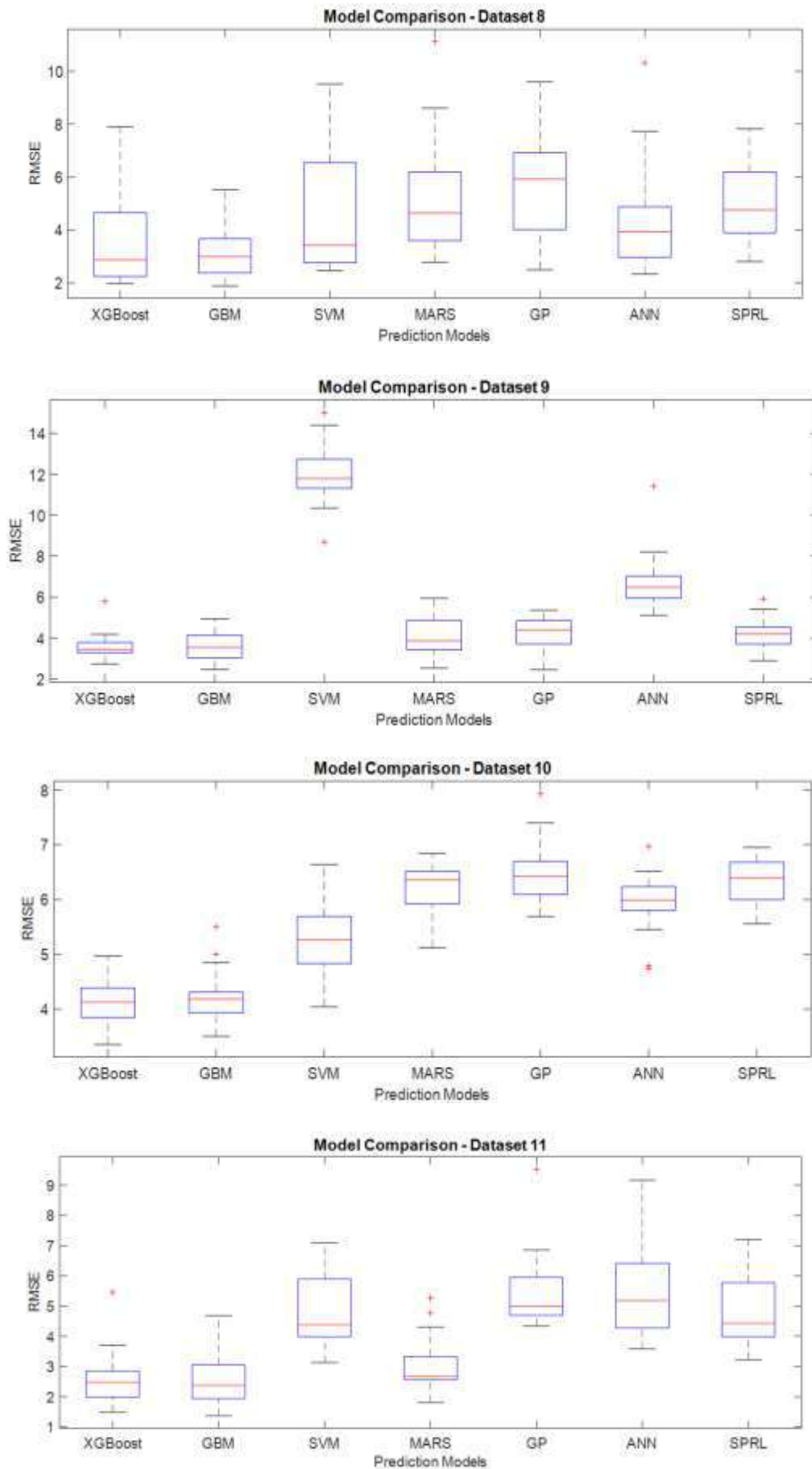Model Comparison - Dataset 6

Model Comparison - Dataset 7
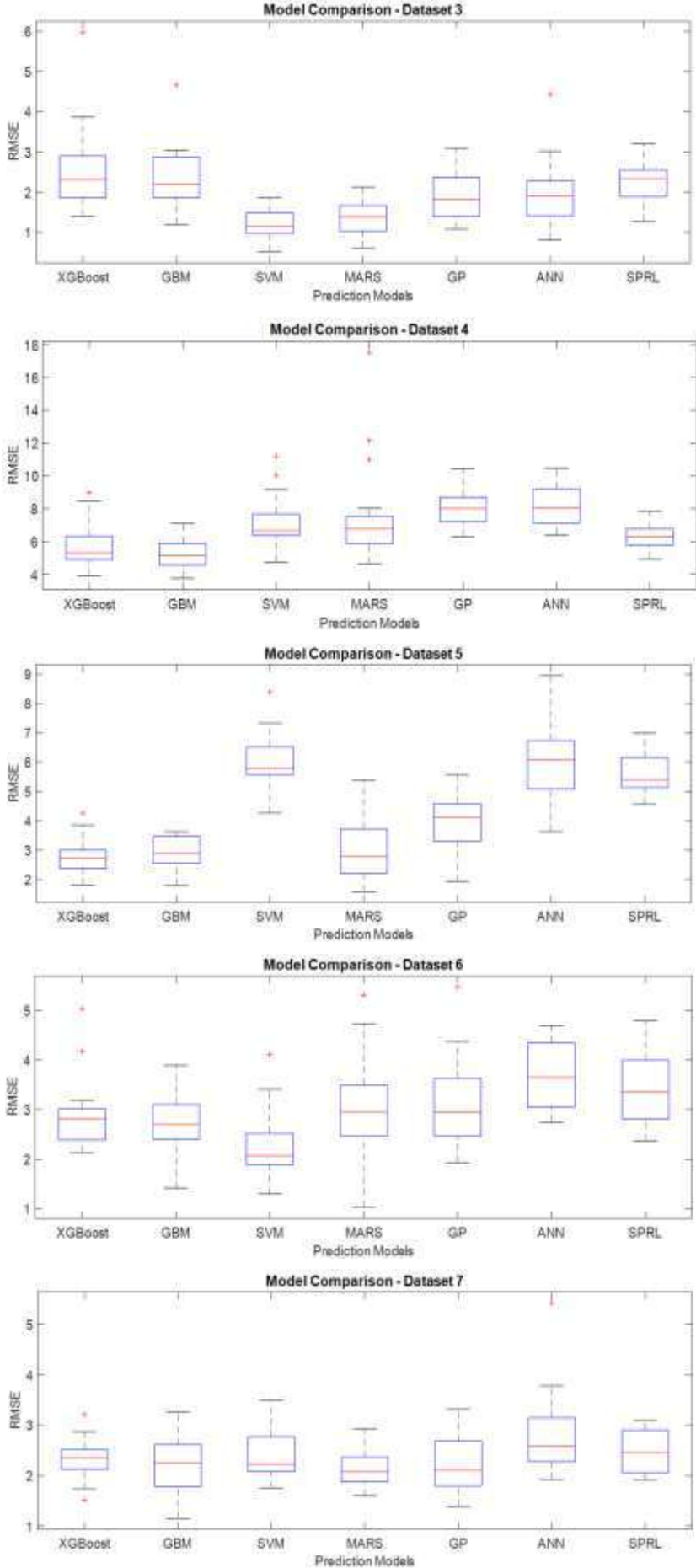
Fig. A1-1. Boxplots of the model performance

Appendix 2

Models' Ranking

Table A2-1. Ranking of the models

Dataset	Models	RMSE	Ranking
1	GP	1.24	1
	SVM	1.33	2
	XGBoost	1.57	3
	MARS	1.58	4
	GBM	1.78	5
	ANN	1.97	6
	SPRL	2.45	7
2	XGBoost	0.31	1
	GBM	0.47	2
	SVM	0.92	3
	MARS	0.93	4
	GP	1.55	5
	ANN	1.62	6
	SPRL	2.02	7
3	SVM	1.20	1
	MARS	1.36	2
	GP	1.92	3
	ANN	1.96	4
	SPRL	2.27	5
	GBM	2.34	6
	XGBoost	2.61	7
4	GBM	5.21	1
	XGBoost	5.74	2
	SPRL	6.35	3
	SVM	7.11	4
	MARS	7.52	5
	GP	8.09	6
	ANN	8.15	7
5	XGBoost	2.78	1
	GBM	2.91	2
	MARS	3.07	3
	GP	3.9	4
	SPRL	5.6	5
	ANN	6.01	6
	SVM	6.02	7

RESEARCH PAPER

Seismic Assessment of Base-Isolated Structure Under a Sequence of Near-Fault Earthquake Records

Yousef, I.[1], Al-Nawaiseh, M.[2] and Al-Rawashdeh, M.[3*]

[1] Assistant Professor, Department of Civil Engineering, Munib and Angela Masri Faculty of Engineering, Aqaba University of Technology, Jordan.
[2] Assistant Professor, Department of Civil Engineering, Faculty of Engineering, Amman Arab University, Jordan.
[3] Assistant Professor, Department of Civil Engineering, Faculty of Engineering, Al-Balqa Applied University, Jordan.

ABSTRACT: This paper investigates the performance and efficacy of Quintuple Friction Pendulum (QTFP) isolators under a sequence of near-fault foreshock, main shock and aftershock earthquake events. The QTFP isolator is an advanced base isolation device utilized in Reinforced Concrete (RC) structures to alleviate damage from severe seismic activity. Despite its proven ability to restrict structural responses and meet particular performance goals under severe seismic excitation, comprehensive analyses of QTFP isolators performance under sequential earthquakes are scarce. This research employs finite element analysis to explore the seismic behavior of RC structures equipped with QTFP isolators during such sequences. It also assesses the effectiveness of QTFP isolators by evaluating the seismic behavior of base-isolated RC structures subjected to sequence earthquakes. In general, the sequence of foreshock, main shock and aftershock earthquake events critically impacts the structural response, with the foreshock producing the highest base shear, inter-story drift and acceleration responses. Furthermore, the aftershock accounted for the most considerable input, damping, and hysteretic energies. The research offers insights into the hysteresis behavior of the isolators, particularly during the main shock, where the combination of 2.15 seconds period and 10% damping showcased the most extensive hysteresis loop cycles. This study underscores the significance of QTFP isolators in enhancing the seismic resistance of RC structures, while shedding light on their performance under different earthquake sequences.

Keywords: Reinforced Concrete, Low-Rise Structure, Multi-Staged Friction Pendulum Isolators, Sequence of Near-Fault Earthquake, Nonlinear Response History Analysis.

1. Introduction

The seismic mitigation of RC structures subjected to strong earthquakes, which may result in a partial or total collapse of the building, has been the interest of many studies (Mesr and Behnamfar, 2023; Nallasivam, 2023). Implementing a base isolation system proved to be an efficient and effective technique for reducing seismic damage by enhancing the structure's resilience and providing an

---

* Corresponding author E-mail: dr_alrawashdeh@bau.edu.jo

overall safety performance in contrast with fixed-base structures (Gandelli, 2017). This can be achieved via alteration of the fundamental period of the building and enhancement of the energy dissipation capacity resulting in lower transmitted energy and hence lower structural responses such as displacement and acceleration (Sodha et al., 2017; Keikha and Ghodrati Amiri, 2021). In general, base isolation systems implemented for seismic protection of RC structures can be categorized into rubber isolators and frictional sliding isolators. Within the group of frictional sliding isolators, flat sliding isolators and friction pendulum isolators are the most used devices. Friction pendulum isolators group includes Single Friction Pendulum (SFP), Double Friction Pendulum (DFP), Triple Friction Pendulum (TFP) and QTFP.

In general, a multi-staged friction isolation system leverages multiple points of energy dissipation to significantly reduce the propagation of mechanical vibrations or shocks. This method essentially uses multiple friction interfaces that convert mechanical energy into heat through friction, mitigating vibration transmission.

The advantage of this system lies in its capability to handle complex or varying energy inputs, as each stage can deal with different energy levels or frequencies. This multi-staged approach distributes the isolation task, preventing any single stage from being overwhelmed. Consequently, it enhances system resilience, ensuring overall stability and protection for sensitive equipment from potentially damaging forces. In effect, they improve energy dissipation and reduce maintenance costs.

With their robustness and enhanced efficiency, multi-staged friction bearings are a valuable choice for high-performance systems. The SFP isolator consists of a single sliding surface and one pendulum (Zayas et al., 1987; Mokha et al., 1991).

The DFP isolator consists of three sliding regimes and two pendula which minimize the heating effects and improve the capacity of displacement (Fenz and Constantinou, 2006). The TFP isolator consists of five sliding regimes and three pendula which exhibit the same performance as DFP with better-enhanced adaptability of behavior (Dhankot and Soni, 2017; Sodha et al., 2017). Naderpour et al. (2019) presented an insightful investigation into the seismic response of high-rise structures, utilizing innovative methods such as base isolation and non-traditional tuned mass dampers.

A different approach was adopted by Sharbatdar et al. (2011), whose work focused on studying the effects of near fault ground motions on base-isolated structures with Lead Rubber Bearings (LRB) and SFP.

Meanwhile, Mir Rashid and Naderpour (2021) made significant strides in the realm of computational intelligence, offering an advanced model for the vulnerability assessment of RC frames under seismic sequences, hence providing a key resource for further seismic research.

The QTFP isolator consists of nine sliding regimes and five pendula, considered the extended version of the TFP isolator (Lee and Constantinou, 2016). In addition, the number of sliding regimes and pendula improves the capacity of adaptive behavior, decreases the heat originating from friction and improves the displacement capacity as well as the difficulty in modeling the behavior of the devices. Indeed, the QTFP isolator device was introduced and investigated by Tsai et al. (2010), where the force-displacement relationship applicable for the loading phase and model of plastic behavior was performed. This article explored the importance and implications of a pioneering study concerning the QTFP isolator, a sophisticated device employed in RC structures to mitigate the damage caused by severe seismic activities. The significance of this research lies in its potential to drastically improve the resilience of these structures during seismic events and contribute substantially to the field of earthquake engineering.

While the QTFP isolator has

demonstrated efficacy in limiting structural responses and achieving specific performance objectives under severe seismic excitation, a comprehensive analysis of its performance under a series of near-fault foreshock, main shock and aftershock events remains unexplored. This study, therefore, strives to fill this gap in the existing literature and aims to understand the performance and efficiency of RC structures equipped with QTFP isolators under such seismic sequences. Specifically, the study will utilize finite element analysis as a crucial tool to investigate the seismic behavior of RC structures with QTFP isolators during sequential earthquakes.

Additionally, the effectiveness of the QTFP isolator will be analyzed by assessing the seismic behavior of base-isolated RC structures subjected to sequence earthquakes. The potential implications of this study are far-reaching. If successful, it could provide key insights into the effectiveness of the QTFP isolator in mitigating seismic damage, potentially revolutionizing our current understanding of structural design in earthquake-prone areas. This could lead to safer and more resilient infrastructures, significantly reducing both human casualties and economic losses associated with seismic events. This is why the understanding and dissemination of this study are essential, as

its findings could serve as a cornerstone for future earthquake engineering research.

2. Materials and Methods

The selection of low-rise RC moment resisting frames representing typical buildings was conducted within this paper, as illustrated in Figure 1. An investigation of the seismic behavior of RC structures equipped with a multi-staged friction pendulum isolator was performed to evaluate the efficiency of the base isolation system under the effect of a sequence of near-fault earthquakes where the bare structure is set to be the benchmark.

QTFP isolator consists of six concave surfaces coated by a Teflon slider, as represented in Figure 2. The change of strength and stiffness of the QTFP isolator corresponds to the direct proportional increase in displacement. The different number of sliding surfaces of the QTFP isolator is accompanied by the increase in complexity in force-deformation performance regarding other friction isolator devices (Sodha et al., 2017).

Furthermore, the curve of the force-deformation relationship of the QTFP isolator is composed of nine operating stages, as shown in Figure 3 (Keikha and Ghodrati Amiri, 2021).
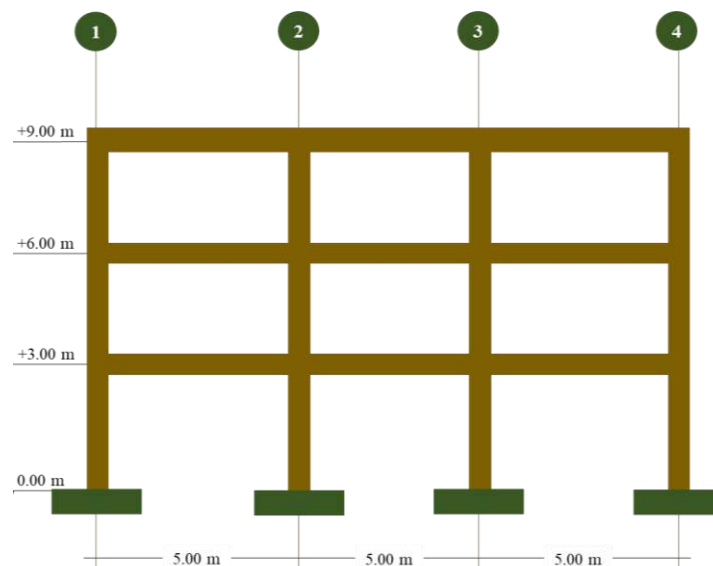

Fig. 1. Selected frame structure

QTFP isolator can operate in two different design configurations depending on the coefficient of friction magnitudes; where the first configuration is composed of the following: $\mu_3 = \mu_4 < \mu_5 \le \mu_2 < \mu_6 \le \mu_1$ while the second configuration is $\mu_3 = \mu_4 < \mu_2 \le \mu_5 < \mu_6 \le \mu_1$. Moreover, the difference between the two configurations is the switch of operating stages between 2-3 and 8-9 resulting in slight variation in the loop. Nonetheless, the QTFP isolator possesses one design configuration depending on the effective radius of curvature, which is composed of the following $L_3 = L_4 \ll L_2 \le L_5 \ll L_1 \le L_6$ where $L_i = R_i - h_i$. In addition, QTFP isolator is governed by the property of geometry which is $d_i^* = d_i \frac{L_i}{R_i}$ where R_i: is the radius of curvature, d_i: is displacement capacity and h_i: is height of the ith surface.

The simultaneous motion in operating stages 3 and 4 begins in the case of $\mu_3 = \mu_4$ and $L_3 = L_4$ where any change in this case can lead to undetected irregular performance by the presented model and increase in complexity demand (Sarlis and Constantinou, 2013). The frictional forces in each element of the QTFP isolator are in

accordance with an extended model by (Constantinou et al., 1990) as the following:

$$F_1 = \bar{\mu}_1(m_b + M)gZ_1 \qquad (1)$$
$$F_2 = \bar{\mu}_2(m_b + m_{s1} + M)gZ_2 \qquad (2)$$
$$F_3 = \bar{\mu}_3(m_b + m_{s1} + m_{s2} + M)gZ_3 \qquad (3)$$
$$F_4 = \bar{\mu}_4(m_b + m_{s1} + m_{s2} + m_{s3} + M)gZ_4 \qquad (4)$$
$$F_5 = \bar{\mu}_5(m_b + m_{s1} + m_{s2} + m_{s3} + m_{s4} + M)gZ_5 \qquad (5)$$

where Z_i: is the hysteretic element meeting the requirement of the following nonlinear differential equation:

$$q\frac{dZ_i}{dt} = A\dot{x}_i - \beta|\dot{x}_i||Z_i||Z_i|^{n-1} - \gamma\dot{x}_i|Z_i|^n \qquad (6)$$

where q: is the displacement quantity while A, β, n and γ: are the dimensionless factors of the hysteresis loop. In this study, the model used for defining the QTFP is an equivalent approach to the one shown in Figure 4 employing a series of TFP and DFP.

Moreover, the isolator's effective stiffness was calculated, as shown in Figure 5, using the method described by Sodha et al. (2017).
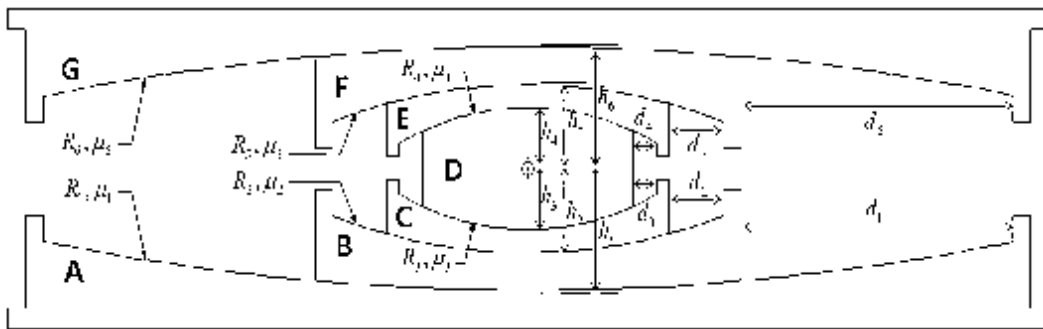

Fig. 2. Demonstration of QTFP isolator as introduced by Lee and Constantinou (2016)

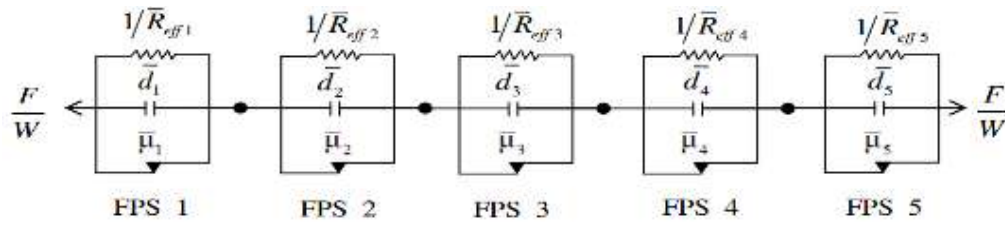**Fig. 3.** Backbone curve and hysteresis loop of QTFP isolator

Fig. 4. Numerical modeling of QTFP behavior (Lee and Constantinou, 2016)
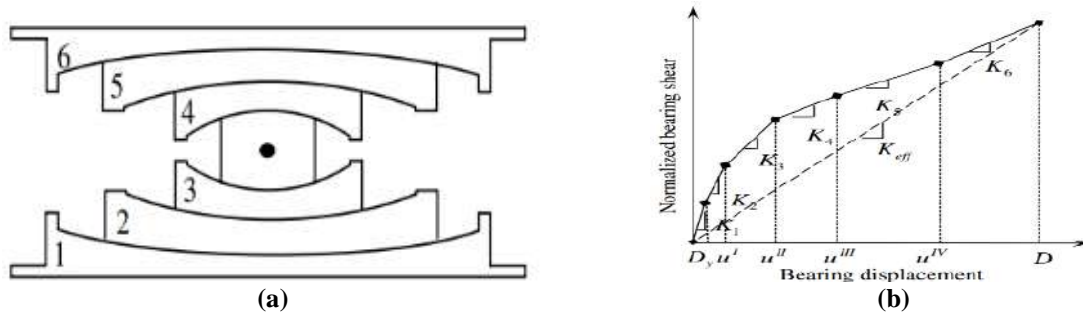

(a)	(b)

Fig. 5. Calculation of the effective stiffness for QTFP as illustrated by Sodha et al. (2017)

Lastly, for the aim of conducting this study, three cases of the period were selected, which were 2.15 seconds, 2.68 seconds, and 3 seconds along with damping ratios of 10%, 20%, and 30 %, respectively.

In general, the displacement requirement of the isolators was first selected based on the requirements of the ASCE 7-16. Since the displacement is the major parameter that physically restrict the isolator from being used (since in many cases it is not possible to provide an isolator with high displacement capacity because there are limitations coming from nearby structures), the same design and ultimate displacements were used in all cases. Then three different cases of isolator with significant differences were selected as a way to simulate a real case of discuss the effect of the properties on the response of the building. The properties of the QTFP isolator are illustrated in Table 1.

The frame structure shown in Figure 1

was designed, and the selected beams and columns sections for the building were 0.4 m × 0.5 m and 0.4 m × 0.4 m, respectively.

Modeling of a two-dimension system was conducted using finite element software (SAP, 2000) to examine the inelastic seismic response of the base-isolated structure where ACI 318-19 code was followed for modeling the stiffness characteristics of beam and columns sections (ACI, 2019). Moreover, the appropriateness of retrofitting was investigated using equivalent lateral force following ASCE/SEI 7-16 (ASCE, 2016).

Finally, three cases of the natural period of 2.15, 2.68, and 3 while three cases of damping ratio of 10%, 20%, and 30% to evaluate the efficiency of the QTFP isolator. Nonlinear time history analysis is a critical tool for understanding and predicting the structural behavior of buildings and other complex structures during seismic events.

Table 1. Selected isolator properties

T2.15-ξ10				T2.68-ξ20				T3-ξ30			
R	μ	h	d	R	μ	h	D	R	μ	h	D
0.85	0.11	0.15	0.34	1.5	0.11	0.15	0.32	3	0.14	0.15	0.31
0.55	0.09	0.1	0.1	0.55	0.06	0.1	0.1	0.8	0.065	0.1	0.08
0.3	0.01	0.05	0.03	0.3	0.02	0.05	0.02	0.3	0.02	0.05	0.02
0.3	0.01	0.05	0.03	0.3	0.02	0.05	0.02	0.3	0.02	0.05	0.02
0.55	0.08	0.1	0.1	0.55	0.05	0.1	0.1	0.8	0.05	0.1	0.08
0.85	0.1	0.15	0.34	1.5	0.09	0.15	0.32	3	0.11	0.15	0.31

This computational procedure aims to forecast the dynamic response of structures to seismic loads. By incorporating time as an essential variable, it assesses the progressive changes in structural responses over a specific period. In the field of earthquake engineering, Nonlinear Time History Analysis (NLTHA) is vital for modeling and testing the seismic performance of structures under real earthquake ground motions. It considers the relationship between stress and strain, accounting for the plastic behavior of materials under high-stress levels. This allows engineers to analyze potential structural deformations and evaluate seismic damage potential. The Finite Element Method (FEM) approach plays a central role in NLTHA. FEM is a numerical technique that divides complex structures into numerous smaller, simpler parts, known as finite elements. Each element can be analyzed for behavior under seismic loads, and when combined, they provide a detailed picture of how the entire structure will respond. The strength of the finite element approach lies in its versatility and precision. It can manage complex geometries, different types of materials and varying boundary conditions, which make it uniquely suited for seismic load modeling.

The model starts with defining the geometry of the structure, the properties of the materials used and the applied loads or displacements. These variables, combined with the known laws of physics, allow to be solved for unknowns such as stress distributions, deformations and natural frequencies. One of the critical aspects of this approach is the formulation of the nonlinear material models. Different construction materials, such as concrete, steel, or timber, respond differently to stress, strain, and high frequencies. These characteristics are integrated into the model, with each element assigned a specific material property. As the seismic load is applied, the model can predict nonlinear responses such as yielding or failure of the materials.

Another fundamental aspect of the FEM in seismic load analysis is capturing the effect of the dynamic nature of earthquakes.

Seismic waves can have a wide range of frequencies and their effect on structures can change drastically depending on the frequency content. Therefore, an effective model should incorporate the dynamic characteristics of the structure, including its natural frequencies and mode shapes. The application of FEM in NLTHA is not limited to buildings. It also extends to other structures such as bridges, dams and tunnels. It helps in analyzing the effect of soil-structure interaction, a significant factor affecting the response of structures during earthquakes. By simulating the nonlinear behavior of soil and its interaction with the structure, engineers can develop more resilient designs. The development of a realistic and reliable structural model requires comprehensive understanding and application of validated methodologies.

This report elaborates on the utilization of the National Institute of Standards and Technology (NIST), NIST GCR 17-917-46v3 guideline for the nonlinear modeling of a RC frame superstructure in various models. Emphasizing the importance of accuracy and precision, this guideline was meticulously applied to address both material and geometric nonlinearity effects.

The RC frames, by nature, are subjected to confinement effects that significantly influence the overall behavior of the structure. These effects were meticulously incorporated in our models through the application of the Mander et al. (1988) approach. This widely accepted method helped to define the confined compressive stress-strain relationship of concrete, yielding more robust and accurate models.

Besides, the behavior of concrete under tension was also accounted for, further enriching the comprehensive representation of the material's performance under varied conditions. In capturing the behavior of steel reinforcements, the Park and Paulay (1975) model, renowned for its ability to effectively represent the stress-strain

response with symmetric compression and tension sections, was judiciously employed.

The concrete compressive strength is 16 MPa and the steel yielding strength is 420 MPa. The structural models boasted of three distinct fiber zones within the beam and column sections. These comprised the concrete cover, the concrete core, and the steel reinforcements, each modeled using separate approaches to ensure an in-depth and precise reflection of the structure's behavior. The outer concrete cover was modeled with unconfined concrete, the inner core with confined concrete, while the steel reinforcements were modeled in accordance with the approach proposed by Kalantari and Roohbakhsh (2020). A significant feature of these models was the employment of the fiber hinge model, a tool that effectively captures the nonlinear behavior of the structural elements. With this, the models transcended the realm of linear behavior, becoming capable of accurately predicting responses under diverse and extreme loadings. This step was particularly crucial in understanding the structure's ultimate behavior and failure mechanism. NLTHA was then executed in SAP 2000, deploying a direct integration approach. This methodology offered an insightful temporal exploration of the structural response, highlighting the time-varying nature of the structure's dynamic behavior. Guided by the approach presented in Kangda and Bakre (2018), the damping ratio in the superstructure was set at 2.5%.

Notably, the first mode of the base isolated structure had its damping ratio overridden to zero to avert the phenomenon of damping leakage, a source of error often overlooked in such analyses. The damping leakage phenomenon in base isolated structures refers to the unintended addition of damping to the system's vibration modes. This occurs when utilizing classical or nonclassical damping models in finite element platforms to solve the equations of motion for base-isolated buildings. In the traditional damping matrix approach, the elastic stiffness of the system, including

isolators, is considered. This method can inadvertently introduce damping to the first and higher vibration modes, leading to an unwarranted suppression of structural responses. The beam-column panel zone, a critical element that significantly influences the structure's overall deformation capacity, was modelled using line elements.

These elements, conforming to NIST GCR 17-917-46v3, extended from the columns and beams towards the panel zone.

This design contributed to a more realistic representation of the structure.

Finally, the analysis incorporated the consideration of P-delta effects, pivotal in capturing the influence of gravity-induced forces on the structure's overall performance. However, the soil-structure interaction was intentionally neglected.

Although it is generally considered in comprehensive models, this exclusion served to maintain a manageable complexity within the study's scope, focusing on the primary elements and their interactions. The 1997 Umbria and Marche near-fault earthquake sequence was selected to conduct the study. The moment Magnitude (M_W) scale for the foreshock record was recorded at the value of 5.7, while the main shock exhibited M_W value of 6, and the aftershock record experienced M_W value of 5.5. In fact, the Pacific Earthquake Engineering Research Center (PEER) was used in order to scale the sequence of near-fault earthquakes, as illustrated in Figure 6. The scaling approach followed in this study was a Mean Square Error (MSE) where the three earthquake records were multiplied by a single scale factor. Lastly, 30 seconds of trailing zeroes were added at the end of the foreshock and main shock earthquake records representing the time difference between the end of sequence foreshock and the beginning of sequence main shock. At the end of the sequence aftershock earthquake record, 15 seconds of trailing zeroes were added to demonstrate the effect of the free vibration response of the structure (Kitayama and Constantinou, 2018).
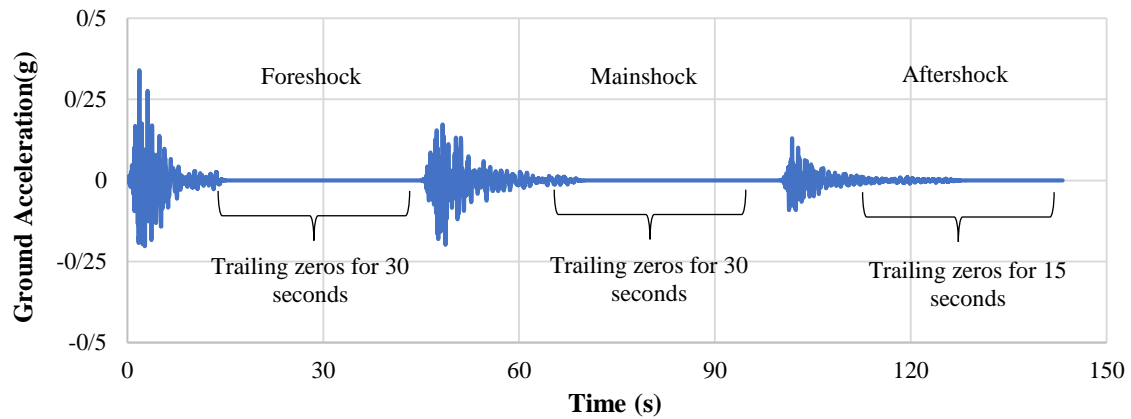
Fig. 6. Developed sequence of foreshock, main shock and aftershock

3. Results and Discussions

This comprehensive evaluation aimed at understanding the seismic response of low-rise RC structures with an integrated MSFP isolator. The focus was primarily on how these structures would react under the influence of a series of near-fault foreshock, main shock and aftershock earthquakes.

This sequence is often considered the most detrimental and damaging for structures due to the cumulative effect of the successive seismic events. Furthermore, the effectiveness and performance of the QTFP isolator, an innovative seismic isolation device, were also scrutinized under these earthquake sequences. Figure 7 exhibits the time domain responses for the base shear of the structures under different earthquake records. The base shear essentially represents the total horizontal force in a building during an earthquake,

and is a critical parameter in evaluating a structure's stability. An essential observation was the significantly high base shear time history response of the bare structure model-a structure without any form of base isolation. The bare model reported the highest values for the foreshock, main shock and aftershock earthquakes as compared to the cases where base isolation was employed. This comparison illuminated the benefits of utilizing base isolation techniques in low-rise RC structures. The results unequivocally highlighted that base isolation can be instrumental in managing the forces encountered during seismic events, thereby reducing the risk of structural damage or collapse. Another salient feature of the study was the exploration of different combinations of periods and damping ratios on the base shear response.
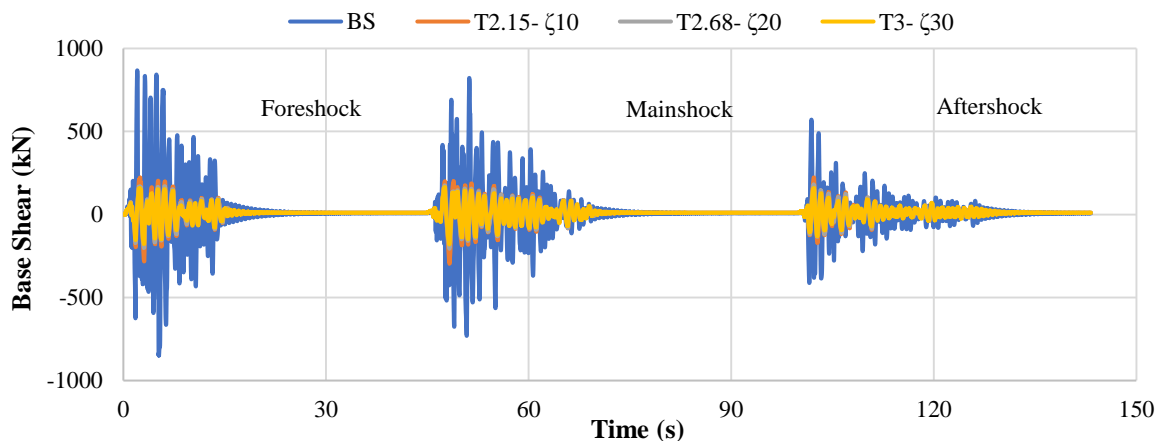

Fig. 7. Base shear time history response

The time-period of a structure is a fundamental attribute in structural dynamics and it is used to describe how a structure vibrates when it is excited. The damping ratio, on the other hand, is an indicator of the energy dissipation capacity of a structure, which becomes particularly important during seismic events. The results illustrated that the combination of 2.15 seconds period and 10% damping ratio resulted in the highest base shear time history magnitudes. This was followed by the combination of 3 seconds period and 30% damping ratio, while the 2.68 seconds period and 20% damping ratio combination reported the lowest base shear magnitudes.

These results could have significant implications for the design and construction of RC structures, specifically in seismically active regions. The data suggests that the performance of a structure during an earthquake can be significantly influenced by its period and damping ratio. The challenge for architects and engineers will be to determine the optimum combination of these variables to enhance the structure's ability to withstand seismic events.

Additionally, the study revealed that the time history base shear values were recorded highest for all combinations and cases during the foreshock earthquake. This could be attributed to the fact that the foreshock earthquake, being the first in the sequence, tends to unsettle the structure, making it more susceptible to the subsequent seismic events. Finally, the bare structure model demonstrated the highest base shear value at 900 kN for the foreshock earthquake. This elevated value for the bare structure indicates the severe implications of omitting base isolation in design strategy.

The study extended this analysis to a wide range of configurations to understand the behavior of the 3-story RC structure subjected to different earthquake events. It is noteworthy to mention that each earthquake type -foreshock, main shock and aftershock-represented unique force parameters in terms of intensity, frequency, and direction. Consequently, the structure's response to these forces could significantly vary, leading to different stress and strain distributions, which in turn translated into varying story shear responses (Figure 8).
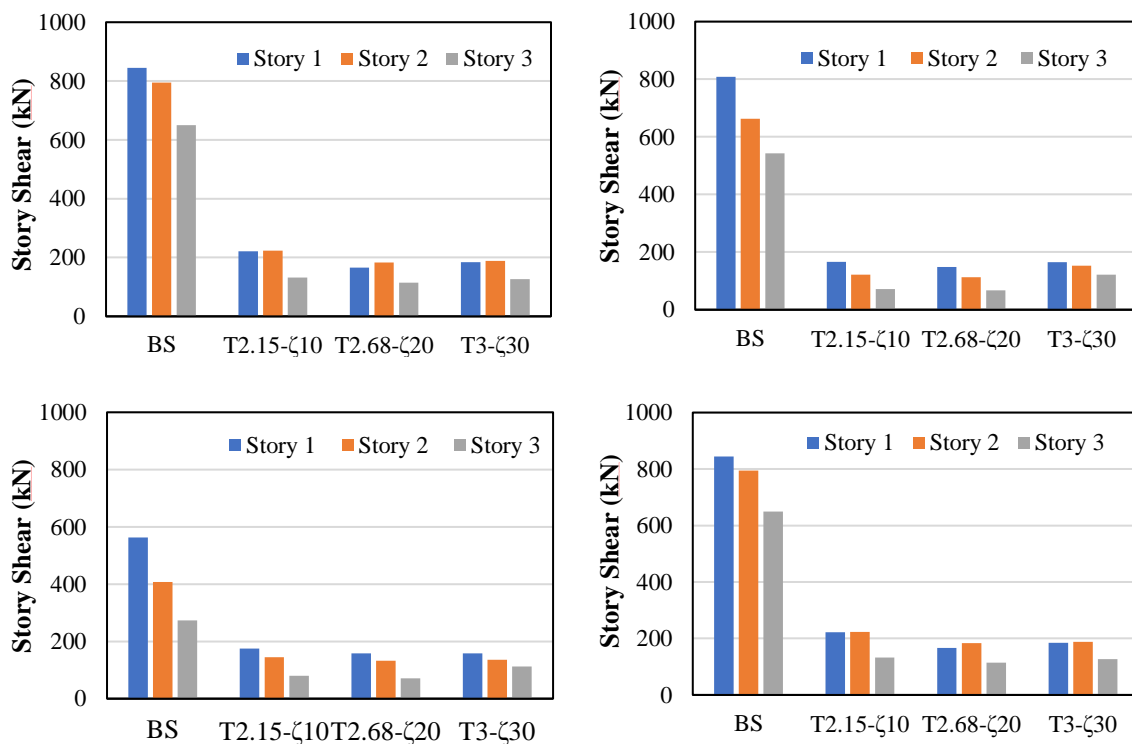

Fig. 8. Story shear responses of the selected buildings

The foreshock, as a preliminary tremor preceding the main shock, had been selected for this analysis based on its high level of ground acceleration. Despite being considered a precursor, the foreshock was found to impose the highest demand on the building in comparison with the main shock and aftershock.

This finding could be attributed to the fact that the input force in the motion equation of a typical multi-degree of freedom system is a product of earthquake acceleration intensity and the building mass. As such, the highest shaking level of the foreshock induced the highest stress on the building. When it came to the base-isolated structures, the combination of specific damping ratio and period parameters made a significant difference in the structure's response.

The optimal combination was found to be 2.15 seconds period and a 10% damping ratio, which triggered the highest story shear for the foreshock. This discovery demonstrates the potential of damping and period selection in alleviating seismic forces, offering designers a path to optimize the seismic resilience of their structures.

Main shock and aftershock analyses presented different results. Here, the highest story shear values were recorded in the combination of a 3 seconds period and a 30% damping ratio. These configurations highlighted the dynamic nature of base isolation technology, proving its efficiency under a wide spectrum of seismic events, not just under the violent shaking of a main shock, but also during the aftershock, which tends to have lower ground acceleration but can still significantly affect a building's stability. However, regardless of the earthquake type, it was observed that the first story consistently experienced the highest story shear magnitudes across all isolator property combinations.

This trend is most likely due to the increase in load towards the base of the building, a phenomenon that is a fundamental aspect of statics and the field of structural engineering.

It is often said that the first floor of a building bears the weight of the world, and this study confirms that assertion, especially when it comes to seismic loads.

Following the first story, the second and third stories showed the next highest magnitudes, respectively. These results underscore the strain a multi-story building undergoes during seismic activity, with each level progressively sharing the burden of the one above. This cumulative effect is essential to consider when designing for earthquake resistance, ensuring that the structure's integrity is maintained at every level. This comprehensive analysis of story shear response sheds light on the complex interplay between building characteristics, isolator properties and seismic event characteristics. It demonstrates how crucial it is to consider not only the nature of the ground shaking but also the inherent structural properties of the building and the characteristics of the isolation system. It is clear that there is no one-size-fits-all solution to this complex problem. Instead, a nuanced approach that accounts for these different parameters will be necessary for the design of resilient buildings. QTFP isolator implemented with RC structures subjected to foreshock, main shock and aftershock earthquake records were investigated to examine these buildings seismic behavior. Figure 9 represents the displacement time history response of the analyzed models. In general, the displacement response in the time domain of the bare structure reflected the highest magnitudes in contrast to base-isolated models. In base-isolated models, the displacement time history results were observed to be the highest in the combination of 2.15 seconds period and 10% damping ratio compared to 2.68 seconds period and 20% damping ratio as well as 3 seconds period and 30% damping ratio.

As can be observed, the inter-story drift ratio results of the 3-story RC structure equipped with a QTFP isolator are demonstrated in Figure 10.
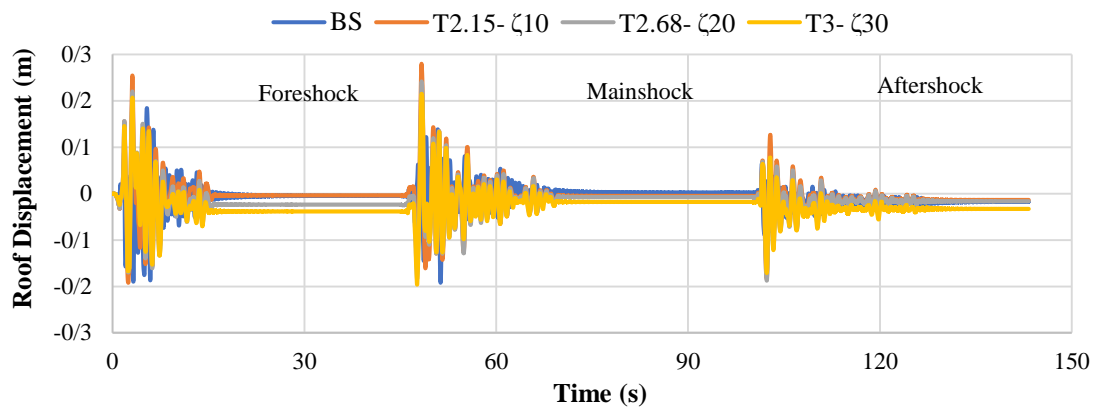
Fig. 9. Displacement time history response

The inter-story drift response in the case of the foreshock earthquake record represented the highest values for the bare structure model. On the contrary, the highest inter-story drift results for the base-isolated models were shown in the case of the main shock earthquake record for all combinations at all story numbers.

Furthermore, the highest inter-story drift results for the base-isolated models were recorded for the combination of 2.15 seconds period and a 10% damping ratio.

The highest inter-story drift results were marked with the highest values in the first story for all cases and combinations under foreshock, main shock and aftershock

earthquake records. The displacement time history response experienced the highest values for the bare structure model in the foreshock earthquake record, while the highest displacement results for the base-isolated models were seen in the case of the main shock earthquake record.

Lastly, the highest displacement time history value in the case of the bare structure was marked at 0.19 m, while the highest displacement result in the case of base-isolated models was recorded at 0.29 m. As can be observed, the inter-story drift ratio results of the 3-story RC structure equipped with a QTFP isolator are demonstrated in Figure 10.
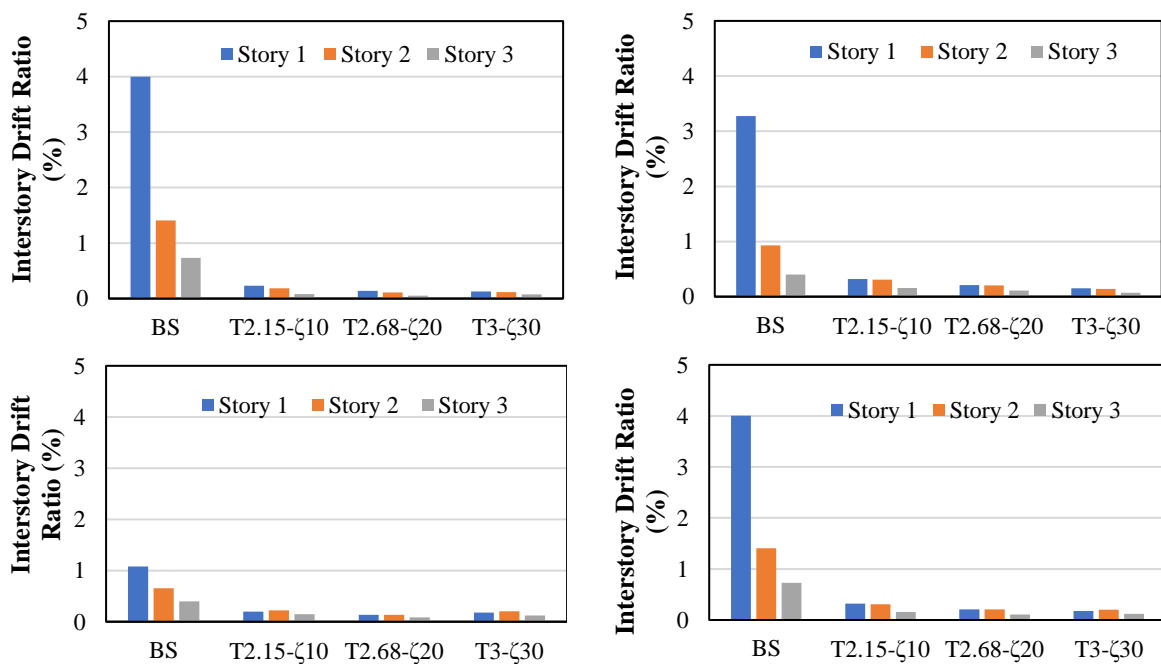

Fig. 10. Inter-story drift ratios response of the selected buildings

The inter-story drift response in the case of the foreshock earthquake record represented the highest values for the bare structure model. On the contrary, the highest inter-story drift results for the base-isolated models were shown in the case of the main shock earthquake record for all combinations at all story numbers. Furthermore, the highest inter-story drift results for the base-isolated models were recorded for the combination of 2.15 seconds period and a 10% damping ratio. The highest inter-story drift results were marked with the highest values in the first story for all cases and combinations under foreshock, main shock and aftershock earthquake records. The acceleration time history response of RC structures incorporated with a multi-staged friction pendulum isolator. The acceleration response in the time domain exhibited the highest results in the case of the bare structure model with respect to base-isolated structures, as illustrated in Figure 11.
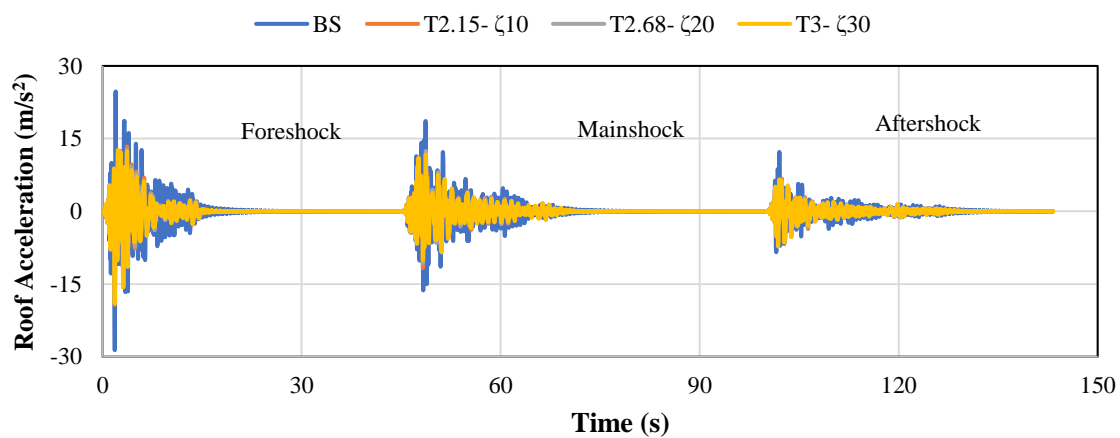

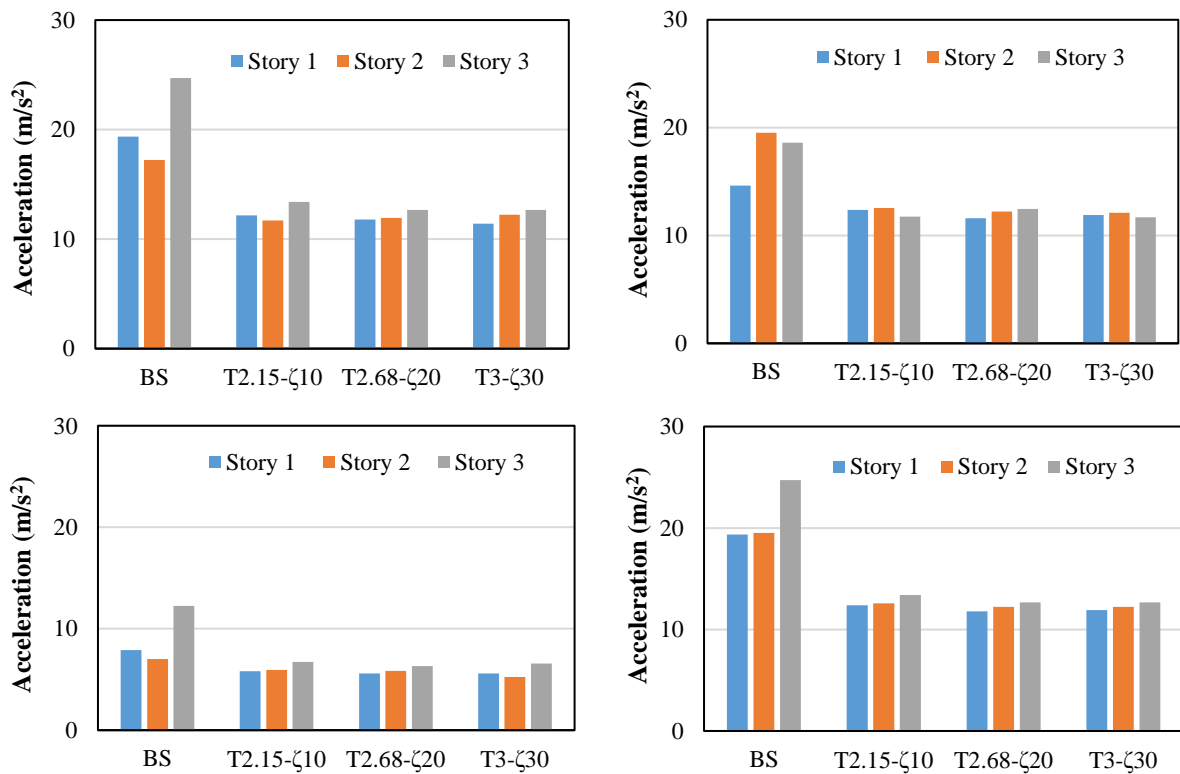**Fig. 11.** Accelerations time history response

Fig. 12. Story accelerations response of the selected buildings

On the other hand, the highest acceleration response in the time domain for the base isolation system was generally recorded in the combination of a 2.15 seconds period and a 10% damping ratio representing the worst efficiency of the QTFP isolator in comparison to other combinations. The best performance of the QTFP isolator implemented with RC structures was seen in the combination of 3 seconds period and a 30% damping ratio, representing the lowest acceleration time history values. In the case of the bare structure model, the highest acceleration time history values were observed for the foreshock earthquake record marking 25 m/s^2 while the highest acceleration results for the case of base-isolated models were shown in the foreshock earthquake, reaching 13 m/s^2. The bare structure model displayed the highest story acceleration time history results in the case of foreshock earthquake, while the highest story acceleration values for the case of base-isolated models were seen in foreshock earthquake for all combinations at all number of stories as shown in Figure 12. In addition to that, the combination of 2.15 seconds period and a 10% damping ratio experienced the highest story acceleration response in the time domain. The story acceleration response recorded the highest magnitudes in the last story for foreshock and aftershock earthquake records, while main shock earthquake expressed the highest story acceleration response in the second story for all combinations. The input energy time history response experienced the highest values in the case of the bare structure model in regard to base-isolated models, as represented in Figure 13. For the base-isolated structures, the highest input energy in the time domain was marked in the combination of 2.15 seconds period and a 10% damping ratio, while the lowest input energy values were seen in the combination of 3 seconds period and 30% damping ratio demonstrating the worst and best efficiency and performance of the multi-staged friction pendulum isolator respectively. The highest input energy for the bare structure model was experienced in the aftershock earthquake record at approximately 1050 kN.m. Moreover, the highest input energy results for the case of base-isolated buildings were displayed in the aftershock earthquake roughly at 930 kN.m, as can be seen in Figure 14.
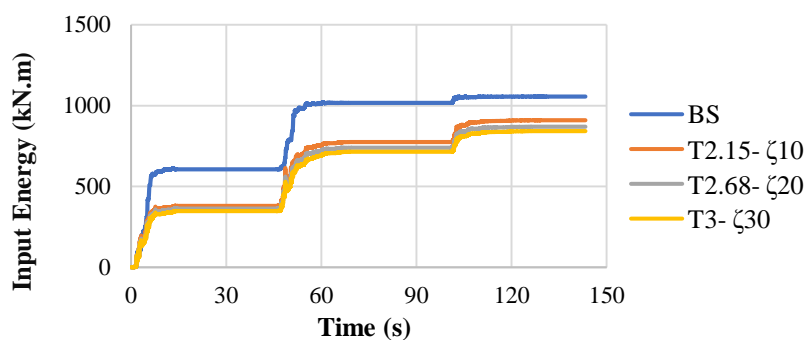

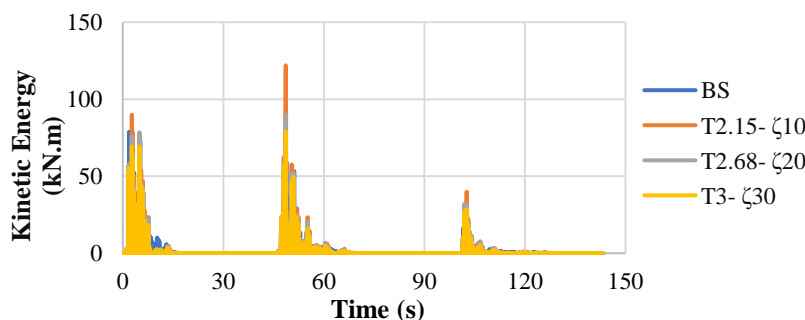**Fig. 13.** Input energy of the selected buildings

Fig. 14. Kinetic energy of the selected buildings

The kinetic energy response in the time domain was expressed the highest in the combination of 2.15 seconds and a 10% damping ratio representing the worst efficiency of the QTFP isolator compared to other buildings under the influence of sequence near-fault foreshock, main shock and aftershock earthquakes. Furthermore, the combination of 3 seconds and 30% damping ratio exhibited the lowest kinetic energy time history results, demonstrating the best base isolation system performance. Main shock earthquake record showed the highest kinetic energy at an approximate value of 125 kN.m. The potential energy time history was observed to exhibit the highest results in the case of bare structure building in comparison to base-isolated models, as illustrated in Figure 15.

Regarding base-isolated buildings, the highest potential energy in the time domain was recorded in the combination of 2.15 seconds period and a 10% damping ratio representing the worst efficacy of the base isolator. In addition to that, the lowest potential energy time history values were experienced in the combination of 3 seconds period and a 30% damping ratio

representing the best efficiency of the QTFP isolator. The highest potential energy for the bare structure case was marked in the foreshock earthquake at 45 kN.m, while the highest potential energy value for the base-isolated case was expressed in the main shock earthquake at 32 kN.m. The combination of 2.15 seconds period and a 10% damping ratio showed the highest damping energy time history response in contrast to the rest of the buildings, as represented in Figure 16. The lowest damping energy results were seen in the case of the bare structure model. The best performance of the multi-staged friction pendulum isolator equipped with RC structures was recorded in the combination of a 2.15 seconds period and a 10% damping ratio, while the lowest efficiency of the QTFP isolator was displayed in the case of bare structure building. The highest damping energy results for the bare structure model and all base-isolated models were exhibited in the case of the aftershock earthquake record, where the highest damping energy in the case of the bare structure was observed at 210 kN.m.
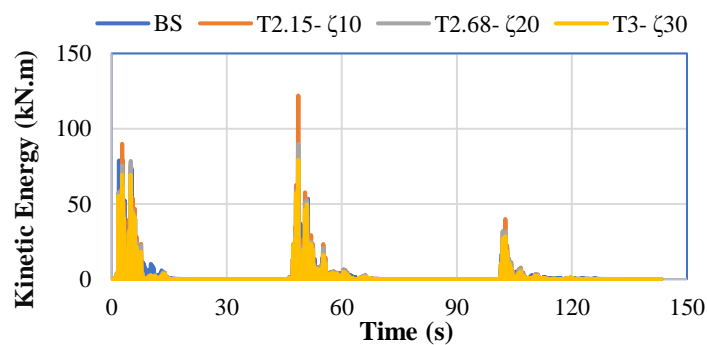

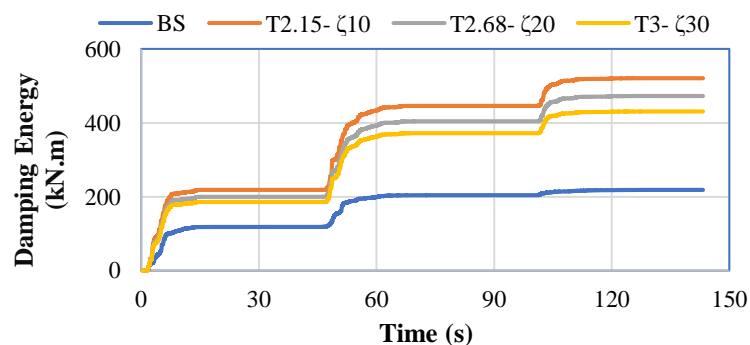**Fig. 15.** Potential energy of the selected buildings

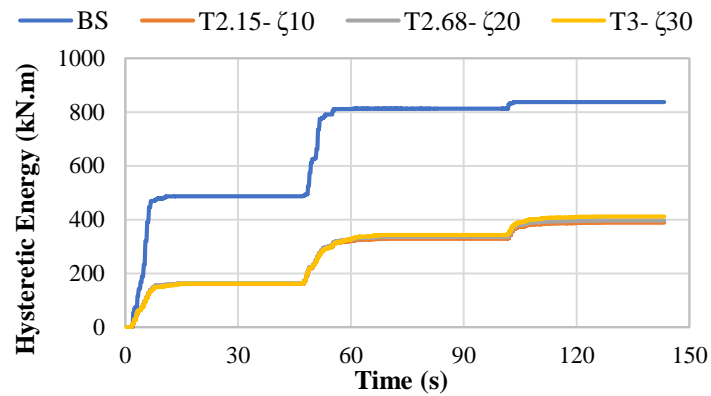**Fig. 16.** Damping energy of the selected buildings

Fig. 17. Hysteretic energy of the selected buildings

In comparison, the highest damping energy for the case of the base isolation system was experienced roughly at 520 kN.m. As can be observed in Figure 17, the hysteretic energy of the RC structures incorporated with the QTFP isolator is represented. The highest hysteretic energy time history response was experienced in the case of bare structure building.

Figure 18 shows the hysteresis loop for the combination of 2.15 seconds period and a 10% damping ratio under the sequence of near-fault foreshock, main shock and aftershock earthquakes. The largest hysteresis loop cycle was observed in the case of the main shock earthquake record, where the highest displacement value was found to be approximately 0.27 m, while the smallest hysteresis loop cycle was seen in the case of the aftershock earthquake, where the lowest displacement result was marked roughly at 0.13 m. The largest hysteresis loop cycle for the combination of 2.68 seconds period and 20% damping ratio was experienced in the case of main shock earthquake record, reaching the displacement result of 0.21 m representing the most significant damage on the QTFP isolator as illustrated in Figure 19.
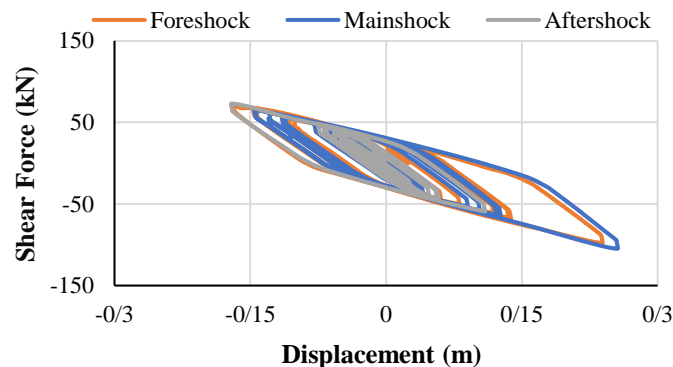

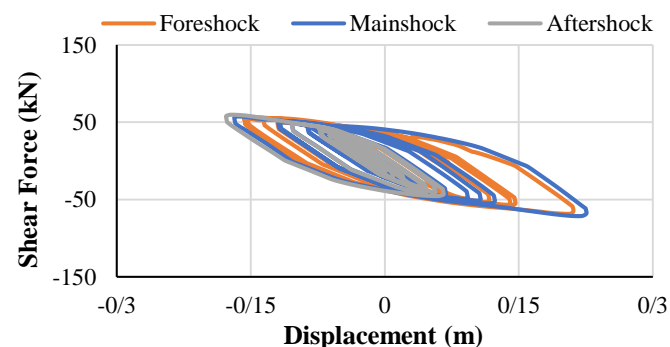**Fig. 18.** Isolator hysteresis behavior for the case of T2.15-ζ10

Fig. 19. Isolator hysteresis behavior for the case of T2.68-ζ20

In addition, the smallest hysteresis loop cycle was exhibited in the case of an aftershock earthquake, where the lowest displacement response was found at 0.9 m demonstrating the least critical damage to the base isolation system. As can be observed in Figure 20, the hysteresis loop for the RC models utilized with a multi-staged friction pendulum isolator for the combination of 3 seconds period and a 30% damping ratio is represented. The main shock earthquake record expressed the largest hysteresis loop cycle, where the highest displacement response was roughly at 0.18 m. Moreover, the smallest hysteresis loop cycle was experienced in the case of an aftershock earthquake, where the lowest displacement result was marked approximately at 0.7 m. The investigation of the efficiency and performance of the QTFP isolator implemented in RC structures was performed in terms of the structural responses, including base shear, acceleration, and inter-story drift, as shown in Table 2. The efficiency of the base isolation system was evaluated for each response in each case of the sequence of near-fault foreshock, main shock and aftershock earthquake records at each story of the 3-story model.
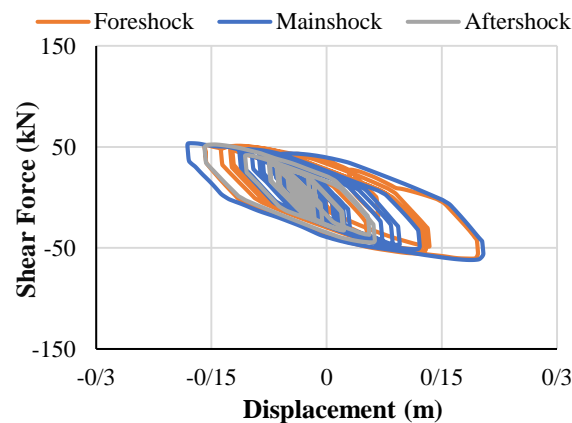

Fig. 20. Isolator hysteresis behavior for the case of T3 -ζ30

Table 2. Efficiency of the quintuple isolators in reducing building's responses under the sequence of earthquake loadings

Story number	Earthquake case	Base shear			Acceleration			Interstory drift		
		T2.15-ζ10	T2.68-ζ20	T3-ζ30	T2.15-ζ10	T2.68-ζ20	T3-ζ30	T2.15-ζ10	T2.68-ζ20	T3-ζ30
1	Foreshock	73.75	80.32	78.16	37.12	39.06	41.02	94.16	96.59	96.89
	Mainshock	79.40	81.70	79.58	15.36	20.58	18.60	90.26	93.64	95.38
	Aftershock	69.02	72.00	71.83	26.33	29.15	29.40	81.90	87.84	83.80
	Mean	74.06	78.01	76.53	26.27	29.60	29.67	88.77	92.69	92.02
2	Foreshock	71.92	76.94	76.31	32.12	30.79	28.99	86.75	92.37	91.60
	Mainshock	81.71	83.07	77.02	35.64	37.40	38.07	67.06	77.76	85.12
	Aftershock	64.45	67.47	66.77	15.27	16.67	25.08	66.21	79.17	68.93
	Mean	72.69	75.83	73.37	27.68	28.29	30.71	73.34	83.10	81.88
3	Foreshock	79.64	82.46	80.50	45.84	48.78	48.73	89.01	92.90	89.63
	Mainshock	86.85	87.61	77.62	36.83	33.09	37.18	61.42	72.91	82.52
	Aftershock	70.91	73.91	59.01	45.14	48.48	46.31	62.32	78.08	69.87
	Mean	79.13	81.32	72.37	42.60	43.45	44.07	70.92	81.30	80.67
Low efficiency									High efficiency	

The base shear results for the three combinations of isolator properties, which are 2.15 seconds period and 10% damping ratio, 2.68 seconds period and 20% damping ratio, as well as 3 seconds period and 30% damping ratio, were observed to exhibit the best performance of the isolator for all cases of earthquakes at all number of stories in the combination of 2.68 seconds period and 20% damping ratio. On the other hand, the worst performance of the QTFP isolator in terms of the base shear response was seen in the combination of a 2.15 seconds period and a 10% damping ratio.

In addition, the acceleration response for the three stories generally expressed the best efficacy of the base isolation system in the combination of 3 seconds period and a 30% damping ratio for the three cases of earthquake loadings. At the same time, the worst performance of the isolator was recorded in the combination of 2.15 seconds period and a 10% damping ratio. Finally, the inter-story drift results for the three stories demonstrated the best efficiency of the isolator for the three cases of earthquake records in the combination of 2.68 seconds and a 20% damping ratio. In contrast, the worst performance of the QTFP isolator for the three cases of earthquakes and all number of stories were displayed in the combination of 2.15 seconds period and a 10% damping ratio.

4. Conclusions

The focus of this study was an exploration into the seismic behavior of low-rise RC models when equipped with a QTFP isolator.

All possible isolator properties were considered under a sequence of near-fault foreshock, main shock and aftershock earthquake events. The study also investigated how these earthquake events influenced the structural responses of the base-isolated RC buildings. A performance evaluation of the QTFP isolator in conjunction with RC structures subjected to sequences of near-fault earthquakes was conducted and the results were compared against a benchmark model of a bare structure. On the basis of the research presented in this study, it can be concluded that:

• The RC models integrated with the QTFP isolator have effectively reduced the responses of base-isolated structures, displaying adequate performance.

• The QTFP isolator showed maximum efficiency in terms of base shear and inter-story drift when combined with a 2.68 seconds period and a 20% damping ratio.

However, the combination of a 3 seconds period and a 30% damping ratio demonstrated the highest performance for the acceleration response in the base isolation system.

• The sequence of near-fault earthquakes, including foreshock, main shock and aftershock events, has a significant influence on the studied structural response. The foreshock event resulted in the greatest values of base shear, inter-story drift, and acceleration responses for both the bare and base-isolated models.

• The record of the aftershock earthquake demonstrated the highest input, damping, and hysteretic energies for both the unadorned structure and the base-isolated buildings.

• The hysteresis behavior of the isolator was noted during the main shock earthquake record for the three QTFP isolator combinations. Among all the instances, the combination of a 2.15 seconds period and a 10% damping produced the largest cycles of the hysteresis loop. In conclusion, this study was limited to analyzing a single natural sequence of motion due to the lack of many causes existing in reality.

Other studies in the literature can focus on comparing natural and artificial sequences of motion and their capabilities in capturing the true response of base-isolated structures when subjected to long seismic loadings.

6. References

ACI. (2019). ACI 318-19, *Building code requirements for structural concrete and commentary*, American Concrete Institute, Farmington Hills, USA, https://doi.org/10.14359/51716937.

ASCE. (2022). ASCE/SEI 7-22, *Minimum design loads for buildings and other structures*, American Society of Civil Engineers, United States, ISBN 978-0-7844-1085-1, https://doi.org/10.1061/9780784412916.

Constantinou, M., Mokha, A. and Reinhorn, A. (1990). "Teflon bearings in base isolation II: Modeling", *Journal of Structural Engineering*, 116(2), 455-474, https://doi.org/10.1061/(ASCE)0733-9445(1990)116:2(455).

CSI. (2022). *SAP 2000 version 22-structural software for analysis and design*, California, Computers and Structures Inc., http://doi.org/10.4236/ojce.2013.33B004.

Dhankot, M.A. and Soni, D.P. (2017). "Behaviour of triple friction pendulum isolator under forward directivity and fling step effect", *KSCE Journal of Civil Engineering*, 21(3), 872-881, http://doi.org/10.1007/s12205-016-0690-3.

Fenz, D.M. and Constantinou, M.C. (2006). "Behaviour of the double concave friction pendulum bearing", *Earthquake Engineering and Structural Dynamics*, 35(11), 1403-1424, https://doi.org/10.1002/eqe.589.

Gandelli, E. (2017). *Advanced tools for the design of sliding isolation systems for seismic-retrofitting of hospitals*, Politecnico di Milano, Milan, Italy, https://iris.unibs.it/handle/11379/531951.

Kalantari, A. and Roohbakhsh, H. (2020). "Expected seismic fragility of code-conforming RC moment resisting frames under twin seismic events", *Journal of Building Engineering*, 28, 101098, https://doi.org/10.1016/j.jobe.2019.101098.

Keikha, H. and Ghodrati Amiri, G. (2021). "Numerical development and assessment of 3D quintuple friction pendulum isolator element based on it is analytical and mathematical models", *Journal of Earthquake Engineering*, 25(13), 2718-2757, https://doi.org/10.1080/13632469.2019.1643808.

Keikha, H. and Ghodrati Amiri, G. (2021). "Seismic performance assessment of quintuple friction pendulum isolator with a focus on frictional behavior impressionability from velocity and temperature", *Journal of Earthquake Engineering*, 25(7), 1256-1286, https://doi.org/10.1080/13632469.2019.1568929.

Kitayama, S. and Constantinou, M.C. (2018). "Seismic performance of buildings with viscous damping systems designed by the procedures of ASCE/SEI 7-16", *Journal of Structural Engineering*, 144(6), 04018050, https://doi.org/10.1061/(ASCE)ST.1943-541X.0002048.

Lee, D. and Constantinou, M.C. (2016). "Quintuple friction pendulum isolator: Behavior, modeling, and validation", *Earthquake Spectra*, 32(3), 1607-1626, https://doi.org/10.1193/040615EQS053M.

Mander, J.B., Priestley, M.J. and Park, R. (1988). "Theoretical stress-strain model for confined concrete", *Journal of Structural Engineering*, 114(8), 1804-1826, https://doi.org/10.1061/(ASCE)0733-9445(1988)114:8(1804).

Mesr Habiby, Y. and Behnamfar, F. (2023). "Seismic fragility analysis of torsionally-coupled steel moment frames against collapse", *Civil Engineering Infrastructures Journal*, 56(2), 415-438, https://doi.org/10.22059/ceij.2023.347246.1862.

Mir Rashid, M. and Naderpour, H. (2021). "Innovative computational intelligence-based model for vulnerability assessment of RC frames subject to seismic sequence", *Journal of Structural Engineering*, 147(3), 04020350, https://doi.org/10.1061/(asce)st.1943-541x.0002921.

Mokha, A., Constantinou, M.C., Reinhorn, A.M. and Zayas, V.A. (1991). "Experimental study of friction-pendulum isolation system", *Journal of Structural Engineering*, 117(4), 1201-1217, https://doi.org/10.1061/(ASCE)0733-9445(1991)117:4(1201).

Mokha, A., Constantinou, M. and Reinhorn, A. (1990). "Teflon bearings in base isolation I: Testing", *Journal of Structural Engineering*, 116(2), 438-454, https://doi.org/10.1061/(ASCE)0733-9445(1990)116:2(438).

Naderpour, H., Naji, N., Burkacki, D. and Jankowski, R. (2019). "Seismic response of high-rise buildings equipped with base isolation and non-traditional tuned mass dampers", *Applied Sciences*, 9(6), 1201, https://doi.org/10.3390/app9061201.

Nallasivam, K. (2023). "Effective location of shear walls in high-rise RCC buildings subjected to lateral loads", *Civil Engineering Infrastructures Journal,* 57(1), 103-117, https://doi.org/10.22059/ceij.2023.350020.1879.

NIST. (2017). *Guidelines for nonlinear structural analysis for design of buildings, Part IIb: Reinforced concrete moment frames*, National Institute of Standards and Technology, Gaithersburg, https://doi.org/10.6028/NIST.GCR.17-917-

46v3.

Park, R. and Paulay, T. (1975). *Reinforced concrete structures*, Wiley 769 p., http://doi.org/10.5459/bnzsee.8.4.291.

Sarlis, A.A. and Constantinou, M.C. (2013). *Model of triple friction pendulum bearing for general geometric and frictional parameters and for uplift conditions*, University at Buffalo, Buffalo, NY: Technical Report MCEER-13-0010, Multidisciplinary Center for Earthquake Engineering Research, https://doi.org/10.1002/eqe.2738.

Sharbatdar, M.K., Vaez, S.H., Amiri, G.G. and Naderpour, H. (2011). "Seismic response of base-isolated structures with LRB and FPS under near fault ground motions", *Procedia Engineering*, 14, 3245-3251, https://doi.org/10.1016/j.proeng.2011.07.410.

Sodha, A.H., Soni, D.P. and Vasanwala, S.A. (2021). "Evaluation of linear visco-elastic model of quintuple friction pendulum isolator", *International Journal of Structural Engineering*, 11(1), 19-43, https://doi.org/10.1504/IJSTRUCTE.2021.112090.

Sodha, A.H., Soni, D.P., Desai, M.K. and Kumar, S. (2017). "Behavior of quintuple friction pendulum system under near-fault earthquakes", *Journal of Earthquake and Tsunami*, 11(5), 1750017, https://doi.org/10.1142/S1793431117500178.

Tsai, C.S., Lin, Y.C. and Su, H.C. (2010). "Characterization and modeling of multiple friction pendulum isolation system with numerous sliding interfaces", *Earthquake Engineering and Structural Dynamics*, 39(13), 1463-1491, https://doi.org/10.1002/eqe.1044.

Zayas, V.A., Low, S.S. and Mahin, S.A. (1987). *The fps earthquake resisting system: Experimental report* (ucb/eerc-87/01), University of California, Berkeley, CA, https://doi.org/10.1002/(SICI)1096-9845(199601)25.

RESEARCH PAPER

Dynamic Analysis of Thermal Crack Propagation in Roller-Compacted Concrete Dams Considering Rotational Component of Ground Motion

Tavakoli, H.[1]* , Mofid, T.[2] and Dehestani, M.[3]

[1] Associate Professor, Faculty of Civil Engineering, Babol Noshirvani University of Technology, Babol, Iran.
[2] Assistant Professor, Department of Civil Engineering, Urmia University of Technology, Urmia, Iran.
[3] Professor, Faculty of Civil Engineering, Babol Noshirvani University of Technology, Babol, Iran.

© University of Tehran 2023

ABSTRACT: In the construction of Roller compacted Concrete Dams (RCD), two types of internal and external concrete are used; thermal cracks are occurred due to hydration of various cements in this type of dams. Ignorance of this issue can lead to crack formation in the susceptible points of the dams. In this research, the behavior of the thermal cracks existed in the RCD body, is investigated through translational and rotational components of the earthquake. Three-dimensional Finite Element (FE) model of the concrete dam is built in Abacus software, and the model was subjected to 7 earthquake records. After validation of the model, the propagation of the crack existed in the dam body is evaluated using fracture mechanics criterion. The results of the FE analysis show that the existence of the cracks in the susceptible points of the dam, leads to propagation of these cracks during an earthquake. Especially, with considering the rotational component of the earthquake which has the significant contribution in the obtained values of the crack propagation criterion; this contribution is related to the frequency content of the earthquake, which can lead to an increase of the crack propagation energy up to 50 percent in some earthquake records.

Keywords: Thermal Crack Propagation, Finite Element Method, Concrete Dam, Fracture Mechanics Criterion.

1. Introduction

Crack propagation is one of the most important reasons of concrete dam failures during an earthquake. The first study on the seismic behavior of the concrete gravity dams were performed by Chopra and Chakraborty (1972). In their study, tensile damages on the dam were shown using linear elastic analysis. In 1989, it was shown that the behavior of the dam was nonlinear under intense earthquakes (El-Aidi and Hall, 1989). In several other studies in 1990, it was demonstrated that the majority of the concrete gravity dams experience cracking even under moderate earthquakes (Ingraffea, 1990; Rescher, 1990). Although many studies have been conducted on the behavior of cracked concrete elements and dams against

---

earthquakes (Alfatlawi et al., 2021; Mofid and Tavakoli, 2020; Mofid and Tavakoli, 2023; Pirooznia and Moradloo, 2020; Priya et al., 2022; Sadeghi and Moradloo, 2022; Singh and Sangle, 2022; Soysal and Arici, 2023; Wang et al., 2022), but fewer studies have been conducted on the behavior of RCD dams against thermal cracks (Hashempour et al., 2023; Koga et al., 2018; Zhang et al., 2020; Zhang et al., 2022).

Whereas, RCD is widely used as a new method in the dam construction industry. As illustrated in Figure 1, in the construction of RCD, two types of internal and external concrete are used. In the external part of the dam, that is, external concrete, conventional concrete with low permeability is used. In the internal part, roller-compacted concrete with low slump is used. Considering that the nature of internal and external concrete and the cement used in them are different.

Therefore, the hydration of different cements in the dam body causes thermal cracks in the external concrete. Neglecting this issue can lead to cracks in vulnerable parts of dams (Koga et al., 2018). In past researches, limited studies have been done on the effect of earthquake components on the behavior of dams.

However, the behavior of thermal cracks created in RCD with fracture mechanics criteria has not been done accurately. In this research, the behavior of the thermal cracks existed in the RCD body, is investigated through translational and rotational components of the seismic ground motion. On the other hand, in most studies on the crack propagation in the concrete dams, only translational component of the earthquake is considered, whereas when an earthquake occurs, rotational components of ground motion are generated which have great effect in the structural responses (Carpiuc-Prisacari et al., 2017; Moradloo and Naiji, 2020).

Generally, in earthquake engineering, rotational effect of the earthquake is recognized for the long structures such as bridges, dams, pipe lines, and transfer systems. In earlier studies, the effects of the rotational component were just considered for asymmetric structures (De la Lira and Chopra, 1994; Lee and Trifunac, 1985), whereas some studies demonstrate that there are many symmetric structures which are excited by rotational modes about vertical axis (Takamori et al., 2009; Teisseyre, 2011). In this paper, the effect of rotational components of earthquake on the behavior of RCD is considered.
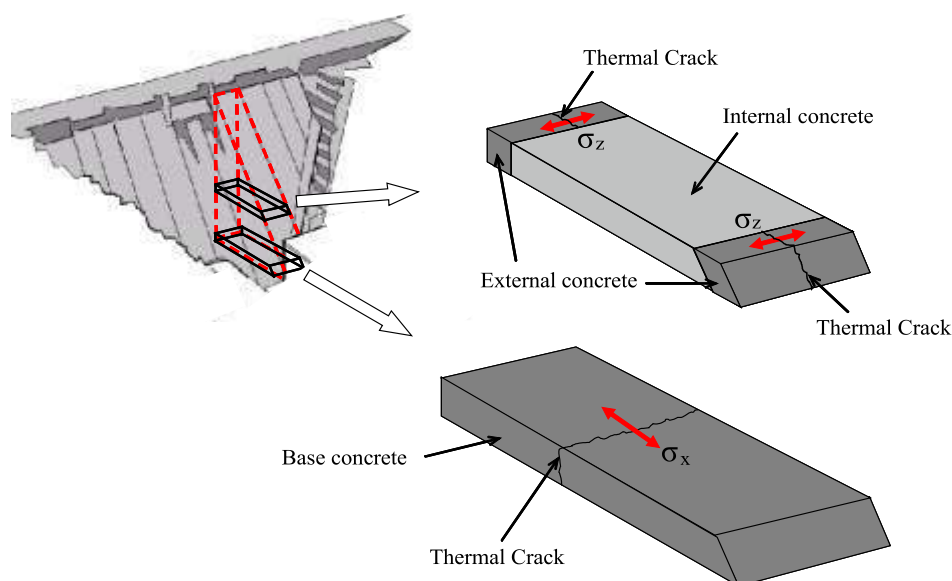
Fig. 1. Position of the thermal cracks in the RCD body (Sato et al., 2015)
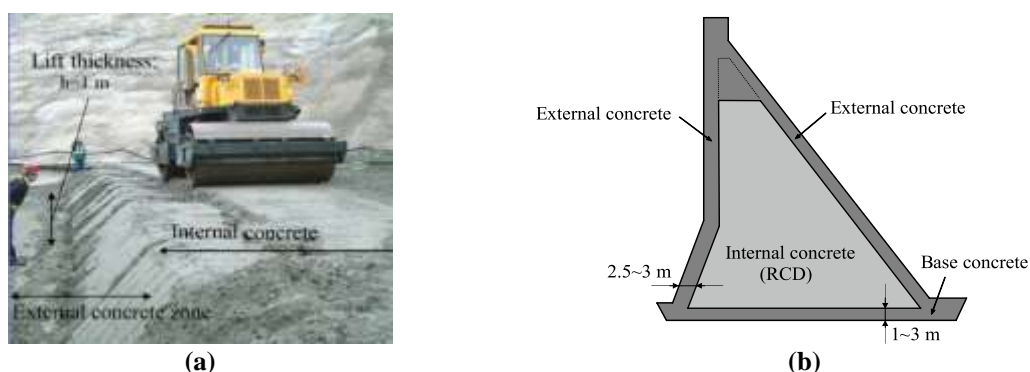
Fig. 2. Details of RCD construction (Nagataki et al., 2008): a) Internal concrete placement; and b) Internal and external concretes in the RCD body.

2. RCD Introduction

RCD are the dams whose concrete is compacted using roller. Because of technical and economic advantages such as reduction in cost and time of construction, this type of dam is widely used by many dam constructors in the world. According to the Figure 2a concrete placement of RCD is performed by Extended Layer Construction Method (ELCM). In ELCM method, the internal concrete of the dam is compacted step by step using rollers.

Generally, 15 meters of concrete with a thickness of 1 meter is compacted in each step (Nagataki et al., 2008). As it is clear in Figure 2b, the concrete used in RCD are divided into two zones of external concrete and internal concrete .The depth of external concrete at upstream and downstream surfaces is 3 m. External concrete is made of conventional concrete while internal concrete is made by RCD method. Slump value of internal concrete must be close to zero to resist the weight of the compaction roller and external conventional concrete must prevent water penetration into the dam body. Due to the difference in the workability of internal and external concrete, the types of these concretes are different. This difference can cause thermal strains and shrinkage between internal and external concretes (Sato et al., 2015). In fact, thermal cracks are generated due to hydration of various cement used in the dam body.

3. Estimating Rotational Component of Ground Motion

In this study, with the aim of more comprehensive investigating the dynamic behavior of the dam, the rotational component of the earthquake is also considered. For this purpose, it is necessary to first calculate the rotational component of the earthquake with methods based on wave theory, which will be briefly explained below. Igel et al. (2007; 2005) completely recorded rotational ground motion, using ring laser gyroscope. There are different methods proposed by the researchers to estimate the rotational components of the earthquake using two recorded translational components. The first method to estimate rotational component was proposed by New Mark (1969). In New Mark method, a simplified relation between translational and rotational components of earthquake was presented, which was investigated more in the further studies. In addition to New Mark method, other methods like time derivative and finite difference methods were also proposed (Ghafory-Ashtiany and Singh, 1986; Li et al., 2004). In this paper, Hong-Nan Li method (Li et al., 2004) is applied to estimate rotational component of the earthquake. Earthquake rotational components are consisted of two rocking components (about x and y axis) and one torsional component (about z axis).
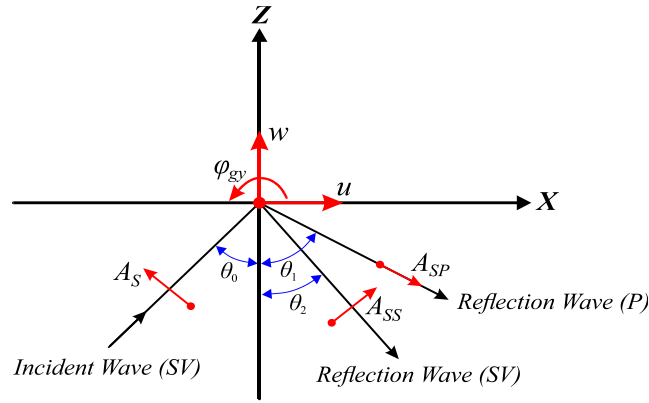
Fig. 3. Propagation of SV wave and its reflection waves on the ground surface (Data, 2010)

In this paper, the rotational component (about y axis) is estimated using horizontal and vertical components of ground motion (x and z directions). The Hang-Nan Li method (Li et al., 2004) is used for this purpose as follows. Seismic motions are generated by planar harmonic waves and according to Figure 3, direction of propagation of these waves line in the vertical plane (x,z). These waves are decomposed into in-plane components of amplitude as in the plane perpendicular to propagation direction of the waves. The incidence and in-plane of the waves generate two rocking components of ϕ_{gx} and ϕ_{gy} at the free surface (Data, 2010).

According to Figure 3, w and u vectors show positive direction of the ground motion coordinates. A_S, A_{SP} and A_{SS} vectors show positive direction of the incident waves displacement amplitude and displacement amplitude of P and SV reflection waves, respectively. θ_0: is the angle of incidence of SV waves, θ_1: is the reflection angle of P waves and θ_2: is the reflection angle of SV waves where θ_0 and θ_2 are equal. In the case of the incident SV waves, u, w and ϕ_{gy}: are none-zero components of the motion in y = 0 plane. Similarly, for x = 0 plane, none-zero components of the motion are v, w and ϕ_{gx}.

In this study, rotational components of earthquake records are extracted using relations 1 to 16. Based on the theory of wave propagation, rocking component (ground motion rotational component about

y axis) is equal to:

$$\varphi_{gy} = \frac{1}{2}(\frac{\partial w}{\partial x} - \frac{\partial u}{\partial z}) \qquad (1)$$

where displacement vectors u and w in the direction of x and z are computed as follows:

$$u = \frac{\partial \phi_{SP}}{\partial x} + \frac{\partial(\psi_{SV} + \psi_{SS})}{\partial z} \qquad (2)$$

$$w = \frac{\partial \phi_{SP}}{\partial z} - \frac{\partial(\psi_{SV} + \psi_{SS})}{\partial x} \qquad (3)$$

For harmonic waves of frequency ω, potential functions are:

$$\psi_{SV} = A_S \exp i\omega\left(\frac{\sin\theta_0}{\beta}x - \frac{\cos\theta_0}{\beta}z - t\right) \qquad (4)$$

$$\varphi_{SP} = A_{SP} \exp i\omega\left(\frac{\sin\theta_1}{\alpha}x + \frac{\cos\theta_1}{\alpha}z - t\right) \qquad (5)$$

$$\psi_{SS} = A_{SS} \exp i\omega\left(\frac{\sin\theta_0}{\beta}x + \frac{\cos\theta_0}{\beta}z - t\right) \qquad (6)$$

where α and β: are propagation velocities of P and S waves, respectively; and can be obtained as follows:

$$\alpha = \left[\frac{E}{\rho}\frac{1-\nu}{(1+\nu)(1-2\nu)}\right]^{\frac{1}{2}} \qquad (7)$$

$$\beta = \left[\frac{G}{\rho}\right]^{\frac{1}{2}} = \left[\frac{E}{\rho}\frac{1}{(1+\nu)^2}\right]^{\frac{1}{2}} \qquad (8)$$

where *E, G, P, and V*: are young's modulus, shear modulus, density and Poisson's ratio of soil, respectively. α, β coefficients are dependent to soil condition and are about 5-7 km/sec and 3-4 km/sec for the ground surface, respectively.

Imposing initial condition of free shear stress at the ground surface, gives:

$$\tau_{xz}\Big|_{z=0} = \left[\frac{\partial w}{\partial x} + \frac{\partial u}{\partial z}\right]_{z=0} = 0 \tag{9}$$

Therefore, Eq. (1) can be rewritten as:

$$
\begin{aligned}
\varphi_{gy} &= \frac{\partial w}{\partial x} = \frac{\partial^2 \phi_{SP}}{\partial z \partial x} - \frac{\partial^2 (\psi_{SV} + \psi_{SS})}{\partial^2 x} \\
&= i\omega \frac{\cos\theta_1}{\alpha} i\omega \frac{\sin\theta_1}{\alpha} \phi_{SP} \\
&- [(i\omega \frac{\sin\theta_0}{\beta})\psi_{SV} + (i\omega \frac{\sin\theta_0}{\beta})^2 \psi_{SS}]
\end{aligned}
\tag{10}
$$

According to Snell's law, $\frac{(\sin\theta_0)}{\beta} = \frac{(\sin\theta_1)}{\alpha}$, therefore:

$$\phi_{gy} = \frac{i\omega}{C_x} w \tag{11}$$

where C_x: is equal to $\beta / \sin\theta_0$.

Moreover, the rocking component (ϕ_{gx}) is estimated in the same way. It is clear from Eq. (11) that, first of all, the angle of incidence must be computed to determine the rocking component.

According to the proposed method of Hong Nan Li, with changing the variable $x = \sin\theta_0$ and based on the Snell's law, and also initial condition of free shear stress at the ground surface, the incident angle of SV waves is obtained from Eqs. (12) to (15) as follows (Li et al., 2004):

$$K^2 \left(\frac{\partial w}{\partial z} + \frac{\partial u}{\partial x}\right) - 2\frac{\partial u}{\partial x}\Big|_{z=0} = 0 \tag{12}$$

$$\left(\frac{\partial w}{\partial x} + \frac{\partial u}{\partial z}\right)\Big|_{z=0} = 0 \tag{13}$$

$$G = \frac{2x\sqrt{1 - K^2 x^2}}{K(1 - 2x^2)}, \qquad \theta_0 < \theta_c \tag{14}$$

$$G = -\frac{2x\sqrt{1 - K^2 x^2}}{iK(1 - 2x^2)}, \qquad \theta_0 > \theta_c \tag{15}$$

where $G = tg\bar{e} = w/u$ and / or $G = tg\bar{e} = w/v$: are of the rocking components of the motion in *x-z* and *y-z* planes due to SV waves, $K = \alpha/\beta$ and $\theta_c = \arcsin(\beta/\alpha)$ incident critical angle and $x = \sin\theta_0$, respectively.

To estimate time history of rocking components, Eq. (11) can be rewritten in the complex form as follows:

$$
\begin{aligned}
\varphi_{gy}(t) &= \frac{i\omega}{C_x} w \\
&= \left(1 e^{\frac{\pi}{2}i}\right) \cdot \left(\frac{\omega}{C_x}\right) \cdot \left(R_w \cdot e^{i\theta_w}\right) \\
&= \left(\frac{\omega}{C_x} R_w\right) \left(e^{\left(\frac{\pi}{2} + \theta_w\right)i}\right)
\end{aligned}
\tag{16}
$$

where ω: is angular velocity of the wave, R_w: is the frequency amplitude of the wave in the desired frequency, and θ_w: is the phase of the wave in desired frequency, obtained from frequency spectrum of the *w* component.

By using discrete Fourier transform and substituting the related equations, the time history of rocking component is obtained (Li et al., 2004). In this paper, 7 near-field earthquake records are used which are given in Table 1.

Table 1. Characteristics of the earthquake records

No	Year	Event	Station	Magnitude (Richter)	Closest Distance to Fault Rupture (km)	Shear wave velocity of Soil (m/s)	PGA (g)
1	1999	Kocaeli	Arcelik	7.51	10.56	523.0	0.21
2	1995	Kobe (1)	Takatori	6.90	1.47	256.0	0.61
3	1995	Kobe (2)	Takarazuka	6.90	0.27	312.0	0.69
4	1978	Tabas	Tabas	7.35	2.05	766.7	0.85
5	2003	Bam	Bam	6.60	1.70	487.4	0.79
6	1999	Duzce (1)	Lamont	7.14	9.14	338.0	0.25
7	1999	Duzce(2)	Bolu	7.14	12.02	293.5	0.78

It is obvious that recent earthquakes can also be used, but considering that the vertical component of the earthquakes presented in Table 1 is significant; and on the other hand, many researchers have used these records. Therefore, these 7 earthquakes have been used in this research. Rotational components of these records are extracted using the aforementioned relations (Hong Nan Li relations) and Matlab software.

4. J Integral as a Criterion for Crack Propagation

J integral is considered as one of the fracture mechanics criteria in linear and nonlinear materials and is widely accepted among researchers. This parameter is related to the amount of released energy associated with crack propagation and is regarded as a measure of crack propagation intensity,

(especially for nonlinear materials). In this paper, the methods proposed by Parks (1977) and Shih et al. (1986) are used to compute J integral values. The method is considered as one of the appropriate methods because of its simplicity and high accuracy. This integral is estimated using FE method by abacus software (Abacus-Documentation, v2021) and considering Eqs. (17-24). In two dimensional problems, J integral is estimated as follows:

$$J = \lim_{\Gamma \to 0} \int_{\Gamma} n.H.q d\Gamma \tag{17}$$

where Γ : defines the minimum path initiating from the bottom crack surface and ending on the top surface (as shown in Figure 4). $\Gamma = 0$: defines the position of the crack tip. q: defines a unit vector which shows the crack propagation direction and n: is the outward normal to Γ.
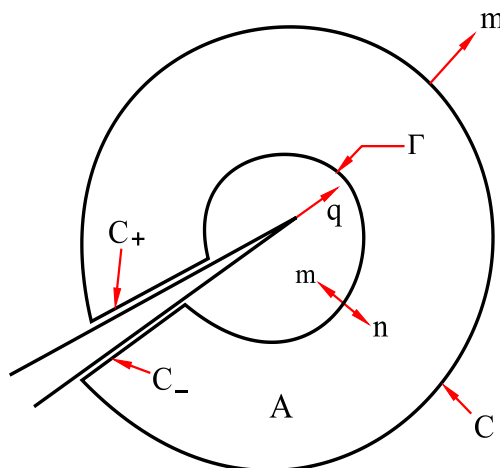

Fig. 4. Two dimensional concept of J integral (Abacus-Documentation, v2021)
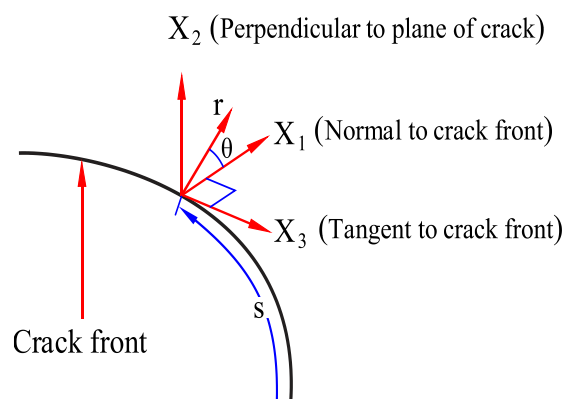

Fig. 5. Three dimensional concept of J integral (Abacus-Documentation, v2021)

According to Figure 5, J integral value of the three dimensional model is given by:

$$J(s) = \lim_{\Gamma \to 0} \int_{\Gamma} n.H.q\,d\Gamma \qquad (18)$$

For a virtual crack, the released energy rate is defined as follows:

$$\bar{J} = \int_L J(s)\,\lambda(s)\,ds = \lim_{\Gamma \to 0} \int_{A_t} \lambda(s)n.H.q\,dA \qquad (19)$$

where L: denotes the crack front, dA: defines an enclosed area around crack front line, and n: is the outward normal to dA ($dA = ds.d\Gamma$).

Integral of the Eq. (19) is converted from surface integral into volume integral. According to Figure 6, an enclosed volume will be generated to compute this integral of three dimensions where V: denotes the crack front line and the area A: is consisted of the following terms:

$$A = A_t + A_o + A_{ends} + A_{cracks} \qquad (20)$$

where A_t : the inner is enclosed surface around the crack front line, A_o : is the outer enclosed surface around the crack front line, A_{cracks} : is the crack surface, and A_{ends} : is the beginning and ending surface of a closed volume. $\bar{q}$: is a weighting function and is defined in a way to have a magnitude of zero on A_o and $\bar{q} = \lambda(s)q$ on A_t. Eq. (19) can be rewritten as follows:

$$\bar{J} = -\oint_A m.H.\bar{q}\,dA - \int_{A_{cracks}+A_{ends}} t.\frac{\partial u}{\partial x}.\bar{q}\,dA \qquad (21)$$

where m: is the outward normal to A ($m = -n$) and t: is a surface traction on the surfaces A_{cracks} and A_{ends} ($t = m.\sigma$). Eq. (21) can be rewritten using divergence theorem as follows:

$$\bar{J} = -\int_V \left[H:\frac{\partial \bar{q}}{\partial x} + (f.\frac{\partial u}{\partial x} - \sigma:\partial \frac{\partial \varepsilon^{th}}{\partial x}).\bar{q} \right] dV - \int_{A_{cracks}+A_{ends}} t.\frac{\partial u}{\partial x}.\bar{q}\,dA \qquad (22)$$

In FE method, to obtain $J(s)$ for the node set P along the crack front line, it is required to consider $\lambda(s)$ as follows:

$$J(s) = N^Q(s)\lambda^Q \qquad (23)$$

where $\lambda^Q = 1$ at the node set P and $\lambda^Q = 0$ for the other ones. Eq. (23 is substituted in Eq. (22) and finally Eq. (22) will be rewritten as follows:

$$J^P = \bar{J}^P / \int_L N^P ds \qquad (24)$$

J integral value is equal to the released strain energy of G. Therefore, the critical released strain energy can be utilized to use J integral as a crack propagation criterion (Gdoutos, 2012). G_c rate is varied for different kinds of concrete and its maximum value is 166.71 (N/M) (Shah and Kishen, 2011).
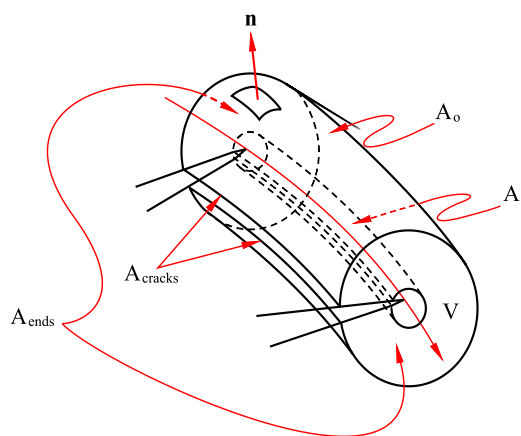

Fig. 6. Enclosed volume to solve the integral

5. Finite Element Modeling of the Dam

There are many analytical and experimental studies on the gravity concrete dams and Koyna dam is used as a benchmark dam in many of these studies, because of the statistical data which are recorded after Koyna earthquake and are comparable with the theory based analysis results (Chopra and Chakrabarti, 1973; Mirzabozorg and Kianoush, 2008). Therefore, in this research, Koyna dam is used as a benchmark structure. As it is clear in Figure 7 it has 103 m height and 850 meters length, located in India.

This dam was subjected to Koyna earthquake of 6.5 Richter scale magnitude and gone thorough serious damages and cracking. The water level behind the dam was 91.75 m, the hydrostatic pressure of which must be considered. In this study, due to the large length to width ratio of the dam, plain strain relations are used to solve the governing equations. On the other hand, it is obvious that considering the interaction of soil and structure has a significant effect on the behavior of the dam. However, in order to simplify the problem and reduce the time of analysis, in this study, the dam base is assumed to be fixed.

As mentioned in Section 2, concrete placing of RCD is performed by ELCM method; in this method, the thickness of each layer is equal to 1 m. The construction of each layer is conducted in several step, in each step, 15 m of the length of the dam is compacted. Therefore, in this research, a three-dimensional FE model was constructed for a block of dam with 15 m length. In order to consider plain strain relations, the displacement perpendicular to the dam length was constrained (Figure 7b). Material characteristics and natural frequency of Koyna dam are given in Tables 2 and 3, respectively. Concrete damaged plasticity is used for introducing the concrete behavior (Lee and Fenves, 1998; Lubliner et al., 1989). In this model, concrete behavior is introduced separately in tension and compression. In addition, uniaxial tension damage parameter of the concrete is applied in accordance with the displacement of the crack.

Table 2. Material properties for the Koyna dam concrete (Chopra and Chakrabarti, 1973)

Parameter	Value
Young's modulus	E = 31027 MPa
Poisson's ratio	υ = 0.15
Density	ρ = 2643 kg/m^3
Dilation angle	ψ = 36.31°
Compressive initial yield stress	σ_{c0} = 13.0 MPa
Compressive ultimate stress	σ_{cu} = 24.1 MPa
Tensile failure stress	σ_{t0} = 2.9 MPa

Table 3. Natural frequencies of the Koyna dam (Chopra and Chakrabarti, 1973)

	Natural frequency (rad sec^{-1})	
Mode	Abacus	Chopra and Chakrabarti (1973)
1	18.86	19.27
2	49.97	51.50
3	68.16	67.56
4	98.27	99.73

(a)

(b)
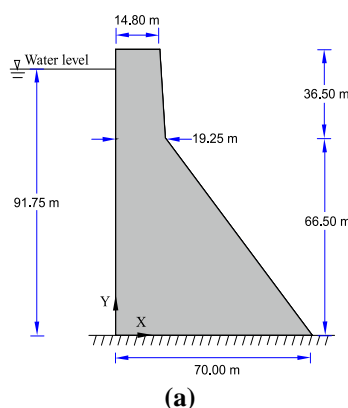
Fig. 7. Details of Koyna dam: a) Geometrical dimensions of the Koyna dam (Chopra and Chakrabarti, 1973); and b) FE mode of Koyna dam

Damping coefficient of the conventional dams is 2-3% which is considered 3% in this research. To introduce damping, it is first required to compute β coefficient as follows:

$$\beta = \frac{2\xi_1}{\omega_1} \qquad (25)$$

where ξ_1 : is the critical damping of the first mode and ω_1 : is the natural frequency of the first mode, which are given in Table 3. Natural frequency of the first mode is 18.86, therefore, β is obtained as 3.2310^{-3} sec.

6. Validation of the Finite Element Model

The model was subjected to the accelerograms of Koyna earthquake, as provided in Figure 8 and FE results are compared with shake table experimental results (Wilcoski et al., 2001) and the reference model results (Mirzabozorg and Kianoush, 2008). Owing to the fact that tensile strength of the concrete is much lower than compressive strength; the concrete will fail in tension. As it is clear in Figure 9 the cracking is initiated from the interface of the structure and foundation from the upstream region (dam heel) and grows to some extent and then stops. Then, the cracking in the upper one-third region of the dam is initiated from the downstream (dam throats) which then propagates to the upstream region of the dam.

As it is shown in Figure 10 in the FE model, shaking table model (Wilcoski et al., 2001) and the reference model (Mirzabozorg and Kianoush, 2008), the position of the crack growth is the same. Figure 11 also compares the relative displacement of the dam crest, with the results of the reference model and shows a little difference between them. Besides, comparing the results of FE model analysis with several other numerical models (Haghani et al., 2020; Haghani et al., 2021, 2022), shows that the constructed model has good accuracy. Therefore, it can be concluded that the FE model built in this research, is valid.
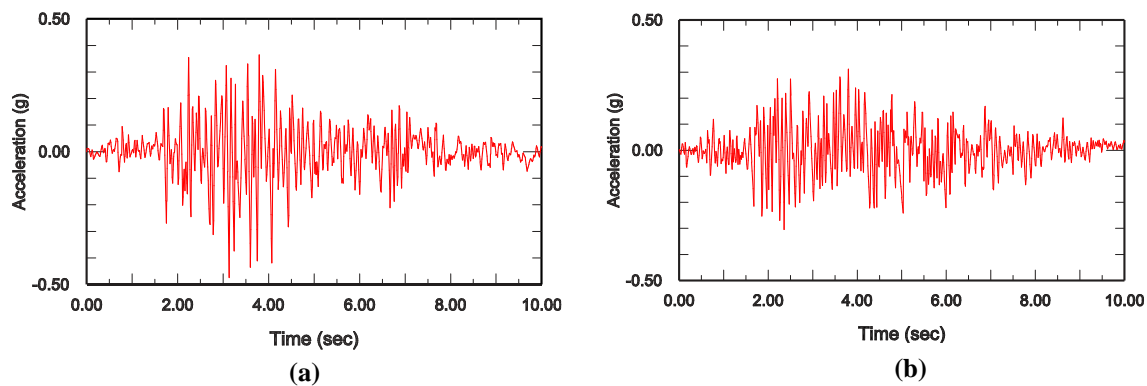

Fig. 8. Koyna earthquake accelerograms: a) Horizontal acceleration; and b) Vertical acceleration

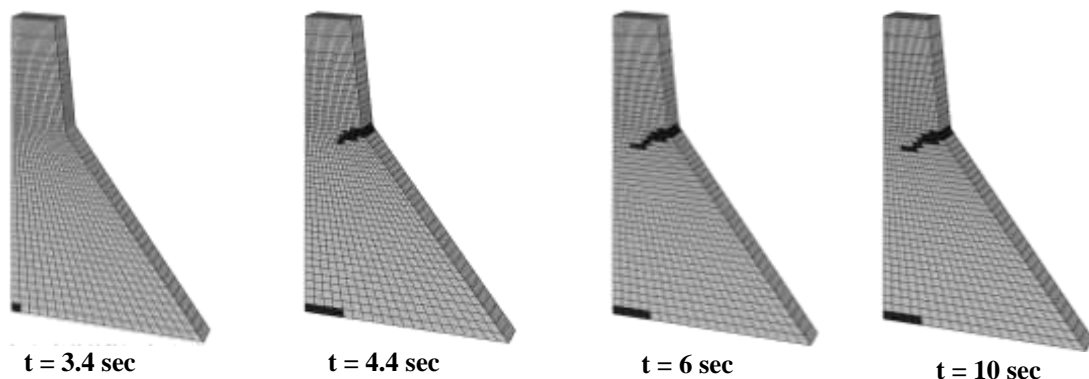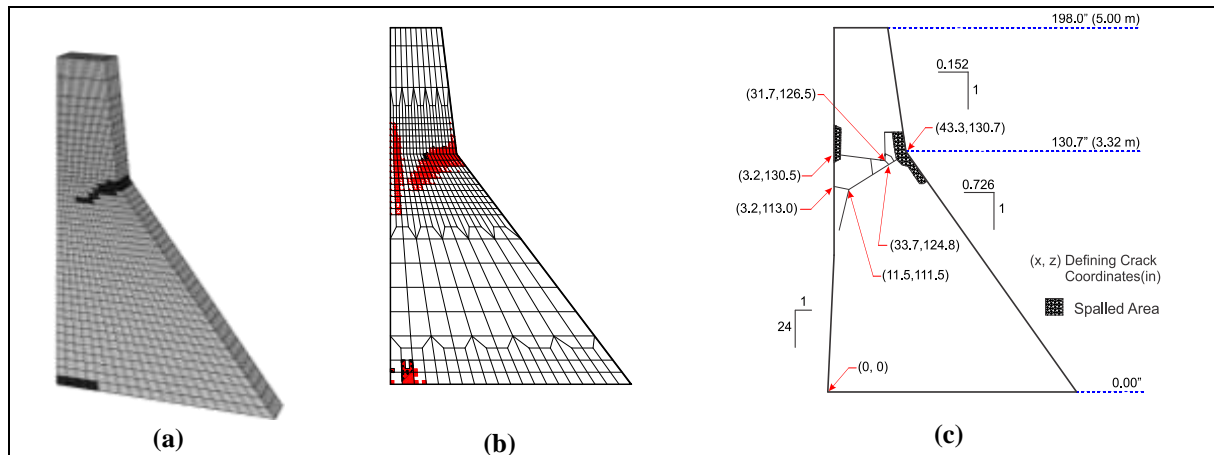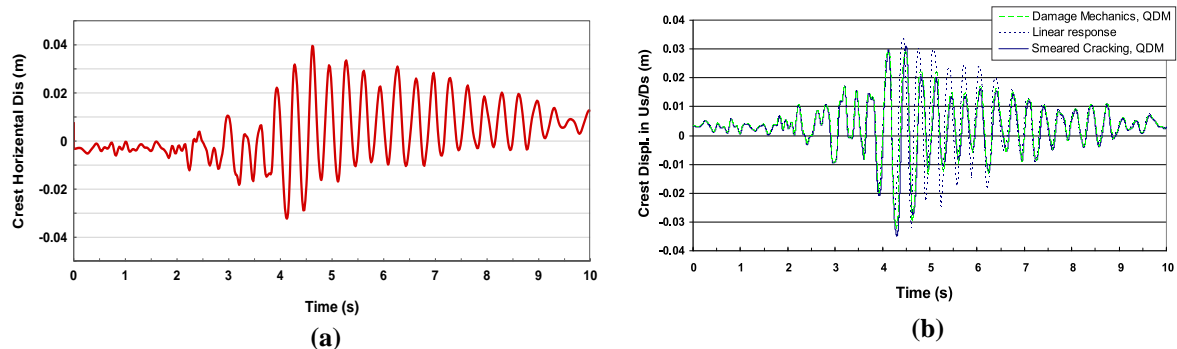t = 3.4 sec   t = 4.4 sec   t = 6 sec   t = 10 sec

Fig. 9. Crack growth after imposing Koyna earthquake

Fig. 10. FE model validation : a) Tensile failure of the concrete after FE analysis; b) Reference model results (Mirzabozorg and Kianoush, 2008); and c) Results obtained from the shaking table (Wilcoski et al., 2001)

Fig. 11. FE model validation: a) Relative displacement of the dam crest in the FE model; and b) Reference model results (Mirzabozorg and Kianoush, 2008)

7. Thermal Crack Modeling

Results of the FE model show that the critical regions of the dam during an earthquake are the upper one-third region of the dam from the downstream side (dam throat) and the interface of the structure and foundation form the upstream side (dam heel), where the dam throat is the most critical region of the dam from seismic point of view. In this paper, as shown in Figure 12 the behavior of a thermal crack is evaluated supposing the crack is located at the dam throat, where is the most critical region on the dam. The crack length is equal to the external concrete thickness (3 m) and the crack height is equal to the thickness of the RCD concrete (1 m).

According to the mentioned details, this crack is generated at the height of 66.5 m in the FE model and is evaluated under 7 earthquake records which were introduced in the Table 1.

8. Finite Element Analysis Results

The FE model is subjected to the rotational and translational components of the earthquake records mentioned in Table 1 and the results of the nonlinear FE analysis are then evaluated. To validate J integral method, the crack behavior is evaluated using concrete tensile damage method under one of the earthquake records and the results are compared with the estimated values of J integral. Then, the crack behavior is also evaluated under 6 remaining earthquake records. Figure 13 shows the results of the FE analysis on Koyna dam under Kocaeli earthquake (1999) for two conditions of regarding rotational component and neglecting it.
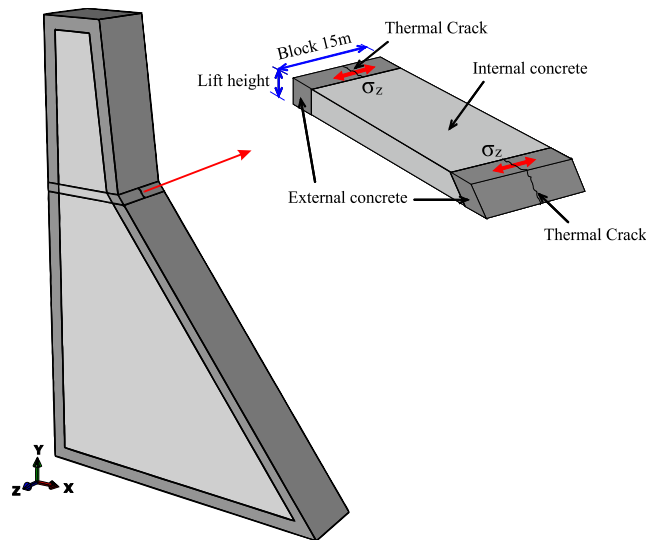
Fig. 12. Thermal crack location in the finite element model

Table 4. The results obtained from the FE analysis under Kocaeli earthquake (1999)

Parameter	Maximum displacement of the dam crest (mm)	Maximum base shear of the dam (N)	Maximum J integral value (N/m)
2 components condition (neglecting rotational component)	20.23	324.2×10^6	106.49
3 components condition (considering rotational component)	19.98	259.5×10^6	202.50
The ratio of 3 component to 2 component	0.98	0.80	1.90

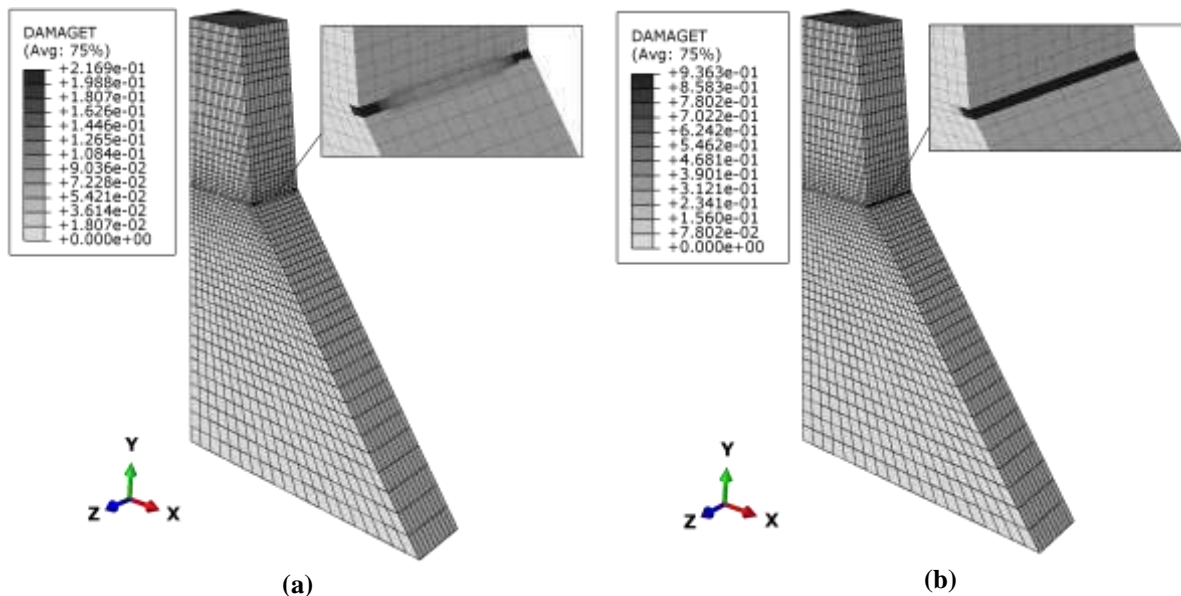**(a)**   **(b)**

Fig. 13. Concrete tensile damage under Kocaeli earthquake (1999): a) Neglecting rotational component (2 Components condition); and b) Considering rotational component (3 Components condition)

The FE analysis results of this dam under Kocaeli earthquake are summarized in Table 4. In this table, the obtained values refer to the maximum relative displacement of the dam, maximum base shear, and maximum J integral value, for both conditions. It can be seen that taking into account of the rotational component leads to

2% reduction in the maximum displacement response and 20% reduction in maximum base shear response of the dam; while the J integral estimated value of the three components condition is about twice of the two component condition value.

It can be seen in Figure 13 that in two components condition, concrete tensile damage is not present at the crack location, which means the crack is not propagated, while in three components condition, the first tensile damage is formed and the crack is ready to propagate. By comparing maximum values of J integral mentioned in Table 4, and the values provided by reference (Shah and Kishen, 2011), it can be concluded that in two components condition, the J integral estimated value is lower than the critical released strain energy $G_C = 166.71$ N/m, while it is higher in three components condition.

Therefore, it can be concluded that J integral is an appropriate criterion to evaluate crack propagation in this model and has enough accuracy. The tensile damage related to the remaining earthquake records mentioned in Table 1 is shown in Figure 14 for both conditions.

The obtained values of the maximum relative displacement of the dam crest, maximum base shear, and maximum J integral value, for both conditions are summarized in Table 5. Comparing response ratios of two components and three components conditions, it can be concluded that considering rotational component can change relative displacement of the dam crest and maximum base shear of the dam up to 25% and this change can be either increasing or decreasing in respect to intensity and frequency content of the earthquake. The results of imposing seven records show that considering rotational components often has decreasing effect in terms of maximum displacement of the dam crest, while this consideration has increasing effect in terms of maximum base shear of the dam.

Rotational components also have considerable effect on J integral estimated values, for instance, earthquake records of Kacaeli (1999) and Kobe 2 (1995), cause more than 50% increase in J integral values. As it was mentioned before, the released strain energy in the thermal crack tip, is equal the estimated J integral value in Table 5, where the maximum value of this integral is for Tabas earthquake (1978) 126.7×10^3 N/m and the minimum value was for Duzce1 earthquake (1999) 32.95 N/m. Therefore, it is expected that the maximum and minimum failure due to thermal crack propagation are related to these earthquake records, Figure 14 confirms this issue.

Table 5. Summarized results obtained from finite element analysis for different earthquake records

Event	Maximum displacement of the dam crest (mm)			Maximum base shear of the dam (N) $\times 10^6$			Maximum J integral value (N/m)		
	2 Comp.[*]	3 Comp.[*]	R[**]	2 Comp.[*]	3 Comp.[*]	R[**]	2 Comp.[*]	3 Comp.[*]	R[**]
Kocaeli (1999)	20.2	19.9	0.98	324.2	259.5	0.80	106.49	202.5	1.90
Kobe 1 (1995)	286.9	282.1	0.98	815.6	786.2	0.96	48.36×10^3	36.1×10^3	0.75
Kobe 2 (1995)	64.7	59.4	0.92	934.4	933.7	0.99	6.74×10^3	10.2×10^3	1.51
Tabas (1978)	115.6	120.0	1.04	1093.2	1336.4	1.22	262.5×10^3	126.7×10^3	0.48
Bam (2003)	117.9	115.9	0.98	815.6	923.4	1.13	37.92×10^3	41.0×10^3	1.08
Duzce1 (1999)	20.5	23.4	1.14	893.1	924.7	1.03	18.71	32.9	1.76
Duzce2 (1999)	168.8	167.2	0.99	837.2	1058.5	1.26	14.48×10^3	13.5×10^3	0.93

2 Comp[*]: 2 components condition (neglecting rotational component)

3 Comp[*]: 3 components condition (considering rotational component)

R[**]: The ratio of 3 components to 2 components

(Considering rotational component)   (Neglecting rotational component)

(a) Kobe 2 (1995)

(Considering rotational component)   (Neglecting rotational component)

(b) Kobe 1 (1995)

(Considering rotational component)   (Neglecting rotational component)

(c) Bam (2003)

(Considering rotational component)   (Neglecting rotational component)

(d) Tabas (1978)

(Considering rotational component)   (Neglecting rotational component)

(e) Duzce 1 (1999)

(Considering rotational component)   (Neglecting rotational component)
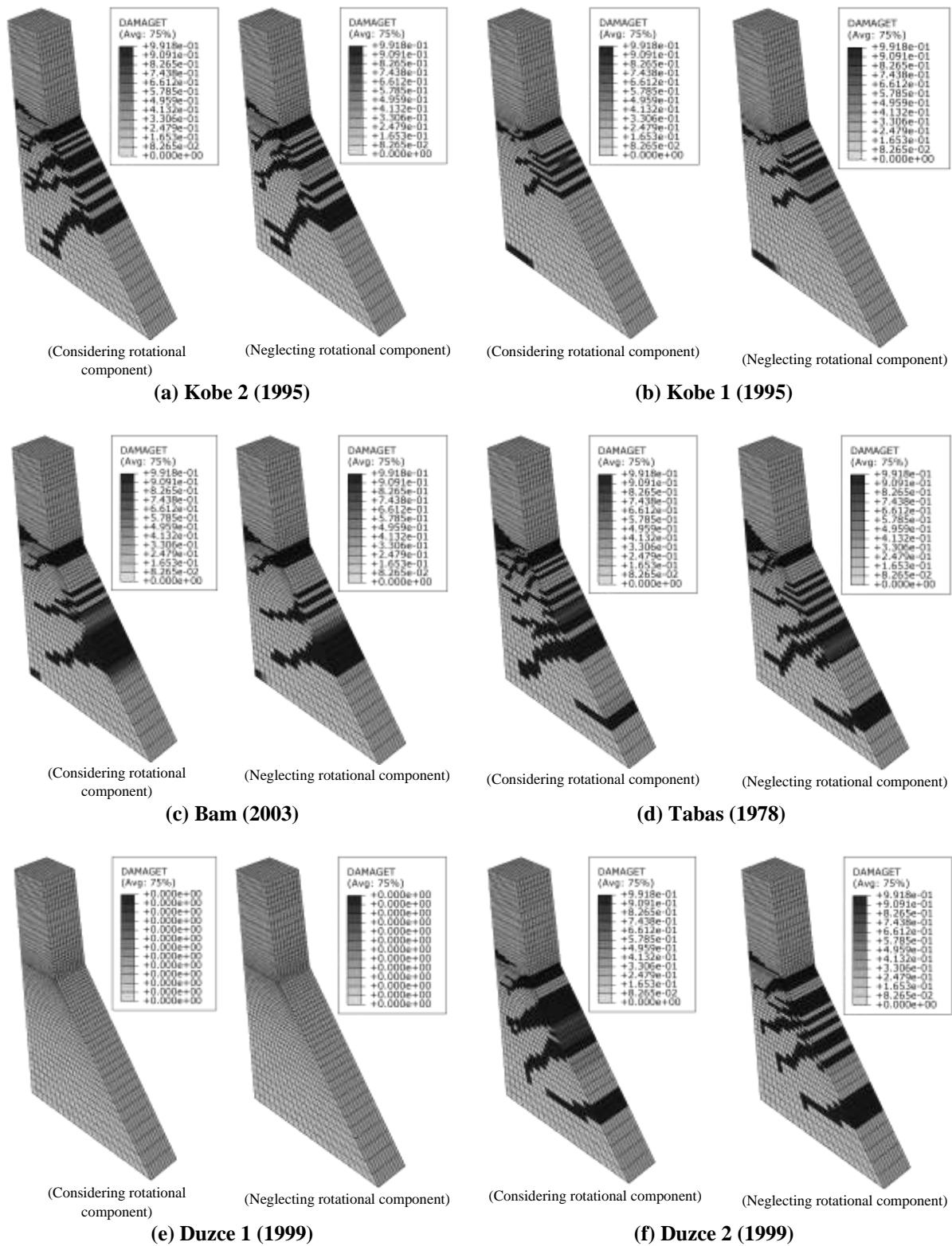
(f) Duzce 2 (1999)

Fig. 14. Concrete tensile damage under earthquake rotational and translational components

9. Conclusions

In this study, the behavior of thermal cracks existed in the concrete dam body, was evaluated under rotational and translational components of the earthquakes. First, three dimensional model of Koyna dam was built in abacus software using FE method and subjected to 7 near field earthquake records. Comparing the results of FE model with experimental data revealed that the built FE model is valid. Then, a thermal crack with 3

m length at the height of 66.5 m from the dam bottom was modeled in downstream side of the dam and the released strain energy due to the crack propagation was obtained using J integral as a fracture criterion, under rotational and translational components of 7 earthquake records. The obtained results from FE analysis are represented as follows:

- Comparing the obtained results from the concrete tensile damage with J integral estimated values, it can be concluded that J integral is an appropriate fracture criterion to evaluate crack propagation in concrete dams and has enough accuracy.

- Considering the rotational components of an earthquake, can change seismic response of the dam up to 25% and this change can be either in form of decreasing or increasing in respect to intensity and frequency content of the earthquake.

- Rotational components of the earthquake records often have decreasing effect in the maximum displacement of the dam crest whereas for base shear, rotational components have increasing effect.

- In comparison with other seismic parameters, rotational components of the earthquake have more significant effect on J integral values, for instance, earthquake records of Kocaeli (1999) and Kobe 2 (1995) show 50% increase in J integral values.

10. Acknowledgments

11. References

Abacus-Documentation. (v2021). *Abacus theory guide, J-integral evaluation*, Dassault Systèmes, http://130.149.89.49:2080/v2016.

Alfatlawi, T.J.M., Kadhim, M.J. and Hussein, M.N. (2021). "Relation between cracks behavior and curvature in cracked concrete arch dam under earthquake", *Materials Today: Proceedings*, https://doi.org/10.1016/j.matpr.2021.02.248.

Carpiuc-Prisacari, A., Poncelet, M., Kazymyrenko, K., Leclerc, H. and Hild, F. (2017). "A complex mixed-mode crack propagation test performed with a 6-axis testing machine and full-field measurements", *Engineering Fracture Mechanics*, 176, 1-22, https://doi.org/10.1016/j.engfracmech.2017.01.013.

Chopra, A.K. and Chakraborty, P. (1972). "The earthquake experience at Koyna dam and stresses in concrete gravity dams", *Earthquake Engineering and Structural Dynamics*, 1(2), 151-164, https://doi.org/10.1002/eqe.4290010204.

Chopra, A.K. and Chakraborti, P. (1973). "The Koyna earthquake and the damage to Koyna dam", *Bulletin of the Seismological Society of America*, 63(2), 381-397.

Data, T.K. (2010). *Seismic analysis of structures*, John Wiley and Sons (Asia) Pte Ltd., https://doi.org/10.1002/9780470824634.

De la Lira, J.C. and Chopra, A.K. (1994). "Accidental torsion in buildings due to stiffness uncertainty", *Earthquake Engineering and Structural Dynamics*, 23(2), 117-136, https://doi.org/10.1002/eqe.4290230202.

El-Aide, B. and Hall, J.F. (1989). "Non-linear earthquake response of concrete gravity dams Part 1: Modelling", *Earthquake Engineering and Structural Dynamics*, 18(6), 837951, https://doi.org/10.1002/eqe.4290180607.

Gdoutos, E.E. (2012). *Fracture mechanics criteria and applications*, Part of the book series: Engineering Applications of Fracture Mechanics (EAFM), (Vol. 10), Springer Science and Business Media.

Ghafory-Ashtiany, M. and Singh, M.P. (1986). "Structural response for six correlated earthquake components", *Earthquake Engineering and Structural Dynamics*, 14(1), 103-119. https://doi.org/10.1002/eqe.4290140108.

Haghani, M., Navayi Neya, B. and Ahmadi, M.T. (2020). "Nonlinear seismic analysis of concrete gravity dams using Extended Finite Element method and Plastic Damage Model", *Modares Civil Engineering Journal*, 20(3), 189-201.

Haghani, M., Neya, B.N., Ahmadi, M.T. and Amiri, J.V. (2021). "Comparative study of smeared crack and extended finite element method for predicting the crack propagation in concrete gravity dams", *Journal of Earthquake Engineering*, 1-34, https://doi.org/10.1080/13632469.2021.199153.

Haghani, M., Neya, B.N., Ahmadi, M.T. and Amiri, J.V. (2022). A new numerical approach in the seismic failure analysis of concrete gravity dams using extended finite element method", *Engineering Failure Analysis*, 132, 105835, https://doi.org/10.1016/j.engfailanal.2021.105835.

Hashempour, S.A., Akbari, R. and Lotfi, V. (2023).

"A simplified continuum damage model for nonlinear seismic analysis of concrete arch dams using different damping algorithms", *Civil Engineering Infrastructures Journal*, 56(2), 235-255, https://doi.org/10.22059/CEIJ.2023.342419.1837.

Igel, H., Cochard, A., Wassermann, J., Flaws, A., Schreiber, U., Velikoseltsev, A. and Pham Dinh, N. (2007). "Broad-band observations of earthquake-induced rotational ground motions", *Geophysical Journal International*, 168(1), 182-196, https://doi.org/10.1111/j.1365-246X.2006.03146.x.

Igel, H., Schreiber, U., Flaws, A., Schubert, B., Velikoseltsev, A. and Cochard, A. (2005). "Rotational motions induced by the M8, 1 Tokachi-oki earthquake, September 25, 2003", *Geophysical Research Letters*, 32(8), https://doi.org/10.1029/2004GL022336.

Ingraffea, A. (1990). "Case studies of simulation of fracture in concrete dams", *Engineering Fracture Mechanics*, 35(1-3), 553-564, https://doi.org/10.1016/0013-7944(90)90230-E.

Koga, H., Katahira, H. and Kawano, H. (2018). "Thermal measurement and analysis of large Roller Compacted Concrete dam", In: *Roller Compacted Concrete Dams,* (pp. 1139-1147), Routledge.

Lee, J. and Fenves, G.L. (1998). "Plastic-damage model for cyclic loading of concrete structures", *Journal of Engineering Mechanics*, 124(8), 892-900.

Lee, V.W. and Trifunac, M.D. (1985). "Torsional accelerograms", *International Journal of Soil Dynamics and Earthquake Engineering*, 4(3), 132-139, https://doi.org/10.1016/0261-7277(85)90007-5.

Li, H.N., Sun, L.Y. and Wang, S.Y. (2004). "Improved approach for obtaining rotational components of seismic motion", *Nuclear Engineering and Design*, 232(2), 131-137, https://doi.org/1016/j.nucengdes.2004.05.002.

Lubliner, J., Oliver, J., Oller, S. and Onate, E. (1989). "A plastic-damage model for concrete", *International Journal of Solids and Structures*, 25(3), 299-326.

Mirzabozorg, H. and Kianoush, M.R. (2008). "Seismic safety evaluation of concrete dams using damage mechanics approach", *The 14th World Conference on Earthquake Engineering*, October 12-17, Beijing, China.

Mofid, T. and Tavakoli, H. (2020). "Experimental investigation of post-earthquake behavior of RC beams", *Journal of Building Engineering*, 32, 101673, https://doi.org/10.1016/j.jobe.2020.101673.

Mofid, T. and Tavakoli, H. (2023). "Experimental investigation of mechanical behavior of lightweight RC elements under repeated loadings", *Structures*, 54, 1608-1622, https://doi.org/10.1016/j.istruc.2023.05.030.

Moradloo, A.J., and Naiji, A. (2020). "Effects of rotational components of earthquake on seismic response of arch concrete dams", *Earthquake Engineering and Engineering Vibration*, 19(2), 349-362, https://doi.org/10.1007/s11803-020-0566-x.

Nagataki, S., Fujisawa, T., and Kawasaki, H. (2008). "State of art of RCD dams in Japan", 50º *Congresso Brasileiro do Concreto*, *Salvado, 1st Brazilian RCC Symposium,* September.

Newmark, N.M. (1969). *Torsion in symmetrical buildings*, IIT Kanpur, https://www.iitk.ac.in/nicee/wcee/article/4_vol2_A3-19.pdf.

Parks, D. (1977). "The virtual crack extension method for nonlinear material behavior", *Computer Methods in Applied Mechanics and Engineering*, 12(3), 353-364.

Pirooznia, A. and Moradloo, A. (2020). "Investigation of size effect and smeared crack models in ordinary and dam concrete fracture tests, *Engineering Fracture Mechanics*, 226, 106863, https://doi.org/1016/j.engfracmech.2019.106863

Priya, M., PriyaPriya, M. and Santhi, A. (2022). "A material model approach on the deflection and crack pattern in different panels of the RCC flat plate using finite element analysis", *Civil Engineering Journal*, 8(3), 472-487.

Rescher, O.J. (1990). "Importance of cracking in concrete dams", *Engineering Fracture Mechanics*, 35(1-3), 503-524, https://doi.org/10.1016/0013-7944(90)90226-7.

Sadeghi, M.H. and Moradloo, J. (2022). "Seismic analysis of damaged concrete gravity dams subjected to main shock-aftershock sequences", *European Journal of Environmental and Civil Engineering*, 26(6), 24172438, https://doi.org/10.1080/1964889.2020.1763475.

Sato, H., Miyazawa, S., and Yatagai, A. (2015). "Thermal crack estimation of dam concrete considering the influence of autogenous shrinkage", In *CONCREEP 10*, (pp. 1289-1298), https://doi.org/https://doi.org/1061/9780784479346.153.

Shah, S. and Kishen, J.C. (2011). "Fracture properties of concrete–concrete interfaces using digital image correlation", *Experimental Mechanics*, 51(3), 303-313.

Shih, C., Moran, B. and Nakamura, T. (1986). "Energy release rate along a three-dimensional crack front in a thermally stressed body", *International Journal of Fracture*, 30(2), 79-102.

Singh, V. and Sangle, K. (2022). "Analysis of vertically oriented coupled shear wall interconnected with coupling beams", *High-Tech and Innovation Journal*, 3(2), 230-242,

https://doi.org/10.28991/HIJ-2022-03-02-010.

Soysal, B.F. and Arici, Y. (2023). "Crack width–seismic intensity relationships for concrete gravity dams", *Journal of Earthquake Engineering*, 1-17, https://doi.org/10.1080/1363246.2023.2220048.

Takamori, A., Araya, A., Otake, Y., Ishidoshiro, K. and Ando, M. (2009). "Research and development status of a new rotational seismometer based on the flux pinning effect of a superconductor", *Bulletin of the Seismological Society of America*, 99(2B), 1174-1180, https://doi.org/10.1785/0120080087.

Teisseyre, R. (2011). "Why rotation seismology: Confrontation between classic and asymmetric theories", *Bulletin of the Seismological Society of America*, 101(4), 16831691, https://doi.org/10.1785/0120100078.

Wang, Y.J., Wu, Z.M., Qu, F.M. and Zhang, W. (2022). "Numerical investigation on crack propagation process of concrete gravity dams under static and dynamic loads with in-crack reservoir pressure", *Theoretical and Applied Fracture Mechanics*, 117, 103221, https://doi.org/10.1016/j.tafmec.2021.103221.

Wilco Ski, J., Hall, R.L., Gambill, J.B., Mathieu, E.E. and Chowdhury, M.R. (2001). *Seismic testing of a 1/20 scale model of Koyna Dam*, Experimental Report, US Army Corps of Engineers.

Zhang, M., Li, M., Zhang, J., Liu, D., Hu, Y., Ren, Q. and Tian, D. (2020). "Experimental study on electro-thermal and compaction properties of electrically conductive roller-compacted concrete overwintering layer in high RCC dams", *Construction and Building Materials*, 263, 120248, https://doi.org/10.1016/j.conbuildmat.2020.120248.

Zhang, X., Yan, T., Liu, Q., Zhang, X. and Wang, L. (2022). "Cracking analysis of induced joints in roller compacted concrete arch dam", *Alexandria Engineering Journal*, 61(5), 3599-3612, https://doi.org/10.1016/j.aej.2021.08.082.

Hyperelastic Models for PET Woven Geotextiles in Civil Engineering: Framework and Insights

Belhadj, F.[1]* , Belhadj, A.[2] and Chabaat, M.[3]

[1] Assistant Professor, Built Environmental Research Lab, Faculty of Civil Engineering, University of Science and Technology, Houari Boumediene, Algeria.
[2] Associate Professor, Department of Civil Engineering, University Ferhat Abbas, Setif, Algeria.
[3] Professor, Built Environmental Research Lab, Faculty of Civil Engineering, University of Science and Technology, Houari Boumediene, Algeria.

ABSTRACT: The material properties of geotextiles play a significant role in shaping the long-term behavior of reinforced soils, potentially leading to issues like instability and excessive deformation. To address these challenges, thorough research into geotextile materials rheological properties and nonlinear behavior is essential. This study specifically focuses on the investigation of six commonly employed isotropic hyper elastic models (Neo-Hooke, Mooney-Rivlin, Ogden, Yeoh, Arruda-Boyce and Van der Waals) for describing the behavior of PET woven geotextiles in civil engineering applications. These models are fine-tuned through uniaxial tension tests conducted in warp and weft directions. Upon analyzing the experimental data, it becomes evident that the Yeoh and Neo-Hooke models exhibit exceptional accuracy in predicting geotextile behavior. The primary objective of this study is to advance our comprehension of how geotextiles react to varying loads, achieved through a combination of testing and finite element simulations. The robust correlation between experimental and simulation results significantly contributes to developing dependable hyper elastic material models tailored for geotextiles. This research framework holds considerable potential value for manufacturers and engineers as it equips them with practical tools to address concerns associated with soil-structure interaction in their projects.

Keywords: Soil-Structure Interaction Interface, Hyperplastic Models, Uniaxial Tension Testing, FEA Modeling.

1. Introduction

In civil engineering, geotextiles find extensive applications, such as soil stabilization, drainage systems, and erosion control. PET woven geotextiles are frequently utilized among various geotextile materials. To comprehensively assess and forecast the performance of PET woven geotextiles under varying loads and environmental conditions, the utilization of hyperplastic models proves beneficial. These models offer a structured approach for gaining insights into the material's mechanical properties and behavior when deformation occurs.

---

* Corresponding author E-mail: fzohra1@yahoo.fr

Hyperplastic models are employed to characterize the stress-strain response of materials that undergo substantially elastic deformations, as is the case with PET-woven geotextiles. These models rely on strain energy density functions, which establish a connection between the energy stored within the material and the deformations it experiences. By selecting an appropriate strain energy density function, it becomes possible to depict the mechanical behavior of the material accurately. Geotextiles and geosynthetics, polymers extensively utilized in civil engineering, geotechnical engineering and transportation, augment lateral resistance and enhance the properties of backfill materials in foundation systems (Wu et al., 2020). Ongoing research is directed toward integrating geotextiles into the design process and scrutinizing the interfaces between geotextiles and geomembranes.

Researchers employ diverse techniques, including shear tests to assess frictional behavior, triaxial compression tests, and advanced constitutive models such as the one proposed by Guo et al. (2022). These methodologies yield valuable insights into geotextile-geomembrane interfaces' performance, stability, and mechanical characteristics under varying loading conditions. Cutting-edge constitutive models consider material properties, stress-strain relationships and interface properties, enabling precise simulation of geotextile behavior and its interaction with geomembranes.

Finite element modeling employs physical tests and a hyperplastic methodology to assess the puncture resistance of needle-punched nonwoven geotextiles (Saberi et al., 2017). This approach scrutinizes these geotextiles structural integrity and durability by examining their response to puncture loads, thereby facilitating performance prediction and design optimization. In a broader context, research within civil and geotechnical engineering is primarily centered around analyzing geotextile-geomembrane interfaces and gaining insights into the behavior of geotextiles within foundation systems. Various techniques, including shear tests, triaxial compression tests, constitutive models, and finite element modeling, collectively advance geotextile design and application, ultimately enhancing efficiency and durability in construction projects.

Various constitutive models have been studied, including quasi-linear, hyperbolic and creep elastoplastic models (Zohra et al., 2022). For simulating reinforced soil, the point material method has been employed, considering fiber interaction through the equivalent additional stress method. Using the estimated rheological viscoelastic behavior presented by Sawicki et al. (1998), some researchers have treated reinforcement as an interface. This involved conducting creep tests on woven and nonwoven geotextiles. To address the phenomenon of creep as the load increases gradually during partial discharge, the Linear Solid Model (LSM) has been developed. Additionally, two modified viscoelastic models have been explored to account for plastic deformations in geotextiles. Ding et al. (2023) proposed a constitutive model that captures the creep behavior and stress relaxation of geogrids under various loading levels.

Wang et al. (2020) investigated the creep deformation and stress relaxation of polymer geosynthetics using conventional test methods. Jeon et al. (2009) examined the stress relaxation behavior of geosynthetics under additional stresses and/or elevated temperatures. Lastly, Peng et al. (2010) introduced an elasto-viscoplastic constitutive model to simulate the velocity-dependent behavior of polymeric geosynthetics.

This study explicitly investigates six commonly employed isotropic hyperelastic models for describing the behavior of PET-woven geotextiles in civil engineering applications.

2. Materials and Methods

Phenomenological and micromechanical models use extensively in characterizing the elastic and nearly incompressible mechanical responses of materials that undergo deformation under low loads and retain their deformations even after the load removal. In polymers and plastics, a common approach involves employing non-Gaussian force-extension relationships (Treloar, 1975), which are tailored to stress-strain data obtained from uniaxial tests (Hackett, 2016). These relationships are instrumental in capturing hyper elasticity curves, along with their corresponding parameters, as well as describing isotropic elastic properties. However, it is important to note that distinct hyperplastic material systems necessitate specific properties for characterizing Cauchy-green tensor strains, central strain ratios, stretching behavior, and simulation stress energies (Mansouri et al., 2014).

Hyperplastic constitutive models, such as the Mooney-Rivlin and Ogden models, find widespread use in the characterization and design of the viscoelastic behavior of various materials under conditions involving finite strains (Heymans et al., 2004). These materials encompass synthetic polymers, vulcanized rubber, and biological substances.

While the Mooney-Rivlin and Ogden models serve as standard choices for isotropic hyperplastic modeling (Kang et al., 2018), other models like the Ogden-Yeoh and Arruda Boyce models have been extensively tested and applied to specific materials like rubber and flexible foams (Kenja et al., 2020; Li et al., 2016).

The calibration of these models for soft and surrogate tissues considers experimental factors that influence uniaxial test data. As a result, this work delves into exploring a range of hyperelastic material models, both phenomenological and micromechanical, intending to describe the mechanical behavior of PET woven geotextiles accurately. This investigation takes into account the viscoelastic properties and finite-strain conditions characteristic of these materials. The Zener coefficient model (Figure 1) was proposed to consider the rheological behavior of PET material as proposed by (Chevalier, 2001).
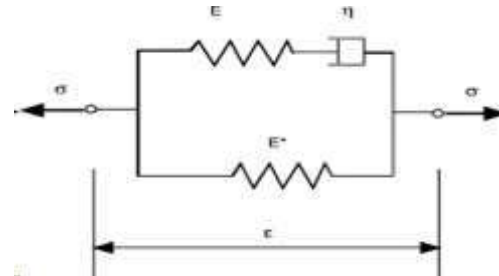

Fig. 1. Rheological coefficients of the Zener model (Chevalier, 2001)

The Mooney-Rivlin model (Mihai et al., 2017) utilizes a strain energy density function resembling the Neo-Hookean model and is frequently employed in characterizing material behavior. However, in cases involving rubber materials or flexible foams with restricted elasticity, alternative models like Ogden-Yeoh, Arruda Boyce, and Blatz have undergone thorough testing and are commonly utilized.

In a study conducted by Narayanan et al. (2023), a range of hyperelastic constitutive models, including polynomial, Ogden, Arruda-Boyce, and Van der Waals forms, were investigated for their suitability in Finite Element Analysis (FEA) of large elastic deformations in isotropic materials. These materials encompassed incompressible and nearly incompressible substances, such as elastomers and PET polymers used in geotextiles. Notably, the Ogden (Yun et al., 2021), Arruda-Boyce (Mokhireva et al., 2020), and Van der Waals models were found to exhibit viscoelastic behavior (Brinson et al., 2008). The study demonstrated that even relatively simple constitutive models, readily available in FEA software, yielded promising results for nearly incompressible materials. This comparative analysis examines various hyperelastic constitutive models for their applicability in characterizing the mechanical behavior of

PET woven geotextiles. The results provide valuable insights into selecting suitable models for accurately representing the viscoelastic properties and accommodating large elastic deformations in these materials.

The optimization technique known as the Levenberg-Marquardt algorithm is used to calibrate the hyperelastic material models. This technique is widely recognized for minimizing errors between model predictions and experimental data. It is a nonlinear least squares optimization algorithm often used to calibrate hyperelastic material models (Gavin et al., 2019, Van et al., 2020), based on the Gauss-Newton algorithm.

The Gauss-Newton method is a linearization method that assumes the model is linear around the current parameter estimates. This assumption is often violated in nonlinear problems, leading to convergence problems. The Marquardt method introduces a regularization term into the objective function that penalizes significant changes in the parameter estimates. This helps to improve the algorithm's robustness to ill-conditioning and can help prevent it from getting stuck in local minima. The Levenberg-Marquardt algorithm is a powerful and versatile optimization algorithm that can be used to calibrate a wide variety of models. It is particularly well-suited for calibrating hyperelastic material models because it is robust to ill-conditioning and can converge quickly.

2.1. Insights into Stress-Strain Relationships for Hyperplastic Models

This study focuses on geotextile samples comprising synthetic fibers, notably Polyethylene Terephthalate (PET) (Chevalier et al., 2012). Polyester, the material employed to produce these fibers, is a composite of ethylene glycol and terephthalic acid (or dimethyl terephthalate) (Carreau et al., 2021). Polyester is selected for geotextiles owing to its advantageous characteristics, including a high modulus,

resistance to creep, and chemical inertness.

The scope of this study is primarily limited to hyperelastic constitutive models that establish the relationship between strain and stress based on material properties. The strain energy function (*w*) is a crucial aspect of these models and is differentiated for each invariant of the Cauchy-Green deformation tensor. It can be expanded in an infinite power series of the Cauchy-Green deformation tensor. Under the condition of incompressibility, the strain energy function can be expressed as:

$$w = f(I_1, I_2, I_3) \qquad (1)$$

where w: is the strain energy potential, I_1, I_2, I_3: are the invariants of the Cauchy-Green deformation tensors.

Through the examination of these hyperelastic constitutive models, the objective is to attain a more profound comprehension of the mechanical characteristics exhibited by PET geotextiles and how they react under diverse loading conditions. The strain energy function for hyperelastic constitutive models is expressed in Eq. (1). The material properties are determined based on the invariants of the I_1, I_2, and I_3. These invariants are mathematically defined in terms of the principal stretches, λ_1, λ_2, and λ_3, derived from the deformation tensor. Hyperelastic constitutive models are highly effective in accurately describing material behavior during significant deformations. They achieve this by utilizing the strain energy function and the derivation of material parameters from the Cauchy-Green deformation tensors. A comprehensive understanding of this interplay is essential for accurately predicting and analyzing material responses in various engineering applications.

In the scenario of uniaxial tension applied to an incompressible material, where $\sigma_2 = \sigma_3 = 0$, the invariants can be conveniently expressed in terms of the stretch along the direction of tension, λ_1, as demonstrated in Eq. (5). To compute both

the strain, ε, and the stretches, λ_i, specifically for this situation, one can effectively utilize Eqs. (6-7), respectively. These equations employ the initial length of the sample as a reference point for the calculations.

$$I_1 = \lambda_1^2 + \lambda_2^2 + \lambda_3^2 \tag{2}$$
$$I_2 = \lambda_1^2 \lambda_2^2 + \lambda_2^2 \lambda_3^2 + \lambda_3^2 \lambda_1^2 \tag{3}$$
$$I_3 = \lambda_1^2 \lambda_2^2 \lambda_3^2 \tag{4}$$
$$\lambda_1^2 \lambda_2^2 \lambda_3^2 = 1 \tag{5}$$

where λ_1, λ_2 and λ_3 : are the principal stretches, derived from the deformation tensor I_1, I_2 and I_3.

A clear relationship between the applied uniaxial tension, the resulting strain and the stretches in various directions can be established using these equations. This knowledge holds significant importance in comprehending how materials behave under uniaxial tension and is pivotal for making accurate predictions regarding material responses in engineering applications.

$$\varepsilon = \frac{\Delta l}{l_0} \tag{6}$$
$$\lambda = \varepsilon + 1 \tag{7}$$

where ε: is the stain ratio, l_0: is the inial lenth and Δl: is the leth variation.

The following are some of the hyperelastic constitutive models that are commonly used to describe the mechanical behavior of materials:

• Reduced polynomial model: This model is a simplified version of the Ogden model that uses a polynomial function of the first invariant of the Cauchy-Green tensor. It is a good choice for materials that exhibit a linear relationship between stress and strain.

• Mooney-Rivlin model: This is a two-parameter model that uses the first and second invariants of the Cauchy-Green tensor to describe the strain energy function. It is a good choice for materials that exhibit nonlinear elastic behavior.

• Neo-Hookean model: This one-parameter model uses the second invariant of the Cauchy-Green tensor to describe the strain energy function. It is a good choice for materials that exhibit small elastic deformations.

• Yeoh model: This three-parameter model uses the first invariant of the Cauchy-Green tensor to describe the strain energy function. It is a good choice for materials that exhibit nonlinear elastic behavior and are incompressible.

• Arruda-Boyce model: This four-parameter model uses the first invariant of the Cauchy-Green tensor to describe the strain energy function. It is a good choice for materials that exhibit nonlinear elastic behavior and are compressible.

2.2. Reduced Polynomial Model

Initially introduced by Rivlin (1948), the reduced polynomial model has been expanded to encompass N values up to 6, significantly enhancing its capacity to capture intricate strain behaviors. At N=3, this model aligns with the Yeoh model, and at N=1, it corresponds to the Neo-Hookean model. The reduced polynomial model primarily leverages the first invariance (I1) and demonstrates minimal sensitivity to variations in stress-energy encompassed within the second invariance (I2). This distinctive characteristic renders it an attractive choice for predicting complex strain behaviors, even in scenarios with limited experimental data. The shear modulus of the reduced polynomial model is explicitly defined as $\mu_0 = 2c_{10}$ and its energy potential is expressed by Eq. (8).

Researchers and engineers can harness this model effectively to anticipate and analyze material strain responses, providing valuable insights for various engineering applications.

$$W = \sum_{i=1}^{N} C_{10}(I_1 - 3)^i \sum_{i=1}^{N} \frac{1}{D_i}(j_{el} - 1)^{2i} \tag{8}$$

where W: is the strain energy potential, j_{el}: is the elastic volume ratio, C_{10}: is the material shear behavior constant and D_i: is

a constant for incomprsessible metrials.

2.3. The Mooney-Rivlin Model

Prior research has convincingly demonstrated the efficacy of the Mooney-Rivlin model, an elastic model, in accurately characterizing moderate to large strains and shear deformations occurring in uniformly dilated or contracted planes (Mooney, 1940; Rivlin, 1948).

This model finds widespread use for representing the elasticity of gels and tissues. The strain-energy function for the Mooney-Rivlin model has been derived in a general form (Barbero, 2023), with its specific expression provided in Eq. (9).

The Mooney - Rivlin model is pivotal in faith fully modeling the mechanical behavior of materials undergoing significant strains and shear deformations. Its formulation yields valuable insights for comprehending and forecasting the behavior of diverse materials, especially in contexts involving gels and tissues.

$$W = C_{10} (I_1 - 3) C_{01}(I_2 - 3) \frac{1}{D_i}(J_{el} - 1)^2$$
$$C_{10} = \frac{\mu_1}{2} \quad \text{and } C_{01} = -\mu_2 \qquad (9)$$

where C_{01} and C_{10}: are material constants or parameters repectively, define the behavior of the material being modeled. μ_1, μ_2: are constants related to the material's viscoelastic properties.

2.4. Neo-Hooke model

The Neo-Hooke, an elastic model that employs a nonlinear approach grounded in Hooke's law, excels at handling relatively modest deformations effectively. However, it is limited because it cannot account for stress recovery. In scenarios where material data is unavailable, the model can be simplified by setting C_{01} to 0, resulting in a widely used subset of the Mooney-Rivlin model (Shahzad et al., 2015). While the Neo-Hooke model is user-friendly and performs admirably for small deformations, it cannot account for stress and strain recovery.

The mathematical representation for the strain-energy function employed in the Neo-Hooke model is provided in Eq. (10). This model imparts valuable insights into the mechanical behavior of materials subjected to small deformations. Still, its inability to capture stress recovery must be considered when applying it to engineering analyses. The Yeoh model presents a mathematical approach employing a third-order polynomial equation grounded in the first invariant of the strain tensor.

$$W = C_{10} (I_2 - 3) \frac{1}{D_1} (J_{el} - 1)^2 \qquad (10)$$

The Yeoh model presents a mathematical approach employing a third-order polynomial equation grounded in the first invariant of the strain tensor. It is adept at accurately characterizing the nonlinear elastic behavior of materials like rubber and plastic when subjected to significant deformations.

This model can fit experimental data and capture a broad spectrum of deformation patterns, demanding only minimal input information. Furthermore, the reduced polynomial variant of the Yeoh model is suitable for compressible materials. It yields precise forecasts of the stress-strain response for various substances, including carbon-filled black rubber. The strain-energy function utilized in the Yeoh model is expressed mathematically through Eq. (10). By employing the Yeoh model, researchers and engineers can proficiently analyze and predict the nonlinear elastic behavior of materials, delivering invaluable insights applicable across a wide array of applications generalised form mentioned in Eq. (11).

$$W = \sum_{i=1}^{3} C_{i0}(I_1 - 3)^i \sum_{i=1}^{3} \frac{1}{D_i}(J_{el} - 1)^{2i} \qquad (11)$$

2.5. Arruda-Boyce Model

A third-order polynomial model, relying on the first invariant of the strain

tensor, finds extensive use in characterizing the nonlinear elastic behavior of materials such as rubber and plastics when subjected to significant deformations (Arruda et al., 1993). This versatile model fits experimental data and effectively describes a wide range of deformation patterns.

Moreover, the reduced polynomial variant of this model is especially well-suited for compressible materials, offering precise forecasts of the stress-strain response across diverse materials, including carbon-filled black rubber. Mathematically, the strain-energy function employed in this model can be expressed as follows:

$$W = \mu \sum_{i=1}^{5} \frac{C_i}{\lambda_m^{2i-2}} \left(I_1^i - 3^i\right) \frac{1}{D} \left\{ \frac{j_{el}^2 - 1}{2} - \ln j_{el} \right\}$$

$$C_1 = \frac{1}{2}, C_2 = \frac{1}{20}, C_3 = \frac{11}{1050}, C_4 = \frac{19}{7000} \quad (12)$$
$$C_5 = \frac{519}{673750}$$

$$D = \frac{9K + 8\mu}{3(K + 2\mu)}$$

where, λ_m: is the initial shear modulus and the locking stretch, which refers to the point where the stress-strain curve experiences a notable increase in the upturn. K: denote the initial bulk modulus and D: is double the inverse initial bulk modulusn, while μ: represents the initial shear modulus. Using this third-order polynomial model, researchers and engineers can proficiently analyze and predict the nonlinear elastic behavior of materials, facilitating a deeper understanding and enabling practical applications across numerous fields.

2.6. Van Der Waals Model

The Van der Waals model, also known as Kilian's model, is a hyperelastic potential extensively employed for describing the nonlinear elastic behavior of materials (Mihai et al., 2017). This comprehensive model encompasses equations for various parameters, including primary stretches, the Jacobean determinant, the locking stretch, λ_m and the linear mixture parameter, β. The strain energy function of the Van der Waals model, as outlined in Eq. (13), relies on the

initial shear modulus μ and the inverse initial bulk modulus D.

$$w = \mu \left\{ -\left(\lambda_m^2 - 3 \ln[(1 - \eta) + \eta] - \frac{2\alpha}{3}\right) \left(\frac{\tilde{I} - 3}{2}\right)^{3/2} + \frac{1}{D} \left[\frac{j_{el}^2 - 1}{2} - \ln(j_{el})\right] \right\} \quad (13)$$

Additionally, the model incorporates three parameters: I, η, and α, which are defined by Eqs. (14-16), respectively.

$$\tilde{I} = (1 - \beta)I_1 + I_2\beta \quad (14)$$

$$\eta = \sqrt{\frac{I - 3}{\lambda_m^2 - 3}} \quad (15)$$

$$\alpha = \frac{2C_{01}}{3\mu} + \frac{\lambda_m^2}{\lambda_m^3 - 1} \quad (16)$$

where, β, η and α: are intermediate variables and measures related to the material's deformation within the Van der Waals hyperelastic model, aiding in the calculation of the strain energy function and providing insights into the material's behavior under deformation. The Van der Waals model facilitates precise analysis and characterization of the nonlinear elastic behavior of materials. Incorporation of multiple parameters yields valuable insights applicable across various engineering applications.

2.7. Ogden Model

The Ogden model, introduced in 2021 (Yun et al., 2021), is a mechanical model that describes the elasticity of materials experiencing non-uniform deformation. It utilizes a strain energy function that integrates material parameters and strain invariants. Diverging from constant-based models, the Ogden model's dependency on the principal strain sets it apart. Eq. (17) depicts the mathematical representation of the strain energy function (Lim et al., 2011).

$$W = \sum_{i=1}^{n} \frac{2\mu_1}{\alpha_i^2} \left(\bar{\lambda}_1^{\alpha_1} + \bar{\lambda}_2^{\alpha_1} + \bar{\lambda}_3^{\alpha_1} - 3\right) \sum_{i=1}^{N} \frac{1}{D_i} (J_{el} - 1)^{2i} \quad (17)$$

The reduced polynomial model is a simplified version of the Ogden model that is easier to implement and can be used to model a broader range of materials. The Mooney-Rivlin model is a two-parameter model often used to model rubber-like materials. The Neo-Hookean model is a one-parameter model often used to model materials exhibiting small elastic deformations. The Yeoh model is a three-parameter model that is often used to model materials that exhibit nonlinear elastic behavior and are incompressible. The Arruda-Boyce model is a four-parameter model often used to model materials that exhibit nonlinear elastic behavior and are compressible. The choice of which model to use depends on the modeled material and the accuracy required. The reduced polynomial model is the simplest option, but it may need to be more accurate for some applications. The Mooney-Rivlin model is a good compromise between accuracy and simplicity. The Neo-Hookean model is the simplest one that can accurately capture the behavior of materials exhibiting small elastic deformations. The Yeoh model is a good choice for materials that exhibit nonlinear elastic behavior and are incompressible. The Arruda-Boyce model is a good choice for materials that exhibit nonlinear elastic behavior and are compressible.

3. Characterizing Geotextile Materials Through Uniaxial Tension Testing

This section is dedicated to the characterization of geotextile materials through uniaxial stress testing. In this testing method, the material undergoes tension in one direction while the other remains constant. This enables the measurement of the material's reaction to deformation along a single axis, offering valuable insights into its mechanical behavior. The mechanical setup, as shown in Figure 2, features a pet-woven geotextile sample and a traction machine equipped with geotextile strips.

Tension tests were performed on dumbbell-shaped PET specimens (Treloar, 1943; Treloar, 1979) with a minimum aspect ratio of 2.5 and a length of 50 mm (Iso, 2008) (refer to Figure 2). These tests were carried out using a constant-speed testing machine and the resultant tensile strength-extension curves were scrutinized to extract the material's stiffness parameters and tensile strength. The curves display nonlinear behavior, underscoring the inapplicability of Hooke's law and emphasizing that the modulus of elasticity can only be valid within a restricted strain range.
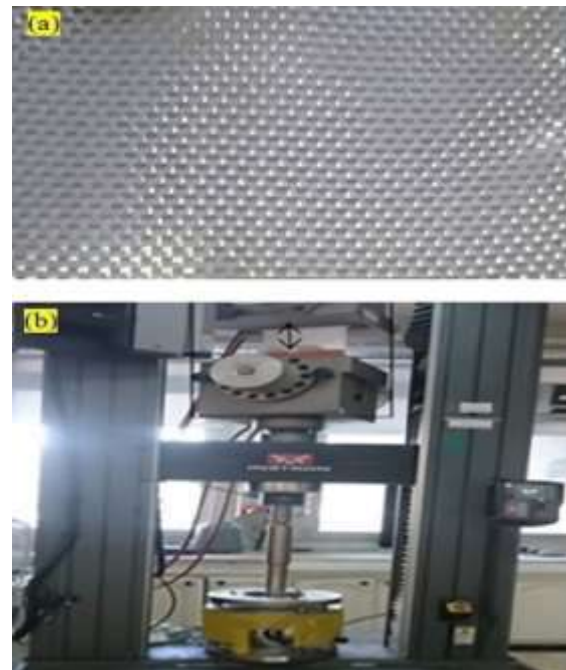
Fig. 2. a) Test specimen (PET woven geotextile); and b) Traction machine with geotextile strips

The material was clamped between two-sheet metal sheets bonded to form a standard tension rod for conducting the uniaxial tension tests. This rod was subsequently affixed to a tensile testing machine for assessment. To measure strain, the thinnest portion of the rod was chosen, and drilled plates were affixed to determine strength and tensile strength. It is worth noting that the modulus of elasticity varies depending on the levels of both linear and nonlinear elastic strain (Lagan et al., 2007). The available approaches consider only

the elastic behavior, and the viscoelastic behavior has been missing. To overcome these shortcomings the following phases are considered in this paper.

Phase I, often called the "toe region", is distinguishable by a low modulus of elasticity and significant deformation. This behavior arises from the presence of elastin fibers in the skin, which are pivotal in facilitating stretching mechanisms (E_I) (Eq. (18)).

Phase II, alternatively termed the "linear region" is marked by an escalation in stiffness. This shift occurs as the fibers within the skin progressively align and straighten (E_{II}) (Eq. (19)).

$$E_I = \frac{\partial \sigma^e}{\partial \varepsilon^e} \tag{18}$$

$$E_{II} = \frac{\partial \sigma^{en}}{\partial \varepsilon^{en}} \tag{19}$$

where E_I and E_{II}: represent the elastic modulus related to phase I and phase II, respectively.

The resultant mechanical properties of the material, encompassing the elastic modulus (E_I and E_{II}) computed using Eqs. (18-19), along with the maximum tensile strength for both the warp and weft test directions, are briefly presented in Table 1. The tests were conducted using a constant-speed testing machine.

Subsequently, the resulting tensile strength-extension curves underwent analysis to ascertain the material's stiffness parameters and tensile strength. It was observed that these curves displayed nonlinear behavior, signifying the inapplicability of Hooke's law and the limited range for which the modulus of elasticity can be employed. The stress-strain curve from the tension test can be categorized into linear elastic and nonlinear plastic regions, as illustrated in Figure 3.

Table 1. Geotextile material properties

Material model	Coefficients	Sample 01	Sample 02	Sample 03	Sample 04
Weft test direction	Elastic modulus EI (MPa)	691.07	652.10	613.63	521.64
	Elastic modulus EII (MPa)	193.22	203.15	191.60	191.60
	Max Tensile strength (KN/m)	149.26	150.28	151.25	152.33
Warp test direction	Elastic modulus EI (MPa)	2,343.58	1,827.31	2,559.77	2,043.58
	Elastic modulus EII (MPa)	1,903.19	1,833.55	1,673.27	1,624.03
	Max force/wide (KN/m)	47.94	49.12	48.12	47.94
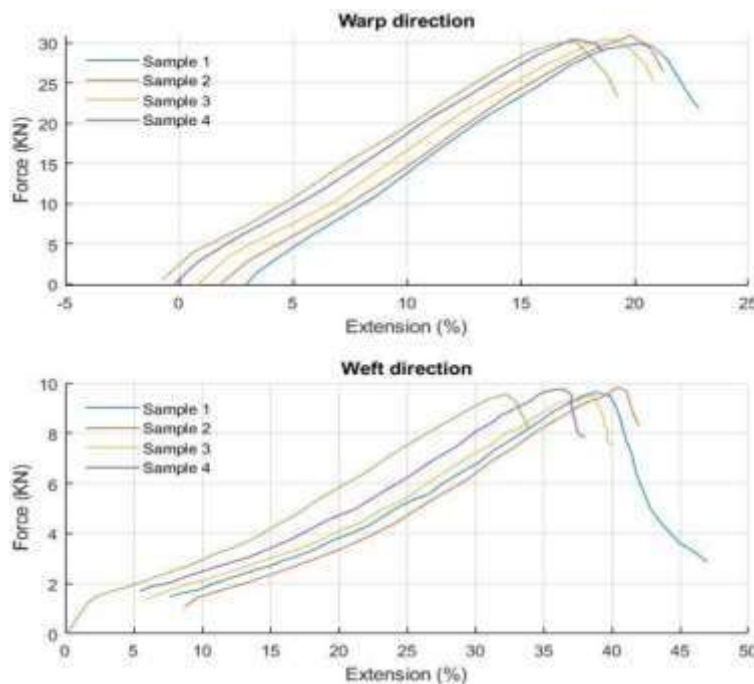
Fig. 3. Stretch test experiments in two orientations with four samples

The mechanical properties of the material, derived by plotting sample strength against stretch, are briefly summarized in Table 1.

According to Ward et al. (2012), Hooke's stress-strain relation represents a linear constitutive relation applicable to ideal elastic, isotropic solids under low strains. This law establishes that stress is directly proportional to strain, with the modulus of elasticity or Young's modulus as the constant of proportionality. However, when grappling with high strains, it becomes essential to employ nonlinear constitutive relationships, as discussed in Hackett (2016), to precisely depict the mechanical characteristics of materials. Table 1 offers an overview of the laboratory properties of geotextiles, encompassing both their elastic and nonlinear behavior when subjected to uniaxial deformation.

3.1. PET Geotextile Samples Per Direction

During the stretching process, the specimens experience irreversible plastic deformation, which progressively increases as the deformation continues. When the strain is below the yield strength, the stress resulting from plastic strain remains relatively constant. The material undergoes stiffening and displays nonlinear behavior due to the increased rigidity of the molecular chains.

The maximum elongation, approximately 40%, corresponds to a stress of nearly 150 KN/m in the weft direction, whereas it is only 50 KN/m in the warp direction, as indicated in the manufacturer's technical data sheet. The following are the key points noted from Table 1.

- The elastic modulus E_I is higher in the warp direction than the E_{II} in the warp and weft test directions. This suggests that the material exhibits greater stiffness in the warp direction than in the weft direction.

- The maximum tensile strength is also notably higher in the warp direction than in the weft direction.

- The material displays nonlinear behavior, as evidenced by the curves in Figure 4. This implies that Hooke's law does not apply to this material, and the modulus of elasticity can only be used within a limited strain range.
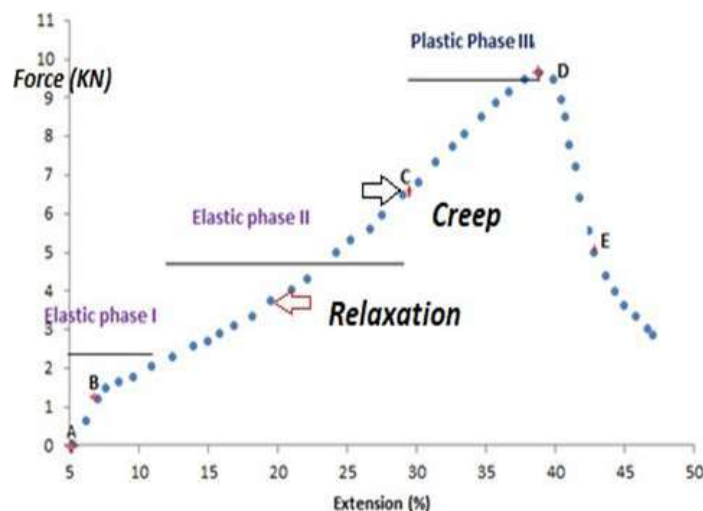

Fig. 4. Load extension segmented curves related to sample in the weft direction

Constitutive relations are mathematical representations used to describe the mechanical behavior of materials and they can be categorized into two main types: linear and nonlinear. Hooke's law exemplifies a linear relation, typically applicable to ideal elastic, isotropic solids undergoing low strains. However, employing nonlinear constitutive relations to represent material behavior accurately becomes essential when dealing with high strains. The stress-strain curve, elaborated

in Powell et al. (2023), illustrates the typical response of polymers, encompassing elastic deformation, yield, plastic flow, necking, strain hardening, and eventual fracture. The diagram presented in Hieu et al. (2023) summarizes typical behavior as follows. The stress-strain curve exhibits three distinct regions.

- Region 1: This initial region is characterized by a linear relationship between stresses, known as the elastic region, where the material undergoes reversible deformation.

- Region 2: This subsequent region is characterized by a nonlinear relationship between stresses, denoted as the plastic region, where the material undergoes irreversible deformation.

- Region 3: The final region is characterized by a decrease in stress with increasing stresses, known as the necking region, where the material forms a neck and eventually fails. The stress-strain curve also includes two transitional phases:

- The yield point marks the point where the material initiates plastic deformation.

- The necking point: This signifies the point at which the material begins to form a neck.

Figure 4 illustrates these three distinct regions and the two transitional phases. In the initial region, stress exhibits a linear increase, followed by a more gradual increment as deformation advances (Phase II), ultimately resulting in irreversible plastic deformation. Significant morphological changes mark this phase, including material fragmentation and the release of stored elastic energy. Additionally, the diagram denotes two transitional regions.

4. Data Test Calibration

The stress-strain curve of polymers displays three distinct regions and two transition phases: elastic deformation, yield, plastic flow, necking, strain hardening, and fracture. To precisely characterize a material's mechanical behavior, the material calibration process is employed. This entails determining the parameters of a constitutive model by comparing experimental data, such as stress-strain curves, with model predictions and fine-tuning the model parameters until a close match is attained.

Optimization techniques, like least squares or maximum likelihood sample orientation, can influence experimental outcomes and the mathematical coefficients employed in evaluating isotropic hyperelastic constitutive laws. Consequently, variations may arise in the selection of the hyperelastic model and the determination of material constants. This influence can be observed in the strain energy function derived from uniaxial testing, as well as in the resulting coefficients and the root mean square error (R^2), which are presented in Tables 2 and 3.

Estimation can be applied for parameter refinement. However, the precision of the calibrated model hinges on the quality and quantity of the experimental data used during the calibration process. These tables present the outcomes of calibrating various hyperelastic material models for the geotextile samples warp and weft directions. These models encompass the Mooney-Rivlin, Ogden, Arruda-Boyce, Neo-Hookean, and Van-der-Waals models. These tables also display the coefficients associated with each model, accompanied by R-squared values.

4.1. Material Evaluation for Warp Sample Orientation

It is important to acknowledge that factors such as sample orientation can also impact the assessment of hyperelastic constitutive laws, as detailed earlier in this section. Uniaxial testing was performed on each pair to assess material behavior for the warp sample orientation. The goal was to identify the most precise model for characterizing material behavior and constructing a strain energy function based on invariants or stretches.

Table 2. Models calibration for warp direction

Materiel model	Coefficients	Sample 01	Sample 02	Sample 03	Sample 04
Mooney-Rivlin D = 0	C10 (MPa)	1.94	1.76	2.00	1.92
	C1 (MPa)	1.39	1.92	-0.87	-1.57
Ogden N = 1	μI	4.24	5.54	3.01	2.10
	α with DI = 0	1.97	1.79	2.13	2.28
	R2	29.8	29.5	10.99	24.09
Arruda-Boyce	$\mu = \mu 0$	4.14	4.23	3.34	2.53
	λm	9197	18579	13	9.15
	R2	29.6	21.18	12.08	25.82
Neo-Hookean	C10 (MPa)	2.07	2.11	1.79	1.45
	R2	16.2	15.2	11.2	12.5
Yeoh material	C10 (MPa)	2.00	2.40	1.51	1.105
	C20 (MPa)	5.54	-5.45	8.28	1.08
	C30 (MPa)	-4.19	1.76	-4.46	-5.14
	R2	18.5	14.3	11.6	13.5
Van-Der-Waals	μ	4.36	5.52	3.11	2.17
	λ	1113	27	1036	867.7
	A	1.27	0.122	-3.3	-9.15
	R2	29.5	19.05	11.36	24.41

Table 3. Calibration of models for weft direction

Material model	Coefficients	Sample 01	Sample 02	Sample 03	Sample 04
Mooney-Rivlin D = 0	C10 (MPa)	0.29	0.28	0.31	0.30
	C01 (MPa)	0.93	0.57	2.05	2.38
Ogden N = 1	μI	1.37	0.92	0.52	0.18
	α with DI = 0	1.72	1.84	2.05	2.38
	R2	12.11	24.89	9.79	10.65
Arruda-Boyce	$\mu = \mu 0$	0.70	0.64	0.55	0.33
	λm	62946	42139	45	22
	R2	12.11	26.3	9.79	10.65
Neo-Hookean	C10 (MPa)	0.35	0.30	0.29	0.20
	R2	18.2	19.12	13.95	14.78
Yeoh material C20 = C30	C10 (MPa)	0.48	0.38	0.27	0.13
	R2	20.82	26.30	9.67	21.10
Van-Der-Waals	Mu	1.17	0.79	0.72	0.24
	λm	59.03	95.68	1064.7	94.31
	A	6.89	3.27	0.013	-0.04
	R2	12.69	25.12	9.35	14.67

The test results for the different deformation modes investigated are detailed in Section 2.1 and illustrated in Figure 3. The calibration process for hyperelastic models involves minimizing the error between the predicted stress-strain response of the model and experimental data. The following steps are involved:

- Initialize the model parameters.
- Calculate the predicted stress-strain response of the model.
- Calculate the error between the predicted stress-strain response and the experimental data.
- Repeat steps 2-4 until the error is minimized.

A numerical optimization algorithm was use to calibrate hyperelastic models by minimizing the error between the predicted and experimental stress-strain responses.

The stress "tu" is the nominal or engineering stress. For the case of uniaxial deformation, the relationship between nominal stress and stretch is given by Eq. (20), regardless of the specific form of the strain energy function. This is because the first invariant of the right Cauchy-Green deformation tensor is the same for all these models.

$$T_U = 2(\lambda - \frac{1}{\lambda})C10 \qquad (20)$$

where, T_U: represents the nominal stress.

Based on the results presented in Table 2, the Van der Waals, Ogden, Arruda-Boyce and Neo-Hook hyperelastic material models were identified as more suitable for predicting geotextile behavior than the Mooney-Rivlin and Yeoh models. This selection was based on several key factors and considerations:

• Model Fit (R^2 Value): As indicated by the coefficient of determination (R^2), the goodness of fit was one of the primary criteria for model selection. Higher R^2 values suggest a better fit of the model to the experimental data. Among the models tested, the Van Der Waals, Ogden, Arruda-Boyce, and Neo-Hook models consistently demonstrated higher R^2 values than the Mooney-Rivlin and Yeoh models; these models better represented the geotextile behavior under the given conditions.

• Parameter Stability: The stability of the model parameters across different samples is crucial for reliable predictions. The selected models exhibited relatively stable parameter values (coefficients) across the tested samples, indicating their robustness and ability to capture the material behavior consistently.

• Physical Justification: Each of the selected models has a physical basis or theoretical foundation that aligns with the behavior of geotextiles under uniaxial loading. These models are well-established in material modeling and have been successfully applied to various materials, including elastomers and polymers.

• Predictive Accuracy: During the calibration process, the selected models demonstrated a higher degree of accuracy in predicting the mechanical behavior of geotextiles under uniaxial loading conditions. This accuracy is essential for practical engineering applications requiring precise material behavior predictions.

• Model Simplicity: While the selected models are sophisticated in their formulation, they do not introduce unnecessary complexity. They balance accuracy and simplicity, making them practical for engineering analysis and design. In sum, the choice of the Van Der Waals, Ogden, Arruda-Boyce and Neo-Hook hyperelastic material models was based on their superior fit to the experimental data, stability across samples, physical relevance, predictive accuracy, and practical applicability in the context of geotextile behavior modeling. These models offer a robust framework for characterizing and predicting the mechanical response of geotextiles under uniaxial loading, which is essential for geotechnical engineering applications.

The findings presented in Table 2 show that the Van Der Waals, Ogden, Arruda-Boyce, and Neo-Hook hyperelastic material models have a higher coefficient of determination (R^2) than the Mooney-Rivlin and Yeoh models. The coefficient of determination measures how well the model fits the data. A higher R^2 value indicates a better fit. In other words, the Van Der Waals, Ogden, Arruda-Boyce and Neo-Hook models can predict the behavior of geotextiles more accurately than the Mooney-Rivlin and Yeoh models because the Van Der Waals, Ogden, Arruda-Boyce, and Neo-Hook models are more complex and consider more factors that affect the behavior of geotextiles.

The Mooney-Rivlin and Yeoh models are simpler based on the assumption that the strain energy density is a function of the first and second strain invariants. The Van Der Waals, Ogden, Arruda-Boyce and Neo-Hook models are more complex based on the assumption that the strain energy density is a function of the first, second and third strain invariants.

This latest invariant is a measure of the volume change of the material. Including the third strain invariant in the Van Der Waals, Ogden, Arruda-Boyce and Neo-Hook models makes them more accurate for predicting the behavior of geotextiles, which are often subjected to significant volume changes. In addition, the Van Der Waals, Ogden, Arruda-Boyce, and Neo-Hook models can capture geotextiles

nonlinear behavior better than the Mooney-Rivlin and Yeoh models. Geotextiles are often subjected to large deformations and the nonlinear behavior of these materials becomes more pronounced at large deformations. The Van Der Waals, Ogden, Arruda-Boyce, and Neo-Hook hyperelastic material models are more suitable for predicting geotextile behavior than the Mooney-Rivlin and Yeoh models.

4.1. Material Evaluation: Weft Sample Orientation

Table 3 presents the calibration results of various hyperelastic material models for the weft direction of geotextiles. These models include Mooney-Rivlin, Ogden, Arruda-Boyce, Neo-Hookean, Yeoh and Van-Der-Waals. This table shows the coefficients of these models for different samples (Samples 01 to 04) in terms of their respective material parameters. The evaluation of the weft sample orientation involved utilizing multiple models, with their results being compared and analyzed.

A significant differentiation among these models lies in how they compute strain energy density. While the Mooney-Rivlin model relies on primary strain invariants, the Ogden model considers three primary sections. Consequently, these two models yield distinct outcomes for the weft direction, as illustrated in Figure 5. The calibration results for the weft direction reveal that the Van Der Waals, Ogden, Arruda-Boyce and Neo-Hook hyperelastic material models exhibit higher R^2 values than the Mooney-Rivlin and Yeoh models. This signifies that the Van Der Waals, Ogden, Arruda-Boyce and Neo-Hook models offer a better fit to the experimental data for the weft direction of the geotextile samples. In contrast, the Mooney-Rivlin and Yeoh models display lower R^2 values, indicating a less accurate fit to the data.

The Neo-Hookean model has the highest R^2 value among the three samples; it implies that, for three out of the four samples, the Neo-Hookean model best aligns with the experimental data for the weft direction of the geotextile samples. Other models show lower R^2 values, suggesting they are less suitable for this dataset.

The Mooney-Rivlin model secures the second-highest R^2 value for three samples, thus suggesting that the Mooney-Rivlin model is also a good fit for the experimental data but might outperform the Neo-Hookean model. On the other hand, the Ogden, Arruda-Boyce, and Van-der-Waals models exhibit lower R^2 values and do not align with the data as effectively as the Neo-Hookean or Mooney-Rivlin models.

Analyzing these results is crucial for comprehending the mechanical behavior of the material in various orientations. This comprehension is pivotal for enhancing material design and performance in specific applications. Therefore, conducting material characterization tests under diverse loading conditions is vital to acquiring precise and reliable data. These findings can provide valuable insights into the material's behavior and support the development of new, innovative materials tailored to diverse engineering applications.

Notably, among the tested samples, Samples 3 and 4 in each orientation exhibit the lowest error rates during calibration, as depicted in Figures 5 and 6. These observations underscore the suitability of the Neo-Hookean and Yeoh models, particularly the reduced polynomial N3 variant, for effectively characterizing the behavior of the geotextile samples in both the warp and weft directions. By adhering to specific foundational hypotheses in experimentation, it has been possible to effectively demonstrate the similarity of geotextile samples to the original material and facilitate the calibration of various hyperelastic material models in warp and weft directions. The hyperelastic material models considered in this study encompass the Mooney-Rivlin, Ogden, Arruda-Boyce, Neo-Hookean, Yeoh and Van-der-Waals models.
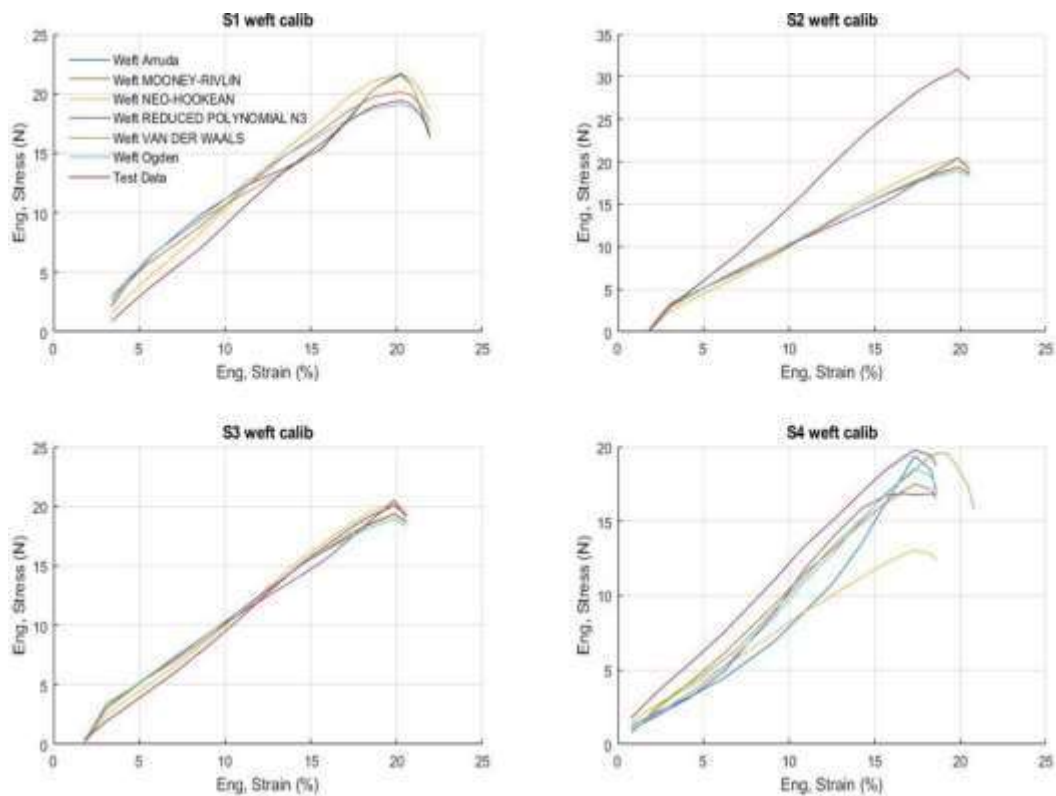
Fig. 5. Fitting hyperplastic models to all sample weft experimental findings
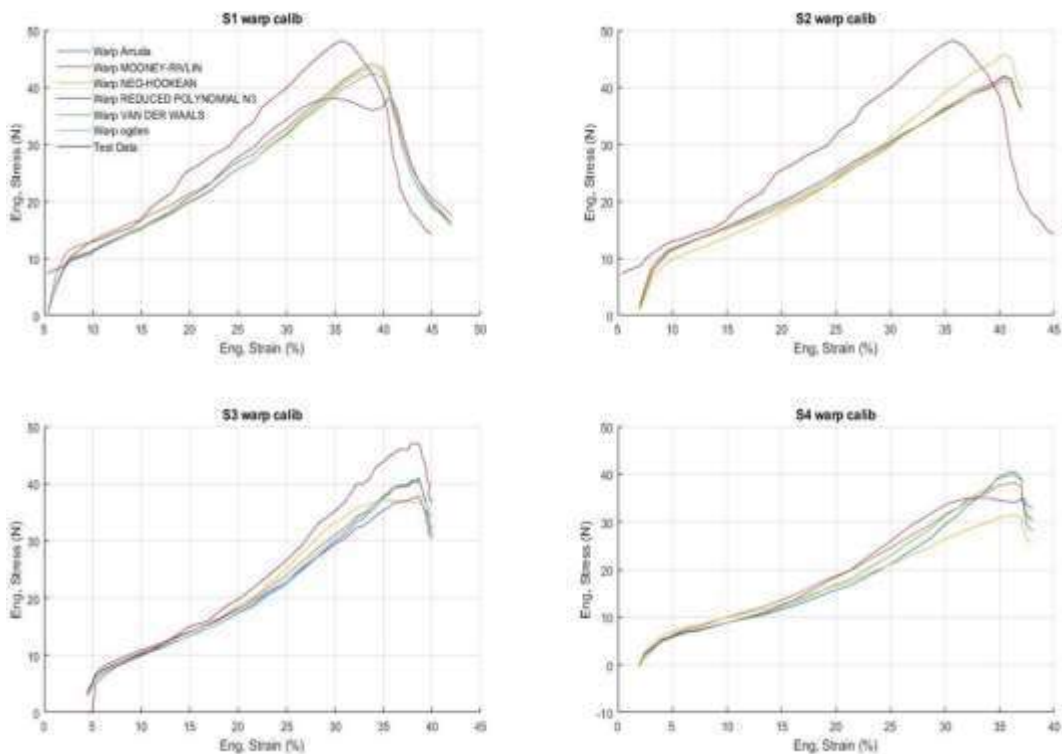
Fig. 6. Fitting hyper-elastic models to all sample warp experimental findings

The Mooney-Rivlin model calculates strain energy density using the principal strain invariants, while the Ogden model considers three principal stretches. These models have proven invaluable for accurately characterizing the mechanical behavior of the geotextile samples in various orientations. When modeling hyperelastic materials, it is common to utilize a scalar-valued energy function

contingent on the right Cauchy-Green deformation tensor. Nonetheless, invariants or stretches are frequently more convenient for practical implementation in FEA codes. This paper presents the successful calibration of material models through Abaqus code test results and numerical simulations. The behavior of geosynthetics over time, as discussed in Luo et al. (2019) is defined by creep and relaxation curves.

Consequently, it is essential to account for the influence of time when assessing material performance. One method for modeling time-dependent materials involves employing exponential basis functions within a Prony series. When subjected to prolonged stress, materials enduring continuous stress can undergo cracking and relaxation. This paper primarily concentrates on applying FEA in stretching tests, particularly in the context of hyperelastic models. Then encompasses a range of facets, including the calibration and simulation of these models within the FEA framework.

5. Stretching Tests Simulation

This section is dedicated to stretching tests conducted using hyperelastic models calibrated through FEA (Luo et al., 2019). One of the prominent challenges in FEA simulations involves establishing the shape of the parts to be simulated, configuring loading and boundary conditions and specifying material properties. The examples showcased in this section illustrate that stress calculations obtained from FEA simulations can anticipate material behavior, enhance strength ratios and streamline the design of intricate components. Figure 7 depicts an Abaqus model employed for a weft stretch simulation, utilizing hyperelastic models previously calibrated in Section 3.3. The finite element model in Figure 8 represents a stretching test conducted on a geotextile sample. The hyperelastic material model, tailored for the weft direction, effectively approximates the sample's behavior under the prescribed boundary conditions. One end of the sample experiences a 50 mm enforced displacement in the stretching direction (Ux), while the other is clamped.

The model comprises 320 hybrid brick elements (C3D8H) for the sample and two bilinear rigid quadrilateral elements (R3D4) for the clamps. It is worth noting that the gripping step must be iterated 500 times to accurately capture the sample's behavior. The hyperelastic models, Yeoh and Neo-Hookean, which have been calibrated as outlined in Table 3 and Figure 4, offer a stable and dependable analytical representation of the stress-strain relationship of the material.
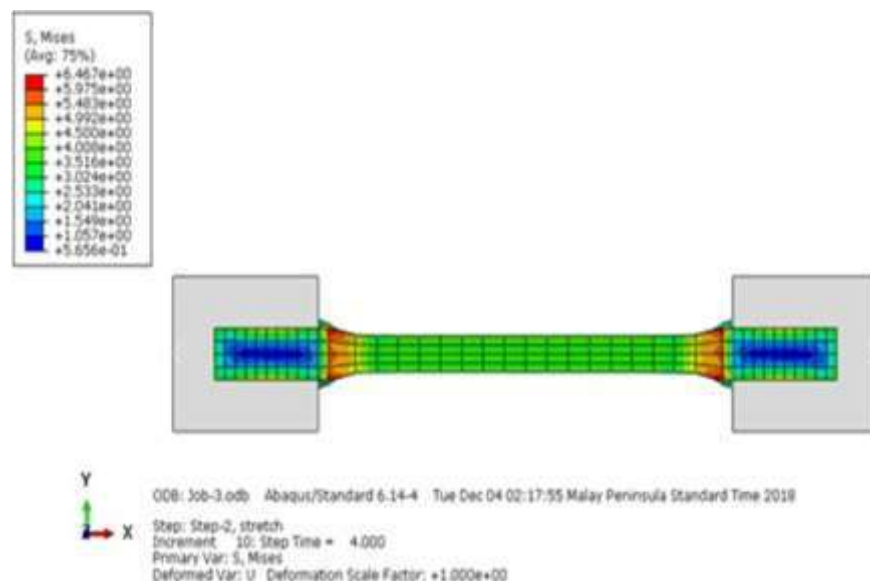
Fig. 7. Abaqus model for weft stretch simulation based on experimental data
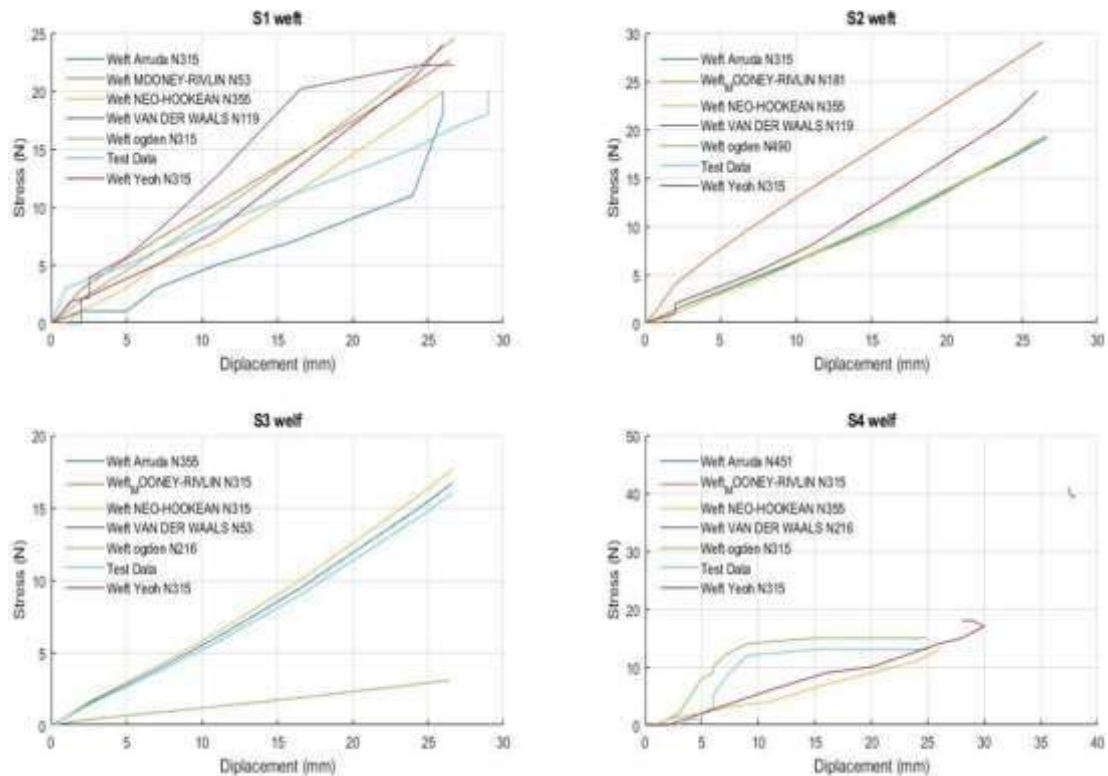
Fig. 8. Examination of FEA predictions (Abaqus): Simulation of frame stretching based on experience

The numerical results closely align with the experimental data, demonstrating a solid agreement. Nevertheless, it is essential to acknowledge that viscous materials release energy during deformation and the simulated test samples can influence the material's behavior.

Despite this limitation, the uniaxial stress-strain test provides ample insights into the behavior of geotextiles and modeling can provide valuable information for integrating the material's properties into the design process. Recognizing that the energy dissipated during material deformation and using simulated test samples can modify the material's behavior is essential.

Therefore, while the uniaxial stress-strain test offers valuable insights into the geotextile's behavior, simulation can further enhance the comprehension and utilization of its characteristics in the design process. However, it is essential to acknowledge that simulation results only encompass a portion of the material's behavior and even minor movements can substantially influence pressure changes owing to quasi-incompressibility. Consequently, care must be exercised when employing simulation outcomes in the design of geotextiles.

6. Conclusions

Calibrating hyperelastic material models is pivotal for thoroughly comprehending how geotextiles react to stress, strain and energy dissipation during deformation. In this study, quasi-incompressibility and strain energy were harnessed as fundamental components to fulfill this objective. Phenomenological models, frequently relying on invariants like polynomials, are extensively utilized in finite element codes for their integration. This research introduced a physically meaningful and mathematically rigorous method, offering a structured approach for selecting suitable geotextile constituent models.

Challenging to predict in civil engineering applications, findings may only be universally applicable to some types of geotextiles. Despite these limitations, this study provided a valuable framework for

calibrating woven geotextile behavior with no time-dependent. Moreover, the calibration of hyperelasticity models considers time-dependent behaviors such as creep and relaxation, which are essential for assessing a material's performance under sustained stress conditions.

With its contributions, this research facilitates the choice of suitable material models for finite element simulations, ultimately augmenting the precision of geotextile analysis. It is crucial to recognize that the models developed in this study were specifically customized to match uniaxial tension tests conducted in both the warp and weft directions.

However, it is important to note that these insights into geotextile behavior lays a foundation for selecting polymers with interface material properties. In this study woven geotextile PET 300 was limited to unidirectional testing of geotextiles. It means that other types of testing, such as biaxial or triaxial were not be considered. The findings may not apply to geotextiles subjected to forces in multiple directions. It is a relatively narrow scope, and it needs help to generalize the behavior of geotextiles in other loading conditions. The results may not apply to geotextiles subjected to different loading conditions, such as compression, tension, or shear. The significance of extending the relevance of the findings are acknowledged to orientations other than warp and weft. To tackle this aspect, it is planned to conduct supplementary experiments and analyses to assess geotextile behavior under diverse loading conditions comprehensively.

7. Nomenclature

PET: Polyethylene terephthalate
RMS: Root Mean Squared Error
FEA: Finite Element Analysis
SLS: The Linear Solid Model
W: Strain Energy Potential
λ_i: Principal Stretches
μ_i: Material Constant Related to Shear Modulus

α_i: Empirically Calculated Material Constant
j_{el}: Elastic Volume Ratio
N: Polynomial Order of the Strain Energy Function
C_{ij} : Material Shear Behavior Constant
D_i: Constant for Incompressible Materials
$\Delta\sigma e$: Represents the discrete increase in stress during phase I of deformation.
$\Delta\sigma k$: This variable represents the discrete increase in stress during Phase II of deformation.
$\Delta\varepsilon e$: Corresponding to Phase I, this variable represents the discrete increase in strain.
TU: The nominal stress
c10: The Neo-Hookean material parameter
λ: The stretch ratio

8. Acknowledgement

9. References

Arruda, E.M. and Boyce, M.C. (1993). "On the dynamic electromechanical loading of dielectric elastomer membranes", *Journal of the Mechanics and Physics of Solids*, 41(2), 389-412, https://doi.org/10.1016/0022-5096(93)90013-6.

Barbero, E.J. (2023). *Finite element analysis of composite materials using Abaqus ®*, CRC Press, Boca Raton, FL, USA, https://doi.org/10.1201/9781003425296.

Brinson, H.F. and Brinson, L.C. (2008). *Polymer engineering science and viscoelasticity*, An introduction, 99-157, Springer, New York, NY, https://doi.org/10.1007/978-0-387-74740-8.

Carreau, P.J., DeKee, D.C. and Chhabra, R.P. (2021). *Rheology of polymeric systems: Principles and applications*, Carl Hanser Verlag GmbH Co. KG, Munich, Germany. https://doi.org/10.3139/9783446457121.

Chevalier, L., Marco, Y. and Regnier, G. (2001). "Modification des propriétés durant le soufflage des bouteilles plastiques en PET", *Mécanique and Industries*, 2(3), 229-248, https://doi.org/10.1051/meca:2001135.

Chevalier, L., Luo, Y.M., Monteiro, E. and Menary,

G.H. (2012). "On visco-elastic modelling of polyethylene terephthalate behavior during multiaxial elongations slightly over the glass transition temperature", *Mechanics of Materials*, 52, 103-116, https://doi.org/10.1016/j.mechmat.2012.05.003

Ding, L., Xiao, C. and Cui, F. (2023). "Analytical model for predicting time-dependent lateral deformation of geosynthetics-reinforced soil walls with modular block facing", *Journal of Rock Mechanics and Geotechnical Engineering*, 16(2), 711-725, https://doi.org/10.1016/j.jrmge.2023.04.021.

Gavin, H.P. (2019). "The Levenberg-Marquardt algorithm for nonlinear least squares curve-fitting problems", Department of Civil and Environmental Engineering, Duke University, 19.

Guo, Z., Fei, J. and Jie, Y. (2022). "An equivalent-additional-stress-based material point method for the deformation of reinforced soil slopes under supergravity", *Computers and Geotechnics*, 142, 104536, https://doi.org/10.1016/j.compgeo.2021.104536.

Hackett, R.M. (2016). *Hyperelasticity primer*, Cham, Springer International Publishing.

Heymans, N. (2004). "Fractional calculus description of non-linear viscoelastic behavior of polymers", *Nonlinear Dynamics*, 38, 221-231, https://doi.org/10.1007/s11071-004-3757-5.

Hieu, D.M., Thong, N.T., Le, L.T.M., Nga, P.T.H., Thanh, N.C. and Trung, H.H. (2023). "Study on tensile strength of high-density polyethylene/polyethylene terephthalate blend", *Advances in Machinery, Materials Science and Engineering Application*, IX (pp. 27-32), IOS Press, https://doi.org/10.3233/ATDE230437.

ISO, E.N. 10319. (2008) *Geosynthetics-wide-width tensile test*, International Organization for Standardization, Geneva, Switzerland.

Jeon, H., an, B., Kim, H., Kim, Y., Cui, G. and Jang, Y. (2008). "Stress relaxation behaviors of nonwoven geotextile composites", *Proceedings of the 4th Asian Regional Conference on Geosynthetics*, (pp. 20-24), June 17-20, Shanghai, China, https://doi.org/10.1007/978-3-540-69313-05.

Kang, M.J., Kim, B.S., Hwang, S. and Yoo, H.H. (2018). "Experimentally derived viscoelastic properties of human skin and muscle in vitro", *Medical Engineering and Physics*, 61, 25-31, https://doi.org/10.1016/j.medengphy.2018.08.001.

Kenja, K., Madireddy, S., Vemaganti, K. (2020). "Calibration of hyperelastic constitutive models: the role of boundary conditions, search algorithms, and experimental variability",

Biomechanics and Modeling in Mechanobiology, 19(5), 1935-1952, https://doi.org/10.1007/s10237-020-01318-3.

Łagan, S.D. and Liber-Kneć, A. (2017). "Experimental testing and constitutive modeling of the mechanical properties of the swine skin tissue", *Acta of Bioengineering and Biomechanics*, 19(2), 93-102, https://doi.org/10.5277/ABB-00755-2016-02.

Li, Y., Tang, S., Kroger, M., and Liu, W.K. (2016). "Molecular simulation guided constitutive modeling on finite strain viscoelasticity of elastomers", *Journal of the Mechanics and Physics of Solids*, 88, 204-226, https://doi.org/10.1016/j.jmps.2015.12.007.

Lim, J., Hong, J., Chen, W.W. and Weerasooriya, T. (2011). "Mechanical response of pig skin under dynamic tensile loading", *International Journal of Impact Engineering*, 38(2-3), 130-135, https://doi.org/10.1016/j.ijimpeng.2010.09.003.

Luo, R.K. (2019). "A general hyper-elastic time model for numerical prediction on rubber relaxation and experimental validation under different environments", *Polymer Engineering and Science*, 59(10), 2159-2168, https://doi.org/10.1002/pen.25218.

Mansouri, M.R. and Darijani, H. (2014). "Constitutive modeling of isotropic hyper-elastic materials in an exponential framework using a self-contained approach", *International Journal of Solids and Structures*, 51(25-26), 4316-4326, https://doi.org/10.1016/j.ijsolstr.2014.08.018.

Mihai, L.A. and Goriely, A. (2017). "How to characterize a nonlinear elastic material? A review on nonlinear constitutive parameters in isotropic finite elasticity", *Proceedings of the Royal Society A: Mathematical, Physical and Engineering Sciences*, 473(2207), 20170607, https://doi.org/10.1098/rspa.2017.0607.

Mokhireva, K.A. and Svistkov, A.L. (2020). "A new approach to describe the elastic behavior of filled rubber-like materials under complex uniaxial loading", *International Journal of Solids and Structures*, 202, 816-821, https://doi.org/10.1016/j.ijsolstr.2020.07.005.

Mooney, M. (1940). "A theory of large elastic deformation", *Journal of Applied Physics*, 11(9), 582-592, https://doi.org/10.1063/1.1712836.

Narayanan, P., Pramanik, R. and Arockiarajan, A. (2023). "A hyperelastic viscoplastic damage model for large deformation mechanics of rate-dependent soft materials", *European Journal of Mechanics-A/Solids*, 98, 104874, https://doi.org/10.1016/j.euromechsol.2022.104874.

Peng, F.L., Li, F.L., Tan, Y. and Kongkitkul, W. (2010). "Effects of loading rate on visco-plastic properties of polymer geosynthetics and its

constitutive modeling", *Polymer Engineering and Science*, 50(3), 550-560, https://doi.org/10.1002/pen.21548.

Powell, P.C. and Housz, A.I. (2023). *Engineering with polymers*, CRC Press, Boca Raton, FL, USA.

Rivlin, R. (1948). "Large elastic deformations of isotropic materials, I, Fundamental concepts", *Philosophical Transactions of the Royal Society of London, Series A, Mathematical and Physical Sciences*, 240(822), 459-490, https://doi.org/10.1098/rsta.1948.0002.

Saberi, E., Najar, S.S., Abdellahi, S.B. and Soltanzadeh, Z. (2017). "A hyper-elastic approach for finite element modelling puncture resistance of needle punched nonwoven geotextiles", *Fibers and Polymers*, 18, 1623-1628, https://doi.org/10.1680/gein.14.00023.

Sawicki, A. and Kazimierowicz-Frankowska, K. (1998). "Creep behavior of geosynthetics", *Geotextiles and Geomembranes*, 16(6), 365-382, https://doi.org/10.1016/S0266-1144(98)00020-X.

Shahzad, M., Kamran, A., Siddiqui, M.Z. and Farhan, M. (2015). "Mechanical characterization and FE modeling of a hyperelastic material", *Materials Research*, 18, 918-924, https://doi.org/10.1590/1516-1439.320414.

Treloar, L. (1943). "The elasticity of a network of long-chain molecules-ii", *Transactions of the Faraday Society*, 39, 241-246.

Treloar, L.G. (1975). *The physics of rubber elasticity*, OUP Oxford.

Treloar, L. and Riding, G. (1979). "A non-Gaussian theory for rubber in biaxial strain: mechanical properties", *Proceedings of the Royal Society of London, A, Mathematical and Physical Sciences*, 369(1737), 261-280, https://doi.org/10.1098/rspa.1979.0163.

Van Lancker, B., De Corte, W. and Belis, J. (2020). "Calibration of hyperelastic material models for structural silicone and hybrid polymer adhesives for the application of bonded glass", *Construction and Building Materials*, 254, 119204, https://doi.org/10.1016/j.conbuildmat.2020.119204.

Wang, J.Q., Xu, L.J., Lin, Z.N. and Tang, Y. (2020). "Study on creep characteristics of geogrids considering sand-geosynthetics interaction under different loading levels", *Journal of Engineered Fibers and Fabrics,* 15, 1558925020958520, https://doi.org/10-117715589250209585.

Ward, I.M. and Sweeney, J. (2012). *Mechanical properties of solid polymers*, John Wiley and Sons, Hoboken, NJ, USA.

Wu, H., Yao, C., Li, C., Miao, M., Zhong, Y., Lu, Y. and Liu, T. (2020). "Review of application and innovation of geotextiles in geotechnical engineering", *Materials*, 13(7), 1774, https://doi.org/10.3390/ma13071774.

Yun, S., Jung, J., Jun, S., Jeong, J., Moon, Y.H. and Kim, J.H. (2021). "Constitutive and fracture modeling of biaxially oriented polyethylene terephthalate film and its application to polymer-coated sheet metal forming", *Journal of Manufacturing Science and Engineering*, 143(6), 061005, https://doi.org/10.1115/1.4049190.

Zohra, B.F., Fouad, B.A. and Mohamed, C. (2022). "Soil-structure interaction interfaces: Literature review", *Arabian Journal of Geosciences*, 15(12), 1-16, https://doi.org/10.1007/s12517-022-10336-7.

Microstructural Investigation of Compressive Strength and Permeability of Concrete Containing Fly Ash in the Marine Environment of the Persian Gulf

Amiri, M.[1]* , Mandegari, M.[2] and Karimi, H.[3]

[1] Associate Professor, University of Hormozgan, Faculty of Engineering, Bandar Abbas, Iran.
[2] M.Sc., Islamic Azad University of Bandar Abbas, Faculty of Engineering, Bandar Abbas, Iran.
[3] M.Sc., University of Hormozgan, Faculty of Engineering, Bandar Abbas, Iran.

ABSTRACT: Investigating the impact of fly ash on concrete strength and durability in the challenging marine environment of the Persian Gulf is crucial due to sulfate attacks and salt effects. This study aims to enhance the lifespan of these structures by increasing strength and reducing permeability. The innovative approach involves microstructural assessment of fly ash's influence on Calcium Hydroxide (CH) and C-S-H nanostructure formation in concrete. Around 120 concrete samples with varying fly ash content were exposed to the Persian Gulf for three months, undergoing compressive strength, permeability, and microstructural analysis. Results reveal fly ash addition decreases permeability and boosts concrete strength. Notably, concrete containing 10% fly ash exhibited a 15.4% strength increase and reduced permeability from 22.4×10^{-7} cm/h to 8.98×10^{-7} cm/h after 90 days. Scanning Electron Microscopy (SEM) and Energy Dispersive X-ray (EDX) analysis showcased CH reduction and enhanced C-S-H nanostructure, bolstering concrete durability. This study offers valuable insights for engineers constructing coastal Persian Gulf structures, indicating fly ash augmentation enhances microstructural properties, reduces permeability, and bolsters strength.

Keywords: Concrete, Fly Ash, Marine Environment, Permeability, Compressive Strength, Microstructure, Sulfate Attack, Calcium Hydroxide (CH), Pozzolanic Materials, SEM.

1. Introduction

The production of cement involves high-temperature calcination, which leads to the release of 5-8% CO_2 emissions (Afroz et al., 2023; Chaudhury et al., 2023). In light of environmental concerns and the adverse impacts of cement misuse on nature, the use of recycled materials in concrete or mortar has become more prevalent (Modarres and Ghalehnovi, 2023). Inorganic alum inosilicate materials (Abhishek et al., 2022) can be utilized in various chemical processes (Pan et al., 2014) to transform different industrial wastes, such as iron smelting furnace slag, fly ash, fuel ash, rice husk ash, met kaolin, natural pozzolans and any source containing amorphous alum

---

* Corresponding author E-mail: amirii@hormozgan.ac.ir

inosilicates (Wang et al., 1995), into construction materials (Amiri and Tanide., 2020; Xu et al., 2014). The incorporation of industrial waste as a cement substitute in concrete not only helps to mitigate environmental pollution and address waste disposal issues, but also enhances concrete properties, leading to increased compressive (Jindal and RN, 2022).

Therefore, reducing the permeability of concrete is crucial for improving its durability and lifespan, especially in harsh environments such as coastal regions where concrete structures are exposed to saltwater and sulfate attacks. The addition of fly ash to concrete has been shown to be an effective method for reducing permeability and increasing durability, making it a viable solution for enhancing the performance of concrete structures in such environments (Junior et al., 2021). Chlorides can also cause the loss of bond strength between steel reinforcement and concrete (Amiri and Tanide., 2020), which further weakens the concrete structure.

Therefore, reducing the permeability of concrete is essential to improve its durability and increase its service life in chloride-rich environments (Rezaei et al., 2022). Moreover, the use of fly ash as a pozzolanic material in concrete has been reported to reduce the risk of Alkali-Silica Reaction (ASR) in concrete structures, which can lead to cracking and reduced durability (Taylor, 1997). ASR occurs when aggregates containing reactive silica come into contact with the highly alkaline environment of concrete, leading to the formation of an expansive gel that causes cracking and damage to the concrete (Mehta et al., 2014). Fly ash, when used as a partial replacement for cement, reduces the amount of reactive silica available in the concrete, thereby reducing the risk of ASR (Rigi and Ziaei, 2022).

Sulfate attacks on concrete structures in marine environments can cause extensive damage and decrease the strength and durability of the structure. The sulfate ions penetrate the concrete pores, resulting in

chemical reactions that lead to cracking, expansion, and energy loss (Amiri and Tanide., 2020). This can eventually result in the failure of the structure, posing a threat to the safety of people and property. Therefore, it is important to study the effects of sulfate ions on concrete and find ways to improve the durability and strength of concrete in these harsh environments.

Concrete containing fly ash as a partial replacement for cement has shown significant improvement in its resistance to sulfate and chloride ions compared to concrete containing only ordinary Portland cement (Taylor, 1997). The presence of fly ash in the concrete mixture results in a denser pore structure, which reduces the permeability of the concrete and, consequently, limits the penetration of aggressive ions into the concrete (Mehta et al., 2014; Rigi and Ziaei, 2022).

Fly ash also has a pozzolanic reaction with the cement hydration products, which results in the formation of additional C-S-H nanostructure (Kang et al., 2019). The formation of C-S-H nanostructure in fly ash concrete can lead to increased strength and durability (Glosser et al., 2019; Jindal and RN, 2022). Additionally, the use of fly ash in concrete mixtures can also help to reduce the heat of hydration and improve the workability of the mixture (Behl et al., 2022; ACI Committee, 2005). It should be noted that the harmful effects of ettringite on the strength and durability of concrete are more pronounced in corrosive chloride and acidic environments (Mehta et al., 2014). Ettringite is formed in a needle-like shape after the reaction of tricalcium silicate, tricalcium aluminate (C_3A) and its formation is accompanied by the development of a nanostructure of C-S-H and Calcium Hydroxide $Ca(OH)_2$ during the hydration process (Taylor, 1997). The density of the C-S-H nanostructure is directly related to the strength of the concrete. However, the increase in the ettringite structure has been found to decrease the strength and durability of the concrete. Fly ash has a significant impact on

the microstructure of concrete, particularly on the pore size distribution and shape. This results in the formation of more C-S-H bonds, which improves the strength and durability of concrete. High-calcium fly ash types are more reactive than low-calcium ones, as they contain crystallized reactive compounds such as C_3A and CS. The presence of C_3A in fly ash is beneficial because it reacts with chlorides and forms calcium aluminate chloride (Friedel's Salt), which enhances the chloride binding capacity of the cement system and delays the onset of corrosion.

The amount of Friedel and Kozel salts formed due to the inclusion of fly ash increases the amount of bound chlorides in the system, thereby reducing the amount of free chlorides and the risk of corrosion of steel reinforcement (Ortiz-Salcedo et al., 2022; Saffari and Firuzi, 2011). In addition to reducing the risk of corrosion, the use of fly ash in concrete can also improve its strength and reduce its permeability. Fly ash particles can fill in the gaps and voids in the concrete matrix, resulting in a denser and more compact structure. This, in turn, can reduce the permeability of concrete, making it more resistant to the penetration of aggressive agents such as water, sulfate and chloride ions (Khankhaje et al., 2023; Supit and Shaikh., 2015; Thomas and Matthews, 1992). Furthermore, fly ash is a sustainable alternative to traditional cement, as it is a waste product that would otherwise be sent to landfills. By using fly ash in concrete, the amount of cement required can be reduced, thereby reducing the carbon footprint of the construction industry (Rigi and Ziaei, 2022).

The use of natural pozzolans as a replacement for cement is a popular and cost-effective solution, as it can reduce concrete heat generation, lower permeability, and increase chemical resistance, which can improve the durability of the concrete mixture. When fly ash is added to concrete, pozzolanic reactions occur, leading to a reduction in permeability and increased durability in sulfate and chloride environments.

The reaction of fly ash plays a key role in determining the durability of the concrete mixture, influencing parameters such as the amount of CH, type and amount of C-S-H, and pH of the pore solution. In this study, the effect of adding different percentages of fly ash as a substitute for part of cement on the microstructural level of concrete durability and strength in the marine environment of the Persian Gulf was evaluated, with a focus on changes in the amount of CH and C-S-H.

The samples were naturally preserved in the sea of the Persian Gulf, and the study's innovative aspect lies in its detailed microstructural investigation of the compressive strength and permeability of concrete containing fly ash in the harsh marine environment. The results of this study can provide valuable insights into the development of durable concrete mixtures suitable for marine environments.

2. Materials and Methods

An innovative approach was taken to investigate the compressive strength and permeability of concrete containing fly ash in the aggressive marine environment of the Persian Gulf. Ordinary Type II Portland cement, obtained from Hormozgan Cement Company in Bandar Khamir, and fly ash produced at the Bandar Abbas power plant were used to prepare the concrete samples.

The tests were conducted in accordance with ASTM standards. The chemical analysis of the ordinary Portland cement Type II and fly ash Class F (ASTM, 2018) were performed through X-Ray Fluorescence (XRF) analysis, and the results are presented in Table 1. Additionally, some characteristics of the Persian Gulf seawater are provided in Table 2. It is noteworthy that any environment with a PH lower than 12.5 can be aggressive, and acidic ions such as SO_4^{-2} and Cl present in seawater can often lower the PH.

Table 1. Chemical characteristics of Portland cement Ttype II and fly ash

Materials	SiO_2	Al_2O_3	Fe_2O_3	CaO	K_2O	Na_2O	SO_3	L.O.I
Cement II	22.00	5.30	4.00	65.00	0.70	0.50	2.50	2.50
Fly ash	56.70	28.20	5.30	2.80	1.73	0.78	0.68	3.70

Table 2. Characteristics of seawater in the Persian Gulf

Properties	pH	SO_4^{-2}(mg/L)	Cl(mg/L)	NaCl	TDS (g/L)	Ec (mS/cm)
Persian golf	7.9	2541	23491.77	3.5%	39	59
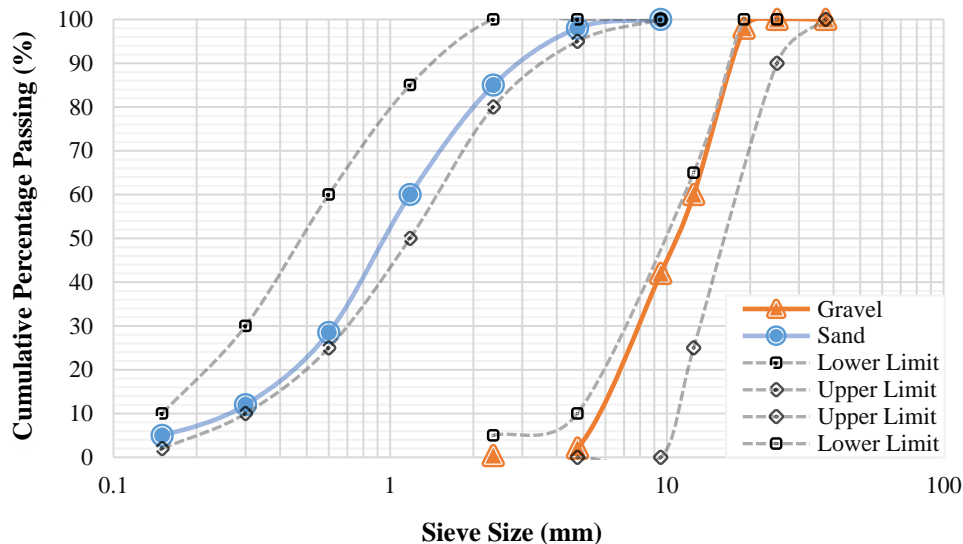
Fig. 1. Granulometry curve of the materials used (sand and gravel) based on ASTM C33 standard

The Persian Gulf environment is classified as moderate according to the ACI 318-19 standard with a sulfate level of 2541 mg/L (ACI Committee, 2005). The chloride content of 23491.77 mg/L in the Persian Gulf environment is harmful to Portland cement concrete, as the limit value of chloride ions to initiate corrosion has been reported in the range of 600-900 mg/L for a conventional sample of concrete mixture (Mehta et al., 2014). To investigate the impact of fly ash on the compressive strength and durability of concrete samples exposed to the sulfate and chloride environment of the Persian Gulf, varying amounts of 5%, 10%, 15% and 20% of fly ash were used as a partial substitute for cement. The aggregates used in this research included gravel and sand. The granulomere curve of the sand used, based on ASTM C33 standard, is presented in Figure 1 (ASTM, 2009).

To achieve the research objectives, an appropriate mixing plan related to the research subject was presented based on the ACI-211 standard, as shown in Table 3. In this regard, the materials were first weighed according to each mixing plan in a workshop environment. Then, the desired sample was made using a mixer, and after conducting the slump test, the concrete was poured into standard molds with dimensions of $15 \times 15 \times 15$.

The mold was filled and compacted three times. The samples were removed from the molds after 24 hours, and then 12 specimens from each mixing design (four specimens for the 7-day test, four for the 28-day test, and four for the 90-day test) were stored under normal environmental conditions (water) and the marine environment of the Persian Gulf. The compressive strength of the samples was measured in the laboratory at 7-day, 28-day, and 90-day intervals (ASTM, 2009). The mixing plan used for cement samples had a water-to-cement ratio of 0.45.

Table 3. Concrete mix design using type 2 portland cement according to ACI-211 standard

Constituents	Gravel (kg/m³)	Sand (kg/m³)	Water (kg/m³)	Cement (kg/m³)	Fly ash (kg/m³)
Concrete	693.6	1069	157.5	350	0
Concrete + %5 fly ash	693.6	1069	157.5	332.5	17.5
Concrete + %10 fly ash	693.6	1069	157.5	315	35
Concrete + %15 fly ash	693.6	1069	157.5	297.5	52.5
Concrete + %20 fly ash	693.6	1069	157.5	280	70

The water used to make the samples was water from Bandar Abbas with a pH of 7.5. To perform the compressive strength test, the samples were made according to the ASTM C39 standard at laboratory temperature and based on the mixing scheme in Table 3 (ASTM, 2009). It is worth noting that the samples were in the Persian Gulf, and the tests were conducted from the beginning of September to the end of November when the water temperature ranged between 18 and 28 degrees Celsius. To analyze the microstructure of the concrete samples, Scanning Electron Microscopy (SEM) was employed.

3. Discussion and Results Analysis

3.1. Microstructure of Samples in Seawater and Tap Water Conditions

Figure 2 displays SEM images of the control sample and samples containing 5%, 10%, 15% and 20% fly ash stored in tap water and seawater for 90 days. The concrete microstructure changes with an increase in the percentage of fly ash, as seen in Figures 2a to 2e. Figure 2a shows the morphology of the control sample after being exposed to tap water.
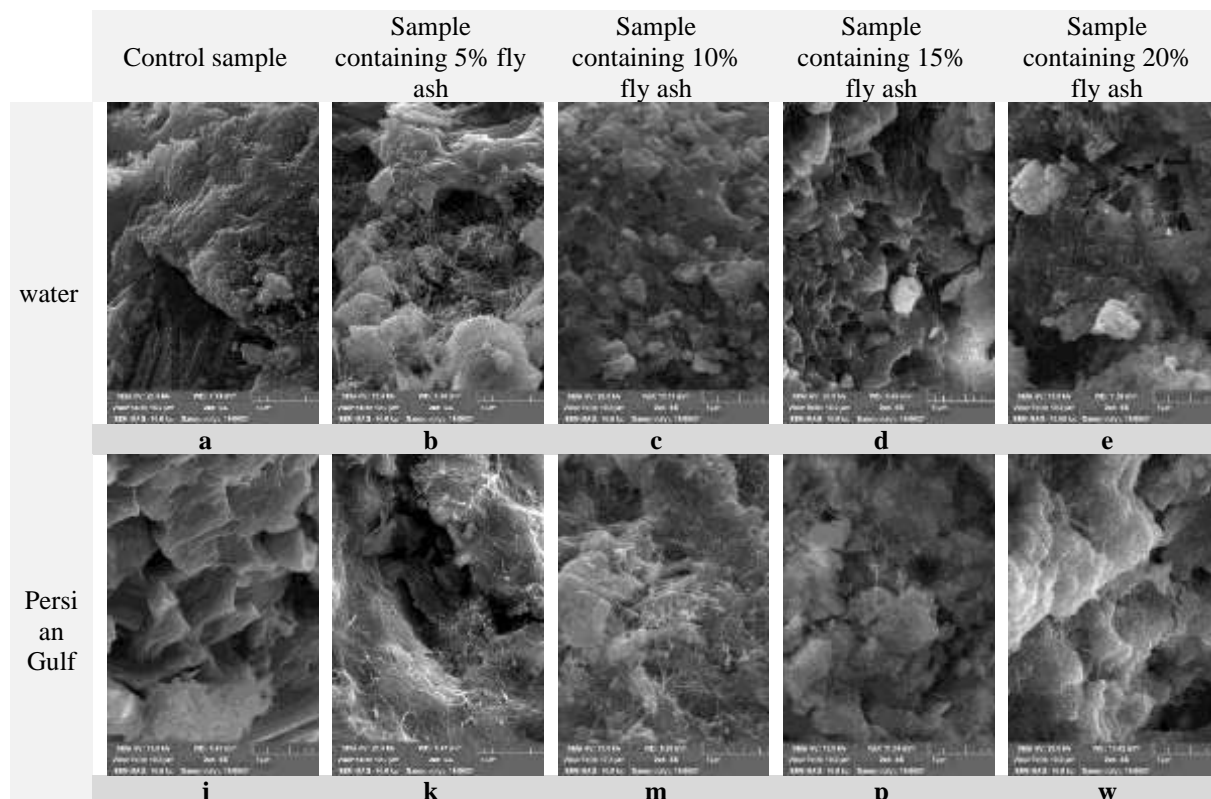
Fig. 2. SEM images of concrete samples, including: a) Control sample stored in water; b) Sample containing 5% fly ash stored in water; c) Sample containing 10% fly ash stored in water; d) Sample containing 15% fly ash stored in water; e) sample containing 20% fly ash stored in water; j) Control sample stored in the Persian Gulf; k) Sample containing 5% fly ash stored in the Persian Gulf, m) Sample containing 10% fly ash stored in the Persian Gulf; p) Sample containing 15% fly ash stored in the Persian Gulf; and w) Sample containing 20% fly ash stored in the Persian Gulf.

The completion of the hydration process and the growth of the nanoscale sponge-like structure of calcium silicate hydrate (C-S-H) reduces the porosity and enhances the cohesion in the cement paste of this sample. The amount of Calcium Hydroxide Ca(OH)$_2$ or CH, in the cement paste without fly ash is not visible. Typically, CH appears as distinct hexagonal crystals that vary in shape depending on the available space in the cement paste. Due to its low Van der Waals force, the role of CH in the strength of concrete is limited.

Additionally, the effect of CH on the chemical durability of concrete against acids is undesirable because of its high solubility. Figures 2b to 2e show the morphology of samples containing different percentages of fly ash, stored in potable water for 90 days. The amount of CH in samples containing fly ash has decreased. In fact, fly ash has less CaO in its chemical composition, and its pozzolanic activity consumes CH significantly. When C$_3$S (tricalcium silicate) comes into contact with water, the calcium silicate minerals separate into calcium and silicate ions. This loaded ions deposit as a thin layer on the surface of C$_3$S to delay the reaction between C$_3$S and water. The nucleation and growth of CH crystals fill the empty spaces between the particles. In addition, C-S-H particles in water precipitate as a silicate-rich layer on C$_3$S grains and gradually transform into needle-like ettringite-like compounds. In cement paste containing fly ash, the amount of nanostructure C-S-H has increased, and a limited amount of ettringite has formed.

Therefore, these processes can reduce porosity and potentially decrease permeability. Figures 2j to 2w show SEM micrographs of control samples and samples containing 5%, 10%, 15%, and 20% fly ash maintained in the Persian Gulf environment for 90 days. Figure 2j shows the morphology of the control sample treated in the Persian Gulf environment.

Due to the penetration of sulfate and chloride ions present in the Persian Gulf waters, gypsum crystals and needle-like ettringite structures have occupied a large volume, which is why this sample is associated with more destructive effects than the sample maintained in water (Figure 2a). Figure 2k shows the microstructure of the concrete sample containing 5% fly ash treated in a chloride and sulfate environment of the Persian Gulf for 90 days.

This image shows the formation of six-sided calcium hydroxide crystals (CH) and C-S-H nanostructure. The formation of ettringite in the sample is limited. Figure 2w shows the morphology of the concrete sample containing 20% fly ash treated in the Persian Gulf environment. In this image, the C-S-H nanostructure has grown in the samples treated in seawater, and six-sided CH are also observed. In this sample, the needle-like ettringite structure is observable but is not the dominant structure. In this study, the presence of needle-like ettringite structures in the samples was observed, although they were not the predominant structures.

Generally, it can be concluded that the addition of fly ash resulted in a decrease in the amount of CH and a relative increase in the amount of calcium silicate hydrate (C-S-H) in the samples. Furthermore, in samples exposed to the marine environment of the Persian Gulf, the addition of fly ash resulted in a reduction in ettringite formation, as well as a decrease in CH content.

3.2. Structural Analysis by Energy Dispersive X-ray Spectroscopy (EDX)

Energy Dispersive X-ray spectroscopy (EDX) is an analytical method used for the structural and chemical analysis of a sample. Figure 3 displays the results obtained from EDX spectroscopy for the samples at 90 days. Figure 3a shows the EDX pattern of the control sample maintained in water at 90 days. The peak corresponding to CaKα is observed at 3.7 Kev.
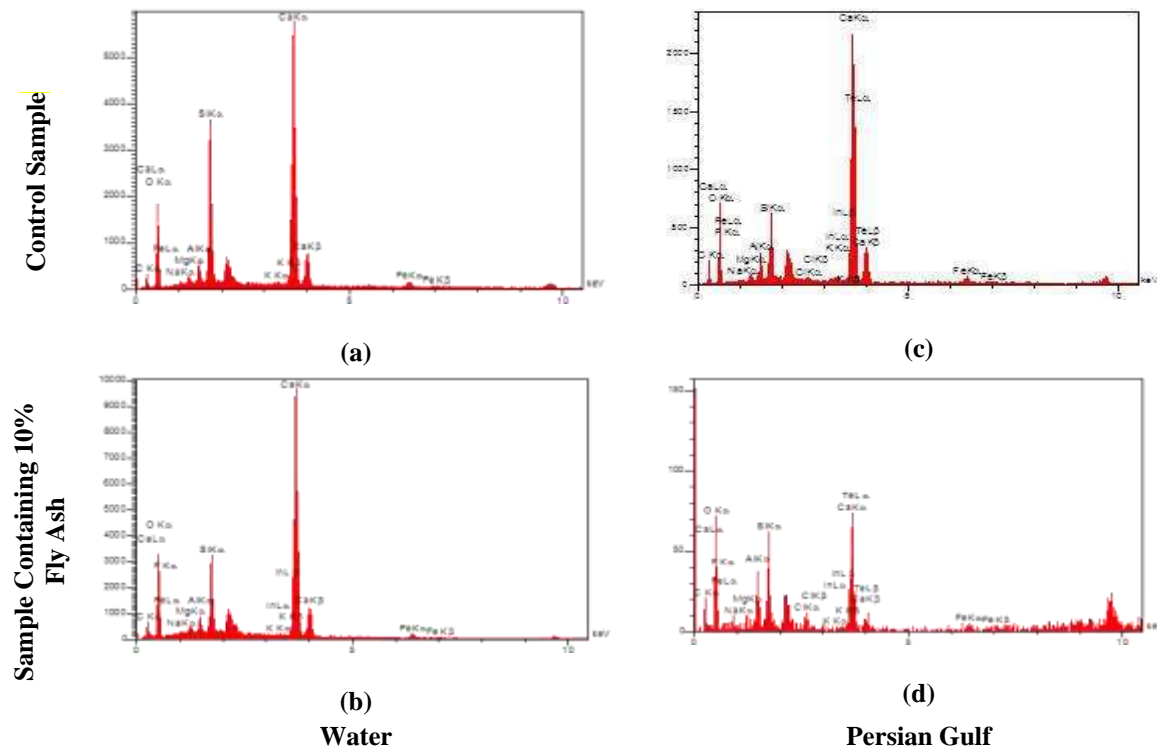
Fig. 3. EDX images of concrete samples, including: a) Control sample stored in water; b) Sample containing 10% fly ash stored in water; c) Control sample stored in the Persian Gulf; and d) Sample containing 10% fly ash stored in the Persian Gulf.

Figure 3b shows the EDX pattern of the sample containing 10% ash maintained in water. The peak corresponding to CaKα is observed at 3.7 Kev, and a peak corresponding to SiKα is observable at 1.7 Kev. Figure 3c shows the EDX pattern of the sample without ash maintained in the environmental conditions of the Persian Gulf at 90 days. As shown in Figure 3c, a peak for CaKα is observable at 3.7 Kev. Figure 3d shows the EDX pattern of the sample containing 10% ash maintained in the Persian Gulf seawater at 90 days. The peak for CaKα in this sample is at 3.7 Kev.

Furthermore, the EDX spectra in samples containing ash indicate the presence of a Ca ion peak. The changes in the weight percentage of elements present in concrete samples obtained from EDX analysis show that the Ca/Si and Ca/ (Al + Si) ratios in the control sample maintained in water are 5.313 and 4.148, respectively. These ratios indicate that the sponge-like nanostructure of C-S-H is formed to a large extent, and the volume of small pores at the micro and nano level is very small.

The EDX results of the sample containing 10% fly ash maintained in water also show Ca/Si and Ca/ (Al + Si) ratios of 2.816 and 2.405, respectively. The addition of nano silica results in a decrease in CH, an increase in C-S-H, and consequently, a decrease in Ca/Si ratios. The weight percentage of Si and Al ions in the sample containing 10% fly ash maintained in the Persian Gulf seawater has decreased compared to the control sample. The Ca/Si and Ca/ (Al + Si) ratios obtained from the EDX results for the control sample maintained in the Persian Gulf seawater are 1.943 and 1.072, respectively.

In addition, the Ca/Si and Ca/ (Al + Si) ratios for the sample containing 10% fly ash maintained in the Persian Gulf seawater are 5.941 and 3.970, respectively. As observed, the Ca/Si and Ca/ (Al + Si) ratios in the sample containing 10% fly ash maintained in the Persian Gulf seawater have increased compared to the control sample. In general, it can be stated that the amount of cations in all samples maintained in water and Persian Gulf seawater increases with an increase in

fly ash percentage. The results of the EDX test show that the Ca/Si and Ca/ (Al+Si) ratios in the control sample maintained in the Persian Gulf marine environment have reached the lowest values compared to other samples.

This ratio indicates the severe penetration of chloride and sulfate ions from seawater into the sample and also indicates the formation of a destructive structure of ettringite and gypsum and the destruction of C-S-H nanostructures in the samples, which is well matched with the results shown in the SEM images in Figure 2. As chloride and sulfate attacks progress, the calcium content within the C-S-H nanostructure decreases, leading to a decrease in the molar ratio of Ca/Si. The molar ratio of Ca/Si serves as an indicator for identifying the C-S-H nanostructure, with the minimum and maximum ratios observed in the C-S-H phase being 1.943 and 5.941, respectively. However, the use of fly ash as an additive has been found to increase the Ca/Si ratio in the samples. This suggests that incorporating fly ash into concrete mixtures may improve the performance of the material in marine environments. The literature supporting this finding is derived from authentic journals in the field of concrete technology.

3.3. Investigation of Changes in Compressive Strength in the Marine Environment of the Persian Gulf

The compressive strength changes in concrete specimens containing various percentages of fly ash in contact with two different environments, water and Persian Gulf seawater, at the ages of 7, 28 and 90 days are presented in Figures 4 and 5.

Based on the results presented in Figure 4, the compressive strength of the control sample reached 278 kg/cm^2 after 7 days of exposure to tap water. After 28 days, the compressive strength of the control sample increased to 285 kg/cm^2 and reached 304 kg/cm^2 after 90 days. The results show that the control sample exposure to tap water at the age of 28 and 90 days had a 2.27% and

9.09% increase in compressive strength compared to the 7-day sample, respectively. The SEM images in Figure 2 show that this increase in strength is due to the completion of the hydration process and the evolution of C-S-H nanostructures, as well as a reduction in the porosity of the samples over time. The compressive strength of 7-day-old specimens containing 5%, 10%, 15%, and 20% fly ash and treated with tap water were 319 kg/cm^2, 293 kg/cm^2, 258 kg/cm^2, and 231 kg/cm^2, respectively.

Samples containing 5%, 10%, 15% and 20% of fly ash processed with water showed an increase in compressive strength compared to the control sample of 25.98%, 31.48%, 19.0 % and 0.65%, respectively, at the age of 90 days. Samples containing 10% fly ash exposure to tap water at the ages of 7, 28 and 90 days obtained compressive strength of 293 kg/cm^2, 369 kg/cm^2 and 399 kg/cm^2, respectively. The results show that the sample containing 10% fly ash exposure to tap water at the age of 28 and 90 day had a 25.59% and 36.04% increase in compressive strength compared to 7-day sample, respectively. Samples containing 20% fly ash exposure to tap water at the ages of 7, 28 and 90 days obtained compressive strength of 231 kg/cm^2, 257 kg/cm^2 and 306 kg/cm^2, respectively. The results show that the sample containing 20% fly ash exposure to tap water at the age of 28 and 90 days had an 11.51% and 32.41% increase in compressive strength compared to 7 days samples, respectively.

The use of fly ash led to an increase in the long-term strength of the concrete. According to the SEM images shown in Figure 2, with the passage of time, the C-S-H nanostructure in the samples treated with water grew, creating a high specific surface area that improves adsorption characteristics and fills the pores (Hong and Glasser, 2002; Amiri and Tanide, 2020). During the hydration of concrete in the presence of fly ash, there are two possible mechanical reactions.
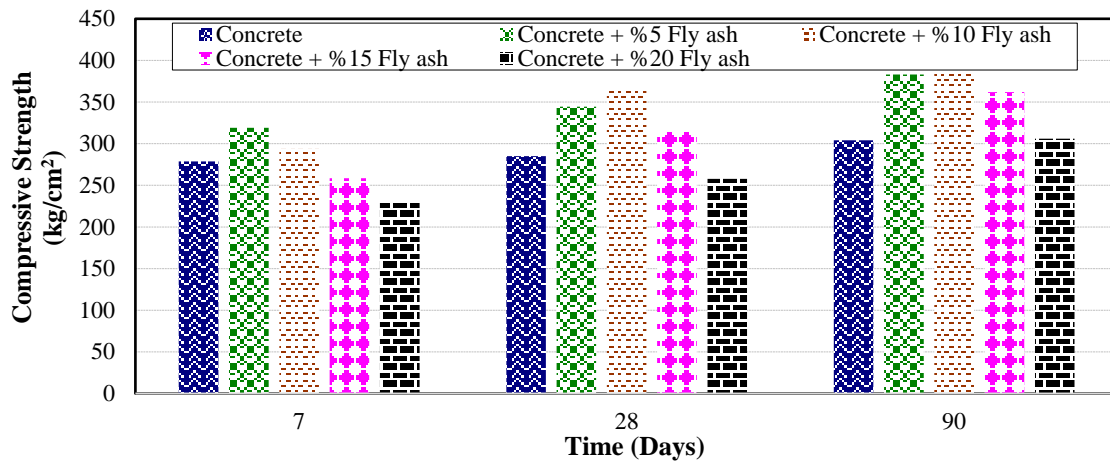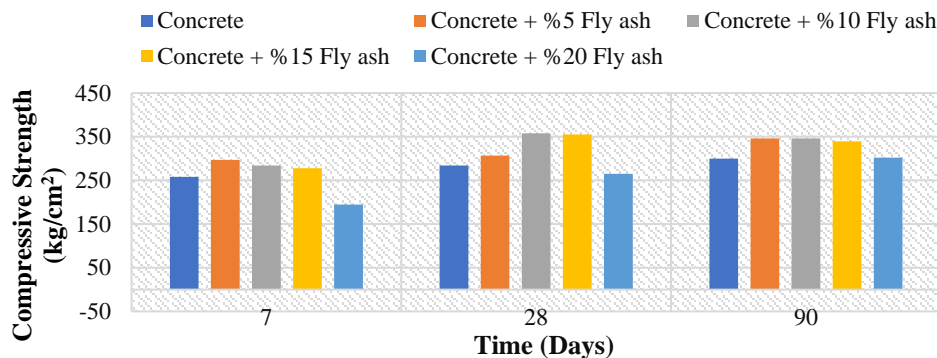
Fig. 4. Changes in compressive strength of concrete samples stored in water

Fly ash particles can accelerate cement hydration by forming $H_2SiO_4^{-2}$ which reacts with Ca^{+2} present, producing additional calcium-silicate-hydrate (C-S-H) (Singh et al., 2013). C-S-H constitutes approximately 75% of the weight of hydrated cement and forms at temperatures near ambient conditions, contributing to the increased strength of the concrete (Wang et al., 2019).

Based on the results presented in Figure 5, the control sample stored in seawater in the Persian Gulf achieved compressive strengths of 258 kg/cm², 284 kg/cm² and 300 kg/cm² at ages of 7, 28, and 90 days, respectively. The control sample stored in seawater at the age of 28 and 90 days had a 10.07% and 16.27% increase in compressive strength, respectively, compared to the 7-day sample. The compressive strengths of 5%, 10%, 15%, and 20% fly ash concrete samples stored in seawater for 7 days were 297 kg/cm², 284 kg/cm², 277 kg/cm², and 194 kg/cm²,

respectively. The results showed that at the age of 90 days, the samples containing 5%, 10%, 15%, and 20% fly ash had an increase in compressive strength of 15.34%, 15.4%, 13.16%, and 0.74%, respectively, compared to the control sample.

Samples containing 10% fly ash stored in seawater at the ages of 7, 28 and 90 days obtained compressive strength of 284 kg/cm², 357 kg/cm² and 346 kg/cm², respectively. Sample stored in seawater at the age of 28 and 90 days had a 25.85% and 21.79% increase in compressive strength compared to 7-day samples, respectively.

Samples containing 20% fly ash stored in seawater at the ages of 7, 28 and 90 days obtained compressive strength of 194 kg/cm², 365 kg/cm² and 302 kg/cm², respectively. Sample stored in seawater at the age of 28 and 90 day had an 87.46% and 55.77% increase in compressive strength compared to 7-day sample, respectively.

Fig. 5. Changes in compressive strength of concrete samples stored in Persian Gulf sea water

These results indicate that adding fly ash improves the mechanical properties and durability of concrete in the Persian Gulf seawater at later ages. However, concrete samples stored in seawater showed a reduction in compressive strength compared to samples stored in water at ages of 7, 28, and 90 days, with reductions of 7.41%, 0.35%, and 1.32%, respectively.

This reduction in strength is due to the penetration of sulfate and chloride ions into the concrete structure. For the concrete samples stored in seawater, the effect of the sulfate and chloride environment is intensified by the consumption of hydration products such as CH and C-S-H. Therefore, the dissolution of hydration products and the formation of Friedel's salt, the needle-shaped structure of ettringite, and gypsum crystals due to attacks by sulfate, chloride, and acid in the seawater have occurred, which is consistent with the SEM image results shown in Figure 2 and leads to the breakdown of the concrete structure. The result of these destructive effects is the destruction of the nanostructure of C-S-H and CH, causing a decrease in the compressive strength of the concrete samples.

In addition, the EDX test results show that the Ca/Si and Ca/ (Al + Si) molar ratios in the concrete samples stored in the Persian Gulf environment have reached their lowest values compared to other samples. Generally, with the progress of sulfate and chloride attacks, the calcium present in the C-S-H nanostructure is lost, and the Ca/Si and Ca/ (Al + Si) molar ratios decrease.

The 28-day concrete samples stored in seawater showed a reduction in compressive strength of 10.8% and 3.25%, respectively, compared to the samples stored in water containing 5% and 10% fly ash. Increasing the percentage of fly ash used in concrete samples can help improve concrete impermeability, resulting in increased resistance of concrete samples to sulfate and chloride-containing water and a denser sample structure. An increase in compressive strength in concretes containing fly ash even after long-term exposure to marine environments was observed by Supit and Shaikh (2015) and Lopez-Calvo et al. (2012).

3.4. Effect of Fly Ash on Permeability Coefficient in the Persian Gulf Marine Environment

The chart depicting the permeability coefficient and depth of water penetration for concrete samples containing varying percentages of fly ash in two environments, namely water and the Persian Gulf marine environment, is presented in Figure 6.

Based on the results, the permeability coefficient of the control sample in water was 18.3×10^{-7} cm/h. The permeability coefficients of samples containing 5%, 10%, 15%, and 20% fly ash treated in water were 6.45×10^{-7} cm/h, 5.70×10^{-7} cm/h, 4.90×10^{-7} cm/h, and 3.19×10^{-7} cm/h, respectively. The results indicate that the sample containing 20% fly ash in water showed an 82.56% reduction in permeability coefficient compared to the control sample. The depth of water penetration of samples containing 5%, 10%, 15%, and 20% fly ash treated in water decreased by 41.66%, 46.5%, 50%, and 60%, respectively, compared to the control sample.

Overall, the results showed that with increasing dust deposition, the permeability coefficient and the depth of water penetration decreased. According to the presented results, the permeability coefficient of the control sample maintained in the Persian Gulf was 22.4×10^{-7} cm/h. The permeability coefficients of samples containing 5, 10, 15, and 20% dust deposition and treated in the Persian Gulf were 12.38×10^{-7} cm/h, 8.98×10^{-7} cm/h, 7.75×10^{-7} cm/h, and 5.84×10^{-7} cm/h, respectively. The results indicate that the sample containing 20% dust deposition maintained in the Persian Gulf showed a 73.92% decrease in permeability coefficient compared to the control sample.
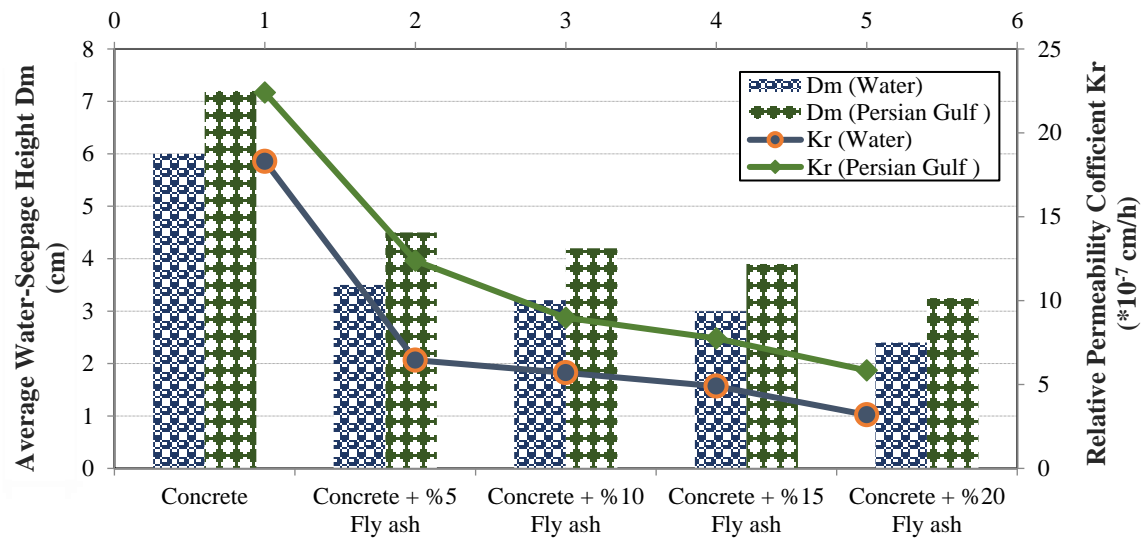
Fig. 6. Permeability coefficient and depth of water penetration of concrete samples containing different percentages of fly ash stored in water and the Persian Gulf environment

The depth of water penetration in concrete samples containing 5%, 10%, 15%, and 20% dust deposition and treated in the Persian Gulf exhibited significant reductions of 37.5%, 41.66%, 45.83% and 54.86%, respectively, compared to the control sample. SEM images in Figure 2 demonstrated that the utilization of dust deposition improved the microstructure of concrete, leading to a substantial reduction in permeability coefficient and depth of water penetration. This is attributed to the small particle size and low specific surface area of dust deposition, which fills the pores and reduces porosity. As a result, the permeability of chloride and sulfate ions in concrete decreases, leading to enhanced durability against attacks by these ions in the Persian Gulf environment (Abedi, 2021).

However, the permeability coefficient of concrete samples containing 5%, 10%, 15%, and 20% dust deposition stored in the Persian Gulf increased by 91.93%, 57.54%, 58.16%, and 83.07%, respectively, compared to the samples stored in water. This increase is due to the penetration of sulfate and chloride ions in the concrete structure by seawater in the Persian Gulf.

The reaction between fly ash particles and calcium hydroxide produces C-S-H nanostructure, which fills the pores and

enhances the fine structure of concrete (Abedi, 2021). This improvement in the fine structure of concrete results in reduced permeability and water penetration depth, leading to increased durability against sulfate and chloride attacks in the Persian Gulf environment.

A decrease in permeability and depth of penetration in concrete containing fly ash was also observed in the research of Moffatt et al. (2017); Thomas and Matthews (1992); Supit and Shaikh (2015) and Chalee et al. (2010)

4. Conclusions

In this study, the effect of the Persian Gulf marine environment on concrete containing different percentages of fly ash as a cement substitute was investigated from the perspective of microstructure. The laboratory studies revealed the following key findings:
- Scanning Electron Microscopy (SEM) images indicated that the hydration process and the growth of a sponge-like C-S-H nanostructure in samples immersed in water reduced permeability and increased compressive strength.
- EDX and SEM results demonstrated that in samples exposed to the aggressive Persian Gulf marine environment, the Ca/Si

and Ca/ (Al + Si) ratios reached their lowest values. This emphasizes the pronounced influence of chloride attack, while sulfate attack had a comparatively minor impact. The penetration of chloride and sulfate ions from the Persian Gulf waters led to the formation of destructive compounds, including ettringite and gypsum, and the degradation of the C-S-H nanostructure, ultimately diminishing the strength of the samples.

- The sample containing 10% fly ash, kept in the Persian Gulf, exhibited a 25.70% and 15.4% increase in compressive strength compared to the sample without additives after 28 and 90 days, respectively.

- The sample containing 10% fly ash displayed the highest compressive strength after 90 days of exposure to the Persian Gulf environment and tap water, with values of 346 kg/m² and 399 kg/m², respectively. Incorporating 10% fly ash, particularly at a water-cement ratio of 0.45, not only improved compressive strength but also reduced permeability and penetration depth.

- Increasing the percentage of fly ash as a cement substitute for samples immersed in the aggressive Persian Gulf environment increased the durability and compressive strength of the samples and reduced the porosity and permeability of the concrete over time. Fly ash increased the hydration process over time and the pore structure was gradually modified with more processing time, increasing density and resulting in a denser sample structure. Concrete containing fly ash had higher strength than concrete without fly ash at older ages.

- Adding fly ash reduced the amount of CH and increased the relative amounts of C-S-H in the samples. In samples immersed in the Persian Gulf's marine environment, adding fly ash reduced the destructive effects of chloride and sulfate ions and increased the durability of concrete. In general, the results suggested that adding fly ash as a cement substitute can improve the durability of concrete in the Persian Gulf marine environment.

- In the Persian Gulf's marine environment,

chloride attack is the primary cause of concrete erosion, expansion, and cracking, while sulfate attack has a limited impact. Incorporating fly ash as a supplementary cementitious material can enhance concrete's resistance to chloride-induced deterioration.

Overall, the microstructural investigation demonstrated that fly ash is an effective cement substitute for enhancing the durability and compressive strength of concrete in the aggressive marine environment of the Persian Gulf. In marine environments, the significance of chloride attack in concrete deterioration takes precedence over sulfate attacks, emphasizing its dominant role.

The findings of this study could be useful in designing and constructing durable concrete structures in coastal regions with similar marine environments.

5. Availability of Data and Materials

The datasets generated during and/or analyzed during the current study are available from the corresponding author on reasonable request.

6. Acknowledgments

7. References

Abedi, M. (2021). "Comparative evaluation of the effect of water/cement ratio (W/C), type and percentage of fly ash on concrete strength against chloride ion penetration and its porosity", *Amirkabir Journal of Civil Engineering*, 53, 1067-1082, https://doi.org/10.22060/ceej.2019.16760.6336.

Abhishek, H.S., Prashant, S., Kamath, M.V. and Kumar, M. (2022). "Fresh mechanical and durability properties of alkali-activated fly ash-slag concrete: A review", *Innovative*

Infrastructure Solutions, 7, 1-14, https://doi.org/10.1007/s41062-021-00711-w.

ACI Committee. (2005). *Building code requirements for structural concrete (ACI 318-05) and commentary (ACI 318R-05)*, American Concrete Institute.

Afroz, S., Zhang, Y., Nguyen Q.N., Kim, T. and Castel, A. (2023). "Shrinkage of blended cement concrete with fly ash or limestone calcined clay", *Materials and Structures*, 56, 15, https://doi.org/10.1617/s11527-023-02099-8.

Amiri, M. and Tanideh, P. (2020). "Microstructural assessment of the effect of sulfate environments on the mechanical properties of geopolymer concrete", *Concrete Research*, 13, 45-57, https://doi.org/10.22124/jcr.2020.13701.1375.

Amiri, M. and Tanide, P. (2020). "Microstructural assessment of the effect of sulfate environments on the mechanical properties of concrete", *Modares Civil Engineering*, 19, 1-14, https://sid.ir/paper/1037377/en.

ASTM. (2009)."*American society for testing and materials*, ASTM International, West Conshohocken, PA.

ASTM. (2018). *ASTM C618-19 standard specification for coal fly ash and raw or calcined natural pozzolan for use in concrete*, ASTM International, West Conshohocken, PA.

Behl, V., Singh, V., Dahiya, V. and Kumar, A. (2022). "Characterization of physico-chemical and functional properties of fly ash concrete mix", *Materials Today, Proceedings*, 50, 941-945, https://doi.org/10.1016/j.matpr.2021.06.353.

Chalee, W., Ausapanit, P. and Jaturapitakkul, C. (2010). "Utilization of fly ash concrete in marine environment for long term design life analysis", *Materials and Design*, 31, 1242-1249, https://doi.org/10.1016/j.matdes.2009.09.024.

Chaudhury, R., Sharma, U., Thapliyal, P.C. and Singh, L.P. (2023). "Low-CO_2 emission strategies to achieve net zero target in cement sector", *Journal of Cleaner Production*, 137466, https://doi.org/10.1016/j.jclepro.2023.137466.

Glosser, D., Choudhary, A., Isgor, O.B. and Weiss, W.J. (2019). "Investigation of reactivity of fly ash and its effect on mixture properties", *ACI Materials Journal*, 116, 193-200, https://doi.org/10.14359/51716722.

Hong, S.Y. and Glasser, F.P. (2002). "Alkali sorption by CSH and CASH gels: Part II, Role of alumina", *Cement and Concrete research*, 32, 110111, https://doi.org/10.1016/S0008-8846(02)00753-6.

Jindal, A. and RN, G.D. (2022). "Behavioral study of incorporation of recycled concrete aggregates and mineral admixtures in pavement quality concrete", *Civil Engineering Infrastructures Journal*, 55, 351-372, https://doi.org/10.22059/ceij.2022.326564.1766.

Junior, J.R.H., Balestra, C.E. and Medeiros-Junior, R.A. (2021). "Comparison of test methods to determine resistance to chloride penetration in concrete: Sensitivity to the effect of fly ash", *Construction and Building Materials*, 277, 122265, https://doi.org/10.1016/j.conbuildmat.2021.122265.

Kang, S.H., Jeong, Y., Kim, M.O. and Moon, J. (2019). "Pozzolanic reaction on alkali-activated Class F fly ash for ambient condition curable structural materials", *Construction and Building Materials*, 218, 235-244, https://doi.org/10.1016/j.conbuildmat.2019.05.129.

Khankhaje, E., Kim, T., Jang, H., Kim, CH. and Kim, J. (2023). "Properties of pervious concrete incorporating fly ash as partial replacement of cement: A review", *Developments in the Built Environment*, 100130, https://doi.org/10.1016j.dibe.2023.100130.

Lopez-Calvo, H.Z., Montes-Garcia, P., Bremner, T.W., Thomas, M.D.A. and Jiménez-Quero, V.G. (2012). "Compressive strength of HPC containing CNI and fly ash after long-term exposure to a marine environment", *Cement and Concrete Composites*, 34, 110-118, https://doi.org/10.1016/j.cemconcomp.2011.08.007.

Mehta, P.K. and Paulo J.M. (2014). *Concrete, microstructure, properties and materials,* McGraw-Hill Education.

Modarres, Y. and Ghalehnovi, M. (2023). "The effect of recycled steel fibers from waste tires on concrete properties", *Civil Engineering Infrastructures Journal*, 56, 1-18, http://doi.org/10.22059/CEIJ.2022.339592.1820.

Moffatt, E.G. Thomas, M.D.A. and Fahim, A. (2017). "Performance of high-volume fly ash concrete in marine environment", *Cement and Concrete research*, 102, 127-135, https://doi.org/10.1016/j.cemconres.2017.09.008.

Ortiz-Salcedo, B.H., Paris, J.M, Ferraro, C.C., Minkara, R. and Riding, K.A. (2022). "Evaluation of chlorides in fly ash for use in concrete", *Cleaner Materials*, 5, 100098, https://doi.org/10.1016/j.clema.2022.100098.

Pan, Z.h., Sanjayan, J.G. and Collins, F. (2014). "Effect of transient creep on compressive strength of geopolymer concrete for elevated temperature exposure", *Cement and Concrete Research*, 56, 182-189, https://doi.org/10.1016/j.cemconres.2013.11.014.

Rezaei, M., Delnavaz, A. and Delnavaz, M. (2022). "Investigating the durability of steel fiber reinforced concrete composite in sulfate and chloride environments", *Concrete Research*, 15,

99-107,
https://doi.org/10.22124/JCR.2022.21122.1536.

Rigi, A.H. and Ziaei, M. (2022). "Experimental study of durability of self compacting concrete containing micro-silica and slag in Persian Gulf tidal environment", *Concrete Research*, 15, 59-72,
https://doi.org/10.22124/JCR.2023.21298.1541.

Saffari jourshari, M.F. (2011). "Properties of fly ash and its effects in producing chloride-resisting concrete", *Proceedings of the 1st International Conference on Non Osmosis Concrete (1st ICNOC)-Water Storage Tanks*, Guilan, Iran.

Singh, L.P., Karade, S.R., Bhattacharyya, S.K., Yousuf, M.M. and Ahalawat, S. (2013). "Beneficial role of nanosilica in cement based materials, A review", *Construction and Building Materials*, 47, 1069-77,
https://doi.org/10.1016/j.conbuildmat.2013.05.052.

Supit, S.W.M. and Shaikh, F.U.A. (2015). "Durability properties of high volume fly ash concrete containing nano-silica", *Materials and Structures*, 48, 2431-45,
https://doi.org/10.1617/s11527-014-0329-0.

Taylor, HF. (1997). *Cement Chemistry*, (Vol. 2, p. 459), Thomas Telford, London.

Thomas, M.D.A. and Matthews, J.D. (1992). "The permeability of fly ash concrete", *Materials and Structures*, 25, 388-396,
https://doi.org/10.1007/BF02472254.

Wang, S.D., Pu, X.C., Scrivener, K.L. and Pratt, P.L. (1995). "Alkali-activated slag cement and concrete: A review of properties and problems", *Advances in Cement Research*, 7, 93-102,
https://doi.org/10.1680/adcr.1995.7.27.93.

Wang, X., Ni, W., Li, J., Zhang, S., Hitch, M. and Pascual, R. (2019). "Carbonation of steel slag and gypsum for building materials and associated reaction mechanisms", *Cement and Concrete Research*, 125, 105893, https://doi.org/10.1016/j.cemconres.2019.105893.

Xu, H., Gong, W., Syltebo, L., Lutze, W. and Pegg, I.L. (2014). "DuraLith geopolymer waste form for Hanford secondary waste: Correlating setting behavior to hydration heat evolution", *Journal of hazardous materials*, 278, 34-39,
https://doi.org/10.1016/j.jhazmat.2014.05.070.

Development and Testing of a Novel High-Damping Chlorobutyl Rubber for Structural Viscoelastic Damper Devices

Roshan-Tabari, F.[1]* , Toopchi Nezhad, H.[2] and Hashemi Motlagh, G.[3]

[1] Ph.D. Candidate, Department of Civil Engineering, Razi University, Kermanshah, Iran.
[2] Associate Professor, Department of Civil Engineering, Razi University, Kermanshah, Iran.
[3] Assistant Professor, School of Chemical Engineering, College of Engineering, University of Tehran, Iran.

ABSTRACT: The main objective of this study is to modify the blend formulation of a Chlorobutyl rubber compound to improve its damping properties for structural applications. A new rubber composite was created by adding Acrylonitrile Butadiene Rubber (NBR) and Chlorinated Polyethylene (CPE) to Chlorobutyl rubber. The viscoelastic parameters of the cured original CIIR (control sample) and modified CIIR (i.e., CIIR/NBR/CPE) compounds were determined by Dynamic Mechanical Thermal Analysis (DMTA) in tension mode. Subsequently, cyclic shear tests were performed at room temperature and loading frequencies of 0.5, 0.75, 1 and 3 Hz on prototype viscoelastic damper devices fabricated from the rubber blends. The shear force-deformation hysteresis loops of the prototype dampers at shear strains of 0.5, 1.0 and 1.5 revealed that the viscoelastic properties (i.e., shear storage and loss moduli as well as loss factor) of the modified CIIR significantly improved as compared to the original CIIR. The test results demonstrated an increase exceeding 100% and 160% in the shear storage and loss moduli, respectively, of the modified CIIR compared to the reference CIIR.

Keywords: Viscoelastic Damper, High Damping Rubber, Chlorobutyl, Cyclic Shear Tests, Force-Deformation Hysteresis Loops.

1. Introduction

Viscoelastic dampers are supplemental devices used in structural control to mitigate the seismic response of structures, attenuate wind-induced vibrations in tall buildings (Shu et al., 2022), mitigate the seismic pounding of structures (Ramakrishna and Mohan, 2020; Taleshian et al., 2022) and reduce the vibration of floor diaphragms under live loads (Nikravesh and Toopchi-Nezhad, 2022).

Structural seismic control offers an additional opportunity through an integrated design approach. It enables the creation of new structural forms and configurations, such as slender buildings, without compromising their performance (Castaldo and De Iuliis, 2014). Viscoelastic dampers typically employ one or more elastomeric pads made of high-damping rubber with special formulations.

* Corresponding author E-mail: h.toopchinezhad@razi.ac.ir

During vibrations of the structure, the elastomeric pads are subjected to cyclic shear deformation and owing to their inherently high damping, they dissipate a significant portion of the structural vibration energy. By using viscoelastic supplemental dampers, in addition to effective damping, the stiffness of the structure also increases. Owing to the viscoelastic nature of the elastomer pads within the damper, the effective damping and stiffness of the dampers are generally affected by strain, excitation frequency and ambient temperature (Achenbach and Duarte, 2003; Christopoulos and Filiatrault, 2006; He et al., 2023; Tsai, 1994; Xiang and Xie, 2021).

Numerous types of structural viscoelastic dampers have been explored in existing literature. These include sandwich viscoelastic dampers (Xu et al., 2021), Rotary Rubber Braced Dampers (RRBDs) (Fazli Shahgoli et al., 2021), Viscoelastic Coupling Dampers (VCDs) (Montgomery and Christopoulos, 2015), Visco-Hyperelastic Dampers (VHDs) (Modhej and Zahrai, 2021), and viscoelastic Tuned Mass Dampers (TMDs) (Nikravesh and Toopchi-Nezhad, 2022). Each of these has the potential to improve the dynamic performance of a variety of structures. In most applications, the energy dissipation of viscoelastic material is achieved through shear strain.

However, there are instances where energy dissipation is facilitated by amplified axial strain (Modhej and Zahrai, 2020, 2022). One of the critical factors affecting the performance of a viscoelastic damper is the inherent damping of the elastomer used in the damper, which is attributed to the molecular structure of the base rubber and combination of the constituent components in the rubber compound. The inherent damping of polyethylene, polymathic methacrylate, polypropylene, Styrene-Butadiene Rubber (SBR), Isobutylene-Isoprene Rubber (IIR), and urethane compounds was investigated (Hujare and Sahasrabudhe, 2014). It was found that the effective damping of polyethylene and IIR (commonly known as butyl) compounds was higher than that of other rubbers. The damping property of IIR can be enhanced using miscible polymer oligomers, such as polyisobutylene, as an additional relaxation component (Xia et al., 2018). The effective damping of rubber can be increased using physical methods. For example, innovative pre-compressed viscoelastic dampers made of Chlorobutyl Rubber (CIIR) have been developed (Ghotb and Toopchi-Nezhad, 2019). By pre-compressing the elastomeric pads, the frictional resistance between the chain molecules of the rubber is increased. This results in an increase in effective damping when the damper pads are subjected to shear strain and the rubber molecules slide against each other. The influence of the compressive load on rate-dependent high-damping rubber bearings was also studied (Wei et al., 2019)

Numerous studies have addressed the improvement in the inherent damping of rubber materials used in viscoelastic dampers by modifying their compound formulations. A compound of EPDM and butyl (IIR) rubber materials with the addition of 20 parts of carbon black and 20 parts of paraffinic oil was found to be a suitable option for producing rubber with high inherent damping (Jose et al., 2009).

Application of a type of modified silica fume as an alternative reinforcing filler to improve the damping properties of natural rubber has been investigated (Suntako, 2017). The addition of different kinds and amounts of organic small molecule modifiers (AO1035, AO60 and AO80) to neat Nitrile-Butadiene Rubber (NBR) for improving its energy dissipation capability has been studied (Ge et al., 2022). The addition of CIIR to a compound with Ethylene Propylene Diene Monomer (EPDM) as the base rubber effectively improved the thermal and mechanical properties of the resulting blend, leading to an increase in its inherent damping at room temperature. However, the inherent

damping of the resulting composition was not higher than that of chlorobutyl alone (Jose et al., 2009; Therattil et al., 2008).

Adding aliphatic C5 resin and aromatic C9 resin to the components of CIIR rubber leads to an increase in the effective damping of the rubber (Zhang et al., 2014). Likewise, the use of terpene resin was found to be effective in regulating glass transition and widening the effective damping temperature range of CIIR (Liu et al., 2019).

The multilayer combination of CIIR and PVC in the rubber compound increases its effective damping over a wider temperature range (Zhang et al., 2015). The viscoelastic properties of NBR and CIIR were investigated in the frequency range of 10-10^5 Hz to evaluate the effect of the carbon black ratio on these properties (Capps and Beumel, 1990).

Lu et al. (2014) developed a high damping rubber at ambient temperatures by combining CIIR, NBR and neoprene. In a composite of CIIR and Lead Zirconate Titanate (PZT), the damping properties were improved by transforming the mechanical energy of vibration into electrical energy using PZT. Another material whose application as a viscoelastic damper has been reported in the literature is silicon rubber (Alhasan et al., 2023).

The inherent damping of rubber varies with temperature and reaches a maximum value at the glass transition temperature (T_g), which usually occurs between -20 °C to -100 °C depending on its molecular structure. A rubber material below its glass transition temperature is brittle and the rubber chains are consolidated without any segmental movement.

When the temperature of the rubber part increases and reaches Tg, segmental movement of the chains is initiated and the part starts to become soft. Therefore, at Tg, a relatively large amount of energy is required to initiate chain movements, at such temperatures, the material can absorb a large amount of energy. However, this property significantly decreases at temperatures above 0° C. Therefore, one of the objectives of improving the viscoelastic properties of rubber is to increase its inherent damping at ambient temperature.

As mentioned, CIIR rubber is one of the rubbers with relatively high damping properties. Similar to many other types of rubber, the inherent damping of CIIR decreases significantly at ambient temperatures above 0° C, rendering its use in supplemental viscoelastic dampers unjustifiable. The objective of this study is to enhance the inherent damping of CIIR at ambient temperatures by improving its compound composition. The mechanical and damping properties of the modified rubber at ambient temperatures were assessed via cyclic shear tests at various shear strains and loading frequencies, which are typically expected in many building structures. In the following sections, the modification of rubber compounds by adding new compositional components, testing methods and determination of the viscoelastic properties of both the reference and modified rubber blends are presented.

2. Modified Chlorobutyl Rubber Blend

The base rubber used in the formulations in this study was of the chlorobutyl (CIIR) type. Chlorobutyl rubber, a relatively high-damping rubber, has a wide range of industrial applications. Butyl rubber is a copolymer of isobutylene and small amounts of isoprene, usually 0.8-2.5 mole%, which provides unsaturated bonds for crosslinking by sulfur curing. Chlorobutyl is produced by the halogenation of butyl rubber. Butyl rubber exhibits good resistance to weathering agents and is highly resistant to air and water penetration (Mark et al., 2013). The addition of halogens increased the polymer chain flexibility of butyl and enhanced its compatibility when combined with polar rubbers. Compared to butyl, chlorobutyl exhibits better damping properties and demonstrates better bonding and compatibility with polar rubbers in the

production of multi-rubber compounds (Hanhi et al., 2020).

Several factors affect the dynamic mechanical properties of elastomeric materials, including excitation frequency, temperature, molecular structure of the base polymer and chemical cross-linking systems. Moreover, the physical properties and viscoelastic behavior of these materials are significantly influenced by reinforcing fillers such as different types of carbon black. During cyclic deformations, the stress and strain are out of phase with each other by a certain angle δ, which falls within the range of 0 to π/2 rad. The behavior of a material is described by a complex elastic modulus that comprises both real and imaginary components. The ratio between the imaginary and real components represents the tangent of the phase angle δ and is often referred to as the loss factor or loss tangent (tan δ) (Capps and Beumel, 1990).

The components of chlorobutyl rubber compounds with their designations used in this study are listed in Table 1. The compounds were prepared by mixing all components except the curing agents in a 60

cc, internal mixer with Banbury-type rotors, Misagh Afzar (Tehran, Iran), at 60 rpm and 130 °C for 10 min. After a day of rest at room temperature and prior to molding, the compounds from the internal mixer were mixed with the curing agents, that is, sulfur, CBS and Zinc Dibenzyldithiocarbamate (ZBEC), in a lab-scale two-roll mill (Berstorff, Hannover, Germany) at room temperature for 20 min. The compounds were molded into 2 mm thick sheets in a hot press at 100 bar and 160 °C for 8 min for DMTA analysis.

The mechanical properties of the rubber under dynamic loading were obtained through DMTA tests using a Netzsch-DMA 242 C instrument capable of determining the mechanical properties of the rubber under dynamic loads at different temperatures and frequencies. In the aforementioned test, which was conducted according to the ASTM D5026 standard (ASTM, 2015), the laboratory rubber samples were subjected to cyclic tensile stresses at a frequency of 1 Hz and the temperature was changed from -100 to +100 °C at a heating rate of 3 °C/min.

Table 1. Components of different rubber formulations

Ingredient (phr)	Compound			
	Ref. CIIR	NBR	CIIR-NBR	Mod. CIIR
CIIR	100	0	80	80
NBR	0	100	20	20
CPE	0	0	0	10
N550	30	30	30	30
Sulfur	2	2	2	2
Paraffinic oil	20	20	20	20
Cumarone resin	3.5	3.5	3.5	3.5
ZnO	5	5	5	5
Acid stearic	1	1	1	1
CBS	1.5	1.5	1.5	1.5
ZBEC	1.5	1.5	1.5	1.5

Figure 1 illustrates the changes in the loss factor (tan δ) in the reference CIIR rubber at ambient temperature. As observed, the tan δ curve in CIIR rubber has a peak value of 1.35 at a temperature of -45 °C. The maximum value of the loss factor for this rubber, similar to other rubbers, occurs at its glass transition temperature,

which is usually much below zero degrees. The mechanical properties of polymers undergo significant changes at the glass transition temperature (Landel and Nielsen, 1993). As shown in Figure 1, the tan δ value of the reference CIIR rubber reached 0.4 at 0 °C and decreased significantly at temperatures above 0 °C. A necessary

requirement for effective performance of a viscoelastic damper is the use of rubber with a high loss factor (damping) within the expected temperature range. The main objective of this study was to achieve a rubber compound with high damping properties under an excitation frequency range of 0.5 Hz to 3 Hz (the dominant frequency range of a wide range of building structures) at room temperature.

A glass transition temperature of -45 °C was assigned to CIIR according to the location of the peak in Figure 1. According to this figure, tan δ of CIIR rubber significantly decreases at temperatures above 0 °C and has negligible values at room temperature. One way to shift the damping temperature range of CIIR to higher temperatures is to blend CIIR with other compatible rubbers or materials. In this study, NBR with a higher glass transition temperature range and therefore, a higher damping temperature range, was selected to extend the damping temperature range of CIIR. NBR and CIIR contain polar groups that are expected to provide good interactions and compatibility. Therefore, their blends are expected to preserve the mechanical properties of their constituents without severe deterioration.
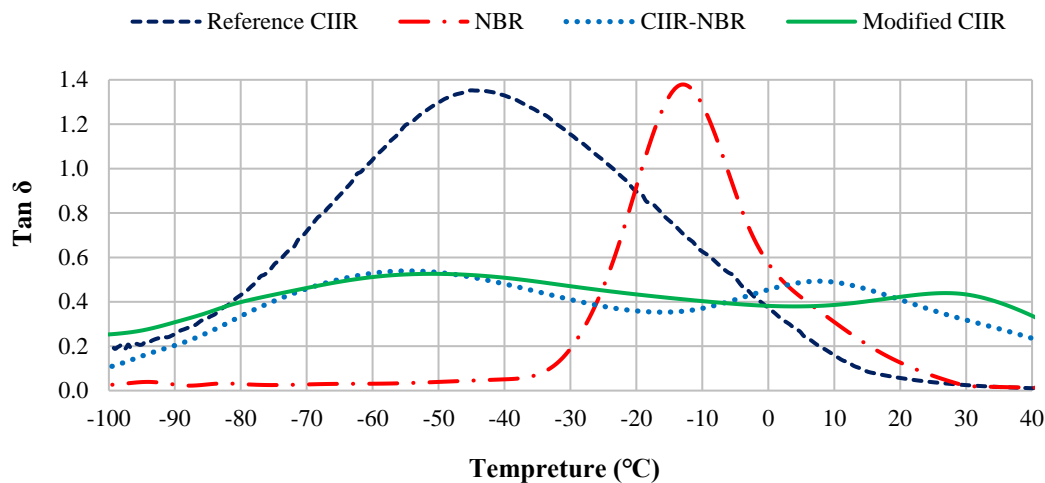
Fig. 1. Variations of the loss factor (tan δ) with temperature for various compounds obtained from DMTA tests conducted at the frequency of 1 Hz

Before blending the two rubbers, it was necessary to determine the changes in the loss factor of NBR with temperature through DMTA tests. The rubber compound formula for NBR (with 33 mole% acrylonitrile) is listed in Table 1 and the variations in the loss factor with temperature (DMTA test results) for this rubber are shown in Figure1. According to Figure 1, the peak loss factor in this rubber is 1.4, which occurs at -17 °C.

Therefore, NBR has an inherent damping capacity that is suitable and comparable to that of CIIR but at higher temperatures. However, the loss factor in the rubber decreased significantly at positive temperatures.

A new compound, CIIR-NBR, was prepared by blending CIIR with NBR (33 mol% nitrile). The composition of the recently developed compound is presented in Table 1 and the variations in the loss factor with temperature (DMTA test results) for this compound are shown in Figure 1. As observed in Figure 1, by blending these two rubber compounds, the value of tanδ decreased at negative temperatures, but in the positive temperature range, the value of tanδ increased significantly and reached a maximum value of approximately 0.5. In contrast to the previous two compounds, the loss factor curve of CIIR-NBR compound exhibited two peaks at temperatures of -45 ˚C and +22 ˚C. The appearance of these two peaks indicates that the blend was

immiscible. In addition, the corresponding peak of NBR shifted from -17 °C to +22 °C, while that of CIIR remained unchanged.

Therefore, the blend is not sufficiently compatible; otherwise, the temperature peak of CIIR increases and the temperature peak of NBR decreases. The minimum value of the loss factor within the desired temperature range (i.e., ±20 °C) occurs at a temperature close to zero.

At 0 °C, the loss factor decreased by up to approximately 40% compared with its peak value, which was a significant reduction. The significant variations in the loss factor between the two peaks of the CIIR-NBR curve can be attributed to the polar compatibility issues of the blended rubbers.

CIIR rubber has low polarity, whereas NBR has high polarity (Lu et al., 2014). It is noteworthy that the peak temperature of NBR has experienced a significant shift, rising from -17 °C to +22 °C. This enhancement broadens the utility of the blend, particularly as a damper in environments with positive ambient temperatures. As CIIR (1.6 mole% chlorine) and NBR (33 mole% nitrile) are largely different in polarity, this study used CPE as an intermediate material for their compatibility.

In addition, it was of interest to see whether CPE, which is a near-amorphous thermoplastic material with rubbery behavior but a higher glass transition temperature (approximately 0 °C), can increase the damping temperature range of the CIIR/NBR blend.

Hence, the use of CPE extends beyond merely enhancing compatibility between CIIR and NBR. The formula for the newly modified compound, named Modified CIIR, is shown in Table 1. This nomenclature indicates that the base rubber of the modified compound was chlorobutyl rubber. Variations in the loss factor, tanδ, with temperature for the modified chlorobutyl rubber, evaluated using DMTA testing, are shown in Figure 1.

An inspection of this figure shows that the modified composition has a higher loss coefficient than the previous composition (CIIR-NBR) within the temperature range of -40 °C to 15 °C. In the modified chlorobutyl rubber, the minimum tanδ increased from approximately 0.3 to approximately 0.4 with a 33% increase within the temperature range of -40 °C to +25 °C. Additionally, the curve was more uniform in this temperature range, and the maximum variation in tan delta compared to its peak value was approximately -24%.

CPE shifted the corresponding peak of NBR from +22 °C to +30 °C. The damping factor of the modified CIIR was more adequate in the positive temperature range than that of the original CIIR (control sample) up to +35 °C. To investigate the morphology of the compositions at the microscale and compare the fracture surfaces between the phases, SEM images (Figure 2) were used.
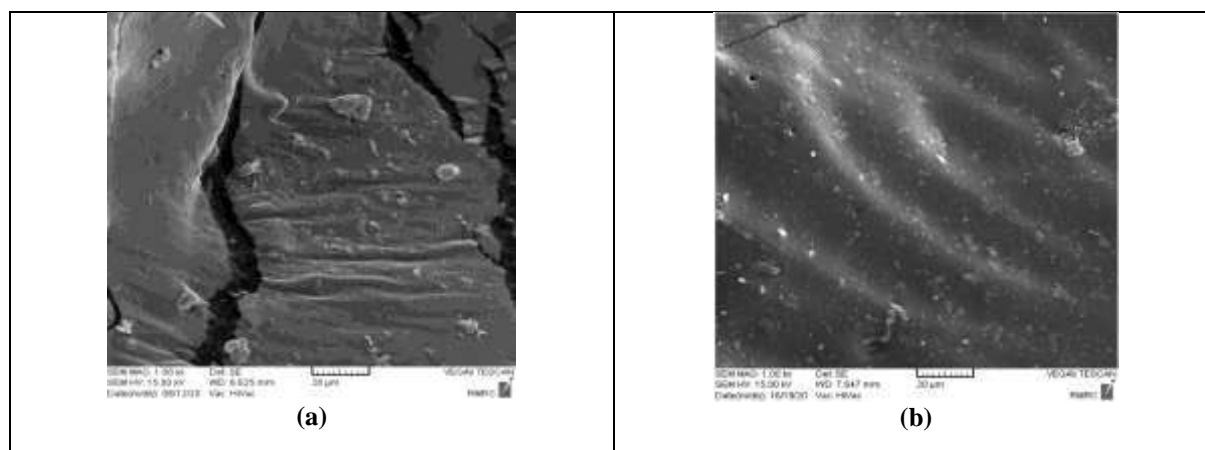
Fig. 2. Microscopic images of rubber compositions before curing: a) CIIR-NBR composition; and b) CIIR-NBR-CPE composition

The microscopic images presented in Figure 2 were captured from the cryo-fractured surfaces of the compounds before curing. A common disperse-matrix morphology for immiscible polymer blends was observed, in which the major polymer (CIIR) was the continuous phase (matrix), and the minor polymer (NBR) was the dispersed phase (particles).

The NBR droplets did not have a spherical shape because of their relative compatibility with the matrix. Figure 2a corresponds to the CIIR-NBR blend. As shown in Figure 2a, the fracture surfaces between the rubber phases were created discontinuously and unevenly with large NBR particles. This defect can cause the formation of small cracks on the macroscopic scale and significantly degrade the properties of the rubber composition. By contrast, Figure 2b corresponds to a rubber composition with 10 CPE parts and it is clear that the fracture surfaces changed from discontinuous and rough to smoother and continuous regions without cracks. More importantly, by adding 10 parts of CPE, the average droplet size of the NBR phase decreased from 8 to 3 µm because of the increased interfacial adhesion between CIIR and NBR provided by CPE as a compatibilizer.

Therefore, it was expected that the final composition would have fewer defects. It appears that CPE serves as a reinforcing agent between two polar and non-polar rubbers, and its elastomeric nature effectively covers the defects between phases. The other CPE dosages were not as effective as 10 phr.

This section pertained to DMTA testing, in which specimens of rubber blends were subjected to dynamic tension. In supplemental viscoelastic dampers, the rubber pads within the damper are typically subjected to cyclic shear deformation. To assess the mechanical response of rubber materials under cyclic shear loads, several prototype viscoelastic dampers have been fabricated using the reference CIIR and Mod. CIIR is the rubber pad of the damper. The test output includes the shear force-deformation hysteresis loops of the prototype dampers under various shear strain amplitudes and excitation frequencies.

2. Prototype Viscoelastic Dampers

To evaluate the viscoelastic hysteretic response of rubber materials under cyclic shear loads, two types of viscoelastic dampers with identical geometrical dimensions but different rubber materials (Ref. CIIR and Mod. CIIR) were fabricated. These damper types are hereafter referred to as Ref. Damper and Mod. Damper, respectively.

Figure 3 shows images of the prototype viscoelastic dampers constructed in this study. As shown in this figure, two individual specimens were fabricated for each type of damper. The geometric dimensions of the dampers were the same for both types, with the only difference being the type of rubber material employed. Figure 4 shows the components of the viscoelastic damper units used in this study.

(a)   (b)

Fig. 3. Damper units of various rubber pads: a) Ref. CIIR pads; and b) Mod. CIIR pads
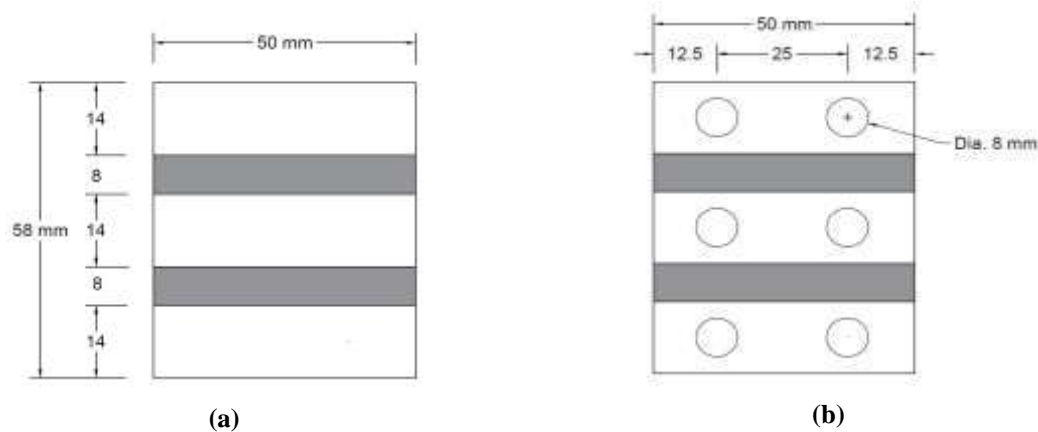
Fig. 4. Sketch of the damper units: a) Front view; and b) Side view

As can be seen in Figures 3 and 4, each unit consisted two layers of rubber pads attached to three metal sheets. The rubber pads were separately vulcanized and bonded to the metal sheets using a cold bonding agent. Threaded holes with diameters of 8 mm were drilled on the opposite sides of the metal sheets to provide support for connecting the inner and outer metal plates of the dampers.

Figure 5 shows the damper assembly and the manner in which the damper unit was attached to the universal fatigue-testing machine. An inner extending Plate (A), was bolted to the inner plate of the damper unit, whereas two outer extending Plates (B), were connected to the outer plates of the damper unit via four bolts (D). To ensure that the damper unit was subjected to pure shear, Plate (C) as an interface plate was inserted between outer Plate B via two E

bolts, such that it was perfectly aligned with Plate A. The wedge Grips F of the testing machine were clamped to the roughened ends of Plates A and C. The tensile and compressive forces applied to the specimen via Grips F are transferred to the rubber pads of the damper unit as reciprocating (cyclic) shear forces. Figure 6 shows the images of one of the viscoelastic damper specimens connected to extending Plates A and B, as well as interface Plate C.

Owing to the ability to assemble and disassemble the setup shown in Figures 5 and 6, only one set of Plates A, B and C, was fabricated for all tests conducted in this study. Each of the prototype dampers in this study could be assembled in the aforementioned setup and placed in the fatigue testing machine to perform cyclic shear loading tests.
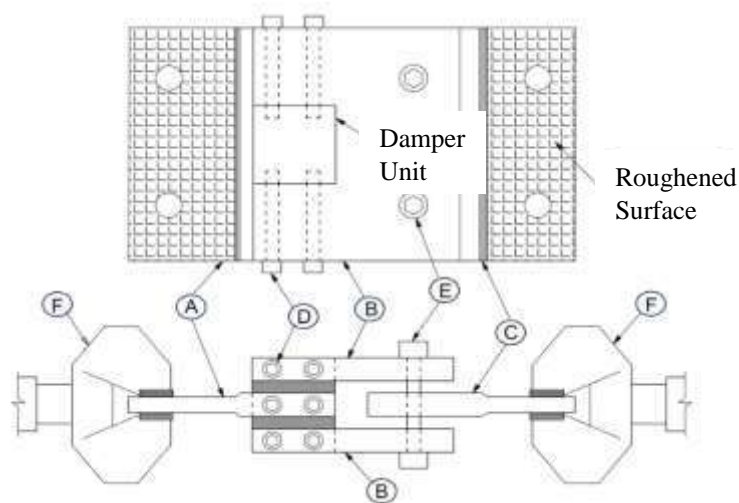
Fig. 5. Components of damper assembly (plan and side views)
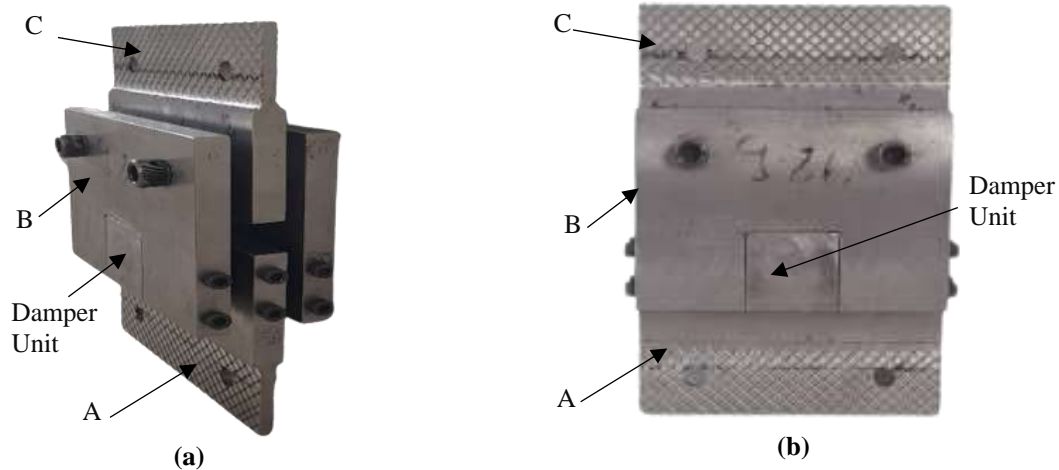
Fig. 6. Assembly of prototype viscoelastic damper: a) 3D view; and b) Front view

Owing to the payload capacity limitations of the test machine, the viscoelastic dampers used in this study were fabricated on a scale of 1:5. It was assumed that by installing supplemental dampers, the performance of the structure would be improved and the story drift ratio would be limited to a maximum of 1% for a Design Basis Earthquake (DBE). Additionally, it was assumed that the damper was installed on rigid chevron bracing; thus, its deformation remained the same as the story drift of the structure. For a typical full-scale story height of 3 m, the displacement amplitude imposed on the damper at the DBE risk level was 30 mm. The corresponding damper displacement was 6 mm, at a scale of 1:5 based on the principles of similitude law (Kahrizi et al., 2022). If the shear strain of the rubber pads of the damper at this displacement level is limited to 75%, the required thickness of the rubber pads is calculated to be 8 mm. Based on these calculations, the rubber pad thickness within the damper was determined to be 8 mm (Figure 4).

3. Test Protocol and Viscoelastic Response Evaluation

Cyclic shear tests were conducted at ambient temperature to evaluate the shear force-displacement hysteresis loops of the damper specimens and calculate their effective stiffness and damping properties corresponding to various shear strain levels.

Given a target displacement of 8 mm at the DBE, the test protocol included the following stages (ASCE/SEI7, 2017):

i) 10 fully reversed load cycles with a displacement amplitude of 4 mm equivalent to 0.67 times the target displacement at the DBE hazard level.

ii) 5 fully reversed load cycles with a displacement amplitude of 8 mm equivalent to 1.33 times the target displacement at the DBE hazard level.

iii) 3 fully reversed load cycles with a displacement amplitude of 12 mm equivalent to 2 times the target displacement at the DBE hazard level.

Figure 7 shows the time history of sinusoidal input displacements, which is consistent with the loading protocol mentioned above. Input displacements were applied to the prototype dampers with different frequencies in individual test runs.

After the aforementioned cyclic tests were performed, the shear force-displacement curves of the dampers were evaluated. Using the Kelvin solid model, the reaction force in a viscoelastic damper $F(t)$, which is affected by displacement $u(t)$ and velocity $u(t)$, can be obtained from Eq. (1) (Christopoulos and Filiatrault, 2006).

$$F(t) = Ku(t) + Cu(t) \qquad (1)$$

where, K and C: represents the effective stiffness and damping coefficient of the damper specimen, respectively. These parameters can be evaluated at each cycle of

the tests as follows:

$$K = \frac{|F^-| + |F^+|}{|\Delta^-| + |\Delta^+|} \tag{2}$$

$$C = \frac{W_D}{\pi \Delta_{ave}^2 \bar{\omega}} \tag{3}$$

where F^- and F^+: represent the peak negative and positive forces resisted by the damper during the test cycle of negative and positive peak displacement amplitudes Δ^- and Δ^+, respectively. W_D: denotes the area enclosed by the force-displacement hysteresis curve obtained for the load cycle of interest. $\bar{\omega}$: represents the excitation circular frequency, and Δ_{ave} in each load cycle is calculated as below.

$$\Delta_{ave} = \frac{|\Delta^-| + |\Delta^+|}{2} \tag{4}$$

The equivalent viscous damping ratio of the viscoelastic prototype dampers, β, at each cycle of the test can be evaluated as follows.

$$\beta = \frac{1}{2\pi} \frac{W_D}{K \Delta_{ave}^2} \tag{5}$$

The mechanical properties of viscoelastic dampers under cyclic shear loads can be determined at each cycle of the test based on the characteristics of the rubber material within the damper, that is, the storage shear modulus G_e, the shear loss modulus, $G_c \bar{\omega}$, and the loss coefficient η (Smith et al., 1983). In this case, the effect of the physical dimensions of the damper was excluded when comparing the mechanical properties of rubber materials. These parameters can be calculated using the following equations (Christopoulos and Filiatrault, 2006):

$$G_e = \frac{Kh}{A_s} \tag{6}$$

$$G_c = \frac{Ch}{A_s} \tag{7}$$

$$\eta = \frac{G_c \bar{\omega}}{G_e} \tag{8}$$

where h, A_s: are the thickness and plane area of the rubber pad of the damper, respectively. Considering that two rubber pads with the same thickness are used in parallel in the dampers in this study, parameter h is multiplied by 2 in Eqs. (6) and (7). The loss factor η calculated using Eq. (8) represents the tangent of the phase angle δ. The phase angle shows the time delay between the occurrence of the peak shear strain imposed on the rubber material and the peak shear stress experienced therein. The loss factor calculated from Eq. (8) is twice the equivalent critical damping ratio, β, calculated using Eq. (5).
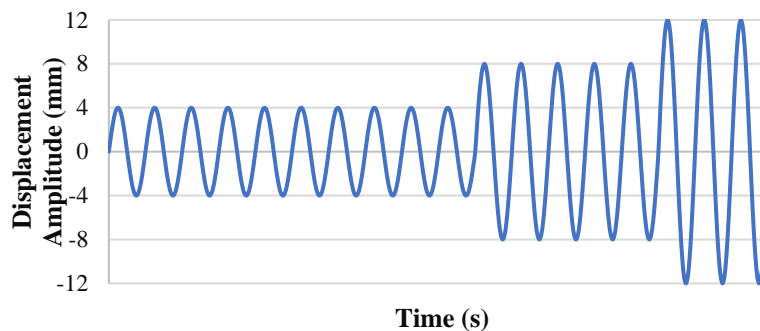
Fig. 7. Time history of input displacements during cyclic shear testing

4. Cyclic Shear Test Results and Discussion

Figure 8 shows the Dartec (UK) fatigue and tensile test machine used for the cyclic loading tests on the prototype viscoelastic dampers used in this study. The machine has a load capacity of 50 kN which can be applied at a maximum loading frequency of 100 Hz, depending on the displacement amplitude of the load cycles.

Fig. 8. Cyclic shear test setup: a) Installation of damper specimen in test machine; and b) Front view of damper under cyclic loading
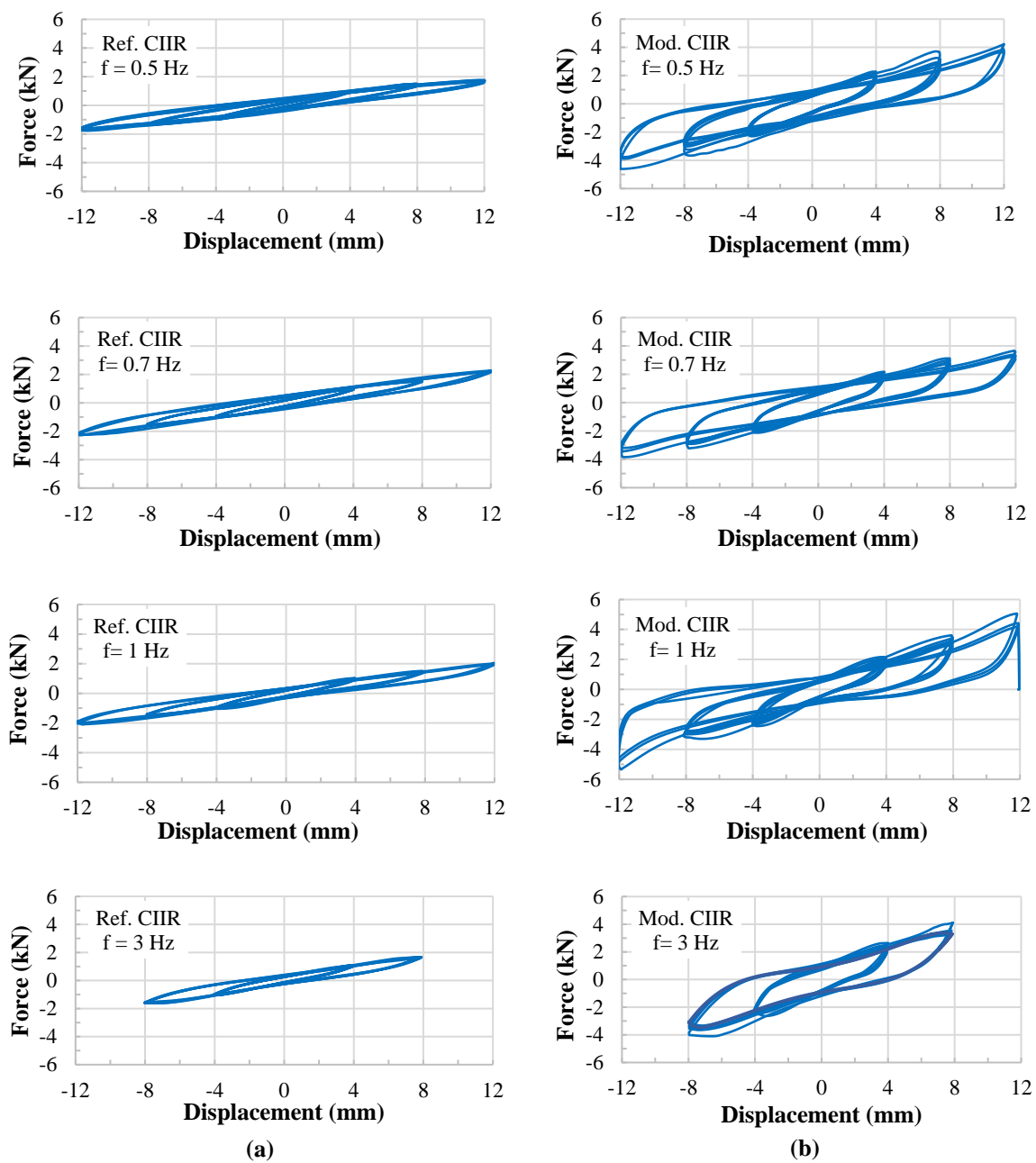
Fig. 9. Cyclic load-displacement hysteresis loops of the damper specimens at various excitation frequencies: a) Reference damper (Ref. CIIR); and b) Modified damper (Mod. CIIR)

It consists of a test frame with a movable crosshead, a piston head with interchangeable load cells and a hydraulic unit that supplies the pressure for the actuator. Given the payload capacity of the test machine, the sinusoidal displacements of the protocol shown in Figure 6 with target displacement amplitudes of 4, 8, and 12 mm, were applied at frequencies of 0.5, 0.7, 1, and 3 Hz.

Moreover, owing to test machine limitations, it was not possible to apply load cycles of different displacement amplitudes in a single test run. Therefore, displacement cycles of the same amplitude were applied individually to the test specimens. The test machine is capable of measuring the axial force and relative displacements of its two jaws in real time. The output of load cell and displacement transducers were recorded by a dynamic data logger at a frequency rate of 50 Hz. All of the tests were performed at room temperature (24 °C).

The force-displacement hysteresis loops of the prototype dampers under fully reversed cycles of shear loading at different excitation frequencies from 0.5 Hz to 3 Hz are shown in Figure 9. At a frequency of 3 Hz, owing to the payload capacity limitation of the testing machine, it was not possible to apply a displacement amplitude of 12 mm and the damper specimens were loaded with this frequency only in the range of 4-8 mm.

Cyclic shear testing of the second specimen of each damper type yielded similar results to those obtained for the first specimen. The variations in the dynamic response parameters (effective stiffness, damping coefficient, and equivalent viscous damping ratio) evaluated for the two specimens of each damper type were less than 10%. This verifies the repeatability of the dynamic response characteristics of each damper type. The damper specimens were visually inspected at the end of each test run to detect physical damage. No significant physical damage was observed in the damper specimens during the testing.

As shown in Figure 9, at all excitation frequencies, the reaction force and area enclosed by the force-displacement hysteresis loops of the modified damper employing Mod. CIIR rubber material was significantly larger than the reference damper. An increase in the reaction force implies an increase in the effective stiffness of the damper in each test cycle. In addition, an increase in the enclosed area of the hysteresis loops indicates the superior energy-dissipation capability of the modified damper.

Figures 10 to 12 show the variations in the shear storage modulus, G_e, shear loss modulus, $G_c\overline{\omega}$, and loss factor, η, of the rubber material of the two damper types with the shear strain amplitude for different excitation frequencies.

Tables 2 and 3 provides the numerical values of the parameters. The viscoelastic parameters shown in these tables and Figures 10-12 represent the average values of the load cycles applied at each displacement amplitude. Parameters G_{e0}, G_{c0} and η_0 in Figures 10-12 represent the average values for the Reference Chlorobutyl Rubber (Ref. CIIR), and likewise G_e, G_c, and η indicate the corresponding values of the Modified Chlorobutyl Rubber (Mod. CIIR). An inspection of Figures 10a and 10b indicates that the shear storage modulus in the modified rubber has a significant increase (at least 100%) compared to the reference rubber.

In both types of rubber materials, at a constant excitation frequency, the shear storage modulus, G_e, decreased with increasing shear strain. This behavior is consistent with the results of previous studies, e.g. Vasina et al. (2021). As shown in Figure 10, the rate of variation of the shear storage modulus with shear strain was similar for both types of rubber materials investigated in this study. By tripling the shear strain (from 0.5 to 1.5), the storage modulus in rubber materials decreases by approximately 30%. According to Figure 10, the shear storage modulus generally increases with increasing excitation frequency.
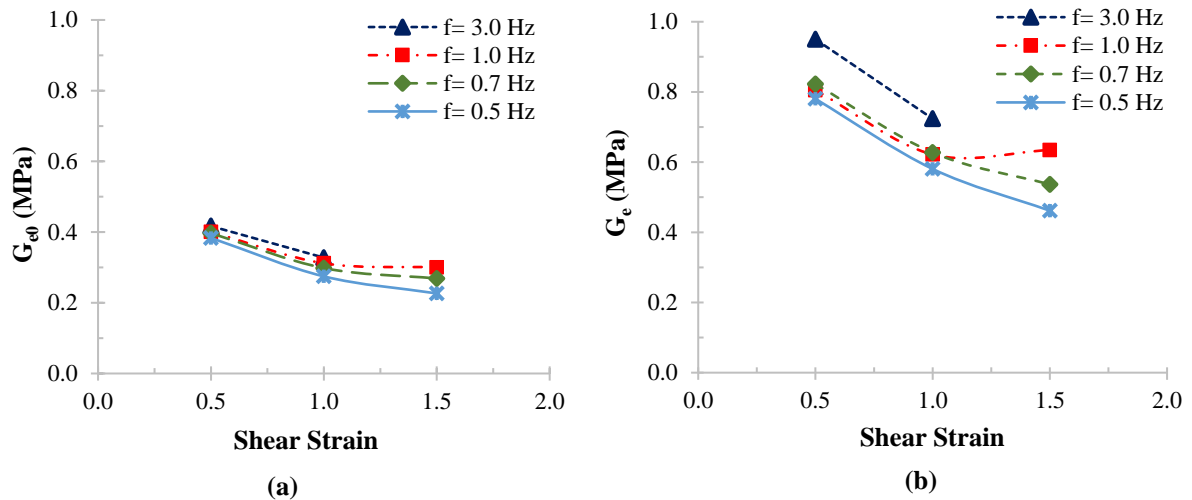
Fig. 10. Variations of shear storage modulus with shear strain at different excitation frequencies: a) Ref. CIIR and b) Mod. CIIR
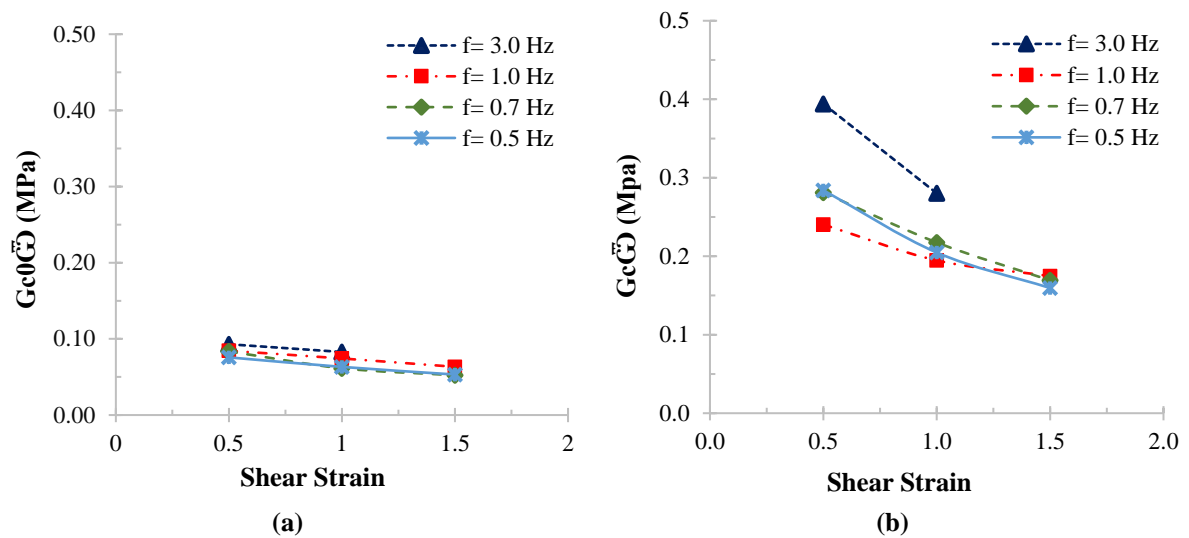
Fig. 11. Variations of shear loss modulus with shear strain at different excitation frequencies: a) Ref. CIIR; and b) Mod. CIIR
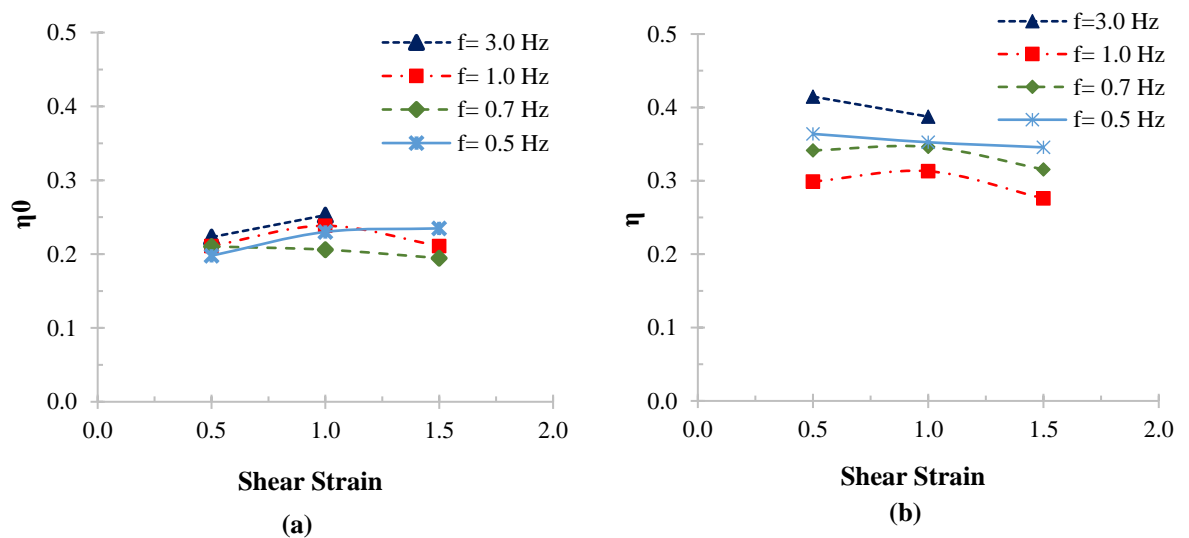
Fig. 12. Variations of loss factor with shear strain at different excitation frequencies: a) Ref. CIIR; and b) Mod. CIIR

Table 2. Viscoelastic properties of reference CIIR

f (Hz)	Amplitude (mm)	G_e (MPa)	$G_c\bar{\omega}$	η
	4	0.38	0.06	0.15
0.5	8	0.27	0.06	0.23
	12	0.23	0.05	0.23
	4	0.40	0.08	0.21
0.7	8	0.31	0.07	0.24
	12	0.30	0.06	0.21
	4	0.40	0.08	0.21
1	8	0.30	0.06	0.21
	12	0.27	0.05	0.19
3	4	0.42	0.09	0.22
	8	0.33	0.08	0.25

Table 3. Viscoelastic properties of modified CIIR

f (Hz)	Amplitude (mm)	G_e (MPa)	$G_c\bar{\omega}$	η
	4	0.82	0.28	0.34
0.5	8	0.63	0.22	0.35
	12	0.54	0.17	0.32
	4	0.78	0.28	0.36
0.7	8	0.58	0.20	0.35
	12	0.46	0.16	0.35
	4	0.80	0.24	0.30
1	8	0.62	0.19	0.31
	12	0.63	0.17	0.28
3	4	0.95	0.39	0.41
	8	0.72	0.28	0.39

The influence of excitation frequency (up to 1 Hz) on the storage modulus of the studied rubber materials at strains of 0.5 and 1 is not significant. At a shear strain of 1.5, the influence of excitation frequency on the shear storage modulus was more noticeable.

In this strain range, the shear storage modulus increased by 32% in the reference rubber and by 37% in the modified rubber with an increase in the excitation frequency from 0.5 Hz to 1 Hz. At the loading frequency of 3 Hz, the shear storage modulus of the modified rubber increased significantly.

At a strain of 0.5, the shear storage modulus of this rubber increased by about 16% from 0.82 MPa at an excitation frequency of 1 Hz to 0.95 MPa at an excitation frequency of 3 Hz. The variation in the shear storage modulus of the reference rubber at an excitation frequency of 3 Hz was not significant compared to other previous lower frequencies. Figure 11 shows the variations in the shear loss modulus with the shear strain applied to rubber materials at different excitation frequencies.

Comparing Figures 11a and 11b, it can be seen that, overall, the shear loss modulus of the modified rubber was approximately three times that of the reference rubber. This revealed that the modifications made to the compound of the reference rubber effectively resulted in a significant increase in the energy dissipation capability of the rubber material. For both rubber types, the shear loss modulus decreased with increasing shear strain. Compared to the reference rubber, the shear loss modulus of the modified rubber was found to be relatively more sensitive to the excitation frequency. A significant increase (approximately 40%) in the shear loss modulus of the modified rubber was observed at an excitation frequency of 3 Hz.

The variations in the loss factor, η, of the rubber materials with the amplitude of shear strain at different excitation frequencies are shown in Figure 11. The loss factor represents the tangent of the phase angle (time lag) between the peak shear stress and the shear strain in the

rubber material at each load cycle. The loss factor values for each test cycle were calculated using Eq. (8). Given the definition of η in Eq. (8) and the decreasing trend of G_e and $G_c\bar{\omega}$ with increasing shear strain for the strain range of 0.5 to 1.5, the loss factor exhibited insignificant variations with shear strain.

Overall, the loss factor in the examined rubber materials at different excitation frequencies varied by $\pm 15\%$ compared with the excitation frequency of 0.5 Hz. At an excitation frequency of 3 Hz, the modified rubber exhibited the highest loss factor. The effective stiffness, K, of the devices can be deduced from Eq. (6). Experimental results demonstrated a substantial enhancement in the stiffness of the modified damper compared to the reference damper. For instance, at the minimal test excitation frequency of 0.5 Hz, the effective stiffness of the reference damper was estimated to range from 0.24 kN/mm (at a displacement amplitude of 4 mm) to 0.14 kN/mm (at a displacement amplitude of 12 mm). In contrast, the modified damper exhibited stiffness values of 0.57 kN/mm and 0.37 kN/mm, respectively, representing an increase of 138% to 164%. Similar enhancements in stiffness properties were observed for the modified damper under cyclic tests with varying excitation frequencies. At the maximal test frequency of 3.0 Hz, the average effective stiffness of the reference damper was calculated to be 0.23 kN/mm, while the modified damper demonstrated an average stiffness of 0.59 kN/mm, marking an approximate increase of 157%. Eq. (7) may be solved for the damping coefficient, C, of the devices. The average damping coefficient for both the reference and modified dampers, at the lowest test excitation frequency of 0.5 Hz, was found to be 0.011 kN.s/mm and 0.051 kN.s/mm, respectively. However, at the highest test frequency of 3.0 Hz, the average damping ratio for the reference damper was determined to be 0.003 kN.s/mm. In contrast, the modified damper exhibited an average damping ratio of 0.013

kN.s/mm, indicating an approximate increase of 333%.

As shown in Figures 10-12, the viscoelastic properties of the modified rubber were significantly higher than those of the reference rubber. Figure 13 shows the ratio of the viscoelastic parameters of the modified rubber to those of the reference rubber at various excitation frequencies under different shear strains.

According to this figure, the ratios of G_e/G_{e0}, G_c/G_{c0}, and η/η_0 depending on the excitation frequency and shear strain amplitude experienced by the rubber material were between 2 to 2.3, 2.6 to 4.3, and 1.3 to 1.9, respectively. An examination of Figure 13 indicates that the ratio of the shear storage moduli of the rubber materials (G_e/G_{e0}) showed the least sensitivity to the excitation frequency and shear strain amplitude.

The ratio of shear loss moduli (G_c/G_{c0}) and loss factors (η/η_0) of the rubber materials did not follow a specific variation with excitation frequency. However, these ratios decreased with an increase in shear strain amplitude.

5. Summary and Conclusions

The main objective of this study was to modify the formulation of a CIIR compound to improve its damping properties under low excitation frequencies at room temperature. The modified rubber was designed as supplemental viscoelastic damper devices to mitigate the earthquake response of building structures. Therefore, by modifying the formulation of the original rubber compound (also referred to as CIIR), a new compound called modified CIIR was prepared, in which NBR and CPE were blended with the reference chlorobutyl rubber in a new formula.

Two sets of tests were conducted to evaluate the viscoelastic characteristics of the rubber. First, the DMTA tests under dynamic tension were performed at a frequency of 1 Hz. Next, cyclic shear tests were conducted on individual prototype

viscoelastic dampers made of the reference and modified rubber materials. Cyclic shear tests were performed at shear strain amplitudes of 0.5, 1.0 and 1.5, under excitation frequencies of 0.5, 0.75, 1.0, and 3 Hz.
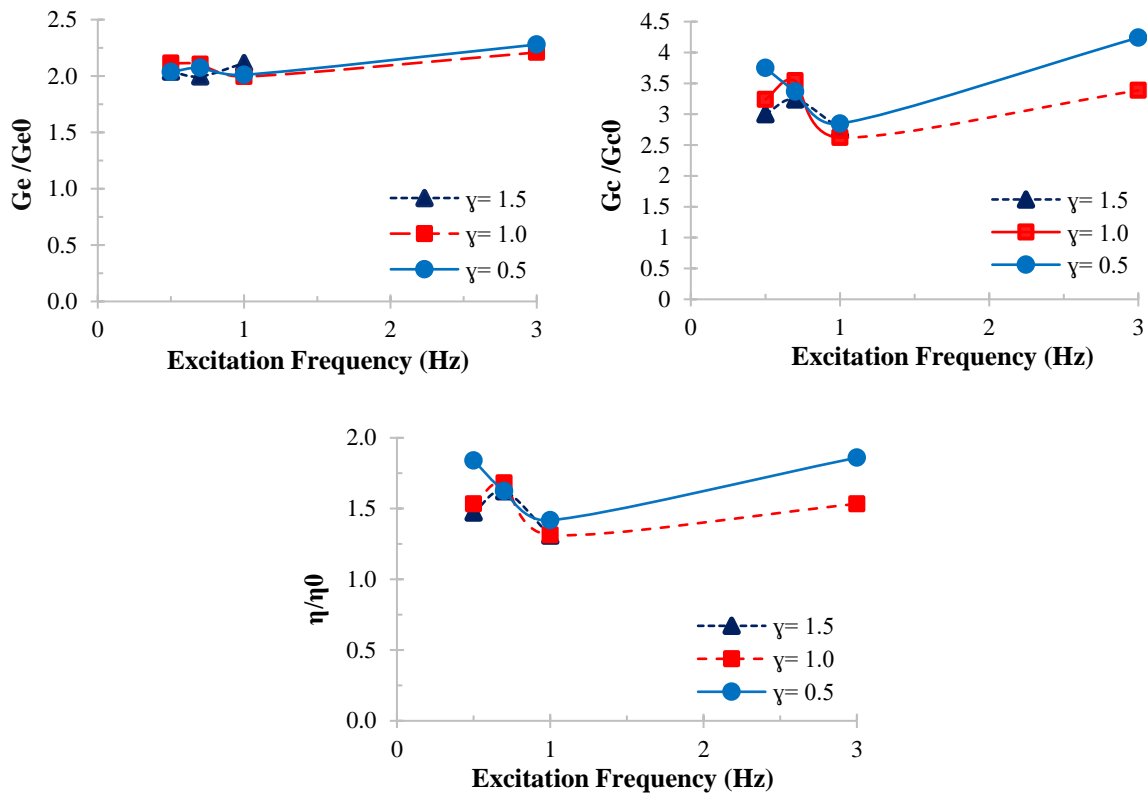
Fig. 13. Variations of the ratio of viscoelastic properties of the modified rubber to the reference rubber with the excitation frequency and shear strain amplitude

The main results obtained from the DMTA tests include:

- In a blend of CIIR and NBR, the magnitude of the loss factor (tanδ), which indicates damping, increased significantly in the positive temperature range and reached a maximum value of approximately 0.5. The variations in tanδ with temperature indicated two peak values at -45 °C and +25 °C. The minimum value of tanδ that occurred at a temperature close to 0 °C was approximately 40% lower than its absolute peak value. The significant variations in tanδ between the two peak values indicated the incompatible polarity of the blended rubber.

- With the use of CPE as an intermediate material in the modified rubber compound, a more polar compatibility was achieved between CIIR and NBR. The two peak values of tanδ occurred at larger temperature intervals (from -50 °C to 30 °C). The modified rubber exhibited a more uniform tanδ over this temperature interval, with a maximum variation of -20% compared to its absolute peak value of 0.5.

The main results obtained from the cyclic shear tests with strain amplitudes ranging from 0.5 to 1.5 and excitation frequencies ranging from 0.5 to 3.0 Hz are as follows:

- The shear storage modulus of the modified CIIR increased on average between 100% and 130% compared to that of the reference CIIR.

- The average shear loss modulus of the modified CIIR increased between 160% and 330% compared to that of the reference CIIR.

- The loss factor, η, of the modified CIIR on average ranged between 0.3 and 0.4, that is, an increase of approximately 30% to 90% compared to the values obtained for the reference CIIR.

- Overall, the viscoelastic parameters of both rubber types exhibited a similar trend of variation with excitation frequency and shear strain amplitude.

The results of this experimental study suggest that the modified CIIR with improved stiffness and damping properties can be effectively used in the fabrication of supplemental viscoelastic damper devices for seismic mitigation of building structures.

6. Data Availability Statement

The experimental data that supports the findings of this study is available from the corresponding author upon reasonable request.

7. Acknowledgements

8. References

Achenbach, M. and Duarte, J. (2003). "A finite element methodology to predict age-related mechanical properties and performance changes in rubber components", *Constitutive Models for Rubber*, (pp. 59-70).

Alhasan, A.A., Vafaei, M. and Ali, S.C. (2023). "Use of silicon rubber as a viscoelastic material in dampers", *IOP Conference Series, Earth and Environmental Science*, https://doi.org/10.1088/1755-1315/1205/1/012047.

ASCE/SEI7. (2017). *Seismic evaluation and retrofit of existing buildings*, ASCE Standard, ASCE/SEI, 41-17, American Society of Civil Engineers, Reston, Virginia, https://doi.org/10.1061/9780784414859.

ASTM. (2015). *Standard test method for plastics, Dynamic mechanical properties, in tension*, In ASTM D5026, American Society for Testing and Materials, PA, United States, https://doi.org/10.1520/D5026-15.

Capps, R.N. and Beumel, L.L. (1990). *Dynamic mechanical testing*, Application of polymer development to constrained-layer damping, ACS Publications, https://doi.org/10.1021/bk-1990-0424.ch004.

Castaldo, P. and De Iuliis, M. (2014). "Optimal integrated seismic design of structural and viscoelastic bracing-damper systems", *Earthquake Engineering and Structural Dynamics*, 43(12), 1809-1827, https://doi.org/10.1002/eqe.2425.

Christopoulos, C. and Filiatrault, A. (2006). *Principles of passive supplemental damping and seismic*, IUSS Press, Pavia, Italy.

Fazli Shahgoli, A., Zandi, Y., Rava, A., Baharom, S., Paknahad, M., Ahmadi, M. and Wakil, K. (2021). "Estimation of the most influential parameters affecting the rotary braces damper", *Iranian Journal of Science and Technology, Transactions of Civil Engineering*, 45, 2463-2475, https://doi.org/10.1007/s40996-02000551-1.

Ge, T., Xu, Z.D. and Yuan, F.G. (2022). "Development of viscoelastic damper based on NBR and organic small-molecule composites", *Journal of Materials in Civil Engineering*, 34(8), 04022192, https://doi.org/10.1061/(ASCE)MT.1943-5533.0004339.

Ghotb, M. and Toopchi-Nezhad, H. (2019). "A feasibility study on pre-compressed partially bonded viscoelastic dampers", *Engineering Structures*, 201, 109796, https://doi.org/10.1016/j.engstruct.2019.109796.

Hanhi, K., Poikelispaa, M. and Tirila, H. (2020). *Elastomeric materials*, Tampere University of Technology, Tampere.

He, Z., Shi, F., Lin, Z., Zhang, C., Zhou, Y. and Zhao, F. (2023). "Experimental characterization on cyclic stability behavior of a high-damping viscoelastic damper", *Construction and Building Materials*, 371, 130749, https://doi.org/10.1016/j.conbuildmat.2023.130749.

Hujare, P.P. and Sahasrabudhe, A.D. (2014). "Experimental investigation of damping performance of viscoelastic material using constrained layer damping treatment", *Procedia Materials Science*, 5, 726733, https://doi.org/10.1016/j.mspro.2014.07.321.

Jose, S.T., Anand, A.K. and Joseph, R. (2009). "EPDM/CIIR blends, improved mechanical properties through procuring", *Polymer Bulletin*, 63, 135-146, https://doi.org/10.1007/s00289-009-0073-8.

Kahrizi, E., Aghayari, R., Bahrami, M. and Toopchi-nezhad, H. (2022). "On compressive stress-strain behavior of standard half-scale concrete masonry prisms", *Civil Engineering Infrastructures Journal*, 55(2), 293-307, https://doi:10.22059/CEIJ.2022.324782.1758.

Landel, R.F. and Nielsen, L.E. (1993). *Mechanical properties of polymers and composites*, CRC Press.

Liu, C., Fan, J. and Chen, Y. (2019). "Design of regulable chlorobutyl rubber damping materials with high-damping value for a wide temperature range", *Polymer Testing*, 79, 106003, https://doi.org/10.1016/j.polymertesting.2019.106003.

Liu, Z., Wang, Y., Huang, G. and Wu, J. (2008). "Damping characteristics of chlorobutyl rubber/poly (ethyl acrylate)/piezoelectric ceramic/carbon black composites", *Journal of Applied Polymer Science*, 108(6), 3670-3676, https://doi.org/10.1002/app.27141.

Lu, X., Li, X. and Tian, M. (2014). "Preparation of high damping elastomer with broad temperature and frequency ranges based on ternary rubber blends", *Polymers for Advanced Technologies*, 25(1), 21-28, https://doi.org/10.1002/pat.3199.

Mark, J.E., Erman, B. and Roland, M. (2013). *The science and technology of rubber*, Academic Press.

Modhej, A. and Zahrai, S.M. (2020). "Experimental study of High Axial Damping Rubber (HADR) in new viscoelastic dampers", *Journal of Testing and Evaluation*, 48(6), 4387-4401, https://doi.org/10.1016/j.istruc.2020.12.033.

Modhej, A. and Zahrai, S.M. (2021). "Numerical study of visco-hyperelastic damper with high axial damping rubber subjected to harmonic loading", *Structures*, 29, 1550-1561, https://doi.org/10.1520/JTE20180104.

Modhej, A. and Zahrai, S.M. (2022). "Cyclic testing of a new visco-plastic damper subjected to harmonic and quasi-static loading", *Structural Engineering and Mechanics,* 81(3), 317333, https://doi.org/10.12989/sem.2022.81.3.317.

Montgomery, M. and Christopoulos, C. (2015). "Experimental validation of viscoelastic coupling dampers for enhanced dynamic performance of high-rise buildings", *Journal of Structural Engineering*, 141(5), 04014145, https://doi.org/10.1061/(ASCE)ST.1943-541X.0001092.

Nikravesh, F. and Toopchi-Nezhad, H. (2022). "Application of viscoelastic tuned mass dampers in vibration mitigation of steel joist jack arch floor structures", *Shock and Vibration*, 2022(1), 5196600, https://doi.org/10.1155/2022/5196600.

Ramakrishna, U. and Mohan, S. (2020). "Performance of low-cost viscoelastic damper for coupling adjacent structures subjected

dynamic loads", *Materials Today, Proceedings*, 28, 10241029, https://doi.org/10.1016/j.matpr.2019.12.343.

Shu, Z., You, R. and Zhou, Y. (2022). "Viscoelastic materials for structural dampers, A review", *Construction and Building Materials*, 342, 127955, https://doi.org/10.1016/j.conbuildmat.2022.127955.

Smith, G., Bierman, R. and Zitek, S. (1983). "Determination of dynamic properties of elastomers over broad frequency range", *Experimental Mechanics*, 23, 158-164, https://doi.org/10.1007/BF02320404.

Suntako, R. (2017). "The rubber damper reinforced by Modified Silica Fume (MSF) as an alternative reinforcing filler in rubber industry", *Journal of Polymer Research*, 24, 17, https://doi.org/10.1007/s10965-017-1293-5.

Taleshian, H.A., Roshan, A.M. and Amiri, J.V. (2022). "Seismic pounding mitigation of asymmetric-plan buildings by using viscoelastic links", *Structures*, https://doi.org/10.1016/j.istruc.2021.11.036.

Therattil, S.J., Kuzhuppully, A.A. and Rani, J. (2008), "Compatibility studies on sulphur cured EPDM/CIIR blends", Iranian Polymer Journal, 17(6), 419-430.

Tsai, C. (1994). "Temperature effect of viscoelastic dampers during earthquakes", *Journal of Structural Engineering*, 120(2), 394-409, https://doi.org/10.1061/(ASCE)07339445(1994)120:2(394).

Vasina, M., Poschl, M. and Zadrapa, P. (2021). "Influence of rubber composition on mechanical properties", *Manufacturing Technology*, 21(2), 260-268, https://doi.org/10.21062/mft.2021.021.

Wei, W., Tan, P., Yuan, Y. and Zhu, H. (2019). "Experimental and analytical investigation of the influence of compressive load on rate-dependent high-damping rubber bearings", *Construction and Building Materials*, 200(10 March), 26-35, https://doi.org/10.1016/j.conbuildmat.2018.12.086.

Xia, L., Li, C., Zhang, X., Wang, J., Wu, H. and Guo, S. (2018). "Effect of chain length of polyisobutylene oligomers on the molecular motion modes of butyl rubber, damping property", *Polymer*, 141, 70-78, https://doi.org/10.1016/j.polymer.2018.03.009.

Xiang, Y. and Xie, H.R. (2021). "Probabilistic effectiveness of visco-elastic dampers considering earthquake excitation uncertainty and ambient temperature fluctuation", *Engineering Structures*, 226, 111379, https://doi.org/10.1016/j.engstruct.2020.111379.

Xu, Y., Xu, Z., Guo, Y., Huang, X., Dong, Y. and Li, Q. (2021). "Dynamic properties and energy dissipation study of sandwich viscoelastic damper considering temperature influence",

Buildings, 11(10), 470, https://doi.org/10.3390/buildings11100470.

Zhang, F., He, G., Xu, K., Wu, H. and Guo, S. (2015). "The damping and flame-retardant properties of poly (vinyl chloride)/chlorinated butyl rubber multilayered composites", *Journal of Applied Polymer Science*, 132(2), https://doi.org/10.1002/app.40464.

Zhang, F., He, G., Xu, K., Wu, H., Guo, S. and Zhang, C. (2014). "Damping mechanism and different modes of molecular motion through the glass transition of chlorinated butyl rubber and petroleum resin blends", *Journal of Applied Polymer Science*, 131(13), https://doi.org/10.1002/app.41259.

TECHNICAL NOTE

Construction Pre and Post Analyses of Air Quality Parameters (PM$_{2.5}$, PM$_{10}$ and CO) and Noise Levels: A Case Study of Lal Shahbaz Qalandar Underpass, Lahore, Pakistan.

Urmia, A.[1] , Saman, S.[2*]

[1] M.Sc., Department of Civil Engineering, National University of Computer and Emerging Sciences (NUCES), FAST Lahore Campus.
[2] Professor, Department of Sciences and Humanities, NUCES -FAST Lahore Campus

© University of Tehran 2023

ABSTRACT: Daily high traffic loads were reported at junctions, resulting in increased fuel consumption and air pollution at the Lal Shahbaz Qalandar underpass in Lahore. The post-EIA monitoring of Carbon Monoxide (CO), Particulate Matter (PM$_{2.5}$ / PM$_{10}$) and noise levels were done near Lal Shahbaz Qalandar Underpass in four different seasons. Pre-EIA (Environment Impact Assessment) monitored levels of CO, PM$_{2.5}$, and PM$_{10}$ of the underpass were used for the comparison. Sensor MQ7 was used for monitoring CO levels in the air, and HT608 air quality detector gas checker tester environmental meter was used to monitor particulate matter 2.5 and 10. BeneTech GM1356 digital sound level meter was used for noise level monitoring. For southwest monsoon and winter seasons, CO emissions exceeded the limit for the post-EIA phase (from 7.85 to 8.96 mg/m^3). PM$_{2.5}$ emissions exceeded the normal range both during pre/post-EIA phases. In all seasons, their emissions were constantly increasing (from 40-49 mg/m^3) to the pre-EIA phase. Similarly, PM$_{10}$ emissions exceeded the normal range during pre/post-EIA phases. In all seasons, their emissions have constantly been increasing (from 152-160 g/m^3) during the pre-EIA phase. In the pre-EIA phase, the noise level was 81 dB(A), whereas, during the post-EIA phase, the noise level range was from 85-96 dB(A) with a maximum in spring. A significant difference existed for PM$_{2.5}$ and PM$_{10}$ between pre-EIA data with post-EIA data. The general trend reveals that carbon monoxide, PM$_{2.5}$ and PM$_{10}$ emissions are rising. Poor quality car fuel, unnecessary honking, increased automobile sales, new car manufacturers in Pakistan, very little use of efficient vehicles, and very few public transportation options are the causes of rising air pollution and noise levels following the completion of this underpass's megaproject. The optimal solution to ease traffic congestion and conflicts is to build another underpass/flyover at the next intersection.

Keywords: Traffic Pollution, Carbon Monoxide, Particulate Matter 2.5, Particulate Matter 10, Underpass, Post-Environmental Impact Assessment (EIA)

1. Introduction

The approach to Environmental Impact Assessment (EIA) is critical to any systematic management or environmental sciences practice. The process used to evaluate the project's social, environmental, and political ramifications is known as EIA.

---

* Corresponding author E-mail: drshahidsaman@gmail.com

It is a method of anticipating any project's effects before it is built, whereas post-project EIA analysis helps analyze the accuracy of such estimations suggested in the pre-EIA phase (Loomis et al., 2018).

Post-Project Analysis (EIA-PPA) within the EIA process may be understood as a method of monitoring and analyzing the actual environmental effect of projects that were examined in the EIA process during planning and authorization (Zitkova et al., 2022). All development projects must undertake an EIA before they can be facilitated. The ADB (Asian Development Bank), World Bank, and UNEP (United Nations Environment Program) have mentioned regulations for EIA processes. In Pakistan, the Environmental Protection Ordinance (PEPO) rules for legal EIA significance. The benefits of the EIA procedure should be clarified by confirming stakeholder interests, carrying out a post-EIA review, giving environmental agencies resources and assuring openness (Ehtasham et al., 2022).

The environmental impact assessment is a very beneficial tool that is significantly used to diagnose the economic, environmental and social impacts of purposed projects before decision-making. The process starts with the selection of a project based on sustainable development to assure that the disadvantages of the new projects were mitigated or controlled through intelligent decision-making. For many years EIA has not been taken seriously in South Asian countries in the world. Developing countries need more development programs to enhance their economic growth (Shah et al., 2010; Babu, 2016).

All across the world, flyovers and underpasses are utilized to control traffic flow. Road traffic contributes to air and noise pollution in metropolitan areas, which has a detrimental influence on human health. Therefore, pre and post-EIA are very much important for projects involving flyovers and underpasses. Abbasi et al. (2021) assessed the environmental impacts

of the Tariq Road underpass at the construction site in Karachi. It was identified that much improvement is required in terms of health, safety and environmental aspects.

The Kano State Ministry of Works, Housing, and Transport in Nigeria conducted an EIA and suggested the building of the Gadon Kaya Underpass Bridge. The project's purpose was to eliminate the identified urban mobility issues that had hampered the region's social and environmental health. The immediate ramifications of the project involved the construction and direct usage of an underpass bridge. The most significant consequences addressed in this study were clearing, grading and roadbed construction, other land use, cultural site damage and interference with local people's movement.

The direct effects observed were those associated with increased demand for motor fuels, incidents involving and/or displacement of non-motorized transportation methods, increased air pollution, noise, roadside litter, injury or death to animals and people attempting to crossroads and environmental harm from accidents involving hazardous materials in transit and water pollution (Nabegu, 2013).

The only way to guarantee that the development authorities abide by the rules set forth by the government concerning this construction project is to conduct a post-monitoring. With the use of post-EIA analysis reports, one can track environmental degradation and begin appropriate mitigating action. Dipper (1998) examined a wide range of literature to highlight the advantages of post-project analysis. He described the post-project study of eight building projects. Post-project activities reveal critical truths that obstruct optimistic constructions. An assessment of post-project analysis indicated that there is a lot of room to raise the visibility of post-auditing in EIA throughout the world. The term post-project analysis refers to research and supporting activities that are carried out after a project

has been built and is ready to enter the operational phase. The primary strategy for monitoring is to evaluate important environmental implications versus baseline conditions before and after the project.

There are essential elements of EIA follow-up:

I) Monitoring: Data gathering and comparison with standards, projections, or expectations.

II) Evaluation: Assessment of the activity's compliance with standards, projections, or expectations, as well as its environmental performance.

III) Management: Decision-making and appropriate action in response to concerns raised by monitoring and evaluation activities and

IV) Communication: Informing stakeholders and the broader public on the outcomes of the EIA follow-up (Pinto et al., 2019).

There are very limited studies available on Post-EIA or EIA after construction. The Lal Shahbaz Qalandar underpass in Lahore is therefore studied to compare its environmental impacts before and after construction. Firdous market chowk is located at the crossing of Ali Zaib Road and M. M. Alam Road. At intersections, high traffic volumes are observed daily.

Significant traffic volumes occur during peak hours between vehicles moving towards the center point. Firdous market which results in massive traffic jams extended up to cavalry ground resulting in consequently more fuel consumption and high noise and air pollution. The newly constructed underpass at Firdous Market is facilitating daily traffic to access the commercial hubs, offices, schools, business places and residences with reduced travel time and vehicle operating costs.

The basic aim of the study is to determine the post-environmental impacts by assessing noise levels and emissions of carbon monoxide and particulate matter ($PM_{2.5}$ and PM_{10}) from road traffic. Congestion in traffic increases vehicle emissions and negatively impacts ambient air quality and noise levels in the area. According to recent studies, traffic congestion is the leading cause of increased sickness and death among drivers and those who live near major roadways.

Traffic on roads is significantly increased in Lahore. Before the construction of the underpass at Firdous Market Chowk, the values of PM_{10} and $PM_{2.5}$ were slightly higher than the limits prescribed imposed by Punjab Environmental Quality Standards (PEQS, 2016).

The higher values were due to high traffic flow and traffic congestion at the Ferrousz Market Underpass. The ESPAK (Environmental Services Pakistan) laboratory conducted noise measurement before the construction of the Lal Shahbaz Qalandar underpass and found that it exceeded the allowable limits (both residential and commercial) as per Punjab Environmental Quality Standard (PEQS, 2016). Vehicle emissions are the primary source of air pollutants such as Carbon Monoxide (CO), Carbon Dioxide (CO_2), Sulfur Dioxide (SO_2), Nitrogen Oxides (NO), and Particulate Matter ($PM_{2.5}$, PM_{10}).

The current study conducted the post-project evaluation, which focused on the analysis of CO, $PM_{2.5}$, PM_{10} and noise levels before and after construction completion. To make sure the development authorities obey the regulations set forth by the Government of Pakistan for this project, a comparison of CO, $PM_{2.5}$, and PM_{10} as well as noise pre- and post-EIA data was done. Particulate matter is a combination of solids and liquids, drops and aerosols, and dry-solid fragments.

2. Materials and Methods

The main goal of this study is to investigate the post-environmental impacts in the form of noise and air pollution (carbon monoxide, $PM_{2.5}$ and PM_{10}) emissions. A simple random sampling method was used for this study.

2.1. Study Location

The area of the Firdous Market intersection consisted of hotels, plazas, a park, a graveyard, bus stands, institutes, petrol pumps and a water pumping station. The area also included an under-constructed grand mall. A receptor-based technique was used to sample noise levels and air pollution parameters. The monitoring was carried out at the Royal Star Hotel as it was the busiest area prior to the construction of the underpass (See Figure 1 for the land use near the underpass). The monitoring was done near the Hotel Royal Star located at 13A-J Gulberg III Ali Zaib Road Lahore which represents commercial and residential areas along the alignment.

2.2. CO, PM$_{2.5}$, and PM$_{10}$ Monitoring (Pre EIA: March 2020)

In March 2020, the ambient air quality of the project site was done by monitoring the primary pollutants i.e. CO, PM$_{2.5}$ and PM$_{10}$. The sampling locations were selected through a receptor-based approach. The sampling was conducted for 24-hour period in March 2020. One 8-hour data slot (i.e., 8.00 am – 4.00 pm) was included.

The data of pre-EIA was collected by Environmental Services Pakistan (ESPAK), Laboratory. The results indicated that the values of PM$_{10}$ and PM$_{2.5}$ were slightly higher than the limits and all other parameters are within the permissible limits of PEQS (2016) (Table 1). The higher values were due to high traffic flow and traffic congestion at the Firdous Market Intersection.

2.3. Noise Levels Monitoring (Pre EIA March 2020)

Noise level monitoring was carried out at different locations.

Fig. 1. Land use map of Lal Shahbaz Qalandar underpass

Table 1. CO, PM$_{2.5}$ and PM$_{10}$ monitoring near hotel royal star (Courtesy: Nespak laboratory Lahore) (lda, 2020)

Parameters	Unit	Allowable values (PEQS 2016 standards)	Mean concentration
CO	mg/m^3	5 mg/m^3 (8 hours)	0.94±0.35
PM$_{2.5}$	μg/m^3	35 μg/m^3 (8 hours)	36.9±7.02
PM$_{10}$	μg/m^3	150 μg/m^3 (8 hours)	150.2±13.1

Key: Exceeding allowable limits (red); within allowable limits (green)

Noise levels were monitored with the help of a potable digital sound meter at the project site for 24 hours and compared with PEQS for noise. As the area is surrounded by under-construction commercial shops so the noise levels measured during the monitoring are compared with Category B i.e., 'noise levels for commercial area' as specified under PEQS.

Therefore, 65 dB during the daytime and 55 dB during the nighttime was used as a reference standard. The average values of noise levels are given in Table 2. Noise monitoring results showed that the noise levels at day and night time exceed the permissible limits (both residential and commercial) of PEQS (2016), which may be due to noise generated by the usage of horns by vehicles, commercial activities, and traffic congestions in the project area. The pre-EIA was done by ESPAK, Lahore.

2.4. Ambient Air Quality Monitoring (Post EIA)

The monitoring point was selected at Firdous Market commercial area near Hotel Royal Star. This location represents a dense commercial activity and serves as an intersection for commuters from all directions using the project alignment. The selection of monitoring locations was based on environmental factors including the direction of the wind on a particular day and the amount of turbulence in the air etc. The noise and air quality monitoring (CO, $PM_{2.5}$, PM_{10}) for post-EIA of the project was done in four seasons on weekdays to compare the readings and give authentic results. Ambient air quality and noise levels monitoring was done for a time duration of eight hours continuously from morning 8 am to 4 pm. Monitoring activity was started on June 2021 and completed on February 2022 (Table 3). The testing of ambient air quality and noise levels was done in June 2021, September 2021, December 2021, and February 2022.

Table 2. Average values of noise levels (Nespak laboratory Lahore) (lda, 2020)

Sampling locations	Equivalent hourly mean-dba	PEQS (2016) (commercial)-dba		Peqs (2016) (residential)-dba	
Hotel Royal Star	Day time (8 hours)	Day time (0600-2200 hours)	Night time (2200-0600 hours)	Day time (0600-2200 hours)	Night time (2200-0600 hours)
	81	65	55	55	45

Table 3. Timetable for data collection for CO, $PM_{2.5}$, PM_{10} and noise levels

Season	Month	Year	Start time	End time
Summer	June	2021	8:00:00 am (87.8 °F)	4:00:00 pm (105.4 °F)
Southwest monsoon	September	2021	8:00:00 am (83.2 °F)	4:00:00 pm (95.1 °F)
Winter	December	2021	8:00:00 am (44.6 °F)	4:00:00 pm (66.2 °F)
Spring	February	2022	8:00:00 am (46.9 °F)	4:00:00 pm (68.0 °F)

Note: Temperature values are averages

2.5. Sensor Used for Measuring CO (Post EIA)

The concentration of Carbon Monoxide (CO) was monitored by placing the sensor on the trunk of the Honda Civic Turbo 2017 model. The sensor used for the estimation of the concentration of carbon monoxide is MQ-7. This sensor has a fast response and high sensitivity. It requires a +5 voltage and 150 mA power for smooth operations. The

structure of the MQ-7 gas sensor consists of a micro Al_2O_3 ceramic tube, Tin Dioxide (SnO_2) sensitive layer, a calculating electrode and a heater. All of these components are attached into a crust made of plastic and a stainless-steel net.

The heater provides necessary work conditions for the working of sensitive components of the sensor. The MQ-7 has 6 pins, 4 of which were used to fetch signals,

and the other 2 are used for giving heating current. It can detect the concentration from 10-10,000 ppm of CO in the environment. Its main components are tin dioxide (SnO_2), which is a very sensitive material with low conductivity in clean air. Because of this very interesting property when ammonia is present in the air, the conductivity of this sensor gets increased too. This immense rise in conductivity because of the presence of ammonia in the environment is different in output signals representing the concentration of ammonia through a connected computer board.

The detection range is from 5 to 500 ppm and requires 5V for its smooth operation. To record the traffic emissions accurately, the sensor device was placed on the trunk of the car in front of Hotel Royal Star. The spot was selected based on safety and accuracy. The sensing device measured carbon monoxide. The readings were represented in ppm. The ppm values were then converted to mg/m^3 to compare the values of pre-EIA. The sensing device measured vehicular pollution emission data for 8 hours. The data was collected from 8.00 am to 4.00 pm (week days). This time includes the peak hours. The data was collected for the following seasons: Summer, Southwest Monsoon, Winter and Spring. The sampling point for CO measurement was done at Firdous Market (near Hotel Royal Star).

2.6. Noise Levels Monitoring (Post EIA)

Noise levels monitoring was done at Hotel Royal Star for 8 hours continuously through BeneTech GM1356 digital sound level meter. BeneTech GM1356 digital sound level meter measures the noise level of air / environment for 8 hours. It gives the result in the form of a text file that has noise levels in units of decibels weighted average 'A' (dba). To simulate how the human ear hears, dba levels are "A" weighted using the weighting curves. This meter has accuracy up to +/- 1.5 db. It has a measurement range of 30-130 dBA. Alternating Current (AC) and Pulse Width Modulation (PWM) both signal outputs are available in this digital sound meter. To get recorded data to connect with a PC through an USB cable, then it gives real-time data analysis. The Benetech GM1356 digital sound meter measured the mean, minimum and maximum ambient sound levels in decibels.

This low-cost sound meter is designed for simple noise surveys and sound levels checked. This sound meter only needed to be turned on to begin measuring using the most common settings. Monitoring was done in four different seasons that is Summer, Southwest Monsoon, Winter and Spring, from 8:00 am to 4:00 pm (week days) near Hotel Royal Star.

2.7. Monitoring of PM$_{2.5}$ and PM$_{10}$ (Post EIA)

Monitoring of particulate matter was done by the HT608 indoor/outdoor air quality detector gas checker tester environmental meter. It monitors PM$_{2.5}$ and PM$_{10}$ in µg/m$_3$. The sensor was placed on the trunk of the Honda Civic Turbo 2017 model.

This multi-function air quality detector gives real-time and highly stable particulate matter PM$_{2.5}$ and PM$_{10}$ concentration data. It has completely customizable settings for convenience during its use (US Department of Labor, 2022). See Table 4, to record concentration data of PM$_{2.5}$ and PM$_{10}$ held it firmly in the air and then turned it on with the power button.

Table 4. Specifications of air quality detector

Specification	Measuring range	Resolving	Accuracy
PM$_{2.5}$	0-999 µg/m^3	1.0 µg/m^3	+/- 10%
PM$_{10}$	0-999 µg/m^3	1.0 µg/m^3	+/- 10%

Once the power button is turned on it started giving concentrations of air quality.

All the readings were then collected in the form of a pdf file by connecting the meter

to the computer with the help of an USB cable. Monitoring was carried out near Hotel Royal Star on week days from 8:00 am to 4:00 pm during the four distinct seasons of summer, southwest monsoon, winter and spring.

3. Results

3.1. Mean Emissions in Summer June 2021 (Post EIA)

Table 5 shows the mean emissions of CO, $PM_{2.5}$ and PM_{10} on week days in the summer season of June 2021. It can be seen that the values of carbon mono oxide were under the limit i.e. 3.58 mg/m^3, but the values of $PM_{2.5}$ and PM_{10} were 39.5 (mg/m^3) and 152.2 (mg/m^3), respectively that were exceeding the limits.

The higher values were due to high traffic flows. A significant difference (p value < 0.0001) existed for CO, between pre-EIA (March 2020) data with post-EIA (June 2021) data.

3.2. Mean Emissions in Southwest

Monsoon September 2021 (Post EIA)

Table 6 shows the mean emissions of CO, $PM_{2.5}$ and PM_{10} on week days in the Southwest Monsoon season of September 2021. It can be seen that carbon mono oxide (mean emission: 7.85 mg/m^3) has exceeded the limit. $PM_{2.5}$ and PM_{10} also gradually increased in the environment near Hotel Royal Star Lahore. The concentration of particulate matter $PM_{2.5}$ was 40.1 μg/m^3 and the concentration of particulate matter PM_{10} was 154.2 μg/m^3. A significant difference (p value < 0.0001) existed for CO, between pre-EIA (March 2020) data with post EIA (September 2021) data.

3.3. Mean Emissions in Winter December 2021(Post EIA)

Table 7 shows the mean emission of CO, $PM_{2.5}$ and PM_{10} on week days in the winter season of December 2021. It can be seen that the trend among the three gases is increasing at its extreme due to smog season in Pakistan. The value of CO was increased from 7.85 mg/m^3 to 8.96 mg/m^3.

Table 5. Mean emissions of CO, $PM_{2.5}$ and PM_{10} on week days in the summer season (June 2021)
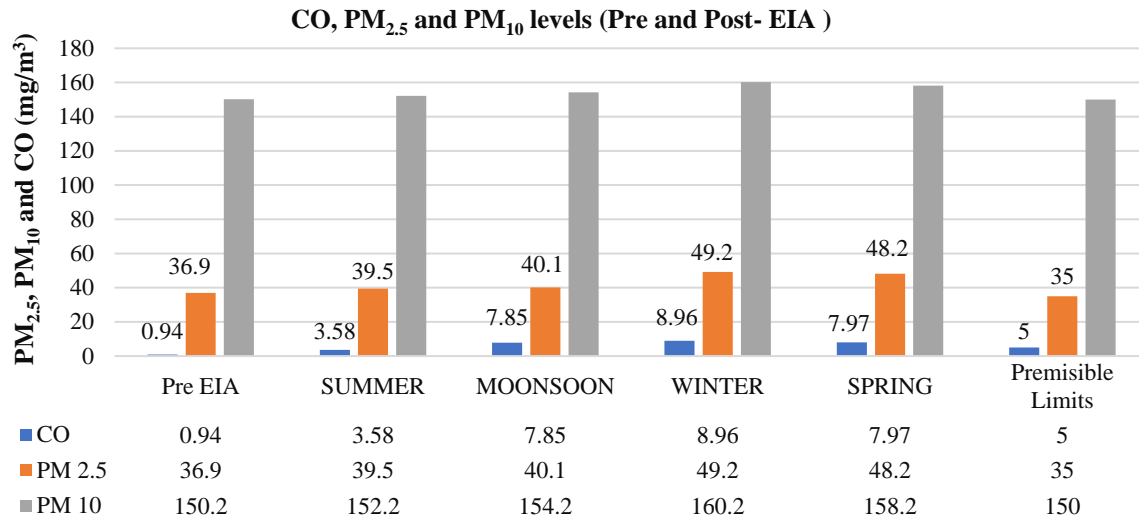
Parameters	Units	Limit values (PEQS)	Pre-EIA (march 2020) 24 readings	Post EIA mean concentration (2021) 9 readings	T-test comparisons between pre and post-EIA measurements
CO	mg/m^3	5 mg/m^3	0.94±0.35	3.58±0.6	P value < 0.0001* t = 15.75; df = 31 CI (95%): -2.98 to -2.29
$PM_{2.5}$	μg/m^3	35 μg/m^3	36.9±7.02	39.5±1.5	P value = 0.28 t = 1.09; df = 31 CI (95%) = -7.45 to 2.25
PM_{10}	μg/m^3	150 μg/m^3	150.2±13.1	152.2±3.75	P value = 0.65 t = 0.44; df = 31 CI (95%) = -11.12 to 7.12

Key: Exceeding allowable limits (red); within allowable limits (green), *Significant difference

The values of $PM_{2.5}$ and PM_{10} were 49.2 μg/m^3 and 160.2 μg/m^3, respectively. The effect of winter inversion is so visible in December as air pollution increase due to trapped air pollutants in the air. The values of CO were exceeding the limits and particulate matter was also high due to smog from brick kilns and automobile exhausts pollution and excessive traffic on the underpass. A significant difference existed for CO (p value < 0.0001), $PM_{2.5}$ (p

value < 0.0001), and PM_{10} (p value = 0.03) between pre-EIA (March 2020) data with post-EIA (December 2021) data.

3.4. Mean Emissions in Spring February 2022 (Post EIA)

Table 8 shows the mean emission of CO, $PM_{2.5}$ and PM_{10} on week days in the spring season of February 2022. The monitored emission of CO was 7.97 mg/m^3. The monitored emissions of $PM_{2.5}$ and PM_{10}

were 48.2 $\mu g/m^3$ and 158.2 $\mu g/m^3$, respectively. The emissions of gasses were lower than in December 2021 but still higher than the limits (PEQS, 2016).

A significant difference (p value < 0.0001) existed for CO, between pre-EIA (March 2020) data with post-EIA (February 2022) data. The overall trend shows that the emissions of carbon mono oxide, PM$_{2.5}$, and PM$_{10}$ have been increasing. The graphical comparison is given in Figure 2.

3.5. Noise Levels Results

The results are straightly showing an obvious increase in noise levels at Lalshahbaz Qalandar Underpass Lahore. The observed reason for the increase in noise levels is the high use of traffic horns and heavy traffic flow. Figure 3 shows a 2D column graph between seasons /month on the x-axis and noise levels in dBA on the y-axis.

Table 6. Mean emissions of CO, PM$_{2.5}$ and PM$_{10}$ on week days in the southwest monsoon season (September 2021).

Parameters	Units	Limit values (PEQS)	Pre-EIA (march 2020) 24 readings	Post EIA mean Concentration (2021) 9 reading	T-test comparisons between pre and post-EIA measurements
CO	mg/m³	5 mg/m³	0.94±0.35	7.85±0.8	P value < 0.0001* t = 34.93; df = 31 CI (95%): -7.31 to -6.50
PM$_{2.5}$	µg/m³	35 µg/m³	36.9±7.02	40.1±1.6	P value = 0.189 t = 1.34; df = 31 CI (95%): -8.06 to 1.66
PM$_{10}$	µg/m³	150 µg/m³	150.2±13.1	154.2±3.82	P value = 0.378 t = 0.89; df = 31 CI (95%): -13.12 to 5.12

Table 7. Mean emissions of CO, PM$_{2.5}$ and PM$_{10}$ on week days in the winter season (December 2021)

Parameters	Units	Limit values (PEQS)	Pre-EIA (March 2020) 24 readings	Post EIA Mean Concentration (2021) 9 readings	T-test comparisons between pre and post-EIA measurements
CO	mg/m³	5mg/m³	0.94±0.35	8.96±0.9	P value < 0.0001* t = 37.46; df = 31 CI (95%): -8.45 to -7.58
PM$_{2.5}$	µg/m³	35µg/m³	36.9±7.02	49.2±1.9	P value < 0.0001* t = 5.13; df = 31 CI (95%): -17.18 to -7.41
PM$_{10}$	µg/m³	150µg/m³	150.2±13.1	160.2±3.96	P value = 0.03* t = 2.23; df = 31 CI (95%): -19.13 to -0.86

Key: Exceeding allowable limits (red); within allowable limits (green), *Significant difference

Table 8. Mean emissions of CO, PM$_{2.5}$ and PM$_{10}$ on week days in the spring season (February 2022)

Parameters	Units	Limit values (PEQS)	Pre-EIA (march 2020) 24 readings	Post EIA Mean concentration (2021) 9 readings	T-test comparisons between pre and post-EIA measurements
CO	mg/m³	5mg/m³	0.94±0.35	7.97±0.9	P value < 0.0001* t = 32.84; df = 31 CI (95%): -7.46 to -6.59
PM$_{2.5}$	µg/m³	35µg/m³	36.9±7.02	48.2±1.7	P value = 0.26 t = 1.14; df = 31 CI (95%): -31.4 to 8.80
PM$_{10}$	µg/m³	150µg/m³	150.2±13.1	158.2±3.91	P value = 0.107 t = 1.65; df = 31 CI (95%): -17.84 to 1.84

Key: Exceeding allowable limits (red); within allowable limits (green), *Significant difference

CO, PM$_{2.5}$ and PM$_{10}$ levels (Pre and Post- EIA)

	Pre EIA	SUMMER	MOONSOON	WINTER	SPRING	Premisible Limits
CO	0.94	3.58	7.85	8.96	7.97	5
PM 2.5	36.9	39.5	40.1	49.2	48.2	35
PM 10	150.2	152.2	154.2	160.2	158.2	150

Fig 2. Chart showing CO, PM$_{2.5}$ and PM$_{10}$ levels collectively of four seasons (Post-EIA)

Note: Air pollution in winter is the highest of all seasons that is due to pollutants remaining for a longer period in the air and breathed out at a higher rate than during the summer season. Cold air is dense and moves slower than warm air. As seen in the spring season as the temperature rises air pollution also decreases.

Monitored Levels of Noise: March 2020 (pre EIA) to Feburary 2021-2022 (Post EIA) at Lal Shahbaz Qalandar Underpass, Lahore
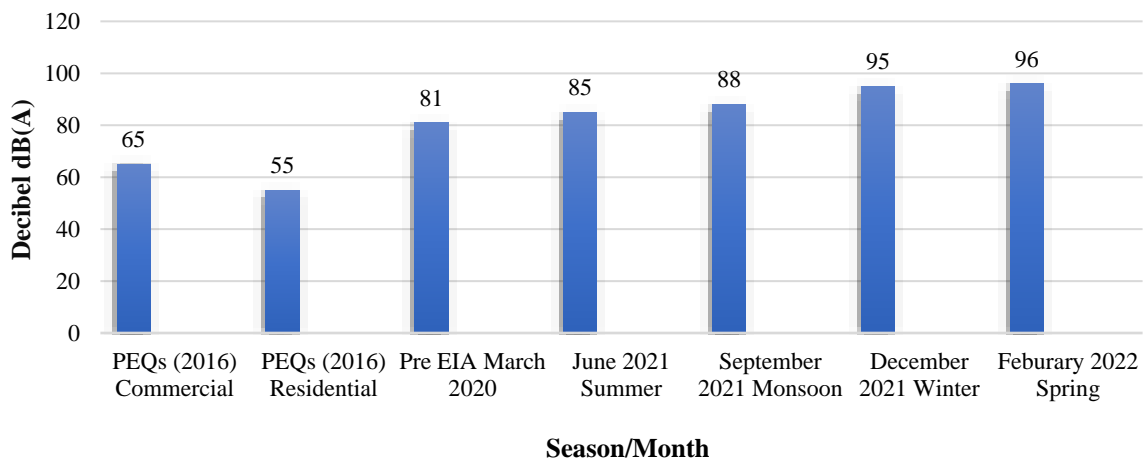
Fig 3. Monitored noise levels in four different seasons at Lal Shahbaz Qalandar Underpass, Lahore

4. Discussion

Road construction projects are particularly important since they provide social, economic, and political advantages to the country. Post-EIA is, therefore, a critical component in assessing the consequences of any developed project related to roads. A post-environmental impact assessment was conducted by measuring emissions of PM and CO and noise levels for the Lal Shahbaz Qalandar Underpass in Lahore, from by road traffic.

Before the construction of the underpass at Firdous market chowk, the values of PM$_{10}$ and PM$_{2.5}$ were slightly higher than the limits of PEQS (2016). The higher values were due to high traffic flow and traffic congestion at the Firdous Market underpass. It was observed that during the summer season, CO emission was within the limits in both Pre/Post-EIA assessments. For southwest monsoon and winter seasons, CO emissions exceeded the limit during the Post-EIA phase (from 7.85 to 8.96 mg/m^3). However, CO emissions reduced a bit during the spring season during the Post-EIA phase. PM$_{2.5}$ emissions

exceeded the normal range both during Pre/Post-EIA phases. In all seasons, their emissions were constantly been increasing (from 40-49 g/m^3) during the Pre-EIA phase. Similarly, PM$_{10}$ emissions were also found to exceed from normal range both during Pre/Post-EIA phases. In all seasons, their emissions were constantly been increasing (from 152-160 g/m^3) Pre-EIA phase.

All noise levels exceeded the standards of PEQS (2016). In the Pre-EIA phase (2020), the noise level was 81 dB(A), whereas, during the Post-EIA phase, the noise level range was from 85-96 dB(A) with a maximum in spring (February 2022). A significant difference existed for CO measurements, between Pre-EIA (March 2020) and Post-EIA (June-September 2021 and February 2022) data. A significant difference existed for PM$_{2.5}$ and PM$_{10}$ between Pre-EIA (March 2020) data with only December (2021) Post-EIA data. It is also observed that as winter approaches, the reported levels of air pollutants rise, which is the consequence of inversion in winter. Because pollutants are trapped in warmer, drier air throughout the summer and monsoon seasons and because air pollution drops abruptly in spring as the temperature rises, it is obvious to see how temperature affects air quality.

Yasin et al. (2017) presented the findings of a massive project of the Faisalabad flyover, which was under construction to reduce high traffic in the city, but unfortunately, the project had a negative environmental impact. A public poll was conducted at the site, and 49.1% of respondents believed that the level of dust rose after the flyover was built. 32.72% of respondents were concerned about the rise in noise pollution levels. According to the experts, the main cause of these issues is that EIA parameters were not fully evaluated and followed effectively. Following the Pre-EIA report, a brief period should be set apart to examine if the project's objectives have been accomplished, and if the findings are

unacceptable, certain preventive measures should be adopted before the project starts.

Aurangzaib et al., (2020) studied the Kashmir underpass project in Faisalabad. The study examined how the project's components influence the environment. During the investigation, a questionnaire survey was conducted. Almost 93% of respondents were unfamiliar with the term EIA and its importance. Workers on the project were unsure whether or not the EIA for this underpass had been completed. The building of the underpass did not cause significant environmental deterioration, but it did increase dust particles, noise, and traffic loads, according to the project activities.

Marshall (2005) mentioned that the follow-up for environmental impact assessment is very necessary. Environmental impact assessment is not an option for developing countries. It is a precaution and protective measure to use against the system. It is very important to perform a survey, to ask stakeholders and to check the contribution of the construction and its impacts on the ecosystem. Follow-ups for EIA also represent the life cycle of highly budgeted projects. It also ensures development and encourages the integration of environmental purposes. Environmental impact assessment is a method for predicting the effects of any project before it is built and post-project analysis helps assess the accuracy of such predictions.

Del Furia and Wallace-Jones (2004) examined the public legislation and EIA processes that contribute the most to the improvement of EIA, as well as their actual execution. Ashraf et al., (2013) measured preliminary air quality at 19 distinct Lahore city locations near major traffic junctions for three months. The results were then compared to National Environmental Quality Standards (NEQS) for air quality and the US-EPA's National Ambient Air Quality Standards. For 24 hours, the concentration of PM$_{2.5}$ was greater than the limits recommended by NEQS and USEPA.

Rehman et al., (2007) completed an environmental impact assessment study on the Faisalabad-Pindi Bhattian Motorway M3. The study identified several practical methodologies utilized in the EIA of highway and road projects, from planning to construction and administration. According to EIA estimates, CO levels will surpass in 2027, SOX levels will exceed specified limits in 2012 and Suspended Particulate Matter (SPM) levels will exceed in 2017. Other emissions, such as NOx and HC (hydrocarbon), will continue to rise until the finalization of the project's design lifetime. Noise levels are not predicted to violate Pakistan's NEQS regulations, although they will most certainly exceed 75 dB(A) in 2010. The influence of traffic car emissions on plants and agriculture is regarded to be negligible.

Road traffic contributes to air and noise pollution in metropolitan areas, which has a detrimental influence on human health. Thus, quantifying exposure to road traffic air and noise pollution (hereinafter, air and noise pollution) is critical in epidemiological investigations to better knowledge of human health effects (Khan et al., 2018). The residents of Lahore are constantly and severely exposed to noise pollution from road traffic. According to (LDA, 2020) a report of Lahore Development Authority (LDA) and National Engineering Services Pakistan, it averages around 95dB +/- 5dB on a particular day. A significant portion of this noise has been generated by auto-rickshaws, which emit noise levels of roughly 100-110 dB. Traffic is one of the biggest sources of noise pollution in Lahore.

Several studies on the traffic noise level in Lahore have been conducted. Aftab et al., (2007) conducted road traffic noise research in Lahore in 2008 in 18 major sites with significant traffic flow during peak hours. The results revealed that the daytime average noise level in Lahore exceeded the statutory limit of 85 dB(A) at 90% of the busiest spots. The highest average decibel noise levels measured in Lahore were 104 dB(A). The high noise level was caused by vehicular activity, including autos/rickshaws with inadequate silencers and the frequent use of pressure horns by buses, wagons and trucks.

The fundamental cause of the significant increase in air pollution is the extensive sale of automobiles in Pakistan from March 2020 to February 2022 as reported by Pakistan Automotive Manufacturers Association (PAMA). This growth has the potential to gravely affect Lahore's built and natural environments. The pollution hazards are continually increasing due to a variety of environmental factors, one of which is the fast growth in automobiles and increased usage of low-quality gasoline. Emissions from automobiles contribute to excessive levels of air pollution in cities. According to a news source, air pollution is responsible for 153 million premature deaths worldwide, with Pakistan accounting for 11 million of them. At sustained CO concentrations of 150 to 200 ppm, disorientation, coma, and death are all possible (Crossley et al., 2021).

The second main cause of increased air pollution in the environment is the lack of ecologically efficient automobiles. Governments should introduce ecologically friendly automobiles. Environmentally friendly vehicles will have lower CO_2 emissions and noise pollution. The engine is the primary generator of noise in a road vehicle. Constant noise exposure causes a variety of health problems, such as high blood pressure, hearing loss/impairment, sleep disruption, insomnia and learning difficulties in children (Sørensen et al., 2020). Traffic congestion at the following junction, which is located in the cantonment district and follows the Lal Shahbaz Qalandar underpass, is one of the sources of high levels of traffic and noise. The best solution is to build another underpass/flyover at the next intersection to relieve traffic congestion and conflicts.

Unnecessary honking is extremely dangerous on the road because it clearly

causes noise pollution and is also a major cause of anxiety in children and adults. Honking is also one of the leading causes of car accidents. The increase in the number of vehicles on the road is proportional to the increase in CO and other toxic levels of air pollution in the environmental system. This rise in automobile emissions contributes to global warming and ozone depletion.

According to Nailya et al., (2019), there is a lack of integration into the global logistic system, stages of post-project assessment, and mechanisms for optimizing transport and environmental risks of international corridors have yet to be developed, considering their impact on the development of the transit regions. There is a need for an overview of the phases of post-project evaluation and monitoring of international transport corridors, their environmental impact, what is required to confirm, assessment of the environmental impact of construction and effective mitigation. The sensitivity of climate change impacts caused by air pollution from automobile emissions should also be addressed in the post-EIA.

Studies concentrating on urban development in the sense of post-EIA principles allow enhancing projections within the EIA process and learning more about how to achieve more sustainable development. The findings of Zítkova et al. (2022) revealed that the predictions and findings about chosen EIA assessment criteria were correct during the building phase and the first year of use of the residential complex. Agah et al., (2021) investigated the environmental parameters in pre and post monsoons at the Chabahar Bay, Gulf of Oman. As a result, environmental impact evaluations and monitoring can alert to potential climate change implications as well.

5. Conclusions

The current case study highlighted the need of doing Post-EIA analysis to identify constructed underpasses as an environmental concern and raise awareness about controlling noxious gases and particle matter to mitigate air pollution. At the Lal Shahbaz Qalandar underpass, during the Post-EIA era, CO emissions surpassed the limit during the southwest monsoon and winter seasons. $PM^{2.5}$ emissions surpassed the normal level both before and after the EIA. In all seasons, their emissions increased steadily as compared to the Pre-EIA period. PM_{10} emissions were likewise determined to be above the usual level during both the Pre-and Post-EIA stages. In all seasons, their emissions increased steadily as compared to the pre-EIA period. All noise levels surpassed PEQS regulations during the post-EIA phase, with a peak in spring.

The following are the primary sources of rising air pollution and noise levels even after the completion of a megaproject of this underpass: poor quality car fuel, unnecessary honking, increased automobile sales, new car manufacturers in Pakistan, very little use of greenest vehicles, very few public transportation options near the Lal Shahbaz Qalandar underpass, no ban on vehicles without catalytic converters and no vehicle rules and regulations.

To alleviate traffic congestion and conflicts, the ideal answer is to construct another underpass/flyover at the next intersection. To lessen the hazards of the urban environment, studies on the post-environmental effect of road, underpass, flyover and bridge construction are urgently needed. More environmental factors should be measured to provide more thorough reporting. The key shortcomings should also be addressed in EIA processes. To protect the environment and comply with existing environmental regulations, mitigation activities should focus on physical data analysis. In addition, an environmental protection plan should be created, which included environmental training, emergency response, environmental reporting, inspection, analysis and environmental monitoring, to ensure successful environmental

management throughout the project's lifespan.

6. References

Abbasi, H.N., Khan, R., Nasir, I. and Ahmad, W. (2021). "A case study of Tariq Road Underpass, Karachi: Environmental analysis", *International Journal of Economic and Environmental Geology*, 12(4), 57-60, https://doi.org/10.46660/ijeeg.v12i4.75.

Agah, H., Saleh, A. and Jalili, M. (2021). "Assessment of environmental parameters in pre-and post-monsoons at Chabahar Bay, Gulf of Oman", *Civil Engineering Infrastructures Journal*, 54(1), 111-27, https://doi.org/10.22059/ceij.2020.291426.1623.

Aftab, T., Bashir, F. and Shafiq, T. (2007). "Road traffic noise pollution a hazard", *Bangladesh Journal of Scientific and Industrial Research*, 42(4), 435-40, https://doi.org/10.3329/BJSIR.V42I4.751.

Ashraf, N., Mushtaq, M., Sultana, B., Iqbal, M., Ullah, I. and Shahid, S.A. (2013). "Preliminary monitoring of tropospheric air quality of Lahore City in Pakistan", *Sustainable Development*, 2013, 3(1), 19-28, https://doi.org/10.1007/978-3-642-37401-2_5.

Aurangzaib, M., Khan, S.N., Touseef, M. and Nasir, A. (2020). "Developing guidelines for environmental impact assessment of Kashmir Underpass Project In Faisalabad", *Engineering Heritage Journal (GWK)*, 4(2), 39-43.

Babu, S. (2016). "Monitoring in EIA", Available at: https://ecointelligent.com/2016/12/11/monitoring-in-eia/, Accessed: 24 Aug. 2021.

Crossley, E., Biggs, T., Brown, P. and Singh, T. (2021). "The accuracy of iPhone applications to monitor environmental noise levels", *The Laryngoscope*, 131(1), E59-62, https://doi.org/10.1002/lary.28590.

Del Furia, L. and Wallace-Jones, J. (2000). "The effectiveness of provisions and quality of practices concerning public participation in EIA in Italy", *Environmental Impact Assessment Review*, 20(4), 457-79, https://doi.org/10.1016/S0195-9255(00)00035-4.

Dipper, B. (1998). "Monitoring and post-auditing in environmental impact assessment: a review", *Journal of environmental planning and management*, 41(6), 731-47, https://doi.org/10.1080/09640569811399.

Ehtasham, L., Sherani, S.H., Younas, K., Izbel, U., Khan, A.H., Bahadur, A. and Akbar, A. (2022). "A review of the status of environmental impact assessment in Pakistan", *Integrated Environmental Assessment and Management*, 18(2), 314-8, https://doi.org/10.1002/ieam.4499.

Fareedi, T. (2021). "Rise in Lahore traffic volume frustrates planners", The Express Tribune, Available at: https://tribune.com.pk/story/2286983/rise-in-lahore-traffic-volume-frustrates-planners, Accessed: 24 Dec. 2021.

Khan, J., Ketzel, M., Kakosimos, K., Sørensen, M. and Jensen, S.S. (2018). "Road traffic air and noise pollution exposure assessment, A review of tools and techniques", *Science of the Total Environment*, 634, 661-76, https://doi.org/10.1016/j.scitotenv.2018.03.374

Lahore Development Authority (LDA), National Engineering Services Pakistan (Pvt.) Ltd. (2020). *Environmental impact assessment (EIA) report*, Construction of Underpass at Firdous Market, Lahore, March 2020.

Loomis, J.J. and Dziedzic, M. (2018). "Evaluating EIA systems effectiveness: a state of the art", *Environmental Impact Assessment Review*, 68, 29-37, https://doi.org/10.1016/j.eiar.2017.10.005.

Marshall, R. (2005). "Environmental impact assessment follow-up and its benefits for industry". *Impact Assessment and Project Appraisal*, 23(3), 191-6, https://doi.org/10.3152/147154605781765571.

Nabegu, A.B. (2013). "Environmental impact assessment of proposed Gadon Kaya Underpass Bridge", Prepared by Prepra Nigeria Limited, Kano, Available at: https://www.academia.edu/9909233/environmental_impact_assessment_of_proposed_gadon_kaya_underpass_bridge, Accessed: 07 Mar, 2021.

Nailya, I., Marina, L., Aislu, T., Vyacheslav, K. and Zumrat, S. (2019). "Post-project assessment of transport and environmental risks of the Western Europe-Western China, international corridor", *Procedia Computer Science*, 149, 441-9, https://doi.org/10.1016/j.procs.2019.01.160.

Pinto, E., Morrison-Saunders, A., Bond, A., Pope, J. and Retief, F. (2019). "Distilling and applying criteria for best practice EIA follow-up", *Journal of Environmental Assessment Policy and Management*, 11, 21(02), 1950008, https://doi.org/10.1142/S146433321950008X.

Shah, A., Khan, S., Shah, M.H., Khan, R. and Jan, I. (2010). "Environmental impact assessment (EIA) of infrastructure development projects in developing countries", *OIDA International Journal of Sustainable Development*, (4), 47-54, http://www.ssrn.com/link/OIDA-Intl-Journal-Sustainable-Dev.html.

Smith, K.R. (2008). "WHO air quality guidelines: Moving indoors", *Air Quality, Atmosphere and Health*, 2008, 1(1), 17-8,

https://doi.org/10.1007/s11869-008-0010-2.

Sørensen, M., Münzel, T., Brink, M., Roswall, N., Wunderli, J.M. and Foraster, M. (2020). *Transport, noise and health*, In Advances in Transportati on and Health, (pp. 105-131), Elsevier, https://doi.org/10.1016/B978-0-12-819136-1.00004-8.

United States Department of Labor. (2022). "*Occupational safety and health administration, Noise exposure computation*", Available at: https://www.osha.gov/laws-regs/regulations/standardnumber/1910/1910.95 AppA, Accessed: 30 Nov. 2022.

Ur Rehman, Z. (2007). "Environmental impact assessment of Faisalabad: Pindi Bhattian motorway (M-3)", M.Sc. Thesis, Industrial Ecology, Royal Institute of Technology, Sweden, https://www.diva-portal.org/smash/get/diva2:412006/fulltext01.pdf.

Yasin, H., Usman, M., Rashid, H., Nasir, A., Sarwar, A. and Randhawa, I.A. (2017). "Guidelines for environmental impact assessment of JHAL flyover and underpass project in Faisalabad", *Geology, Ecology, and Landscapes*, 1(3), 205-12, https://doi.org/10.1080/24749508.2017.1363972.

Zítkova, J., Wimmerova, L., Fronk, K., Zdrazil, V. and Keken, Z. (2022). "Applying principles of EIA post-project analysis in the context of suburban infrastructure development", *Ecological Indicators*, 138, 108820, https://doi.org/10.1016/j.ecolind.2022.108820.

Development and Evaluation of a Computer-Aided Educational Platform for Advancing Understanding of Slope Stability Analysis

Afrazi, M.[1]* , Razavi, M.[2] , Monjezi, M.[3] , Bhatawdekar, R.[4] and Mohamad, E.[4]

[1] M.Sc., New Mexico Institute of Mining and Technology, Socorro, United States of America
[2] Associate Professor, New Mexico Institute of Mining and Technology, Socorro, United States of America
[3] Professor, Department of Mining, Faculty of Engineering, Tarbiat Modares University, Tehran, Iran.
[4] Professor, Institute for Smart Infrastructure and Innovative Construction (IsiiC), University Technology Malaysia.

ABSTRACT: Computer-aided educational platforms are of paramount importance as they provide students and engineers with interactive and personalized learning experiences, catering to their individual needs and enhancing their academic growth. This study presents a novel computer-aided educational platform designed by the authors to enhance the understanding of slope stability analysis for young industrial engineers and civil engineering students. The platform is implemented in Matlab, offering a user-friendly graphical interface and a robust framework. It facilitates a comprehensive investigation of landslides, encompassing crucial aspects such as circular slip surfaces and safety considerations based on the Bishop and Ordinary Method of Slices. Furthermore, it enables the determination of minimum safety factors for various methods applied to specific slopes. This paper provides a detailed exposition of each program function, including complete source code, to enhance comprehension of the underlying techniques. To ascertain its accuracy, a slope with given soil properties and geometry were modeled in the Matlab code and the performance of this code was benchmarked against Slide software. It showed only 5 percent error which shows the accuracy of the developed program.

Keywords: Slope Stability Analysis, Gui, Matlab, Bishop Method, Ordinary Method of Slices.

1. Introduction

Slope stability analysis holds significant importance in civil engineering as it ensures the safety and stability of slopes in geotechnical projects (Hajiazizi and Nasiri, 2019; Maleki and Aminpour, 2023; Kumar et al., 2023). However, comprehending the complex nature of slope stability analysis methods can be challenging for young industrial engineers and civil engineering students (Ghanizadeh et al., 2023; Afrazi and Yazdani, 2021; Mirzazadeh and Hajiazizi, 2020). Various approaches have

---

* Corresponding author E-mail: Mohammad.afrazi@student.nmt.edu

been employed in engineering education to establish effective learning platforms (Katsanos et al., 2014; Cavaleri et al., 2022). These platforms commonly leverage finite element software, encompassing both commercial codes such as Abaqus (Hibbitt et al., 2001), Flac (Flac, 2000; Jamshidi-Chenari, 2018) and Plaxis (Brinkgreve et al., 2012), as well as open-source alternatives (Yang et al., 2004; Novak et al., 2014; Wang et al., 2014).

Over time, computer-aided educational platforms have gained significant popularity in engineering courses due to their ability to enhance teaching and learning (Rezamand et al., 2021; Li et al., 2022; Rezazadeh-Eidgahee et al., 2022; Shan et al., 2022). For instance, (Sonparote and Mahajan, 2018) introduced a java-based platform to illustrate concepts of structural dynamics.

Another noteworthy example is Abel, an educational platform developed by Katsanos et al. (2014), which employs Matlab to acquaint students with soil-structure interaction problems. However, these software solutions often involve complex models that demand a solid grasp of the finite element method, posing challenges for undergraduate and postgraduate students. Consequently, there is a pressing need for a more accessible platform that can effectively assess slope stability while offering simplified interpretation options.

Despite various software solutions designed for slope stability analysis, there are many demands for a significant learning curve and a deep comprehension of intricate mathematical models (Qi and Tang, 2018; Armaghani et al., 2020; Li et al., 2022; Armaghani et al., 2023; He et al., 2023; Fareghian et al., 2023). This presents a notable obstacle for young industrial engineers and civil engineering students still grasping slope stability analysis is fundamental principles. Moreover, existing platforms often lack user-friendly interfaces and simplified interpretation options, impeding the effective teaching and learning of slope stability concepts. Hence, there is an urgent requirement for an educational platform that bridges the gap between theoretical understanding and practical application, providing a more accessible and intuitive approach to slope stability analysis.

Furthermore, conventional educational methods in slope stability analysis primarily rely on theoretical lectures and manual calculations, which can be time-consuming and prone to errors. This approach restricts student is ability to visualize and explore various scenarios and comprehend the practical implications of slope stability analysis. By introducing a computer-aided educational platform, the aim of this paper is to overcome these limitations and offer an interactive learning experience. The platform will empower users to conduct virtual experiments, visualize the impacts of different parameters on slope stability, and acquire a deeper understanding of the underlying principles through hands-on exploration.

The lack of comprehensive and readily available educational resources tailored to slope stability analysis further exacerbates the issue (Wang et al., 2019). While textbooks and research papers provide valuable theoretical knowledge, they often lack practical examples and real-world applications.

Through developing a dedicated educational platform, this research intends to furnish a valuable resource that amalgamates theoretical concepts with practical implementation. Including complete source code and detailed program functions in this paper will contribute to the existing body of knowledge in slope stability analysis and serve as a valuable reference for educators and researchers in the field.

Bishop and ordinary methods are two of well-known methods in slope stability analysis in geotechnical engineering. The Bishop method, widely used in slope stability analysis, assesses the safety factor, and the ordinary method divides a slope into

multiple slices, enabling a more detailed analysis (Hasanipanah et al., 2015; Zolkepli et al., 2019; Fakharian et al., 2023; Dehghani and Mohajer, 2022).

These methods have been incorporated into many platforms, offering users practical insights into their application and addressing safety aspects related to slope stability (Matsui and San, 1992; Gunawan et al., 2023). This study contributes to civil engineering education by introducing a computer-aided educational platform focused on slope stability analysis.

Developed in the Matlab environment, the platform provides an intuitive interface and incorporates the Bishop method and the Ordinary Method of Slices (OMS), offering comprehensive insights into slope stability analysis. The subsequent sections will delve into the methodology, results and evaluation, followed by a discussion of the platform's strengths, limitations, and potential areas for improvement.

2. Methodology

2.1. Ordinary Method of Slices

The method known as the OMS pioneered the use of the slice technique for slope stability analysis (Hovland, 1977;

Jiang and Magnan, 1997; Niromand et al., 2021; Tsang et al., 2023; Skentou et al., 2023). According to this approach, the collective inter-slice forces are assumed to align parallel to the base of each slice.

However, it is essential to acknowledge that this simplifying assumption does not account for inter-slice equilibrium when adjacent slices possess different base inclinations. This limitation represents a significant drawback of the OMS, as it results in the calculation of inconsistent effective stresses at the base of the slices.

If the slice forces are resolved in a direction perpendicular to the base of the slice shown in Figure 1, then:

$$\sum F_\alpha = N' + U_\alpha + k_h W \sin\alpha - W(1 - k_v)\cos\alpha - U_\beta \cos(\beta - \alpha) - Q\cos(\delta - \alpha) = 0 \tag{1}$$

The above equation may be arranged for N' as:

$$N' = -U_\alpha - k_h W \sin\alpha + W(1 - k_v)\cos\alpha + U_\beta \cos(\beta - \alpha) + Q\cos(\delta - \alpha) \tag{2}$$

F = Factor of safety
S_a = Available strength = $C + N' \tan\varphi$
S_m = Mobilized strength
U_a = Pore water pressure
U_β = Surface water force
W = Weight of slice
N' = Effective normal force
Q = External surcharge
k_v = Vertical seismic coefficient
k_h = horizonral seismic coefficient
Z_L = Left interslice force
Z_R = Right interslice force
θ_L = Left interslice force angle
θ_R = Right interslice force angle
h_L = Height to force Z_L
h_R = Height to force Z_R
α = Inclination of slice base
β = Inclination of slice top
b = Width of slice
h = Average height of slice
h_c = Height to centroid of slice

Fig. 1. Division of potential sliding mass into slices

With the Factor of Safety (FOS) against shear failure defined as F and assumed to be the same for all slices, the Mohr coulomb mobilized shear strength, S_m, along the base of each slice is given by:

$$S_m = \frac{C + N' \tan\varphi}{F} \qquad (3)$$

where C and $N' \tan\varphi$: are the cohesive and frictional shear strength components of the soil. The overall moment equilibrium of the forces about the center of the circular failure surface for each slice is given by:

$$\sum M_o = \sum_{i=1}^{n}[W(1-k_v) + U_\beta \cos\beta + Q\cos\delta] R\sin\alpha - \sum_{i=1}^{n}[U_\beta \sin\beta + Q\sin\delta](R\cos\alpha - h) - \sum_{i=1}^{n}[S_m]R + \sum_{i=1}^{n}[k_h W(R\cos\alpha - h_c)] = 0 \qquad (4)$$

where R: is radius of the circular failure surface, h: is average height of the slice and h_c: is vertical height between the center of the base slice and the centroid of the slice.

The influence of the internal inter-slice forces has been excluded from this expression, as their resultant net moment will be zero. The above equation may be simplified by dividing throughout by radius to get.

$$\frac{\sum M_o}{R} = \sum_{1}^{n}[W(1-k_v) + U_\beta \cos\beta + Q\cos\delta]\sin\alpha - \sum_{i=1}^{n}[S_m] + \sum_{i-1}^{n}\left[k_h W\left(R\cos\alpha - \frac{h_c}{R}\right)\right] \qquad (5)$$

If the FOS is assumed to be the same for all slices, substitute Eq. (3) in Eq. (5) gives:

$$F = \frac{\sum_{i=1}^{n}(C + N'\tan\varphi)}{\sum_{i=1}^{n}A_1 - \sum_{i=1}^{n}A_2 + \sum_{i=1}^{n}A_3} \qquad (6)$$

where A_1, A_2 and A_3: are defined as below:

$$A_1 = \left(W(1-k_v) + U_\beta \cos\beta + Q\cos\delta\right)\sin\alpha$$

$$A_2 = (U_\beta \sin\beta + Q\sin\delta)(\cos\alpha - \frac{h}{R})$$

$$A_3 = k_h W(\cos\alpha - \frac{h_c}{R})$$

N': is given by Eq. (2). This is the formulation that is often used to compute the FOS according to the assumption of the OMS.

2.2. Simplified Bishop Method

The simplified Bishop method employs the slice technique to discretize the soil mass and calculate the FOS. This approach ensures vertical force equilibrium for individual slices and achieves overall moment equilibrium around the center of the circular trial surface.

Additionally, the simplified Bishop method assumes negligible shear forces between adjacent slices. Referring to the notation depicted in Figure 1, the overall moment equilibrium of the forces acting on each slice can be expressed as follows:

$$\sum M_o = \sum_{i-1}^{n}[W(1-k_v) + U_\beta \cos\beta + Q\cos\delta] R\sin\alpha - \sum_{i=1}^{n}[U_\beta \sin\beta + Q\sin\delta](R\cos\alpha - h) - \sum_{i=1}^{n}[S_m]R + \sum_{i-1}^{n}[k_h W(R\cos\alpha - h_c)] = 0 \qquad (7)$$

where R: is radius of the circular failure surface, h: is average height of the slice, h_c: is vertical height between the center of the base slice and the centroid of the slice the above equation may be simplified by dividing throughout by radius to get:

$$\frac{\sum M_o}{R} = \sum_{1}^{n}[W(1-k_v) + U_\beta \cos\beta + Q\cos\delta]\sin\alpha - \sum_{i=1}^{n}[S_m] + \sum_{i-1}^{n}\left[k_h W\left(R\cos\alpha - \frac{h_c}{R}\right)\right] \qquad (8)$$

It is important to consider that the effective normal and pore pressure forces, which exert their influence on the base of the slice, do not impact the moment equilibrium expression as they align through the center of the circular surface. As a result, the application of Bishop's method for calculating the FOS is unsuitable for noncircular surfaces which should be considered.

If the FOS is assumed to be the same for all slices, the Mohr coulomb criterion is substituted into Eq. (8) to give:

$$F = \frac{\sum_{i=1}^{n}(C + N'\tan\varphi)}{\sum_{i=1}^{n} A_5 - \sum_{i=1}^{n} A_6 + \sum_{i=1}^{n} A_7} \quad (9)$$

where A_5, A_6 and A_7: are defined as follow:

$$A_5 = (W(1 - k_v) + U_\beta + Q\cos\delta)\sin\alpha$$

$$A_6 = (U_\beta + Q\sin\delta)(\cos\alpha - \frac{h}{R}) \quad (10)$$

$$A_7 = k_h W(\cos\alpha - \frac{h_c}{R})$$

Next, forces are summed in the vertical direction for each slice to determine the effective normal force in the same manner as used for Janbu's method is:

$$N' - \frac{1}{m_\alpha}[W(1 - k_v) - \frac{C\sin\alpha}{F} - U_\alpha\cos\alpha + U_\beta\cos + Q\cos\delta] \quad (11)$$

where m_α: is again given by:

$$m_\alpha = \cos\alpha[1 + \frac{\tan\alpha \tan\varphi}{F}] \quad (12)$$

Eqs. (9-12) are the expressions that are used to calculate the FOS for circular surfaces according to the simplified Bishop method.

3. Platform Interface

Upon launching the software, users are presented with a dialog-box titled "Slope Stability" (refer to Figure 2), which comprises seven distinct panels: "Slope Coordinates", "Axis Limit", "Soil Properties", "Center of Trial Surface Region", "Clear Axes", "Method" and "Final Results". These panels offer white boxes where users can input various values, culminating in the calculation of the final FOS based on the selected method and input values. In the "Slope Coordinates" panel, users enter the "X" and "Y" coordinates of the slope, delineating the points from 1 to 4, as depicted in Figure 2. Notably, the program allows users to draw the slope using mouse clicks to enhance usability.

The "Axis Limit" panel enables users to specify the minimum and maximum values for the "X" and "Y" axes. Within the "Soil Properties" panel, users input parameters such as cohesion, friction angle, unit weight of the soil, number of slices and the desired error.

Cohesion and friction angle represent intrinsic soil properties, while the number of slices determines the division of the failure surface into discrete segments. To explore potential failure surfaces and draw different circles, users define the "Center of Trial Surface Region" boundaries in panel 4. Panel 5 is a convenient tool for clearing the axes and initiating the drawing of a new model.
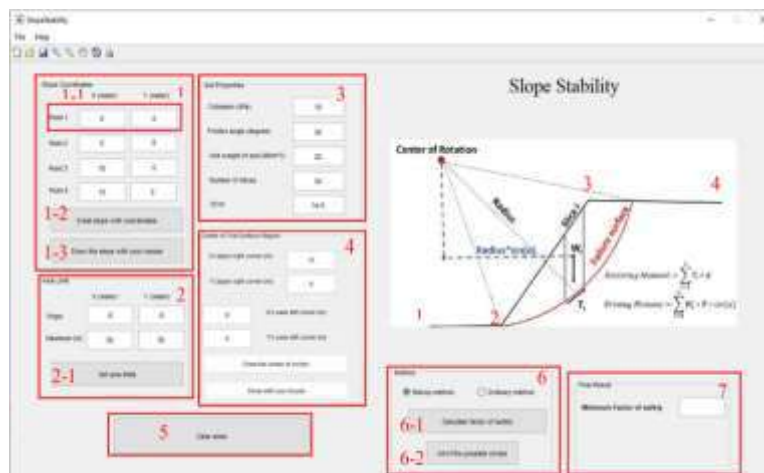
Fig. 2. Graphical user interface of the Matlab code
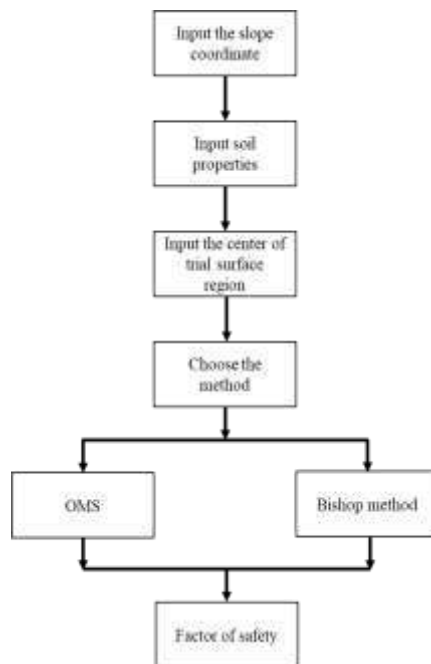
Fig. 3. Matlab procedure

In panel 6, users select the desired method for calculating the safety factor, while panel 7 displays the minimum FOS achieved. The program's flowchart is depicted in Figure 3.

4. The Matlab Code

Once the geometry of the slope and the Boundary of the Center of Trial Surface (BCTS) region are defined, the program identifies the minimum and maximum radii of potential failure circles within the specified boundary, as illustrated in Figure 4.

The program systematically examines the circles for their intersections with the slope geometry. During this process, each point inside the BCTS region is considered as a circle's center.

The program systematically calculates the distances from each corner of the BCTS region to the four points defining the slope geometry to determine these radii. With the distances determined, the program draws circles within the BCTS region, ranging from the minimum to the maximum radius.

For this purpose, the program employs the "intersection points" function to determine the coordinates of the points where circles intersect with the slope. It distinguishes between real and imaginary intersections, as a circle may intersect with an extension of a slope line that lies beyond the region of interest and is, therefore, irrelevant to the analysis. By considering only circles with at least two real intersections, the program ensures that the analyzed circles are plausible representations of potential failure surfaces.
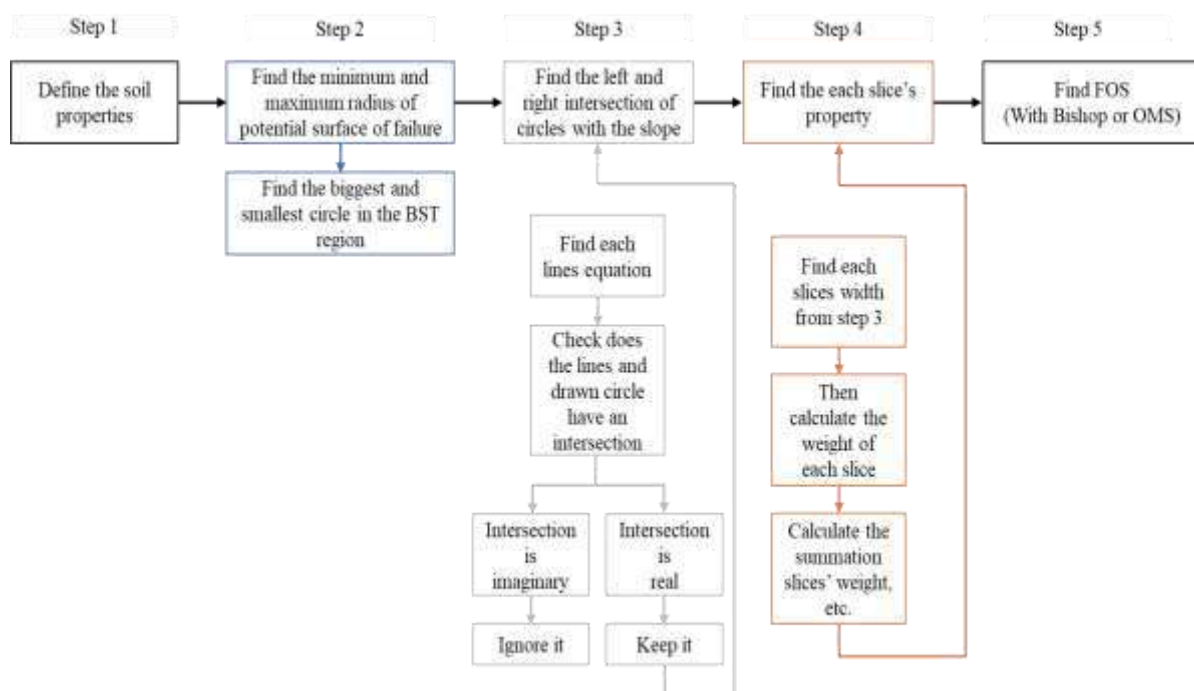
Fig. 4. Matlab flow chart of each function in the program

For each circle that meets the intersection criterion, the program calculates the properties of the associated profile, including each slice's width and weight, etc. The calculation of slice properties is facilitated by the "slice property" function, which enables the determination of weight and other pertinent properties for each slice.

The program performs these calculations for all potential failure surfaces and computes each profile's FOS. The FOS represents a measure of stability, with higher values indicating a more stable slope.

The program compares the calculated FOS values across the analyzed circles to identify the most critical failure surface and determine the minimum FOS. It selects the profile with the lowest FOS as the minimum FOS, indicating the most vulnerable failure surface within the BCTS region. Finally, the program employs the Bishop or OMS to calculate the FOS.

These widely recognized methods are commonly used in slope stability analysis to evaluate the FOS. The minimum FOS, representing the most critical failure surface, is reported as the outcome of the analysis.

5. Validation with SLIDE

To ensure the accuracy and reliability of the Matlab code, a comparative validation study was conducted by constructing a representative slope with predefined properties, Tables 1-3. The same geometry and material properties were employed in the Matlab code and a well-established software tool, Slide. The results obtained from Slide were used as a benchmark for evaluating the performance of the Matlab code.

The validation process involved analyzing the FOS for the constructed slope using both the Matlab code and Slide software. Figure 5 illustrates the FOS values obtained from Slide, serving as a reference for comparison. Upon comparing

the FOS values calculated by the Matlab code, Figure 6, with those obtained from Slide, it was observed that the Matlab code yielded a discrepancy of only 5 percent.

Table 1. The geometry of slope

	X (m)	Y (m)
Point 1	0	0
Point 2	5	0
Point 3	10	5
Point 4	15	5

Table 2. The geometry of slope

Soil property	Value	Unit
Cohesion	10	kPa
Friction angle	34	Degree
Unit weight	20	kN/m^3
Number of slices	30	-
Acceptable error for Bishop method	1e-5	-

Table 3. BCTS location

	X (m)	Y (m)
Upper right corner (m)	10	8
Lower left corner (m)	8	6

This error level falls within an acceptable range, indicating high accuracy and reliability in Matlab implementation. The strong agreement between the results generated by the Matlab code and the Slide software validates the integrity and robustness of the developed computer-aided educational platform for slope stability analysis. The negligible error percentage underscores the exceptional precision and reliability of the Matlab code in calculating FOS with a high degree of accuracy. The observed 6 percent difference can be attributed to various factors inherent in the numerical approximations employed by both Matlab and Slide to solve the equations. Subtle disparities in the specific numerical methods, precision levels, or convergence criteria adopted by the Slide can contribute to variations in the computed results. Additionally, divergent assumptions or simplifications made in the respective slope stability analysis models of the Matlab code and Slide software can generate disparities.

Variances in modeling soil behavior, boundary conditions, or other factors can

impact the calculated FOS, leading to slight discrepancies between the two sets of results. These factors collectively highlight the intricate nature of slope stability analysis and the inherent challenges in achieving absolute agreement between different computational tools.

Nonetheless, the overall close alignment between the Matlab code and Slide software results affirms the suitability and reliability of the developed educational platform for slope stability analysis, providing practitioners and students with an effective tool for understanding and analyzing slope stability in civil engineering applications.
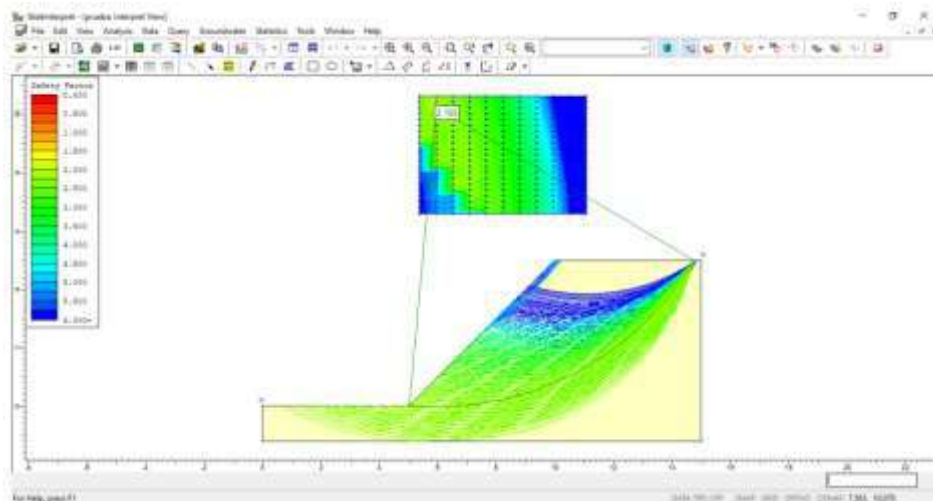
Fig. 5. The FOS from SLIDE
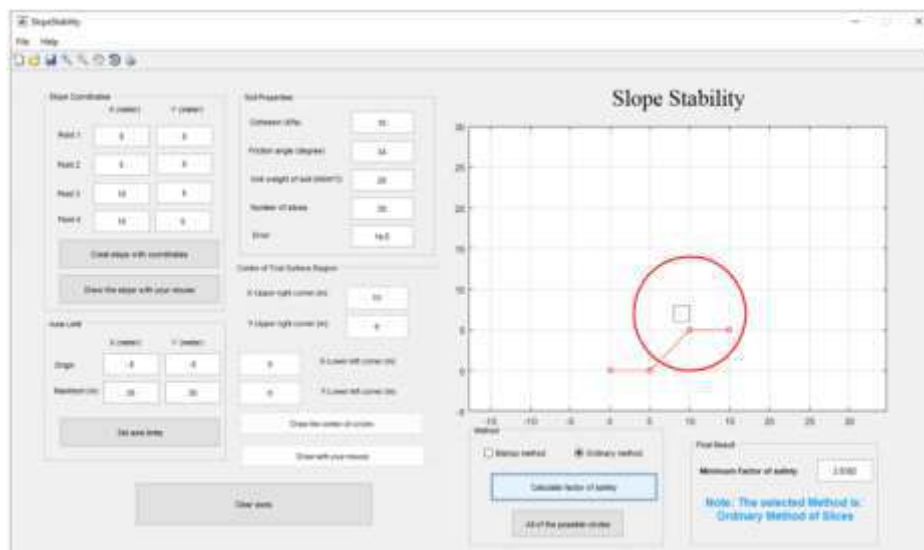
Fig. 6. The FOS from the Matla code

6. Validation with Slide

One of the notable advantages of the developed platform is its effectiveness in enhancing the understanding of slope stability analysis. By integrating the Bishop method and the OMS, the platform offers users a comprehensive toolset to explore and analyze critical aspects of slope stability, including circular slip surfaces and safety considerations.

The user-friendly graphical interface and robust framework provide an intuitive and interactive learning environment, facilitating the comprehension of complex slope stability concepts. The platform's practicality and usability are significant advantages that make it a valuable resource

for young industrial engineers and civil engineering students.

The user-friendly interface allows users to easily input slope coordinates, define axis limits, and enter soil properties, enabling them to set up slope stability scenarios with ease. The platform's capable to draw slopes based on user-defined points or mouse clicks further enhances its practicality, making it accessible to users with varying levels of expertise.

The validation study comparing the platform's results with those obtained from the widely recognized Slide software further strengthens its credibility and reliability. The close agreement between the platform and Slide software results, with a negligible 6 percent difference, demonstrates the accuracy of the platform's calculations. This validation gives users confidence in utilizing the platform for slope stability analysis, knowing that it can produce reliable and precise results.

Furthermore, the platform's user-friendly interface and accurate calculations makes it a valuable tool for professionals and researchers involved in slope stability analysis. The platform's integration of prominent analysis techniques and its adaptability to different slope scenarios enable users to make informed decisions regarding slope safety and stability in practical engineering projects.

While the developed computer-aided educational platform for slope stability analysis offers numerous advantages, it is important to acknowledge certain limitations and identify areas for future improvement and expansion. One of the study's limitations is the focus on specific analysis techniques, namely the Bishop method and the OMS.

While these techniques are widely used and provide valuable insights, the platform could benefit from incorporating a broader range of analysis methods, such as limit equilibrium methods, finite element analysis, or advanced numerical algorithms, to cater to a broader range of slope stability scenarios and research needs. Additionally,

the platform does the modeling in 2D area while it can be developed and start modeling 3D slopes which makes it more accurate. However, at the same time it increases the compellability of analysis and understanding of slope stability for young engineers.

7. Conclusions

In conclusion, this study presented the development and evaluation of a computer-aided educational platform to enhance the understanding of slope stability analysis in civil engineering. The platform, implemented in Matlab, offers a user-friendly graphical interface and a robust framework. It integrates prominent analysis techniques, such as the Bishop method and the OMS, allowing users to explore critical aspects of slope stability and determine minimum safety factors for different slope scenarios. The validation study, comparing the platform's results with those obtained from the well-established Slide software, demonstrated its accuracy and reliability with a negligible 6 percent difference.

This validation provides strong evidence of the platform's effectiveness in generating precise FOS calculations. The developed educational platform fills a crucial gap in the field by providing young industrial engineers and civil engineering students with a practical tool to comprehend complex slope stability concepts.

It facilitates interactive analysis, enabling users to gain hands-on experience in evaluating slope stability scenarios. The inclusion of complete source code enhances transparency and promotes a deeper understanding of the underlying techniques.

The successful development and evaluation of this platform contribute significantly to the field of slope stability analysis. Its user-friendly interface, integration of advanced analysis methods, and validated accuracy make it a valuable resource for researchers, educators, and practitioners. By bridging the gap between theory and practice, the platform equips

users with essential skills for tackling slope stability challenges in geotechnical projects. As future work, the platform can be further improved by incorporating additional analysis methods, expanding its capabilities to handle more complex slope geometries, and integrating data visualization features. These enhancements will ensure the platform remains relevant and adaptable to evolving needs in slope stability analysis.

8. References

Afrazi, M. and Yazdani, M. (2021). "Determination of the effect of soil particle size distribution on the shear behavior of sand", *Journal of Advanced Engineering and Computation*, 5(2), 125-134, http://doi.org/10.25073/jaec.202152.331.

Armaghani, D.J., Asteris, P.G., Fatemi, S.A., Hasanipanah, M., Tarinejad, R., Rashid, A.S.A. and Huynh, V.V. (2020). "On the use of Neuro-Swarm System to forecast the pile settlement", *Applied Sciences*, 10(6), 1904, https://doi.org/10.3390/app10061904.

Armaghani, D.J., Yi, Y. and Salih, M. (2023). "Effect of SVM Kernel functions on bearing capacity assessment of deep foundations", *Journal of Soft Computing in Civil Engineering*, 7(3), 111-128, http://doi.org/10.22115/scce.2023.356959.1510

Brinkgreve, R.B.J., Engin, E. and Swolfs, W. (2012). "*Plaxis 2D 2012 user manual*, Delft, Netherlands.

Cavaleri, L., Barkhordari, M.S., Repapis, C.C., Armaghani, D.J., Ulrikh, D.V. and Asteris, P.G. (2022). "Convolution-based ensemble learning algorithms to estimate the bond strength of the corroded reinforced concrete", *Construction and Building Materials*, 359, 129504, https://doi.org/10.1016/j.conbuildmat.2022.129504.

Dehghani, E. and Soltani Mohajer, M. (2022). "Development of the fragility curves for conventional reinforced concrete moment resistant frame structures in Qods Town, Qom City, Iran", *Civil Engineering Infrastructures Journal*, 55(1), 3141. https://doi.org/10.22059/ceij.2021.306156.1690.

Fakharian, P., Eidgahee, D.R., Akbari, M., Jahangir, H. and Taeb, A.A. (2023). "Compressive strength prediction of hollow concrete masonry blocks using artificial intelligence algorithms", *Structures*, 47, 17901802, https://doi.org/10.1016/j.istruc.2022.12.007.

Fareghian, M., Afrazi, M. and Fakhimi, A. (2023).

"Soil reinforcement by waste tire textile fibers: Small-scale experimental tests"*, Journal of Materials in Civil Engineering*, 35(2), 04022402, https://doi.org/10.1061/(ASCE)MT.19435533.0004574.

FLAC, (2000). *Itasca, Fast Lagrangian analysis of continua*, Itasca Consulting Group Inc., Minneapolis, Minn.

Ghanizadeh, A.R., Ghanizadeh, A., Asteris, P.G., Fakharian, P. and Armaghani, D.J. (2023). "Developing bearing capacity model for geogrid-reinforced stone columns improved soft clay utilizing MARS-EBS hybrid method", *Transportation Geotechnics*, 38, 100906, https://doi.org/10.1016/j.trgeo.2022.100906.

Gunawan, M., Hidayati and Adam, R. (2023). "Slope stability analysis using Bishop method and Slide 2D software at sand stone mining in Sedau Village, Narmada District, Lombok Barat Regency", *IOP Conference Series: Earth and Environmental Science*, 1175(1), 012010, https://doi.org/10.1088/1755-1315/1175/1/012010.

Kumar, V., Priyadarshee, A., Chandra, S., JINDAL, A. and Rana, D. (2023). "Behavioral study of raft reinforced with geogrid and geocell through experiments and neural models", *Civil Engineering Infrastructures Journal*, 56(2), 321-332, https://doi.org/10.22059/ceij.2023.343951.1847.

Mirzazadeh, Z. and Hajiazizi, M. (2020). "Determination of creep-induced displacement of soil slopes based on LEM", *Civil Engineering Infrastructures Journal*, 53(2), 341-358, https://doi.org/10.22059/ceij.2020.285244.1598.

Hajiazizi, M. and Nasiri, M. (2019). "Experimental and numerical investigation of reinforced sand slope using geogird encased stone column", *Civil Engineering Infrastructures Journal*, 52(1), 85-100. https://doi.org/10.22059/ceij.2019.253069.1468.

Hasanipanah, M., Monjezi, M., Shahnazar, A., Armaghani, D.J. and Farazmand, A. (2015). "Feasibility of indirect determination of blast induced ground vibration based on support vector machine", *Measurement*, 75, 289-297, https://doi.org/10.1016/j.measurement.2015.07.019

He, B., Armaghani, D.J. and Lai, S.H. (2023). "Assessment of tunnel blasting-induced overbreak: A novel metaheuristic-based random forest approach", *Tunnelling and Underground Space Technology*, 133, 104979, https://doi.org/10.1016/j.tust.2022.104979.

Hibbitt, Karlsson and Sorensen, (2001). "*ABAQUS/Explicit: User's manual*, Hibbitt,

Karlsson and Sorenson Incorporated.

Hovland, H.J. (1977). "Three-dimensional slope stability analysis method", *Journal of the Geotechnical Engineering Division*, 103(9), 971-986, https://doi.org/10.1061/AJGEB6.0000493.

Jamshidi Chenari, R., Ghorbani, A., Eslami, A. and Mirabbasi, F. (2018). "Behavior of piled raft foundation on heterogeneous clay deposits using random field theory", *Civil Engineering Infrastructures Journal*, 51(1), 35-54. https://doi.org/10.7508/ceij.2018.01.003.

Jiang, G.L. and Magnan, J.P. (1997). "Stability analysis of embankments: comparison of limit analysis with methods of slices", *Geotechnique*, 47(4), 857-872, https://doi.org/10.1680/geot.1997.47.4.857.

Katsanos, E.I., Taskari, O.N. and Sextos, A.G. (2014). "A matlab-based educational tool for the seismic design of flexibly supported RC buildings", *Computer Applications in Engineering Education*, 22(3), 442451, https://doi.org/10.1002/cae.20568.

Li, C., Zhou, J., Tao, M., Du, K., Wang, S., Armaghani, D.J. and Mohamad, E.T. (2022). "Developing hybrid ELM-ALO, ELM-LSO and ELM-SOA models for predicting advance rate of TBM", *Transportation Geotechnics*, 36, 100819, https://doi.org/10.1016/j.trgeo.2022.100819.

Li, D., Liu, Z., Xiao, P., Zhou, J. and Armaghani, D.J. (2022). "Intelligent rockburst prediction model with sample category balance using feedforward neural network and Bayesian optimization", *Underground Space*, 7(5), 833-846, https://doi.org/10.1016/j.undsp.2021.12.009.

Maleki, M. and Aminpour, M.M. (2023). "Upper bound solution for the stability of surcharged soil slope using nonlinear failure criterion", *Civil Engineering Infrastructures Journal*, 57(1), 175-188, https://doi.org/10.22059/CEIJ.2023.353469.1900.

Matsui, T. and San, K.C. (1992). "Finite element slope stability analysis by shear strength reduction technique", *Soils and Foundations*, 32(1), 59-70, https://doi.org/10.3208/sandf1972.32.59.

Niromand, M., Mikaeil, R. and Advay, M. (2021). "Assessment of the slope stability under geological conditions using FDAHP-TOPSIS (A case study for Sungun Open Pit Mine)", *Journal of Soft Computing in Civil Engineering*, 5(4), 2140, https://doi.org/10.22115/scce.2021.290413.1337.

Novak, D., Vorechovsky, M. and Teply, B. (2014). "FReET: Software for the statistical and reliability analysis of engineering problems and FReET-D: Degradation module", *Advances in Engineering Software*, 72, 179-192, https://doi.org/10.1016/j.advengsoft.2013.06.011.

Qi, C. and Tang, X. (2018). "Slope stability prediction using integrated metaheuristic and machine learning approaches: A comparative study", *Computers and Industrial Engineering*, 118, 112-122, https://doi.org/10.1016/j.cie.2018.02.028.

Rezamand, A., Afrazi, M. and Shahidikhah, M. (2021). "Study of convex corners' effect on the displacements induced by soil-nailed excavations", *Journal of Advanced Engineering and Computation*, 5(4), 277-290, https://doi.org/10.55579/jaec.202154.344.

Rezazadeh Eidgahee, D., Jahangir, H., Solatifar, N., Fakharian, P. and Rezaeemanesh, M. (2022). "Data-driven estimation models of asphalt mixtures dynamic modulus using ANN, GP and combinatorial GMDH approaches", *Neural Computing and Applications*, 34(20), 17289-17314, https://doi.org/10.1007/s00521-022-07382-3.

Shan, F., He, X., Armaghani, D.J., Zhang, P. and Sheng, D. (2022). "Success and challenges in predicting TBM penetration rate using recurrent neural networks", *Tunnelling and Underground Space Technology*, 130, 104728, https://doi.org/10.1016/j.tust.2022.104728.

Skentou, A.D., Bardhan, A., Mamou, A., Lemonis, M.E., Kumar, G., Samui, P., Armaghani, D.J. and Asteris, P.G. (2023). "Closed-form equation for estimating unconfined compressive strength of granite from three non-destructive tests using soft computing models", *Rock Mechanics and Rock Engineering*, 56(1), 487-514, https://doi.org/10.1007/s00603-022-03046-9.

Sonparote, R.S. and Mahajan, S.K. (2018). "An educational tool to improve understanding of structural dynamics through idealization of physical structure to analytical model", *Computer Applications in Engineering Education*, 26(5), 12701278, https://doi.org/10.1002/cae.22006.

Tsang, L., He, B., Ghorbani, A. and Khatami, S.M.H. (2023). "Tree-based tTechniques for predicting the compression index of clayey soils", *Journal of Soft Computing in Civil Engineering*, 7-3, 52-67, https://doi.org/10.22115/SCCE.2023.377601.1579.

Wang, H., Li, L., Jiao, Y.Y., Ge, X.R. and Li, S.C. (2014). "A relationship-based and object-oriented software for monitoring management during geotechnical excavation", *Advances in Engineering Software*, 71, 34-45, https://doi.org/10.1016/j.advengsoft.2014.02.001.

Wang, J., Cui, W. and Ye, J. (2019). "Slope stability

evaluation using tangent similarity measure of fuzzy cube sets", *Journal of Soft Computing in Civil Engineering*, 3(1), 2735, https://doi.org/10.22115/SCCE.2019.176352.1100.

Yang, Z., Lu, J. and Elgamal, A. (2004). "A web-based platform for computer simulation of seismic ground response", *Advances in Engineering Software*, 35(5), 249-259, https://doi.org/10.1016/j.advengsoft.2004.03.002.

Zolkepli, M.F., Ishak, M.F. and Zaini, M.S.I. (2019). "Slope stability analysis using modified Fellenius's and Bishop's method", *IOP Conference Series: Materials Science and Engineering*, 527(1), 012004, https://doi.org/10.1088/1757-899X/527/1/012004.

10. Appendix

All of the Matlab codes are uploaded on the following link: https://github.com/mohammadafrazi/matlabcode.

TECHNICAL NOTE

Influence of Variation of Soil Properties in Bearing Capacity and Settlement Analysis of a Strip Footing Using Random Finite Element Method

Vinay, K.[1], Avijit, B.[2], Portelinha, F.[3], Manish, K.[4*] and Guru, D.[5]

[1] Ph.D. Instructor, Department of Civil Engineering-DECiv, Universidad Federal de Sao Carlos, Sao Carlos-SP, Brazil.
[2] Professor, Department of Civil Engineering, National Institute of Technology, Patna, India.
[3] Professor, Department of Civil Engineering-DECiv, Universidad Federal de Sao Carlos, Sao Carlos-SP, Brazil.
[4] Assistant Professor , Department of Civil Engineering, SRM Institute of Science and technology (SRMIST) Tiruchirappalli, TN, India.
[5] Ph.D. Candidate, Research Scholar, Department of Civil Engineering, NIT Patna, India.

ABSTRACT: This study analyzes bearing capacity and settlement for a strip footing at the proposed nit Patna Bihta campus site. It uses the Random Finite Element Method (RFEM) based software, which combines viscoplastic finite element analysis with random field theory. The program generates random realizations of the soil domain using local average subdivision method. The average response of the soil domain with variable properties is estimated using Monte-Carlo simulation. The study assumes random variation of soil parameters like cohesion, friction angle, and elastic modulus, while Poisson's ratio and dilation angle are treated as deterministic variables. The study also considers the cross correlation between cohesion and friction angle. For no cross correlation, theoretical predictions are made for mean and standard deviation of bearing capacity which are verified using Monte Carlo simulation based RFEM results. The probability of bearing capacity failure is also calculated using random finite element analysis and compared with theoretical results. The stochastic analysis of bearing capacity problem indicates that conservative results can be obtained with Prandtl's bearing capacity formula with consideration correlation length equal to the width of the footing. In settlement analysis, elastic settlement of strip footing on spatially variable soil is presented. Locally averaged log normally distributed random fields of elastic modulus are generated to conduct probabilistic settlement analysis using RFEM and it is seen that there is very good agreement between the predicted and the actual value of settlement at small and large correlation lengths. It is concluded that RFEM is a very suitable and efficient tool for investigation of the effect of variation of soil properties in determining the overall mean response for the bearing capacity and settlement behavior.

Keywords: Bearing Capacity Analysis, Settlement Analysis, Mohr-Coulomb Yield Criteria, Random Finite Element Method, Monte Carlo Simulation.

* Corresponding author E-mail: mkumarod@gmail.com

1. Introduction

The foundation is the most important part of a structure as it connects the structure to the ground and transfers the load from the superstructure to the ground. In the literature, deterministic analysis is mostly used to calculate bearing capacity and settlement of foundation (Pan-war and Dutta, 2023). Such analysis assumes the soil to have a uniform value of parameters like cohesion, friction angle, elastic modulus etc. But these values are not uniform over the soil domain. So, for an important structure, one needs to carry out the reliability analysis to find out the probability of failure and the associated risks. For such a purpose Fenton and Griffiths (2008) developed a program called Random Finite Element Method (RFEM) which is based on the combination of finite element method and random field theory.

It has edge over the other reliability methods in the way that it can produce soil domains with spatially varying properties thus considering the uncertainty associated and hence the response of the soil domain to the loads will be more realistic. Many researchers have successfully been able to model this uncertainty using finite element method and other techniques (Halder and Chakraborty, 2022; Jimenez and Sitar, 2009; Johari and Talebi, 2021; Kumar et al., 2023; Mellah et al., 2000; Pula and Zaskorski, 2015; Rezaie Soufi et al., 2020; Zhang and Peil, 1997).

Vivisects et al. (2021) performed uncertainty quantification in the estimation of bearing capacity for shallow foundations in sandy soils using the finite element method. Mofidi Rouchi et al. (2014) performed lower bound limit analysis for strip footings near slopes. Griffiths and Fenton (2008) used the program to carry out the probabilistic analysis of many geotechnical problems like flow problems, bearing capacity analysis, slope stability analysis etcetera.

Fenton and Vanmarcke (1990) developed a method called Local Average Subdivision (LAS) which have been popular for generating a realization of random field. Pieczynska et al. (2011) presented their work on probabilistic analysis of bearing capacity including new factors, like introduction of anisotropy in the random fields of cohesion and friction angle. Another addition made in this study was that the soil was not considered weightless anymore. The inclusion of anisotropy produces more realistic results and effectiveness of RFEM predictions increases.

In recent years as well, many researchers have made use of this program to publish their work. Tan et al. (2009) performed slope stability analysis using fuzzy random finite element method. They said that fuzziness and randomness exist simultaneously in the soil and that is why it was important to carry out fuzzy random reliability analysis of slope. Pramanik et al. (2019) used fuzzy set theory along with RFEM to perform the reliability analysis of elastic settlement of surface strip footing resting on cohesion less soil. Johari et al. (2015) for the case of loose sand, carried out an analysis to find the reliability against static liquefaction. They used the RFEM for doing so. Monotonic loading was considered in their study. They employed a truncated normal probability density function to represent all the random parameters considered in the study.

Jimenez and Sitar (2009) performed RFEM analysis on foundation settlement. They assumed different distributions for elastic modulus like lognormal, gamma and beta. They characterized the elastic modulus using random fields. The scale of fluctuation tooke on the extreme values in their study. They performed their analysis for 2-dimensional shallow footing and the finite element model used was for plane strain condition. In recent years as well, a lot of research has been done on this topic (Zhang and Peil, 1997). Pula and Zaskorski (2015) investigated for a suitable distribution of the bearing capacity in case of cohesion less soil. They assumed a

bounded distribution for friction angle. The underlying Gaussian field was assumed to be tied with an ellipsoidal correlation function. They found that the probability distribution for the bearing capacity had a close resemblance with the Weibull distribution.

Luo and Bathurst (2018) carried out deterministic and random finite element analysis of unreinforced and reinforced embankments brought to failure using strip footing. Chenari et al. (2019) presented immediate settlement analysis of shallow foundation resting on a spatially random anisotropic soil layer. Chawla (2019) studied the worst case correlation length for mean bearing capacity values using RFEM. Selmi et al. (2019) performed capacity assessment of offshore skirted foundations subject to vertical horizontal moment loads using RFEM. Kawa and Pula (2020) carried out probabilistic bearing capacity analysis of footing on spatially variable soils in 3D using RFEM. Shu et al. (2020) studied the effect of autocorrelation distance on mean bearing capacity of Spudcan foundations.

Ning and Zhe (2021) explored the effect of rotated anisotropy of soil property on the bearing capacity of embedded strip footings using RFEM. Arel and Mert (2021) dealt with settlement analysis of a vertically loaded strip footing using 2D RFEM.

Kozlowska and Vessia (2022) calculated bearing capacity of shallow foundations considering drained and undrained condition using RFEM. He et al. (2023) compared the Load and Resistance Factor Design (LRFD) approach with the RFEM in case of shallow foundation in order to calibrate the LRFD based approach. Teshager et al. (2023) examined settlement of a strip footing placed on a two layered soil profile using random finite element model in conjunction with a hardening soil model. Hoek-brown failure criteria was used to form stability charts (Kumar et al., 2023). Bendriss and Harichane (2023) performed seismic bearing capacity analysis of strip footing resting on soils having random soil properties and pseudo static seismic coefficient.

This study investigates influence of variation of soil properties in bearing capacity and settlement analysis of a strip footing in Bihta site where the construction of new campus of NIT Patna is proposed. The results of this study are obtained by using RFEM program (MRBEAR2D and MRSETL2D) developed by Fenton and Griffith (2008).

To get the response of the system to applied loads, the program makes use of the finite element code. Also, the program makes use of Monte Carlo simulation to estimate the probabilistic response a strip footing against bearing capacity failure of soil as well as the probability of failure against the settlement criteria. This research describes the behavior of a strip footing for NIT Patna, Bihta campus for the first time, and this aspect can be regarded as a major contribution in the form of a case study of a real-life project.

2. Methodology

In this section, the concepts, terms, and the formulations that are used in this study will be introduced. As, in this study of bearing capacity and settlement analysis, soil of spatially varying properties is considered. The first step was to take observations from the site. After obtaining the raw data, a suitable distribution was decided upon for the variable. Then, a random field was defined and a realization was generated using random field generator. Evaluation of the response to this generated input was done next. Generation of the realization and evaluation of the response was repeated for as many times as feasible. This whole process is called Monte Carlo simulation, i.e., producing possible replications of actual site conditions, to be able to study the probabilistic nature of response.

2.1. Selection of a Distribution
In this study, the random process being considered is a continuous state and

continuous space/time random process. Continuous state means that a variable can take any real value while continuous space/time means that the points, at which trials are done, are continuous in space or time. To represent continuous state processes, continuous probability distributions are used.

2.1.1. Normal Distribution

As per central limit theorem, when random variables are added together, they follow a normal distribution. Many natural phenomena in our surrounding are generally a sum of many random variables or involve many accumulating factors and hence, they tend to a normal distribution. A random variable (P) follows a normal distribution for the following form of pdf.

$$f(p) = \frac{1}{\sigma\sqrt{2\pi}} e^{\left[-\left(\frac{1}{2}\right)\left(\frac{p-\mu}{\sigma}\right)^2\right]} \text{ for } -\infty < p < \infty \quad (1)$$

A normal distribution can be completely represented by its mean (μ) and variance (σ^2). When multiple variables are involved, then the mean and variance of each random variable can also be used to show their behavior through normal distribution. The multivariate normal pdf has the following form:

$$f(p_1.p_2.\dots.p_k) = \frac{1}{2\pi^{\frac{k}{2}}} * \frac{1}{|C|^{\frac{1}{2}}} *$$
$$e^{\left\{-\frac{1}{2}(p-\mu)^T C^{-1}(p-\mu)\right\}} \quad (2)$$

where p_i: is the random variable, μ: is the vector of mean values, one for each p_i, C: is the covariance matrix between the p_i and $|C|$ is its determinant. C is a k × k symmetric, positive definite matrix.

2.1.2. Lognormal Distribution

It is a non-negative distribution that can be obtained from normal distributions through simple transformation, If H is a normally distributed random variable, having range -∞ < h < ∞, then $P = \exp[H]$ will have a range $0 \leq p \leq \infty$. This random variable P will be log normally distributed.

Conversely, it can also be said that if

$\ln(P)$ is normally distributed, then P will be log normally distributed. So, if P is log normally distributed random variable, it will have the probability density function.

$$f(p) = \frac{1}{p\sigma_{lnP}\sqrt{2\pi}} e^{\left\{-\frac{1}{2}\left(\frac{\ln p - \mu_{lnP}}{\sigma_{lnP}}\right)^2\right\}} . \quad (3)$$
$$0 \leq p < \infty$$

where $\mu_{lnP} = E[\ln P]$: represents expectation of P and $\sigma_{lnP}^2 Var[\ln P]$: is the mean and variance of $\ln P$ can be found from mean and variance of P with the help of the following relations.

$$\sigma_{lnP}^2 = ln\left(1 + \frac{\sigma_P^2}{\mu_P^2}\right) \quad (4)$$

$$\mu_{lnP} = ln(\mu_P) - \frac{1}{2}\sigma_{lnP}^2 \quad (5)$$

2.1.3. Bounded Tanh Distribution

This distribution can also be derived from normal distribution using the following transformation.

$$P = a + \frac{1}{2}(b-a)\left[1 + tanh\left(\frac{m+sG}{2\pi}\right)\right] \quad (6)$$

where, G: is a normally distributed variable and X: is bounded on the interval (a,b), m: is called location parameter. If $m = 0$, then the distribution will be symmetric about midpoint. s: is called scale parameter and it shows variability of the distribution. The pdf of P is:

$$f_P(p)$$
$$= \frac{\sqrt{\pi}(b-a)}{\sqrt{2}s(p-a)(b-p)} \quad (7)$$
$$\times exp^{\left\{-\frac{1}{2s^2}\left[\pi ln\left(\frac{p-a}{p-b}\right) - m\right]^2\right\}}$$

In this study, cohesion and friction angles are treated as random variables with in bearing capacity analysis while elastic modulus will be random variable in settlement analysis. But normal distribution has a shortcoming that it has non-zero probability of getting negative values. So, to overcome this problem, making use of

lognormal distribution will be very helpful as it only yields positive values (Das et al., 2022). Similarly, for elastic modulus, lognormal distribution will be an appropriate one. As friction angle is going to have both an upper bound and a lower bound, a bounded tanh distribution will be appropriate for it (Pula and Griffiths, 2021). Also, it resembles a beta distribution but obtained from transformation of a random field following normal distribution.

2.2. Defining a Random Field

In the present analysis, the random fields of the parameters involved in the determinations of bearing capacity and settlement of a shallow footing are created to conduct the necessary probabilistic analyses. The random fields used are continuous state-space in nature. Using the assumptions of random field being Gaussian and stationary, the requirements to characterize the field reduces to:

- Mean of the field, μ
- Variance of the field, σ
- Variation of the field in space

The last point can be captured by the covariance function (second moment of field's joint distribution).

2.3. Covariance Function and Correlation Function

It is already known that covariance measures how two variables change together. It is similar to variance for a joint probability distribution function. When more than one random variable is involved, it measures how two random variables changes with respect to each other. If P and Q random variables having joint probability distribution $f_{PQ}\,(p,q)$, then the correlation for random variable P at positions x and x^* can be expressed in terms of variances (i.e., σ_P and σ_Q) as well as the covariance matrix $C(x.x^*)$ in the following way:

$$\rho(x.x^*) = \frac{C(x.x^*)}{\sigma_P(x)\sigma_P(x^*)} \tag{8}$$

This helps in simplifying the probability

models. Markov correlation function can be conveniently used in such cases with the following form:

$$\rho(\tau) = exp^{\left\{-\frac{2|\tau|}{\theta}\right\}} \tag{9}$$

where θ: is the correlation length, the length in the space domain up to which soil properties are significantly correlated. In this study, following correlation function is used for cohesion field.

$$\rho_{lnc}(\tau) = e^{\left\{-\frac{2|\tau|}{\theta_{lnc}}\right\}} \tag{10}$$

where θ_{lnc}: is the correlation length which is defined as the separation between two values of lnc that are significantly correlated and τ: is the separation between two points for which correlation is being computed. A similar correlation function has been used for friction angle (ϕ) field. For elastic modulus field, the following correlation function is used.

$$\rho_{lnE}(\tau) = e^{\left\{-\frac{2|\tau|}{\theta_{lnE}}\right\}} \tag{11}$$

where θ_{lnE}: is defined as the separation between two values of lnE that are significantly correlated. The cross correlation between c and ϕ are investigated at the correlation extremes (-1 and +1) as their correlation has no clear evidence in literature.

2.4. Variance Function

Most of the engineering properties are generally the local averages of some kind. Variance reduction function can be used to represent local averaging nature of any variable as:

$$\gamma(X_1.X_2) = \frac{\theta_1^2\theta_2^2}{4X_1^2X_2^2}\left[\frac{2|X_1|}{\theta_1} + e^{\left\{-\frac{2|X_1|}{\theta_1}\right\}} - 1\right]\left[\frac{2|X_2|}{\theta_2} + e^{\left\{-\frac{2|X_2|}{\theta_2}\right\}} - 1\right] \tag{12}$$

where $X_1 \times X_2$: is the area of the plane for which local averaging is done. The

Gaussian quadrature (numerical method) can also be used to compute the variance function instead of using Eq. (23), for more accurate results.

2.5. Generating a Realization of Random Field Using Local Average Subdivision (LAS) Method

This method of generating realization is fast and accurate, and therefore, has been adopted by many researchers in the past (Fenton and Griffiths, 2008). The majority of the measurements taken in the engineering field are actually the local averages of the property. That is why, using this method of generating realization can yield accurate results even for coarser meshes.

As shown in Figure 1, a normally distributed global average (Z_1^0) is generated with variance being same as derived in local averaging theory with zero mean. Next, the field is split up into four equal parts and then four normally distributed values, Z_1^1, Z_2^1, Z_3^1 and Z_4^1 are generated in such a way that their mean and variances follows the below mentioned criteria:

a) As per local averaging theory, the correct variance must be shown by them.

b) Proper correlation among them must be maintained.

c) Their average must be equal to the parent value, i.e. ¼ ($Z_1^1 + Z_2^1 + Z_3^1 + Z_4^1$) = Z_1^0. Each locally averaged cell thus obtained is again split up into four parts that must be equal and the process is repeated. A 2D LAS algorithm for a sample function is shown in Figure 2.

2.5.1. Covariance Matrix Decomposition

Covariance Matrix Decomposition produces homogeneous random field through a simple direct method. However, it is only useful for small fields. A discrete process of zero mean $Z_i = Z(x_i)$, can be produced as per Eq. (13).
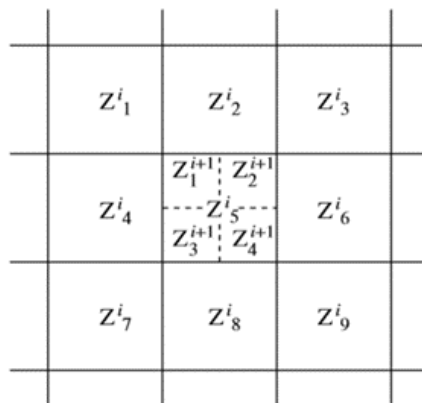
Fig. 1. Local average subdivision in 2 dimensions (Fenton and Griffiths, 2008))
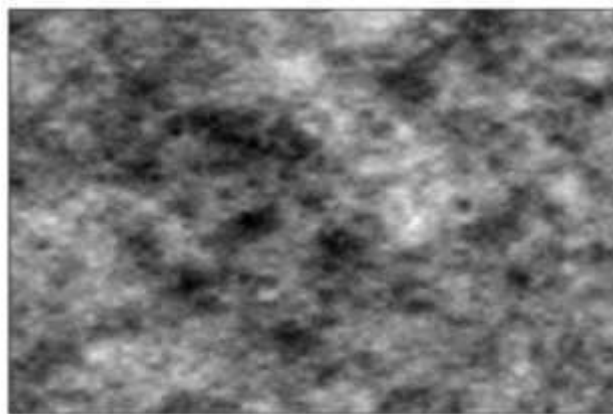
Fig. 2. 2D sample function generated from LAS

$$Z = LU \qquad (13)$$

where L: is a lower triangular matrix and satisfies the relationship $LL^T = C$ and U: is a vector of n random variables of Gaussian nature. Each of them has zero mean and unit variance. C, in this case, represents a covariance matrix having elements $C_{ij} = C(\tau_{ij})$.

2.6. Methods Used in This Study

In this study, in bearing capacity analysis, cross correlation between the field of cohesion and the field of friction angle is implemented using covariance matrix decomposition. The random fields for cohesion, friction angle and elastic modulus are generated using LAS method.

This process involves two steps. In the first step, the underlying Gaussian random field $G_{lnc}(x)$, $G_\phi(x)$ and $G_{lnE}(x)$, having zero mean, unit variance and Markov correlation function, are generated. Then using the following transformations, values of cohesion, c_i (i denotes the ith element), friction angle, ϕ_i and elastic modulus E_i are obtained.

$$c_i = exp^{\{\mu_{lnc} + \sigma_{lnc} \times G_{lnc}(x_i)\}} \qquad (14)$$

$$\phi_i = \phi_{min} + \frac{1}{2}(\phi_{max} - \phi_{min})\left\{1 + tanh\left(\frac{sG_\phi(x_i)}{2\pi}\right)\right\} \qquad (15)$$

$$E_i = exp^{\{\mu_{lnE} + \sigma_{lnE} \times G_{lnE}(x_i)\}} \qquad (16)$$

where x_i: is the centroid of ith element and $H(x_i)$ is the local average value generated by the LAS algorithm.

2.6.1. Finite Element Discretization of the Random Field Domain

In this study, the program by Fenton and Griffiths (2008) makes use of finite element method, is used for both bearing capacity and settlement problems, to obtain response of the system.

In bearing capacity problem, footing is displaced until the failure happens while in settlement problem, a certain amount of load is placed on the footing and the settlement is recorded.

2.6.1.1. Governing Equations

Both the bearing capacity problem and settlement problem are represented using a 2D plane strain model. The governing equations for such a model are:

$$\begin{cases} \frac{\partial \sigma_x}{\partial x} + \frac{\partial \sigma_{xy}}{\partial y} + b_x = \frac{\rho \partial^2 u}{\partial t^2} \frac{\partial \sigma_{xy}}{\partial x} + \frac{\partial \sigma_y}{\partial y} + \\ b_y = \rho \frac{\partial^2 v}{\partial t^2} \end{cases} \qquad (17)$$

where normal stresses are represented by σ_x and σ_y, shear stress on planes xz and yz is represented by σ_{xy}, body forces per unit volume in x and y directions are represented by b_x and b_y, respectively, and displacements in x and y directions are represented by u and v, respectively.

2.6.1.2. Boundary Conditions

In bearing capacity problem, eight-node elements are used while in settlement problem, four-node elements are used for discretizing the domain. The elements used are isoperimetric elements i.e. they use same shape functions to define the element's geometric shape and the displacement within the element.

Boundary conditions have to be satisfied at a part of the boundary or the whole boundary, where a set of differential equations are to be solved. In bearing capacity problem, the left and right faces of the mesh can have translation in vertical direction but restricted against horizontal rotation. The bottom nodes are restricted against rotations as well as translation.

Same boundary conditions apply in case of settlement problem. In this study, for bearing capacity problem, the finite element mesh has 1000 elements. They are laid in such a way that width of the mesh occupies 50 elements while depth of the mesh occupies 20 elements. Each element has a dimension of 0.1 m $\times$ 0.1 m. In settlement problem, the finite element mesh consists of 1200 elements. They are laid in such a way that width of the mesh occupies 60 elements and depth of the mesh occupies 20

elements. Each element has a dimension of 0.05 m × 0.05 m. That makes the mesh 3 m wide and 1 m deep.

2.6.2. Modelling of Soil as a Material

The stress-strain behavior of soil under any general loading is essentially nonlinear. Therefore, it is necessary to consider a proper modelling technique to represent the nonlinear stress-strain behavior of soil. In the present work, Mohr-Coulomb failure criterion is used to represent its constitutive behavior of soil material.

One of the popular methods for modelling material nonlinearity is to use "constant stiffness" approach coupled with altering "loads" vector as described by Smith et al. (2013). In such analysis, global stiffness matrix is only formed once and kept unchanged for rest of load application iterations. It is required to satisfy a properly defined yield criterion (in this case, Mohr-Coulomb failure criteria) to model the nonlinear stress-strain characteristic of the soil material.

The "loads" vector consists of externally applied loads as well as the self-equilibrating "body loads". The self-equilibrating "body loads" vector is managed in such way so that the net loading on the system remains unchanged. The viscoplastic algorithm along with initial stress method is used by RBEAR2D and RSETL2D programs developed by Fenton and Griffiths (2008) to model the nonlinear stress-strain response of soil.

These two programs have been used in the present study. Interested readers can find more information about the application of viscoplastic material nonlinearity for soil modelling in existing literatures (Sienkiewicz et al., 1969, 1977; Sienkiewicz and Ormeau, 1974).

2.6.3. Monte Carlo Simulations

Our objective to perform this simulation is to estimate the variance, mean and probabilities associated with response of system. To analyze the probability of the response of the system through Monte Carlo simulation, it is required to carry out a significant number of simulations. For every simulation, a new realization of the random field is generated and response of the system is recorded. In the bearing capacity analysis, 1000 simulations have been performed for probabilistic analysis. On the other hand, in case of settlement analysis, 5000 simulations have been performed for probabilistic analysis.

2.6.4. Formulations Used for Analysis of Results

2.6.4.1. Bearing Capacity

In literature, following relationship has been used frequently to determine bearing capacity.

$$q_u = cN_c + \underline{q}N_q + \frac{1}{2}B\gamma N_\gamma \qquad (18)$$

where q_u: represents ultimate bearing stress, $\bar{q}$: represents overburden stress, c: represents cohesion, γ: represents unit weight of soil, N_c, N_q and N_γ: represents bearing capacity factors and are the function of ϕ and B: represents footing width. If the weight of the soil assumed to be neglected and that no surcharge is applied on the soil, then the above equation simplifies to:

$$q_u = cN_c \qquad (19)$$

This equation will be employed to get the statistics of bearing capacity. Up on dividing the equation by the cohesion mean, μ_c, it can be expressed in non-dimensional zed form as follows:

$$M_c = \frac{q_u}{\mu_c} = \frac{cN_c}{\mu_c} \qquad (20)$$

where M_c: is the bearing capacity factor and a stochastic equivalent of N_c. Now, it would become necessary to find the distribution of M_c. For that purpose, the distribution assumed for cohesion and friction angle, is lognormal distribution and bounded distribution, respectively, and their expressions are the same as given in Eqs. (14-15). In Eq. (21), geometric averages are

employed for cohesion and friction angle, in order to present an approximate model.

$$M_c = \frac{\bar{c}\overline{N_c}}{\mu_c} \tag{21}$$

where $\overline{N_c} = \frac{e^{\pi tan\bar{\varphi}} tan^2\left(\frac{\pi}{4} + \frac{\bar{\varphi}}{2}\right) - 1}{tan\bar{\varphi}}$, $\bar{c}$ and $\bar{\phi}$: represents geometric averages of cohesion and friction angle. Using probability theory, the following relations showing mean and variance of lnM_c can be found.

$$\mu_{lnM_c} \simeq lnN_c(\mu_\phi) - \frac{1}{2}ln\left(1 + \frac{\sigma_c^2}{\mu_c^2}\right) \tag{22}$$

$$\sigma_{lnM_c}^2 \simeq \gamma(D)\{ln\left(1 + \frac{\sigma_c^2}{\mu_c^2}\right) + \left[\left(\frac{s}{4\pi}\right)(\phi_{max} - \phi_{min})\beta(\mu_\phi)\right]^2\} \tag{23}$$

where $\gamma(D)$: represents variance reduction function and ϕ: is measured in radians. μ_c and μ_ϕ: are the arithmetic mean of cohesion and friction angle fields: $\beta(\phi) = \frac{bd}{bd^2-1}[\pi(1 + a^2)d + 1 + d^2] - \frac{1+a^2}{a}$ here, $a = tan(\phi) \cdot b = e^{\pi a}$ and $d = tan(\frac{\pi}{4} + \frac{\phi}{2})$. All the other symbols have their usual meaning. As the simulation results are in terms of bearing capacity, q_u, following results needs to be used to transform them in terms of bearing capacity factor, M_c, for number of realizations equal to 1000.

$$M_{c_i} = \frac{q_{u_i}}{\mu_c}. \quad i = 1.2. \dots \dots 1000 \tag{24}$$

$$\mu_{lnM_c} = \frac{1}{1000}\sum_{i=1}^{1000} lnM_{c_i}$$
$$\mu_{lnM_c} = \frac{1}{1000}\sum_{i=1}^{1000} ln\left(\frac{q_{u_i}}{\mu_c}\right) \tag{25}$$
$$\mu_{lnM_c} = \mu_{lnq_u} - ln\mu_c$$

$$\sigma_{lnM_c}^2 = \frac{1}{1000}\sum_{i=1}^{1000}(lnM_{c_i} - \mu_{lnM_c}) \tag{26}$$

$$\sigma_{lnM_c}^2 = \frac{1}{1000}\sum_{i=1}^{1000}\left(ln\left(\frac{q_{u_i}}{\mu_c}\right) - \left(\mu_{lnq_u} - ln\mu_c\right)\right)^2 \tag{27}$$

$$\sigma_{lnM_c}^2 = \frac{1}{1000}\sum_{i=1}^{1000}(lnq_{u_i} - \mu_{lnq_u})^2$$
$$\sigma_{lnM_c}^2 = \sigma_{lnq_u}$$

2.6.4.2. Settlement

Settlement problem is linear in many of its parameters. Elastic modulus is one of those parameters. So, a footing founded on a soil layer of uniform (but random) elastic modulus, E, can have the settlement, δ, of following form:

$$\delta = \frac{\delta_{det}\mu_E}{E} \tag{28}$$

where δ_{det}: is the deterministic value of settlement when $E = \mu_E$. Hence:

$$\mu_{ln\delta} = ln(\delta_{det}) + ln(\mu_E) - \mu_{lnE}$$
$$\mu_{ln\delta} = ln(\delta_{det}) + \frac{1}{2}\sigma_{lnE}^2 \tag{29}$$

and as the local averaging is done, the standard deviation of log settlement is given by:

$$\sigma_{ln\delta} = \sqrt{\gamma(B.H)}\sigma_{lnE} \tag{30}$$

where $B{\times}H$: is the averaging region on which variance reduction function, $\gamma(B, H)$ depends.

2.6.5. Chi-Square Test

It is a goodness of fit test used for checking how much a hypothesized distribution fits the actual distribution. To do so, it performs a numerical comparison between predicted histogram and the observed one. Firstly, a histogram having k interval is constructed. Calculating the following value is the next step.

$$\chi^2 = \sum_{j=1}^{k} \frac{(N_j - np_j)^2}{np_j} \tag{31}$$

where N_j: is the number of observations in the jth interval, n: is the total number of observations and p_j: is the probability that an observation lies in j^{th} interval in fitted distribution. The fitted distribution is rejected if:

$$\chi^2 > \chi_{\alpha.k-1}^2 \tag{32}$$

where α: is the level of significance. The

smallest value of α at which the fitted distribution is rejected is called p-value.

3. Results and Discussions

3.1. General

In this section, the results of the study are presented and the efforts are made to explain a certain trend. These results of bearing capacity analysis and settlement analysis are for a strip footing founded on the Bihta site and are carried out by using MRBEAR2D and MRSETL2D part of RFEM software respectively, originally developed by Griffiths and Fenton (2008). The results are presented in two separate sections, one of which is dedicated to bearing capacity analysis while the other has the results of settlement analysis.

In bearing capacity analysis, mean and standard deviation of log bearing capacity factor is plotted for various values of coefficient of variation, correlation length and cross correlation coefficient and also a comparison has been made with the predicted values. In settlement analysis, mean and standard deviation of log settlement is plotted for various values of coefficient of variation, correlation length and cross correlation coefficient. A comparison has also been made with the predicted values. From the data obtained by exploration of Bihta site, on which new NIT Patna building is proposed, the averages for cohesion, friction angle and elastic modulus are calculated and are given below.

In this study, the probabilistic bearing capacity analysis and settlement analysis for a shallow footing is carried out. Hence, while calculating averages, values of soil properties are considered for only up to 2.5 m depth.

$$
\begin{aligned}
\mu_c &\simeq 50\ kN/m^2 \\
\mu_\phi &= 5° \\
\mu_N &= 15
\end{aligned}
\tag{33}
$$

Som and Das (2003) recommended the use of the following empirical relationship to calculate elastic modulus E of soil based on SPT(N) (Standard Penetration Test) value which was originally proposed by Schultz and Menzenbach (1961). The following relation between elastic modulus E and N value is used to calculate elastic modulus:

$$
E = 24 + 5.3N
\tag{34}
$$

where E: is in kg/cm^2. For the present analysis, the average value of elastic modulus (μ_E) is considered to be 10000 kN/m^2.

3.2. Bearing Capacity Analysis
3.2.1. Input Data

In the bearing capacity analysis, a smooth rigid strip footing is considered which is assumed to be founded on weightless soil. Hence a plane stress condition prevailed. In this analysis a Mohr-Coulomb failure criterion is considered along with an elastic-perfectly plastic stress-strain law. A viscoplastic algorithm has been used to accomplish plastic stress redistribution.

The finite element mesh consists of 50 elements wide by 20 elements deep i.e. 1000 elements. Eight node quadrilateral elements are considered and each element has a size of 0.1 m × 0.1 m. The strip footing is assumed to occupy 10 elements which makes its width equals to 1 m.

3.2.1.1. Boundary Conditions

In bearing capacity problem, eight-node elements are used while in settlement problem, four-node elements are used for discretizing the domain. The elements used are isoperimetric elements i.e. they use same shape functions to define the elements geometric shape and the displacement within the element.

Boundary conditions have to be satisfied at a part of the boundary or the whole boundary, where a set of differential equations are to be solved. In bearing capacity problem, the left and right faces of the mesh can have translation in vertical direction but restricted against horizontal

rotation. The bottom nodes are restricted against rotations as well as translation.

Same boundary conditions apply in case of settlement problem. In this study, for bearing capacity problem, the finite element mesh has 1000 elements. They are laid in such a way that width of the mesh occupies 50 elements while depth of the mesh occupies 20 elements. Each element has a dimension of $0.1 \text{ m} \times 0.1 \text{ m}$. Figure 3 shows the geometry of the domain along with dimensions, and the support conditions.

Elastic modulus of soil, Poisson's ratio and dilation angle are assumed to be deterministic. Value of elastic modulus is set at 10000 kN/m^2 as obtained by averaging the field data. Poisson's ratio is set to 0.3 while dilation angle is assumed to be zero. The cohesion and friction angle are set as random parameters. A lognormal distribution is assumed to characterize cohesion while a bounded than distribution is assumed to characterize friction angle.

Local average subdivision method is used to generate random fields of cohesion and friction angle. Covariance matrix decomposition method is used to establish cross correlation between cohesion and friction angle. The scale factor of friction angle is set equal to coefficient of variation of cohesion. The mean of cohesion is set to 50 kN/m^2 as obtained by averaging. The mean of friction angle is set at 5° as obtained by averaging. The upper bound for friction angle is set at 9° and lower bound is set at 1°.

Figures 4 and 5 show the cohesion and friction angle random fields for the 'i^{th}' simulation. Varying values of correlation length, coefficient of variation and cross correlation coefficient are used in this study. Monte Carlo simulations involving 1000 realizations are performed. Each realization has a different soil property random field and hence a different bearing capacity value. In Figure 6, q_u: is the bearing capacity, μ_c: is the mean value of cohesion and δ_v: represents the deformation in the soil. The stress-strain and load-displacement response of soil is nonlinear. Figure 7 plots the deformed finite element mesh of the soil at failure.
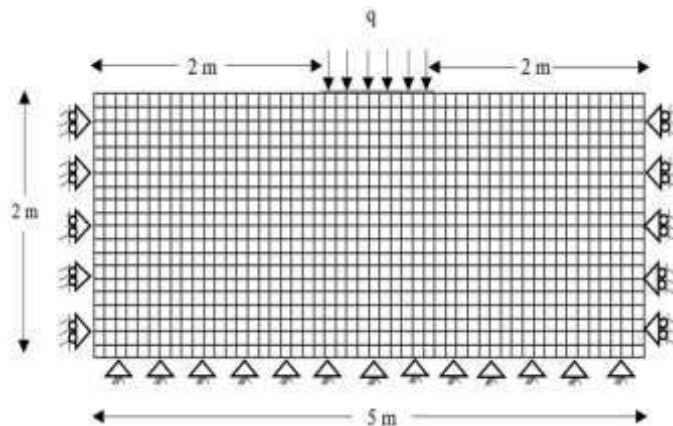
Fig. 3. Geometry of the domain and boundary conditions
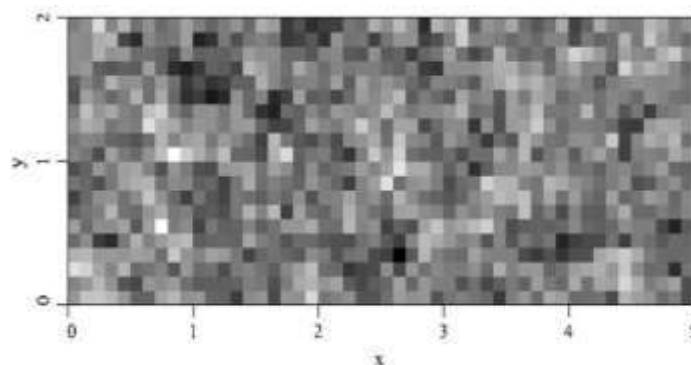
Fig. 4. Cohesion random field
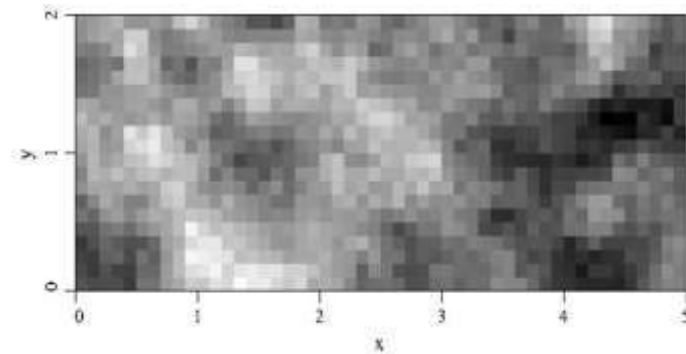
Fig. 5. Friction angle random field
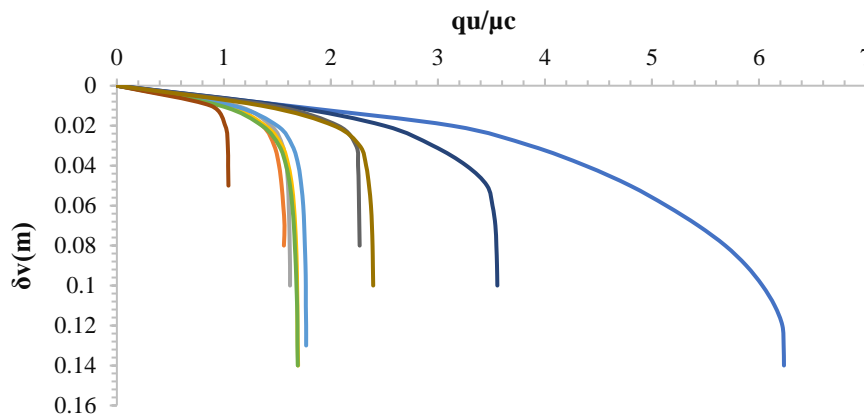
Fig. 6. Load-deformation curves corresponding to different realizations of soil
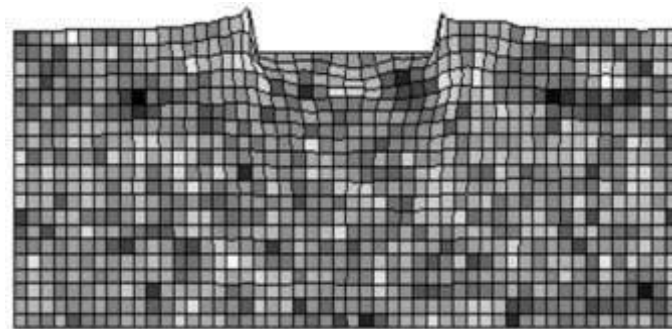
Fig. 7. Deformed finite element mesh at failure of soil having random properties, lighter regions indicate weaker soil

It can be seen that the failure surface is not strictly logarithmic spiral. The reason for the deviation could be that the path followed by the failure surface is through the weakest soil regions which might not be strictly logarithmic spiral in case of spatially variable soil. This deviation indicates that considering the randomness of soil while calculating bearing capacity is important to avoid overestimation or underestimation of N factors (which are calculated by assuming the failure surface to be log-spiral in most cases).

3.2.2. Mean of Log Bearing Capacity Factor vs. Cohesion

In this study, efforts are made to find out the variation of mean of log bearing capacity factor (μ_{lnMc}) with coefficient of variation, correlation length and cross correlation coefficient. A comparison has also been made with the predicted mean as per Eq. (22). Also, as the results of simulation were obtained in terms of bearing capacity, to convert them in terms of log bearing capacity factor, Eq. (25) is used. Results are presented below in

graphical form. P: represents the cross-correlation coefficient while θ represents correlation length.

As predicted by Eq. (22), the value of μ_{lnMc} tends towards deterministic value ln $N_c(\mu_\phi)$, i.e. 1.87008 when variability of soil is small and mean properties are taken everywhere. Several researchers (Haldar and Mahadevan, 2000; Kiureghian and Ke, 1988; Johari et al., 2015) have suggested different choices of the correlation length for use in a RFEM simulation. A ratio varying between 4 and 8 for the correlation length to the length of finite element was suggested by Kiureghian and Ke (1988). However, Fenton and Griffiths (2008) considered correlation length as high as 8 for a similar sized footing considered in the present study, while investigating bearing capacity problem using RFEM.

In this analysis, the correlation length has been varied from 0.1 m to 1.0 m. The minimum correlation length is considered equal to the size of the element used, whereas the maximum correlation length is considered equal to the size of the footing i.e., 1.0 m. However, following the works of Fenton and Griffith (2008), the influence of correlation length $C.L = 8$ is also studied. The variation of μ_{lnMc} vs. dimensionless parameter σ_c/μ_c is shown in Figure 8. As the variability increases, a significant reduction from the Prandtl's solution can be observed. Soils having perfect correlation between cohesion and friction angle appear to be most affected while the least reduction has been observed in negatively correlated soils.

The independent case lies between the two. By some researches in the literature, it has been cited that cohesion and friction angle are negatively correlated (Javankhoshdel and Bathurst, 2015; Liu et al., 2020).
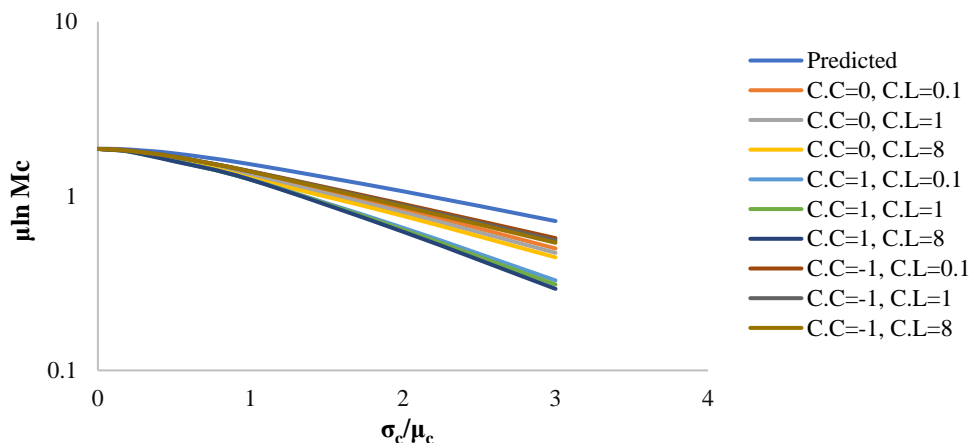
Fig. 8. Sample mean of lnM_c along with the predicted one

So, if the soil parameters are assumed to be uncorrelated while designing, then that will yield results on the conservative side. The effect of θ does not appear too much, but still the values are lower than the predicted ones. Also, Eq. (22) does not incorporate the effect of correlation length. Hence a separate plot is presented in Section 3.2.4 to analyze the effect of correlation length.

3.2.3. Standard Deviation of Log Bearing Capacity Factor vs. Coefficient

of Variation of Soil

Results for standard deviation of log bearing capacity factor are presented as a graphical plot in Figure 9. From the results it is evident that cross-correlation coefficient does not have significant effect on standard deviation of log bearing capacity factor. However, the correlation length does affect it quite significantly. The variation reduction function decreases with decrease in correlation length. From Eq. (23), it is also clear that standard deviation of log bearing capacity factor depends upon

variance reduction function. Hence, with decrease in correlation length, the standard deviation of log bearing capacity factor decreases.

3.2.4. Sample Mean of Log Bearing Capacity Factor vs. Correlation Length

The results presented in this section show how the sample mean of log bearing capacity factor varies with correlation length. The results of the simulation are presented as a graphical plot in Figure 10. When correlation length tends towards infinity, the mean value of log bearing capacity factor tends towards the value as predicted by Eq. (22).
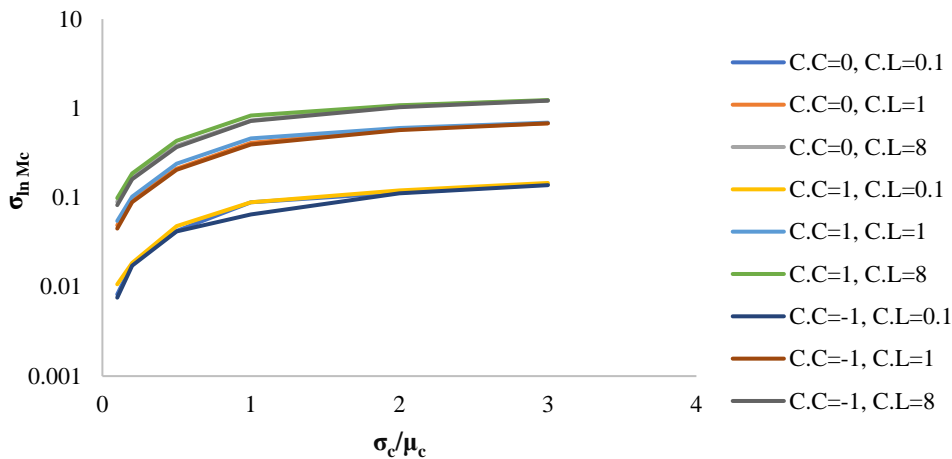
Fig. 9. Sample standard deviation of ln M_c
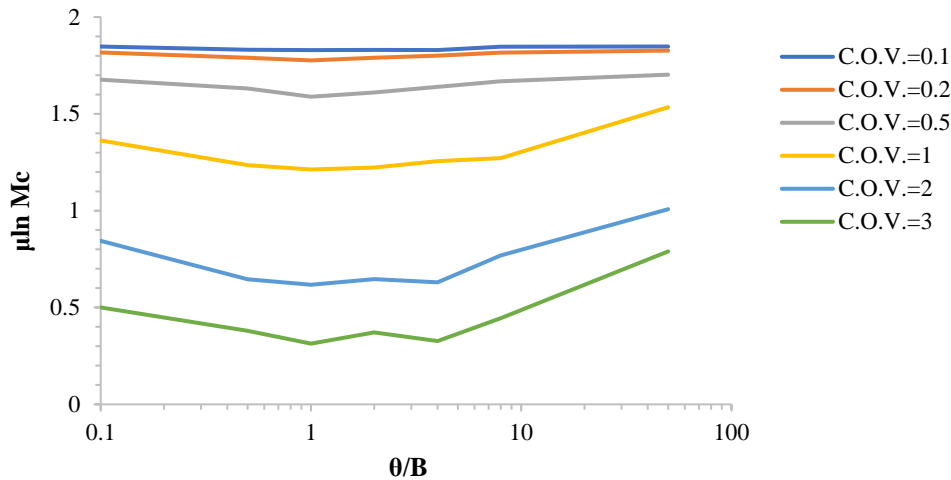
Fig. 10. A plot of sample μ_{lnMc} versus normalized correlation length (θ/B)

An effort can be made to explain the reasoning behind this. When correlation length tends towards infinity, the soil properties becomes spatially constant for a particular realization. Hence the failure surface returns to log spiral and mean values tends towards the predicted ones. It is also evident from the graph that when correlation length tends towards zero (i.e. infinitely rough field), the mean values approaches the predicted ones. In this case, the weakest path becomes very long and

failure surface has to return to log spiral.

From Figure 10, it is clear that for different values of coefficient of variation, the mean of log bearing capacity factor is minimum when correlation length and width of footing are of same order. As the correlation lengths 0.1 and 8 are approximately equally spaced from $\theta = 1$, hence their plots lie so close.

3.2.5. Sample Mean of Log Bearing Capacity Factor vs. Coefficient of

Variation

As observed in the previous plot, when correlation length and width of footing are of same order, the sample mean of log bearing capacity factor deviates most from the value predicted in Eq. (22). Hence the Eq. (22) needs to be modified to give conservative results. This equation is modified in a way to give conservative results for worst correlation length for a zero value of cross correlation coefficient. Weakest path issue and a slight finite element model error are the reasons that such a correction is needed.

The modified equation with empirical correction is:

$$\mu_{lnM_c} \simeq 0.92 lnN_c(\mu_\phi) - 0.7ln\ (1 + \frac{\sigma_c^2}{\mu_c^2}) \qquad (35)$$

Figure 11 shows the plot for μ_{lnMc} for different values of coefficient of variation and θ, is for $\rho = 0$.

3.2.6. Sample Standard Deviation of Log Bearing Capacity Factor vs. Coefficient of Variation

In this section, a comparison is done between the sample standard deviation and the ones predicted from Eq. (23). The domain size required to calculate the variance reduction function is taken as a region having mean wedge zone depth, w and width of $5w$, where w is:

$$w \simeq \frac{1}{2} Btan(\frac{1}{4}\pi + \frac{1}{2}\mu_\phi) \qquad (36)$$

Hence $\gamma(D)$ becomes equal to $\gamma(5w, w)$.

This domain D approximately gives the area involved in failure region. It represents the area between mean log spiral curves on both sides of footing. The results of the simulation along with the predicted ones are given as a graphical plot in Figure 12. They are for a cross-correlation coefficient equals to zero. A close agreement between simulated values and predicted values can easily be seen. The variability involved in the weakest path and the variability involved in any nearby path in a statistically

homogeneous medium will be similar and hence, this close agreement.

3.2.7. Estimation of Probability Density Function of Bearing Capacity

An estimation of probability density function of bearing capacity is done through Monte Carlo simulations and goodness of fit analysis is performed through Chi square test. This test yields a value called p-value. If p-value is high, then goodness of fit is high and vice versa. This test was performed for all the results and an average p value of 30% was obtained, which is high enough for good agreement with hypothesized distribution. Few percentage of simulations have p-value less than 5%. Around 10% of simulations has p-value less than 0.01%. Figures 13a and 13b show two fits with different values of coefficient of variation and correlation length. Even with the smaller p-values, a reasonable fit can be seen. Hence it can be said that bearing capacity approximately follows lognormal distribution.

3.3. Settlement Analysis

3.3.1. Input Data

Two dimensional settlement analysis is done for single footing. Elastic theory is used to calculate both the immediate settlement and consolidation settlement (Terzaghirl, 1943).

The soil on which footing is founded, is assumed to be underlain by bedrock. A 2D plane strain model is used to represent the physical problem. The finite element mesh consists of four nodded quadrilateral elements. Each element is a square of side 0.05 m. The mesh has 100 elements in the horizontal direction and 40 elements in the vertical direction. This makes the width of the mesh equals to 5 m and depth of the mesh equals to 2 m. A fixed load of 1000 kN was applied to the footing. Value of Poisson's ratio was fixed at 0.25. Mean value of elastic modulus was fixed at 10000 kN/m^2. Elastic modulus was assumed to follow lognormal distribution and its

random field was generated using local average subdivision method. Standard deviation of elastic modulus, width of footing and correlation length were varied.

Monte Carlo simulations were used and for each input parameter, 5000 realizations were performed. An RFEM representation of single footing is given in Figure 14.
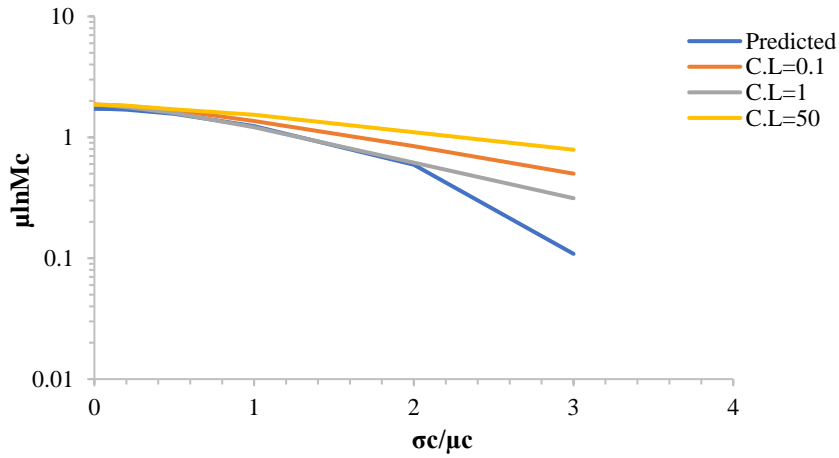
Fig. 11. Plot of Sample and estimated mean of lnM_c versus v, for different θ
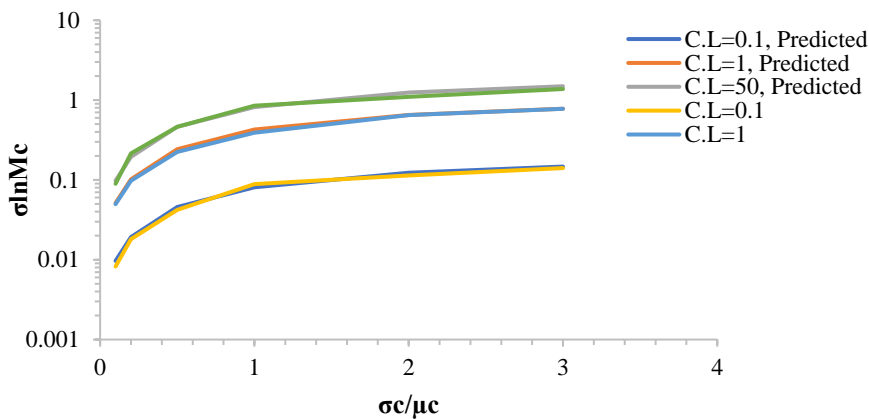
Fig. 12. Plot of Sample and estimated mean of lnM_c versus v, for different θ
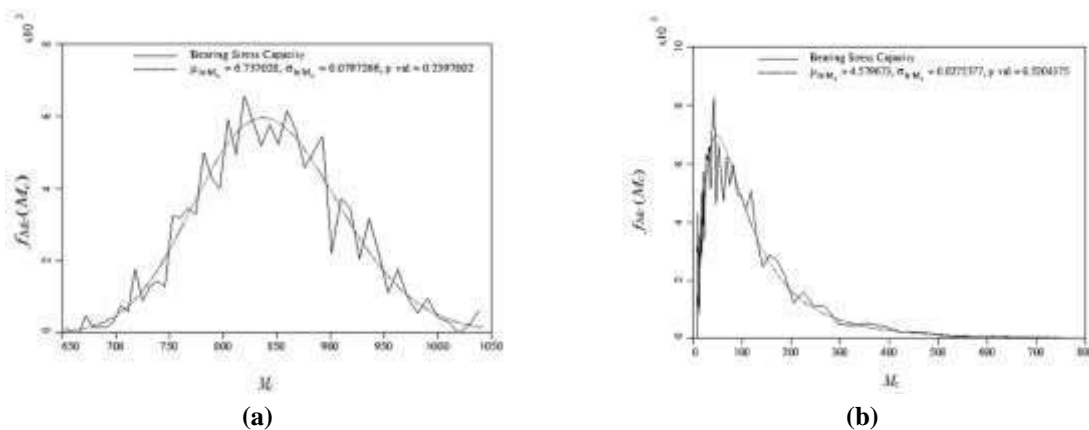
Fig. 13. a) Fitted lognormal distribution for s = σ_c/μ_c = 0.1, θ = 4 and ρ = 0 having large p-value; and b) Fitted lognormal distribution for s = σ_c/μ_c = 5, θ = 1 and ρ = 0 having small p-value

3.3.2. Mean of Log Settlement vs. Variance of Log Elastic Modulus

The results for variation of mean of log

settlement ($m_{ln\delta}$) with respect to variance of log elastic modulus (σ^2_{lnE}) for different values of correlation length are presented as

a graphical plot in Figure 15 to show the variation. These results are for a footing of width 0.1 m. All the correlation length is plotted in the figure but they are not identifiable because they lie very close to each other. This shows that mean of log settlement does not depends very much on the correlation length. As mean of the local averaging process is not affected by correlation length, hence this should not be a surprise. Also, the simulation results show good agreement with the results predicted by Eq. (29).
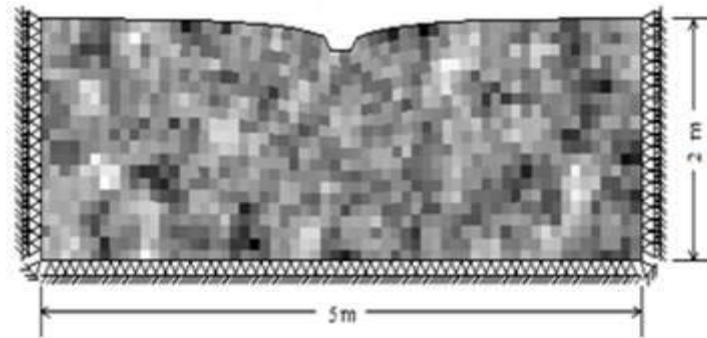
Fig. 14. RFEM representation of single footing
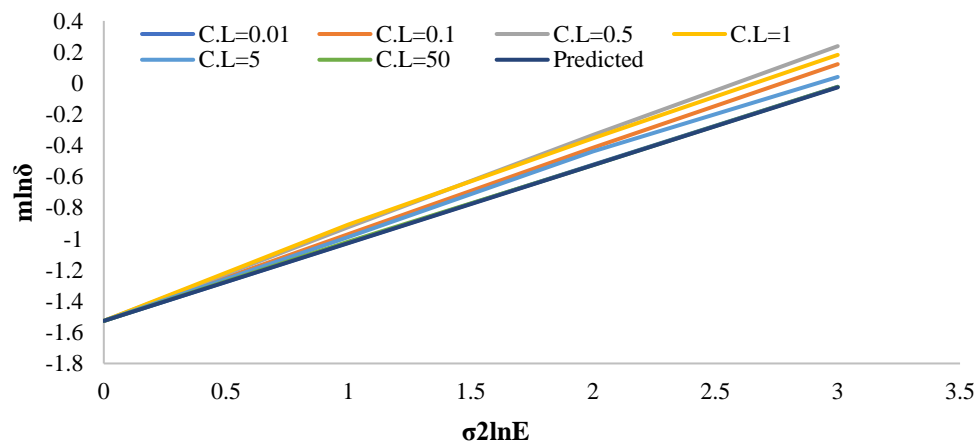
Fig. 15. RFEM representation of single footing

3.3.3. Standard Deviation of Log Settlement vs. Correlation Length for Different Footing Width

The results for simulated standard deviation of log settlement ($s_{ln\delta}$) for different values of correlation length, footing width and coefficient of variation of elastic modulus are shown as a graphical plot in Figure 16 for comparison between simulated results and results predicted from Eq. (30).

As correlation length tends to zero, the values of elastic modulus at any two distinct points becomes independent. Therefore, with decrease in correlation length, the value of variance function decreases. In other words, due to local averaging process, the values of elastic modulus tend towards mean value. Hence, from Eq. (30) it can be said that the standard deviation of log settlement tends towards zero with the mean value approaching deterministic value. While for another limiting case, when correlation length approaches infinity, the elastic modulus field becomes uniform but still random from realization to realization. Variance reduction function for such a field will approach to unity. So basically, the plot is actually showing the variation of variance reduction function with respect to the

correlation length. The agreement between simulated results and predicted results is quite remarkable at small and large correlations lengths and for intermediate correlation lengths also, the agreement is good.

3.3.4. Probability Density Function of Settlement

A histogram of the settlement is shown in Figure 17. This is a normalized histogram as the frequency density plot was desired. Parameters used to produce this histogram are B = 0.1 m, ν = 1 and θ = 0.1. A lognormal distribution is superimposed on it. In appearance, the lognormal distribution seems quite fit. But this simulation had one of the least p-value of Chi square test. For other simulations p-value was not much low. Hence it would be safe to say that settlement follows the lognormal distribution.
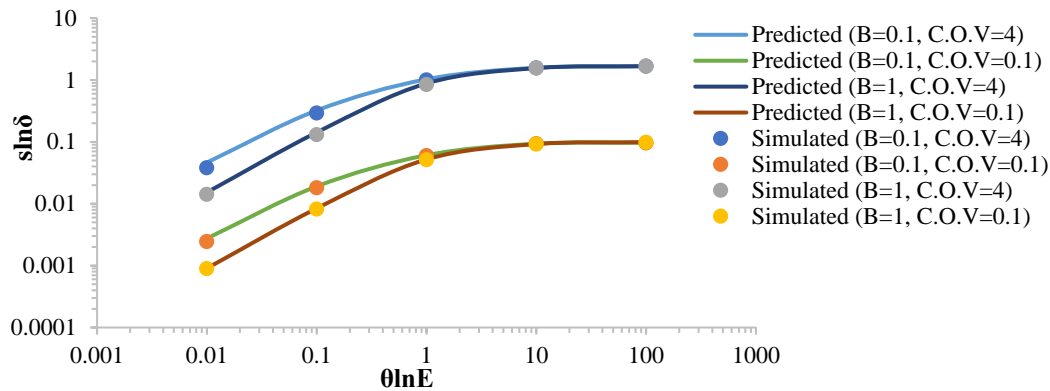
Fig. 16. Comparison of simulated and theoretical standard deviation of log settlement
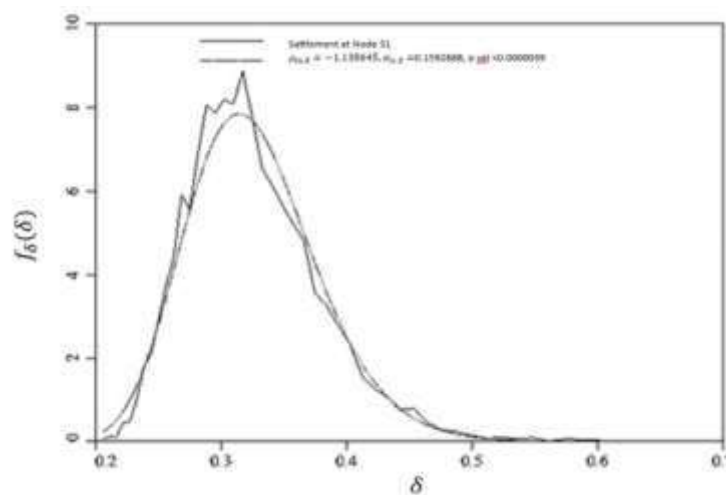
Fig. 17. Frequency density plot of settlement and fitted lognormal distribution

4. Conclusions

The study on the effect of variation of soil properties on baring capacity analysis of a strip footing founded in NIT Patna Bihta campus concludes that on average, the bearing capacity of a soil having spatially varying properties will be less than the bearing capacity calculated from Prandtl's formula using only mean values. When the soil properties become random in nature, the failure surface shifts from logarithmic spiral to a surface which is weaker and exists in the vicinity of the spiral one. To predict the statistics of bearing capacity, it is possible to use Prandtl's formula if the geometric averages are the basis for the properties used in the formula. Although an empirical adjustment is needed for mean. The stochastic behavior of bearing capacity does

not seem to be much affected by cross correlation between cohesion and friction angle.

Anyway, the independent case was found to be conservative. Generally, the information about correlation length at a site is not available. For such instances a worst case correlation length ($\theta \simeq B$) was found. So if the design is based on this correlation length, it would be conservative. The settlement study concludes that lognormal distribution appropriately represents the settlement of the footing placed on the soil having spatially random elastic modulus represented by lognormal distribution itself.

Mean along with the variance of the log elastic modulus field are the parameters that are required to represent mean of log settlement. Using the limiting values of correlation length, it is possible to approximate the mean of log settlement. When log elastic modulus field is locally averaged directly under the footing and its variance is taken, it will produce the quantity that very accurately approximates the standard deviation of log settlement.

5. Funding

6. References

Arel, E. and Mert, A.C. (2021). "Field simulation of settlement analysis for shallow foundation using cone penetration data", *Probabilistic Engineering Mechanics*, 66, 103169, https://doi.org/10.1016/j.probengmech.2021.103169.

Bendriss, F. and Harichane, Z. (2023). "Reliability-based analysis of seismic bearing capacity of shallow strip footings resting on soils with randomly varying geotechnical and earthquake parameters", *Soils and Rocks*, 47, e2024078821, https://doi.org/10.28927/SR.2024.078821.

Chwala, M. (2019). "Undrained bearing capacity of spatially random soil for rectangular footings", *Soil sand Foundations*, 59(5), 15081521,

https://doi.org/10.1016/j.sandf.2019.07.005.

Das, G., Burman, A., Bardhan, A., Kumar, S., Chaudhary, S.S. and Samui, P. (2022). "Risk estimation of soil slope stability problems", *Arabian Journal of Geosciences*, 15(2), 204, https://doi.org/10.1007/s12517-022-09528-y.

Der Kiureghian, A. and Ke, J.B. (1988). "The stochastic finite element method in structural reliability", *Probabilistic Engineering Mechanics*, 3(2), 8391, https://doi.org/10.1016/02668920(88)90019-7

Fenton, G.A. and Griffiths, D.V. (2008). "Risk assessment in geotechnical engineering", In *Risk Assessment in Geotechnical Engineering* (Vol. 461), John Wiley and Sons, New York, https://doi.org/10.1002/9780470284704

Fenton, G.A. and Vanmarcke, E.H. (1990). "Simulation of random fields via local average subdivision", *Journal of Engineering Mechanics*, 116(8), 17331749, https://doi.org/10.1061/(asce)07339399(1990)116:(1733).

Haldar, A. and Mahadevan, S. (2000). *Reliability assessment using stochastic finite element analysis*, John Wiley and Sons, New York.

Halder, K. and Chakraborty, D. (2022). "Probabilistic response of strip footing on reinforced soil slope", *Risk, Reliability and Sustainable Remediation in the Field of Civil and Environmental Engineering*, 116, 333358, https://doi.org/10.1016/B978-0-323-85698-0.00021-6.

He, P., Fenton, G.A. and Griffiths, D.V. (2023). "Load and resistance factor design versus reliability-based design of shallow foundations", *Georisk*, 17(2), 277286. https://doi.org/10.1080/17499518.2022.2083179.

Jamshidi-Chenari, R., Pourvahedi-Roshandeh, S. and Payan, M. (2019). "Stochastic analysis of foundation immediate settlement on heterogeneous spatially random soil considering mechanical anisotropy", *SN Applied Sciences*, 1(7), 1-15, https://doi.org/10.1007/s42452-019-0684-0.

Javankhoshdel, S. and Bathurst, R.J. (2015). "Influence of cross correlation between soil parameters on probability of failure of simple cohesive and c-ϕ slopes", *Canadian Geotechnical Journal*, 53(5), 839-853, https://doi.org/10.1139/cgj-2015-0109.

Jimenez, R. and Sitar, N. (2009). "The importance of distribution types on finite element analyses of foundation settlement", *Computers and Geotechnics*, 36(3), 474483, https://doi.org/10.1016/j.compgeo.2008.05.003

Johari, A., Pour, J.R. and Javadi, A. (2015). "Reliability analysis of static liquefaction of loose sand using the random finite element method", *Engineering Computations*, 32(7),

2100-2119, https://doi.org/10.1108/EC-07-2014-0152.

Johari, A. and Talebi, A. (2021). "Stochastic analysis of piled-raft foundations using the random Finite-Element method", *International Journal of Geomechanics*, 21(4), 4021020, https://doi.org/10.1061/(asce)gm.19435622.0001966.

Kawa, M., and Pula, W. (2020). "3D bearing capacity probabilistic analyses of footings on spatially variable c-φ soil", *Acta Geotechnical*, 15(6), 1453-1466, https://doi.org/10.1007/s11440-019-00853-3.

Kumar, D.R., Samui, P., Wipulanusat, W., Keawsawasvong, S., Sangjinda, K. and Jitchaijaroen, W. (2023). "Soft-computing techniques for predicting seismic bearing capacity of strip footings in slopes", *Buildings*, 13(6), 1371, https://doi.org/10.3390/buildings13061371.

Kumar, V., Burman, A. and Kumar, M. (2023). "Generic form of stability charts using slide software for rock slopes based on the Hoek-Brown failure criterion", *Multiscale and Multidisciplinary Modeling, Experiments and Design*, 7(2), 975-989, https://doi.org/10.1007/S41939-023-00265-7/METRICS.

Liu, X., Tang, X. and Li, D. (2020). "Efficient Bayesian characterization of cohesion and friction angle of soil using parametric bootstrap method", *Bulletin of Engineering Geology and the Environment*, 80(2), 1809-1828, https://doi.org/10.1007/s10064-020-01992-8.

Luo, N. and Bathurst, R.J. (2018). "Deterministic and random FEM analysis of full-scale unreinforced and reinforced embankments", *Geosynthetics International*, 25(2), 164179, https://doi.org/10.1680/jgein.17.00040.

Luo, N. and Luo, Z. (2021). "Reliability analysis of embedded strip footings in rotated anisotropic random fields", *Computers and Geotechnics*, 138, 104338, https://doi.org/10.1016/j.compgeo.2021.104338.

Mellah, R., Auvinet, G. and Masrouri, F. (2000). "Stochastic finite element method applied to non-linear analysis of embankments", *Probabilistic Engineering Mechanics*, 15(3), 251-259, https://doi.org/10.1016/S0266-8920(99)00024-7.

Mofidi Rouchi, J., Farzaneh, O. and Askari, F. (2014). "Bearing capacity of strip footings near slopes using lower bound limit analysis", *Civil Engineering Infrastructures Journal*, 47(1), 89-109, https://doi.org/10.7508/ceij.2014.01.007.

Pan War, V. and Dutta, R.K. (2023). "Development of bearing capacity equation for rectangular footing under inclined loading on layered sand", *Civil Engineering Infrastructures Journal*,

56(1), 173192, https://doi.org/10.22059/CEIJ.2022.339138.1819.

Pieczynska, J., Pula, W., Griffiths, D.V. and Fenton, G.A. (2011). "Probabilistic characteristics of strip footing bearing capacity evaluated by random finite element method", *Proceedings of the 11th International Conference on Applications of Statistics and Probability in Soil and Structural Engineering (ICASP)*, Zurich, 10.

Pieczynska-Kozlowska, J. and Vessia, G. (2022). "Spatially variable soils affecting geotechnical strip foundation design", *Journal of Rock Mechanics and Geotechnical Engineering*, 14(3), 886-895, https://doi.org/10.1016/j.jrmge.2021.10.010.

Pramanik, R., Baidya, D.K. and Dhang, N. (2019). "Implementation of fuzzy reliability analysis for elastic settlement of strip footing on sand considering spatial variability", *International Journal of Geomechanics*, 19(12), 4019126, https://doi.org/10.1061/(asce)gm.19435622.000154.

Pula, W. and Griffiths, D.V. (2021). "Transformations of spatial correlation lengths in random fields", *Computers and Geotechnics*, 136, 104151, https://doi.org/10.1016/j.compgeo.2021.104151.

Pula, W. and Zaskorski, Ł. (2015). "On some methods in safety evaluation in geotechnics", *Stadia geotechnical et Mechanical*, 37(2), 17-32, https://doi.org/10.1515/sgem-2015-0016.

Rezaie Soufi, G., Jamshidi Chenari, R. and Karimpour Fard, M. (2020). "Influence of random heterogeneity of the friction angle on bearing capacity factor Nγ", *Georisk*, 14(1), 69-89, https://doi.org/10.1080/17499518.2019.1566554.

Schultze, E. and Menzenbach, E. (1961). "Standard penetration test and compressibility of soils", *Proceedings of the Fifth International Conference on Soil Mechanics and Foundation Engineering*, 1, 527-532.

Selmi, M., Kormi, T., Hentati, A. and Bel Hadj A.N. (2019). "Capacity assessment of offshore skirted foundations under HM combined loading using RFEM", *Computers and Geotechnics*, 114, 103148, https://doi.org/10.1016/j.compgeo.2019.103148.

Shu, S., Gao, Y., Wu, Y., Ye, Z. and Song, S. (2020). "Bearing capacity and reliability analysis of spud can foundations embedded at various depths based on the non-stationary random finite element method", *Applied Ocean Research*, 100, 102182, https://doi.org/10.1016/j.apor.2020.102182.

Sienkiewicz, O.C., Valliappan, S. and King, I.P. (1969). "Elasto-plastic solutions of engineering problems 'initial stress', finite element approach", *International Journal for Numerical Methods in Engineering*, 1(1), 75-100.

Sienkiewicz, O.C. and Ormeau, I.C. (1974). "Visco-plasticity-plasticity and creep in elastic solids a unified numerical solution approach", *International Journal for Numerical Methods in Engineering*, 8(4), 821-845.

Sienkiewicz, O.C., Humphson, C. and Lewis, R.W. (1977). "Associated and non-associated visco-plasticity and plasticity in soil mechanics", *Geotechnique*, 27(1), 101102, https://doi.org/10.1680/geot.1977.27.1.101.

Smith, I.M., Griffiths, D.V. and Margetts, L. (2013). *Programming the finite element method*, John Wiley and Sons, London.

Som, M.N. and Das, S.C. (2003). *Theory and practice of foundation design*, PHI Learning Pvt, Ltd., Delhi, India.

Tan, X., Hu, X. and Wu, K. (2009). "Fuzzy random finite element reliability analysis of slope stability with fuzzy basic variables and fuzzy states", *Yanshilixue Yu Gongcheng Xuebao/ Chinese Journal of Rock Mechanics and Engineering*, 28 (SUPPL. 2), 3952-3958.

Terzaghi, K. (1943). *Theoretical soil mechanics*, John Wiley and Sons, New York.

Teshager, D.K., Chwała, M. and Puła, W. (2023). "Probabilistic foundation settlement using a hardening soil model on layered and spatially variable soil", In *GeoRisk* 2023, (pp. 447453), https://doi.org/10.3850/978-981-18-51841ms-13-189-cd.

Viviescas, J.C., Mattos, A.J. and Osorio, J.P. (2021). "Uncertainty quantification in the bearing capacity estimation for shallow foundations in sandy soils", *Georisk*, 15(3), 182195, https://doi.org/10.1080/17499518.2020.1753782.

Zhang, Q.L. and Peil, U. (1997). "Random finite element analysis for stochastically responses of structures", *Computers and Structures*, 62(4), 611-616, https://doi.org/10.1016/S0045-7949(96)00246-5.

RESEARCH PAPER

The Effects of Longitudinal Dimension in Three-Dimensional Slope Stability Analysis

Kumar, S.[1]* , Shankar Choudhary, S.[2] and Burman, A.[3]

[1] Ph.D. Instructor, Research Scholar, National Institute of Technology, Patna, India.
[2] Assistant Professor, Department of Civil Engineering, National Institute of Technology, Patna, India.
[3] Associate Professor, Department of Civil Engineering, National Institute of Technology, Patna, India.

ABSTRACT: Of late, three-dimensional slope stability analysis has gained popularity among the geotechnical engineers so that the actual response of slope failure, which essentially occurs in 3D, can be captured. However, three-dimensional slope failure analysis necessitates the proper consideration of the third/longitudinal dimension of the slope. Three-dimensional slope stability analysis can yield erroneous results if inadequate length of the third dimension of the slope is used during analysis. This study employs Bishop's simplified approach to find the minimum length of a 3D soil slope's third/longitudinal direction to be considered during analysis. A parametric study compares the findings of 3D and 2D analyses for different geometries, pore pressure ratios and seismic loading for a cohesive-frictional slope. A total of 15 loading cases have been analyzed to study the convergence behavior of the 3D and 2D Factor of Safety (FS) values for slopes with different inclination angles and longitudinal length-to-height (l/h) ratios. The results presented in this study dictate that the longitudinal/third dimension of a 3D slope model should be at least five times the slope's height for accurate 3D slope analysis. For all loading situations, whether a slope will collapse at the base or toe and the failure mass volumes are estimated. As the base inclination angle increases for a particular slope, the type of failure gradually shifts from base failure to toe failure. The volume of failure mass is seen to follow a decreasing trend with an increase in the slope angle.

Keywords: Limit Equilibrium Method, Safety Factor, Slope Angle, Bishop's Simplified Method, Critical Failure Surface.

1. Introduction

Problems with the stability of slopes are widespread in many civil engineering projects. Construction of large and important projects like embankments, dams, and highways often requires slope stability analysis (Komasi and Beiranvand, 2021; Kalantari and Pourkhosravani, 2011; Soralump et al., 2021). The failure of a slope can cause enormous economic and social losses. The Limit Equilibrium (LE), Strength Reduction Technique based on Finite Element (FE), and Limit Analysis

---

* Corresponding author E-mail: sumitk.phd19.ce@nitp.ac.in

(LA) methods are the most common procedures adopted for analyzing soil slopes (Liu et al., 2020; Qi et al., 2021; Su and Shao, 2021; Wang et al., 2019).

Limit equilibrium procedures have been extensively used in the past as well as in the present day to determine the slope Safety Factor (FS) against failure (Bishop, 1955; Janbu, 1973) and it remains the most preferred method of slope analysis.

Initially, a slope's stability check was formulated in two dimensions (2D), assuming plane strain conditions existed. However, in many situations where the section changes along the longitudinal direction of the slope, the plane strain assumption loses its validity. In such cases, a Three-Dimensional (3D) slope stability analysis is desirable to obtain the correct failure mechanism. In the majority of instances, the width-to-height ratio of the slope is insufficient and varies perpendicular to the movement of the slide.

Therefore, applying 2D studies to 3D problems is not correct but is considered conformist because the end effects are ignored. So, a 2D slope analysis is noticeably conservative when a 3D failure is expected and commonly chosen in the design (Cornforth, 2005). The Limit Equilibrium Method (LEM) remains the most preferred method for analyzing slope stability, despite introducing more advanced numerical methods (Lorig, 1999; Zheng et al., 2018). In reality, though, the failure surfaces of all slope failures are 3D, especially for landslides or natural slopes. Because of this, 3D slope analyses are getting more and more attention with simultaneous advancement in the storage and computing power of modern-day computers. Several researchers presented a detailed and comprehensive account of slope stability analysis (Duncan, 1996; Kumar et al., 2022, 2023). Several processes that account for the third dimension were created by extending their 2D equivalents. Based on the conventional method of slices, many researchers (Baligh and Azzouz, 1975) investigated the slip

surface of a cylinder of limited length with either ellipsoids or cones attached to its ends. Hungr (1987); Chakraborty and Goswami (2021); Johari and Mousavi (2019); Rao et al. (2023); Tozato et al. (2022) had all come up with other 3D methods that are also 3D extensions of limit equilibrium methods.

These methods partly meet equilibrium conditions; in this case, the static indeterminate state would not hold if the failure mass had a symmetrical plane. It is recommended to perform a 3D analysis when performing a back analysis of a slope failure to ensure that the shear strength calculated in the back correctly represents the shear force under three-dimensional loading conditions (Arellano and Stark, 2000). The backwards-calculated shear strength can then be used to fix failed slopes or to design slopes at sites with identical circumstances. The back-calculated shear strengths might be excessively high or unconservative if the 3D end effects are not incorporated. The limit analysis method examines the analysis of slope in terms of energy balance and the analysis is findings are quite accurate. The upper bound LA uses a kinetically admissible velocity field to establish the slope failure mechanism (Qin and Chian, 2018; Wang et al., 2020). The upper bound theorem of LA has been employed to assess slope stability because no assumptions regarding interaction forces and predetermined failure surfaces are required (Michalowski, 2002). Limit Finite Element Analysis (LFEA) was also used to study the slope stability problem. Complex slope geometry and constitutive relationships have been taken into account by many researchers (Loukidis et al., 2003).

The lower bound theorem is appealing because it provides a safe estimate of the load capacity of the slope domain by assuming a rigid plastic material model based on an associated flow rule and most published works show that LA method usually involves finite element discretization of slope problem under consideration. This leads to an optimization

problem with large, sparse constraint matrices (Lyamin and Sloan, 2002).

Many researchers performed 3D slope stability analysis based on an upper bound of the LA method (He et al., 2019; Qian et al., 2019; Wang et al., 2020).

Based on the strength reduction approach, the FEM and Finite Difference (FD) methods, which are undoubtedly superior for deformation studies, have also been applied for slope stability evaluation (Dawson and Roth, 2020; Lin et al., 2020; Yuan et al., 2020). During 3D slope stability analysis, one primary concern is to consider the sufficient extent of the longitudinal dimension of the three-dimensional slope model. If the insufficient length of the longitudinal dimension of the 3D slope model is considered, the analyses will fail to reflect the effects of the third dimension correctly. Chakraborty and Go Swami (2021) recommended that the ratio of the third dimension to the slope's height should be greater than four. These analyses were conducted using 3D LEM using SLIDE 3 software for drained and undrained soil.

The lower bound study performed by Li et al. (2010) showed that 2D solutions could be considered in place of 3D solutions for the preliminary design of the slope when $l/h > 5$. These findings apply to cohesive-frictional drained slopes and purely cohesive undrained slopes. Additionally, this is comparable to the results of Chugh (2003), who analysed frictional soil slopes.

Michalowski and Martel (2010) demonstrated that the suggested 3D FS becomes constant when $B/H = 5.0$, where H: is the slope's height, and B: is its longitudinal length. Based on the studies of previous works related to fixing the length of longitudinal dimension during 3D slope, it is evident that researchers did not consider the effects of pore pressure and seismic loadings.

Usually, the nature of critical failure surface changes as these loadings comprises the loading pore pressure ratio and horizontal earthquake loading. In the present work, a parametric analysis is conducted to determine the significance of 3D longitudinal/end effects by examining the results of 3D and 2D analyses for various geometries, pore pressure ratios and horizontal earthquake loading for cohesive-frictional Slope.

This study aims to establish the minimum extent of the third/longitudinal dimension that must be considered during 3D slope stability analysis for different loading combinations.

2. Research Significance

During a 3D slope stability study, an important consideration is the adequate incorporation of the longitudinal dimension in the three-dimensional slope model. If the longitudinal dimension of the 3D slope model is not adequately fixed, the results of 3D slope analyses will be highly erroneous.

The existing literature on this subject reveal that the effects of only gravity loading has been considered while recommending the required extent of the third dimension of the slope during 3D slope analyses. The effects of other loading parameters such as pore pressure and seismic loading were not accounted for while estimating the required length of the third dimension of the slope. To address these issues, researchers employed various geometries, pore pressure ratios, and horizontal earthquake loading for cohesive-frictional slope.

3. Slope Stability Analysis

This study aims to determine the minimum extent of the third/longitudinal dimension that should be considered during 3D slope stability analysis. While carrying out 3D slope analysis, if the insufficient length of the longitudinal dimension of the slope is considered, it will lead to an incorrect estimation of 3D FS values. Hence, determining the correct minimum longitudinal dimension during 3D slope analysis is paramount. To assess the minimum length of longitudinal dimension

of the slope needed for 3D slope analysis, the convergence behaviour of the ratio of FS values in two and three dimensions are studied against different values of *l/h* where *l* and *h*: represent the longitudinal dimension of a 3D slope and the height of the slope, respectively (refer to Figure 1a). The 2D geometry of slope is shown in Figure 1b. In this study, different slope stability problems are solved in 2D and 3D based on Bishop's method to derive 2D and 3D FS values against sliding. 2D slope stability analyses were carried out using Slope/W software to find the minimum FS of known shear strength parameters along the failure plane. Slope/W permits various methods to determine the factor of safety, but Bishop's Simplified Method (BSM) is used for the the current work. For 3D slope stability, analyses were carried out using the Scoops 3D source program. The investigations have been performed for different slope angles (β).

3.1. 2D FS Determination Using BSM

In this study, the factor of safety of a 2D slope is determined using Slope/W software which permits various methods to determine factor of safety. But in this research work, a well-known limit equilibrium method, i.e., BSM, is used.

This method ensures moment equilibrium of the failure mass is satisfied with any rotation point. Figure 2 represent the free-body diagram of ith slice subjected to all possible combination of forces. In Figure 2, W_i: is weight of the ith slice, $N_i^{'}$: is the effective normal force at the base of the ith slice, S_{mi}: is the mobilized shear force at the base of the ith slice, E_{L_i}: is the interslice normal force acting on the ith slice from the left direction, E_{R_i}: is the interslice normal force acting on the ith slice from right direction, V_{L_i}: is interslice shear force acting on the ith slice from left direction, V_{R_i}: is interslice shear force acting on the ith slice from right direction, k_h: is horizontal earthquake coefficient, *dx*: is width of each slice, β_i: is the length of base of the ith slice, Z_{L_i}: is the perpendicular distance of E_{L_i} from center of rotation, Z_{R_i}: is perpendicular distance of E_{R_i} from center of rotation, x_i: is horizontal distance of the center of ith slice from center of rotation, e_i: is the vertical distance of center of ith slice from center of rotation, r_i: is the perpendicular distance of N_i from center of rotation.
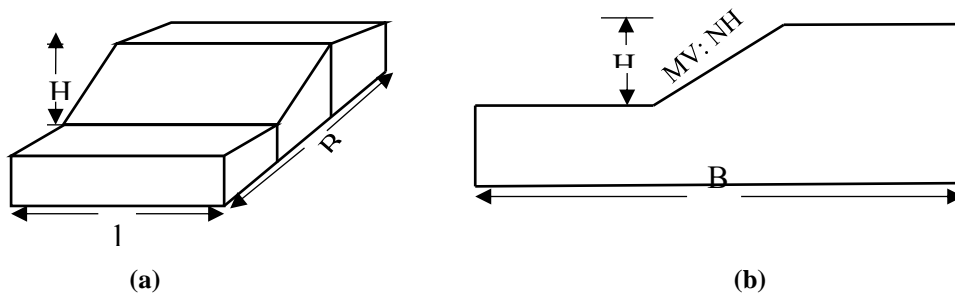
Fig. 1. a) 3D geometry of soil slope; and b) 2D geometry of soil slope
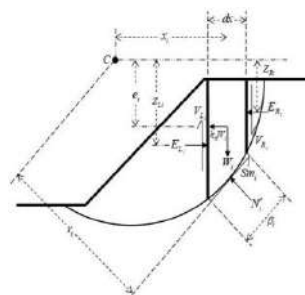
Fig. 2. Free body diagram of ith slice

Bishop's simplified method's final FS expression considering the effects of pore pressure and earthquake forces, is obtained by satisfying the moment equilibrium condition for sliding mass about its center of rotation, given in Eq. (1).

Factor of Safety (FSm) =

$$\frac{\sum\limits_{i=1}^{n\,slices}\left[\left(c'_i\,\beta_i+\left(N_i-u_i\beta_i\right)\tan\phi'_i\right)r_i\right]}{\sum\limits_{i=1}^{n\,slices}\left[W_ix_i+k_hW_ie_i-N_if_i\right]} \quad (1)$$

If a circular failure surface is considered, $f_i = 0.0$ in the above expression. Also, the term u_i: represents the pore water pressure acting on the base of ith slice. In order to determine the pore pressure u, it is necessary to know about the height piezo metric surface of the water. In the absence of such information, an alternative approach to determine pore pressure can be adopted in terms of pore pressure ratio (r_u) defined as:

$$r_u = \frac{u}{\gamma z} \quad (2)$$

Therefore, the expression of FS, in terms of r_u, is expressed as follows:

Factor of Safety (FS) =

$$\frac{\sum\limits_{i=1}^{n\,slices}\left[\left(c'_i\,\beta_i+\left(N_i-\frac{W_ir_u}{d_x}\beta_i\right)\tan\phi'_i\right)r_i\right]}{\sum\limits_{i=1}^{n\,slices}\left[W_ix_i+k_hW_ie_i-N_if_i\right]} \quad (3)$$

where N_i: is the normal force acted at the base of the slice and obtained from the following relation:

$$N_i = \frac{W_i - \frac{\left[c'_i - \frac{W_ir_u\tan\phi'_i}{dx}\right]\beta_i\sin\alpha_i}{FS}}{\cos\alpha_i + \frac{\tan\phi'_i\sin\alpha_i}{FS}} \quad (4)$$

where $\cos\alpha_i + \frac{\tan\phi'_i\sin\alpha_i}{FS} = m_{\alpha i}$ and C': is the effective cohesion of soil, ϕ'_i: is the effective shearing resisting of soil. Also, the summation of the difference between the normal forces over the failure mass, i.e., $\sum(E_{Ri} - E_{Li})$ as well as the summation of shear forces acting on the sides of the columns, i.e., $\sum(V_{Ri} - V_{Li})$ are equated to zero.

3.2. 3D formation of BSM

In this work, the FS of a 3D slope is computed using a Scoops 3D-based computer program. While Scoops 3D provides both Ordinary and Bishop simplified methods for calculating the factor of safety, this study uses Bishop's simplified technique for the assigned problem. Figure 3 illustrates the schematic representation of the free body diagram corresponding to the j, k column, depicting a scenario in which no external force influences the column while subjected to various force combinations.
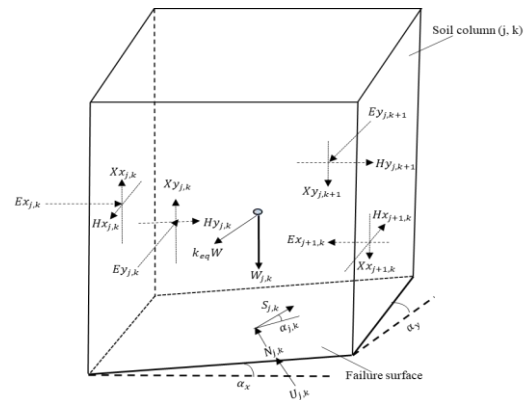
Fig. 3. Illustrating the forces acting on the j,k column

In Figure 3, W: is column's weight, $E_{x_{j,k}}, E_{y_{j,k}}$: denote x and y directions' inter-column normal force, respectively; $H_{x_{j,k}}, H_{y_{j,k}}$: signify horizontal shear forces in the y-z plane, $X_{x_{j,k}}, X_{y_{j,k}}$: represent the inter-column shear forces in the x and z directions, respectively, $N_{j,k}, U_{j,k}$: refer to the effective normal force and the pore water force; $S_{j,k}$: is the mobilized shear force acting on the

column's base; $\alpha_{j,k}$: is the slide angle relative to the x-y plane; α_x, α_y: are the base inclination in the x-z and y-z planes, respectively, at the midpoint of each column. The Scoops 3D program uses the 3D modification of Bishop's 2D formulation, as suggested by earlier studies. The vertical normal force component is found using the vertical force equilibrium equation for a single column (Hungr, 1989) in terms of the trial surface dip angle at the columns base. Moment equilibrium must be maintained according to Bishop's method by equating the global resisting moment to the driving moment. It has been possible to derive the global moment equilibrium for all columns using Eq. (5).

$$\sum M = \sum R_{j.k} \frac{c_{j.k}A_{j.k}+(N_{j.k}-u_{j.k}A_{j.k})\tan\phi_{j.k}}{FS} -$$
$$\sum W_{j.k}R_{j.k}m_z \qquad (5)$$

The vertical force of the equation, as given in Eq. (6), is used to compute the normal force.

$$N_{j.k} = \frac{W_{j.k}-c'_d A_{j.k}m_z + u_{j.k}A_{j.k}\tan\phi'_d m_z}{\cos\varepsilon_{j.k}+\tan\phi'_d m_z} \qquad (6)$$

where, $\cos\varepsilon_{j.k}+\tan\phi'_d m_z = m_{\alpha j.k}$; $c'_d = \frac{c_{j.k}}{FS}$; $\tan\phi'_d = \frac{\tan\phi_{j.k}}{FS}$ and $m_z = \sin\alpha_{j.k}$

Bishop's simplified method's final safety factor expression can be computed as a function of r_u as expressed in Eq. (7).

$$FS = $$
$$\frac{\sum R_{j.k}\left(c_{j.k}A_{j.k}+W_{j.k}\left(1-r_{u_{j.k}}\right)\tan\phi_{j.k}\right)/m_{\alpha j.k}}{\sum W_{j.k}\left[R_{j.k}m_z + k_{eq}e_{j.k}\right]} \qquad (7)$$

where, $c_{j.k}$: is the effective cohesion of soil, $\phi_{j.k}$: is the soil friction angle, $R_{j,k}$: is the distance between the trial slip region and the rotation axis of the *j,k* column; $N_{j,k}$: is the column's normal force; $r_{u_{j.k}}$: is pore pressure ratio; $A_{j,k}$: is the column's trial surface area, $W_{j,k}$: is the column's weight, $\alpha_{j.k}$: is the apparent dip angle between the azimuthal and slip directions, as shown in Figure 3.

3.3. 2D and 3D Slope Geometry Design

For both 2D and 3D slope assessments, the geometry of the domain must be set up first. A method called the Entry and Exit approach is used in 2D slope stability analysis to determine the critical failure surface and associated minimum factor of safety. In Figure 4a, two thick (red) lines run along the ground, representing the range of entry points of the slip circles, whereas the red line on the upper surface represents the range of exit points of the slip circles.

The number of entry and exits can be calculated by specifying increments along these two lines. As seen in Figure 4b, the 2D slip circle comprises vertical slices. In Scoops-3D software, the three-dimensional slope profile is performed using the Digital Elevation Modelling (DEM) technique. DEM is a digital representation of the topographic relief. DEMs are extensively utilized in the field of geomorphology because of their ability to accurately depict diverse landscape features. Regular grids are widely found in the field of digital DEMs and are available in many forms (Xu et al., 2022).

The precision of a DEM is impacted by a range of topographical characteristics, including landforms, altitudes, roughness, and vegetation. The column width, often known as the DEM cell size, is specified by the user. Surface elevation data for DEM cells is included in DEM input files.

The Box Search Method is used in three-dimensional slope stability investigations to find the critical failure surface and calculate the related minimal FS. Figure 5a depicts a three-dimensional search lattice displaying a DEM profile, whereas Figure 5b depicts the DEM cells from a plan perspective. Throughout the search process, Scoops 3D maintains a record of the minimum safety factor computed for each DEM cell among all trial surfaces encompassing that cell.

Each trial surface must be a part of a sphere with a rotational centre point above the DEM and a given radius. So, this helps the search process.
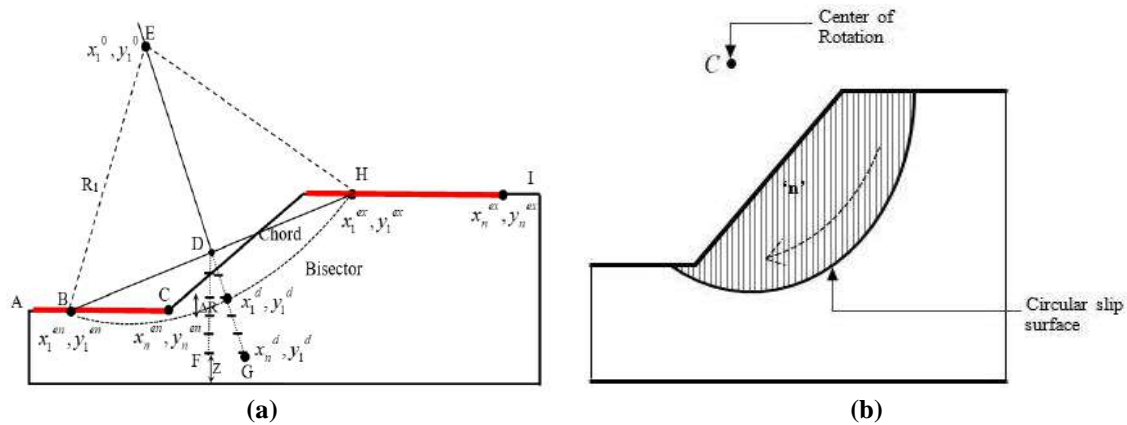
Fig. 4. a) Trial-slip entry and exit areas; and b) 2D slope profile with vertical slice
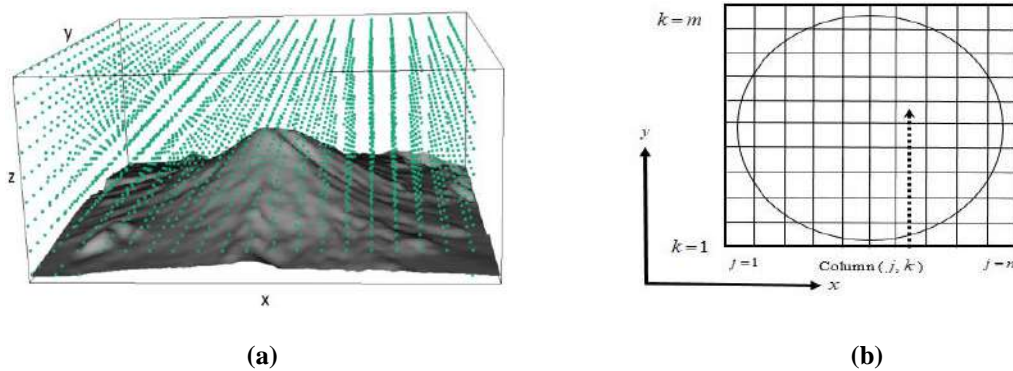
Fig. 5. a) 3D search region of a DEM profile (Reid et al., 2015); and b) Potential sliding mass divided in vertical columns

3.4. Role of longitudinal Extent in 3D Slope Analysis

A parametric study is carried out to examine the importance of 3D longitudinal/end effects by comparing the results of 3D and 2D analyses for different geometries, pore pressure ratio, horizontal earthquake loading and same shear strength parameters along the failure surface. A problem from Arai and Tagyo (1985) work is selected to illustrate the use of parametric research results and the significance of doing a 3D analysis in practice. In this study, the aim is to investigate the convergence behavior of the ratio of the 3D/2D factor of safety in the longitudinal direction, which will help to fix the longitudinal dimension's extent of a 3D slope. At different l/h ratios and for different slope angles, the ratio of 3D and 2D FS values are examined and the l/h ratio at which FS_{3D}/FS_{2D} attains constant value is chosen to fix the minimum extent of the longitudinal dimension of the 3D slope. The ratio of 3D and 2D factor of safeties is expressed as follows:

$$\eta = \frac{FS_{3D}}{FS_{2D}} \tag{8}$$

3.5. Validation of the 2D and 3D Slope Stability Analysis Results

Table 1 demonstrates that the results of the 2D and 3D slope analysis of homogeneous soil with no water table and earthquake loading, developed with Slope/W software and Scoops 3D computer code, match the published results. This exercise determines the validity and precision of the Slope/W and Scoops 3D computer programs. When performing 3D slope analysis, the longitudinal extent of the 3D domain must be fixed correctly in 3D. It is typically accomplished through trial and error by ensuring that the 3D FS value does not change after modifying the slope's longitudinal dimension.

Table 1. Computed 2D and 3D fs with previously reported results

Reference	H (m)	β (°)	c' (kN/m^2)	ϕ' (°)	γ' (kN/m^3)	FS (2D)	FS (3D)	Present study (2D)	Present study (3D)
Arai and Tagyo (1985)	20	33.69	41.65	15	18.816	1.401	-	1.405	-
Reid et al. (2015)	10	26.56	3	19.60	20	0.99	1.04	0.986	1.03
Deng et al. (2015)	20	33.7	42.7	0	18.82	-	1.42	-	1.44
Huang et al. (2002)	12.2	26.5	28.7	20	18.84	-	2.22	-	2.23

For a given height of the slope *H*, and the length of the slope *B* in the longitudinal direction, previous research (Deng et al., 2015; Xie et al., 2006), demonstrates that the predicted 3D FS becomes constant when *B/H* = 4.0. In all instances of 3D slope stability problems, it is a requirement that the width of the third dimension (*B*) be set to a minimum of four times the height (*H*) of the slope.

horizontal seismic coefficient is denoted as k_{eq}, as evident from Eq. (5). The different values of k_h and k_{eq} considered in the present analyses are: 0.0, 0.05, 0.10, 0.15 and 0.20, respectively. Overall, 15 loading combinations have been considered in the current work, out of which the case $r_u = 0.0$ and $k_h = k_{eq} = 0.0$ represents a soil slope subjected to only gravity loading. Figures 6a-6e present the ratio of the 3D factor of safety to the 2D factor of safety, i.e., the η values considering pore pressure ratio $r_u = 0.0$ and different pseudo-static horizontal seismic coefficients $k_h = k_{eq} = 0.0$, 0.05, 0.10, 0.15 and 0.20 with varying inclinations of slopes (1V:3H, 1V:1.5H, 1V:1H and 1V:0.5H) as well as for different l/h ratios (where *l*: is the length in the longitudinal direction and *h*: is the height of the slope). For 1V:3H slope or slope angle $\beta = 18.43^0$, it is observed that the parameter η converges at a l/h value equal to 5.0 or more. When the slope angle β is high, it is noticed that the ratio of the safety factor, i.e., η converges faster and becomes almost constant at $l/h = 3.0$ or more.

4. Results and Discussion

In order to investigate the convergence behavior of the ratio of FS$_{3D}$ and FS$_{2D}$, a soil slope with homogenous material properties is chosen. The material properties considered are effective cohesion $c' = 41.65$ kN/m^2, effective internal friction angle $\phi' = 15^o$ and unit weight $\gamma' = 18.816$ kN/m^3 and height of the slope $h = 20.0$ m. Arai and Tagyo (1985) had already analyzed a 1V: 1.5H homogenous slope with the same material properties. However, a total of four geometric configurations of the slope i.e., 1V:3H, 1V:1.5H, 1V:1H and 1V:0.5H, are analyzed to estimate the 3D and 2D FS ratios i.e., η values as defined in Eq. (6) in the present work. Here, *V* and *H*: denote the slope's vertical and horizontal dimensions, respectively. All these slope problems are analyzed for different loading combinations involving pore pressure and earthquake loadings. The pore pressure loadings on the slope are simulated considering 3 values of pore pressure ratio i.e., $r_u = 0.0$, 0.25 and 0.50. Similarly, the seismic loading on the slope is simulated by applying an equivalent horizontal static loading. For the 2D case, a slice is subjected to horizontal force of value $k_h w_i$, where k_h: is called the pseudo-static horizontal seismic coefficient. In 3D analysis, the same

Similarly, the variation of η values against different l/h ratios is presented for $r_u = 0.25$ and $r_u = 0.50$, considering the same set of $k_h = k_{eq} = 0.0$, 0.05, 0.10, 0.15 and 0.20 values in Figures 7a-7e and 8a-8e, respectively.
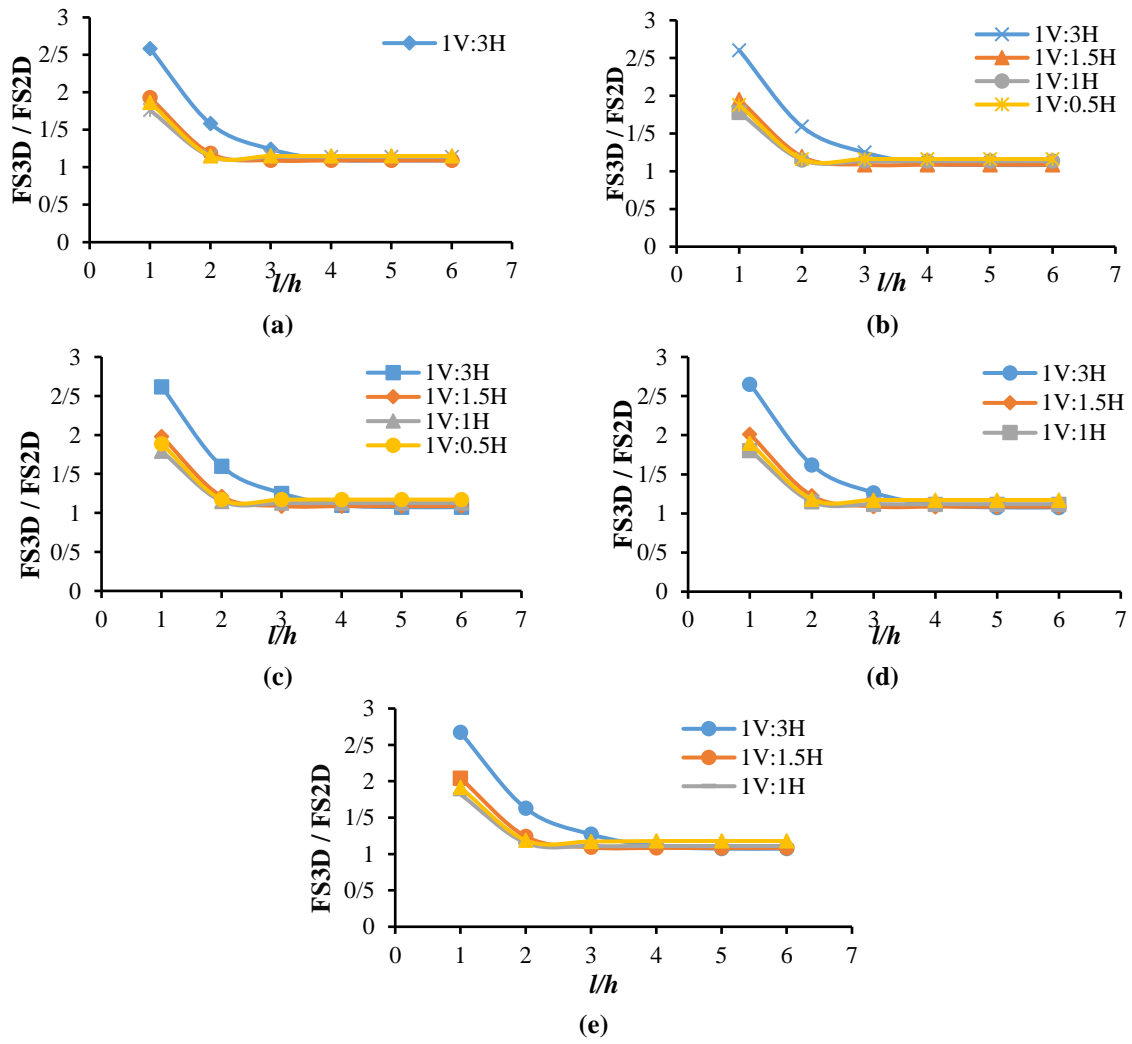
Fig. 6. Influence of l/h on the ratio of 3D/2D FS for condition and: a) $r_u = 0$, $k_{eq} = 0.0$, b) $r_u = 0$, $k_{eq} = 0.05$; c) $r_u = 0$, $k_{eq} = 0.10$; d) $r_u = 0$, $k_{eq} = 0.15$; and e) $r_u = 0$, $k_{eq} = 0.20$

(e)
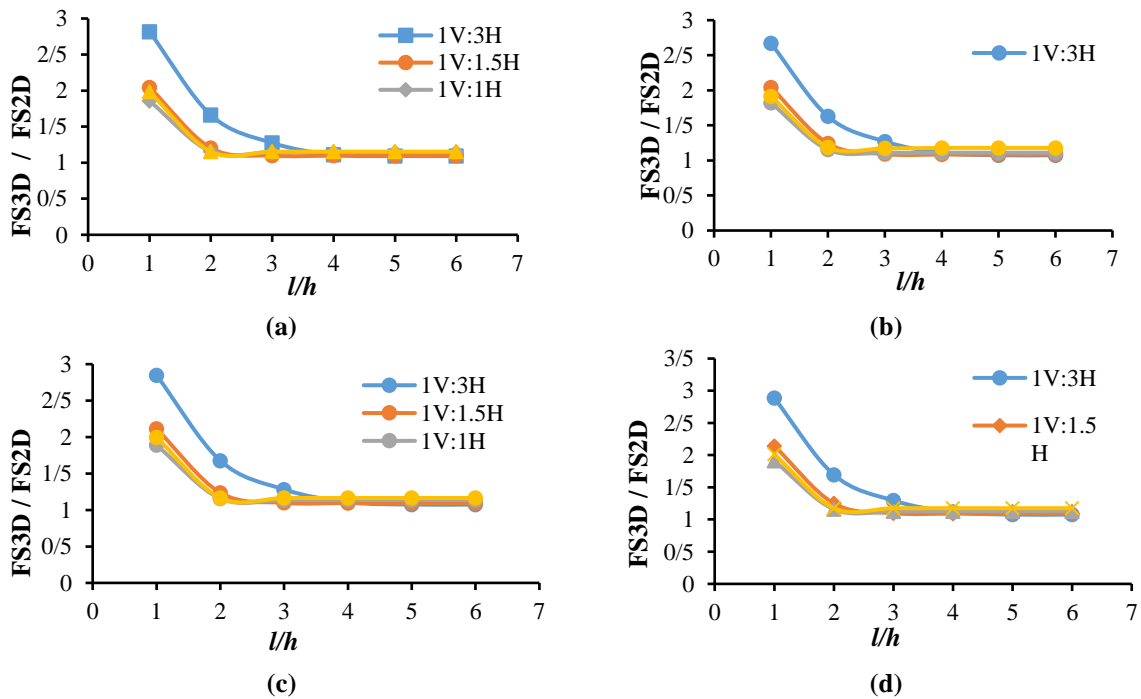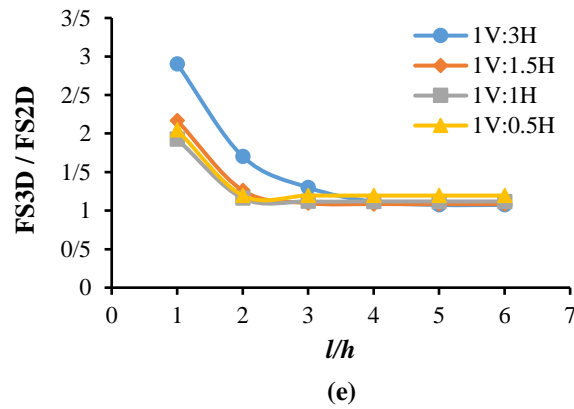
Fig. 7. Influence of *l/h* on the ratio of 3D/2D FS for condition and: a) $r_u = 0.25$, $k_{eq} = 0.0$; b) $r_u = 0.25$, $k_{eq} = 0.05$; c) $r_u = 0.25$, $k_{eq} = 0.10$; d) $r_u = 0.25$, $k_{eq} = 0.15$; and e) $r_u = 0.25$, $k_{eq} = 0.20$

(a)

(b)

(c)

(d)

(e)
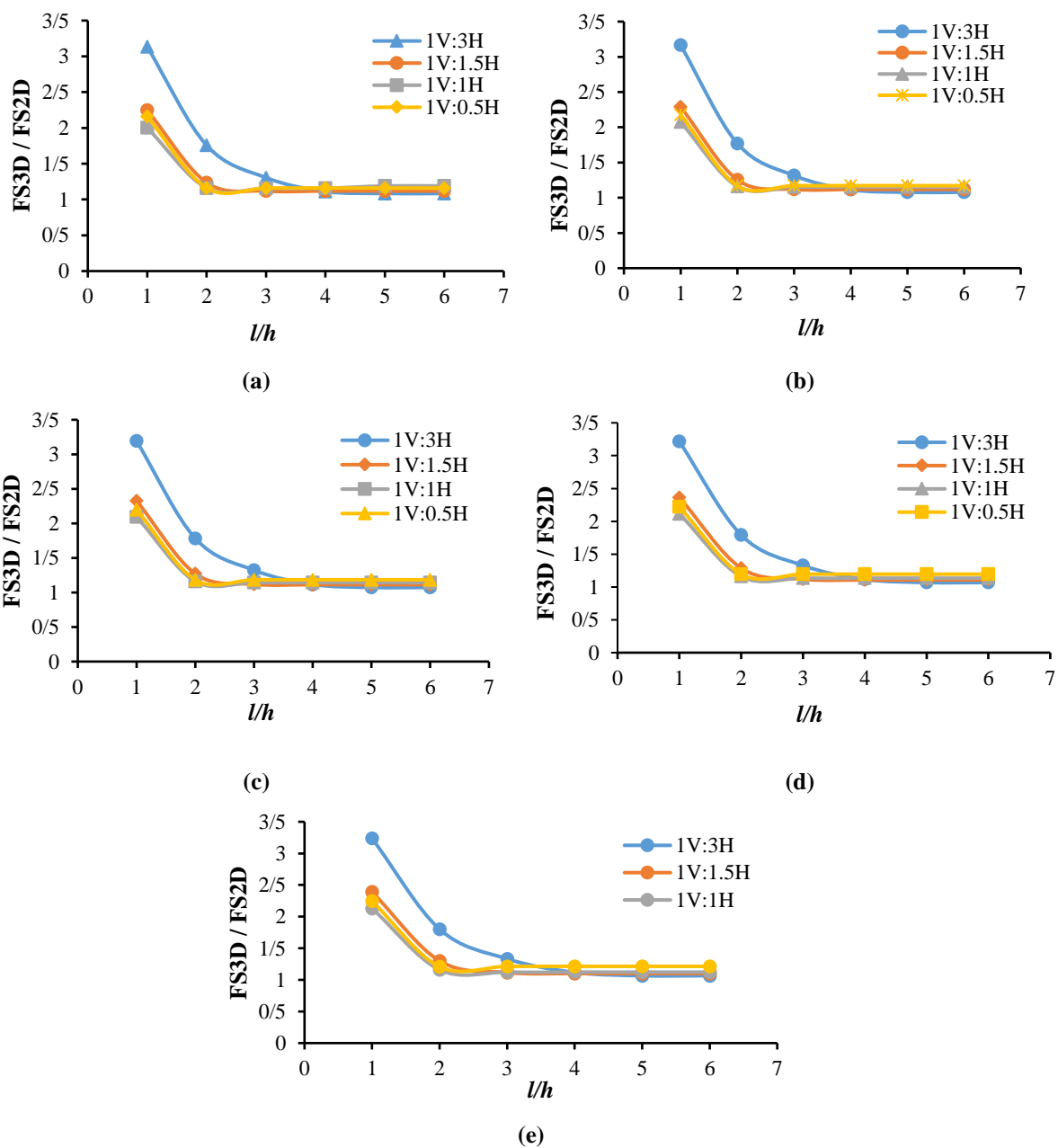
Fig. 8. Influence of *l/h* on the ratio of 3D/2D FS for condition and: a) $r_u = 0.50$, $k_{eq} = 0.0$; b) $r_u = 0.50$, $k_{eq} = 0.05$; c) $r_u = 0.50$, $k_{eq} = 0.10$; d) $r_u = 0.50$, $k_{eq} = 0.15$; and e) $r_u = 0.50$, $k_{eq} = 0.20$

In this case, similar observations regarding the convergence of FS3D and FS2D ratios can be made i.e., η values converge when the longitudinal dimension l is at least equal to $5h$. Therefore, in general, it can be stated the longitudinal dimension l should at least be considered five times the height of the slope (h) to obtain correct 3D FS values.

It is further observed that both 3D and 2D safety factor values decrease with an increase in slope angle β. It is also noted that there is a decrease in the safety factor for both 2D and 3D FS values as the pore pressure ratio increases. However, it has also been observed that an increase in pseudo-static horizontal seismic coefficients leads to a decrease in the safety factor for both 2D and 3D analyses. In most loading scenarios, the ratio FS3D/FS2D is seen to converge at $l/h = 4.0$. However, for the geometric configuration 1V:3H and loading level $r_u = 0.50$, $k_{eq} = 0.20$, it is seen that FS3D/FS2D ratio achieves desired level of convergence at $l/h > 4.0$.

Hence, it is preferred a safe choice of the extent of the third/longitudinal dimension of the slope equaling the 5 times the height of the slope. Studying the nature of 3D failure surfaces for all the loading conditions mentioned earlier is necessary. The present paper considers four different geometric configurations of the slope, i.e., 1V:3H, 1V:1.5H, 1V:1H, and 1V:0.5H. The slope angles for these cases are $\beta = 18.43^0$, 33.69^0, 45.0^0 and 63.43^0, respectively. The analysis performed using $l/h = 5.0$ shows these critical failure surfaces. Figures 9-12 present the Critical Failure Surface (CFS) with minimum FS values obtained from 3D slope analysis. From Figures 9 and 10, the nature of slope failure is identified as a base failure for slopes with $\beta = 18.43^0$ and 33.69^0. Figures 10 and 11 show that for $\beta = 45.0^0$ and 63.43^0, the nature of CFS corresponds to toe failure. Therefore, an observation can be made that the nature of CFS gradually transitions towards toe failure from base failure as the slope angle β increases.
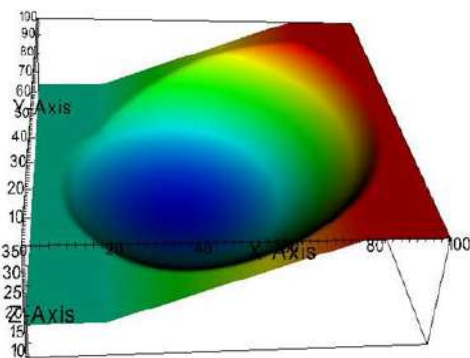
Fig. 9. 3D critical failure surface for slope 1V:3H
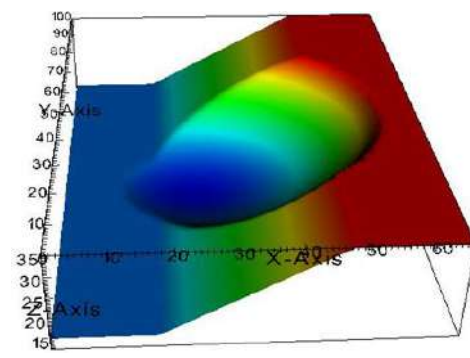
Fig. 10. 3D critical failure surface for slope 1V:1.5H
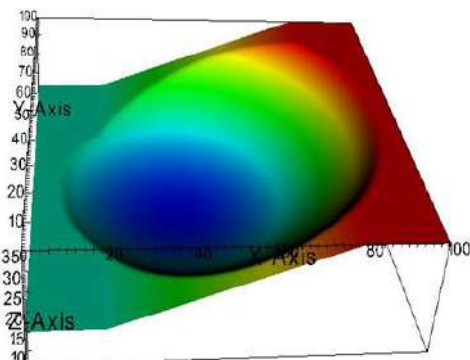
Fig. 11. 3D critical failure surface for slope 1V:1H
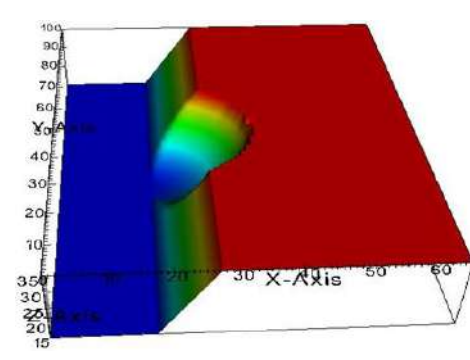
Fig. 12. 3D critical failure surface for slope 1V:0.5H

The corresponding values of the 3D and 2D minimum safety factors are presented in Table 2 for different slope angles, pore pressure ratios, and horizontal earthquake loading combinations. A LEM-based, simplified Bishop's method calculates the minimum safety factors. For various parametric studies, the 2D safety factor is determined using the Slope/W software, while the 3D safety factors are determined using the Scoops 3D computer program. Table 2 only shows the FS3D values for *l/h* = 5.0, as the FS3D values computed for these geometric configurations of the 3D slope show desirable convergence. The safety factor values exhibit a negative correlation with the slope angle, as indicated in Table 2.

It is observed that safety factor values decrease with increased pore pressure ratio and horizontal earthquake loading, as presented in Table 2. It is also verified that the 2D safety factor of a simple slope (1V:1.5H) chosen by Arai and Tagyo (1985) is well matched in this study using Slope/W software. It can be further observed that the failure mass/volume decrease as the slope angle β increases. This fact corresponds to the lowering of the resisting forces, as the resisting forces are usually calculated for the entire failure mass. As a result, it can be stated that when the slope angle β increases, there is an overall decrease in the factor of safety value against sliding failure.

5. Variation of 3D FS with Soil Parameters

To firmly establish the fact that the consideration of proper extent of 3rd dimension of the slope is of utmost importance during 3D slope stability analysis, it is pertinent that convergence behavior of FS3D must be studied when soil parameters are also varying.

For this purpose, the effect of soil characteristics on the evaluated FS values of the 3D slope has been investigated to check the convergence of FS3D. Note that, in this study, five combinations of C', $\emptyset'$ have been considered for three different geometric configurations of the slope, i.e., 1V:1.5H, 1V:1H and vertical cut. The slope angles for these cases are $\beta = 33.69^0, 45.0^0$ and 90^0 respectively. The different combinations of $C', \emptyset'$ and γ' are shown in Table 3. All these slope problems are analyzed for different loading combinations involving pore pressure and earthquake loadings. The pore pressure loadings on the slope are simulated considering two values of pore pressure ratio i.e., $r_u = 0.0$ and 0.50.

Similarly, the seismic loading on the slope is simulated by applying an equivalent horizontal static loading. The different values k_{eq} considered in the present analyses are 0.0 and 0.20, respectively. Overall, two loading combinations have been considered for soil characteristics in the current work, out of which the case $r_u = 0.0$ and $k_{eq} = 0.0$ represents a soil slope subjected to only gravity loading. This investigation aims to check the convergence of 3D factor of safety at different soil characteristics. For this analysis, the convergence of 3D FS is checked at extreme loading conditions for different soil characteristics of soil slopes represented by $r_u = 0.50$ and $k_{eq} = 0.20$.

Figure 13 presents the 3D factor of safety of different soil characteristics for a soil slope subjected to only gravity loading with varying inclinations of slopes (1V:1.5H and 1V:1H) as well as for different l/h ratios (where l is the length in the longitudinal direction and h is the height of the slope).

Table 2. Analysis of 2D and 3D safety factor for different parametric studies

Slope angle (β)	r_u; k_{eq}	FS (2D)	L/H	FS (3D)	Volume of failure soil (m^3)
	0.0; 0.0	2.008		2.188	5.828×10^4
	0.0; 0.0	2.008		2.188	5.828×10^4
	0.0; 0.05	1.727		1.868	6.066×10^4
	0.0; 0.10	1.513		1.626	6.127×10^4
	0.0; 0.15	1.335		1.437	6.272×10^4
	0.0; 0.20	1.199		1.287	6.362×10^4
	0.25; 0.0	1.716		1.875	6.462×10^4
	0.25; 0.05	1.478		1.598	6.562×10^4
1V:3H (18.43°)	0.25; 0.10	1.294	5	1.390	6.751×10^4
	0.25; 0.15	1.141		1.228	6.758×10^4
	0.25; 0.20	1.024		1.099	6.839×10^4
	0.50; 0.0	1.429		1.548	7.549×10^4
	0.50; 0.05	1.224		1.319	7.379×10^4
	0.50; 0.10	1.069		1.146	7.379×10^4
	0.50; 0.15	0.948		1.012	7.467×10^4
	0.50; 0.20	0.850		.9057	7.467×10^4
	0.0; 0.0	1.464		1.596	1.440×10^4
	0.0; 0.05	1.338		1.452	1.664×10^4
	0.0; 0.10	1.221		1.327	1.827×10^4
	0.0; 0.15	1.121		1.217	2.120×10^4
	0.0; 0.20	1.034		1.120	2.347×10^4
	0.25; 0.0	1.264		1.387	1.571×10^4
	0.25; 0.05	1.148		1.258	1.884×10^4
	0.25; 0.10	1.047		1.147	1.884×10^4
1V:1.5H (33.69°)	0.25; 0.15	0.962	5	1.049	2.397×10^4
	0.25; 0.20	0.889		0.964	2.491×10^4
	0.50; 0.0	1.044		1.168	2.107×10^4
	0.50; 0.05	0.945		1.056	2.273×10^4
	0.50; 0.10	0.862		0.959	2.696×10^4
	0.50; 0.15	0.791		0.875	2.743×10^4
	0.50; 0.20	0.731		0.804	2.814×10^4
	0.0; 0.0	1.201		1.365	6.973×10^3
	0.0; 0.05	1.121		1.269	7.473×10^3
	0.0; 0.10	1.049		1.182	8.421×10^3
	0.0; 0.15	0.986		1.103	8.581×10^3
	0.0; 0.20	0.928		1.030	1.041×10^4
	0.25; 0.0	1.034		1.185	7.314×10^3
	0.25; 0.05	0.964		1.101	8.253×10^3
	0.25; 0.10	0.902		1.024	9.102×10^3
	0.25; 0.15	0.846		0.955	9.523×10^3
1V:1H (45°)	0.25; 0.20	0.796	5	0.890	1.099×10^4
	0.50; 0.0	0.862		1.025	7.948×10^3
	0.50; 0.05	0.804		0.926	8.517×10^3
	0.50; 0.10	0.752		0.861	1.011×10^4
	0.50; 0.15	0.706		0.801	1.154×10^4
	0.50; 0.20	0.665		0.746	1.278×10^4
	0.0; 0.0	0.922		1.061	3.675×10^3
	0.0; 0.05	0.872		0.976	3.712×10^3
	0.0; 0.10	0.827		0.968	3.813×10^3
	0.0; 0.15	0.785		0.920	3.953×10^3
	0.0; 0.20	0.746		0.892	4.053×10^3
	0.25; 0.0	0.774		0.901	4.112×10^3
1V:0.5H (63.43°)	0.25; 0.05	0.731	5	0.856	4.153×10^3
	0.25; 0.10	0.691		0.812	4.234×10^3
	0.25; 0.15	0.655		0.782	4.383×10^3
	0.25; 0.20	0.621		0.746	4.453×10^3
	0.50; 0.0	0.626		0.726	4.612×10^3
	0.50; 0.05	0.591		0.690	4.692×10^3
	0.50; 0.10	0.556		0.658	4.709×10^3
	0.50; 0.15	0.525		0.627	4.721×10^3
	0.50; 0.20	0.496		0.602	4.753×10^3

<div align="center">Table 3. Details of C′, Ø′ and γ′ values</div>

Parameter	Cases				
	C 1	C 2	C 3	C 4	C 5
c' (kN/m²)	40	50	60	70	80
ϕ' (°)	20°	15°	10°	5°	0°
γ' (kN/m³)	18.816	18.816	18.816	18.816	18.816

It is noticed that the 3D safety factor converges at l/h = 3.0 or more. Similarly, the variation of 3D FS is presented for r_u = 0.50 and k_{eq} = 0.20 in Figure 14. In this case, similar observations regarding the convergence of FS3D can be made i.e., FS3D values converge when the longitudinal dimension l is at least equal to 5h. Therefore, in general, it can be stated the longitudinal dimension l should at least be considered five times the height of the slope (*h*) to obtain correct 3D FS values.

Figure 15 presents the 3D critical failure surface for Case 1 of vertical cut under gravity loading only (r_u = 0.0; k_{eq} = 0.0). The nature of the failure is observed to be compatible with toe failure.
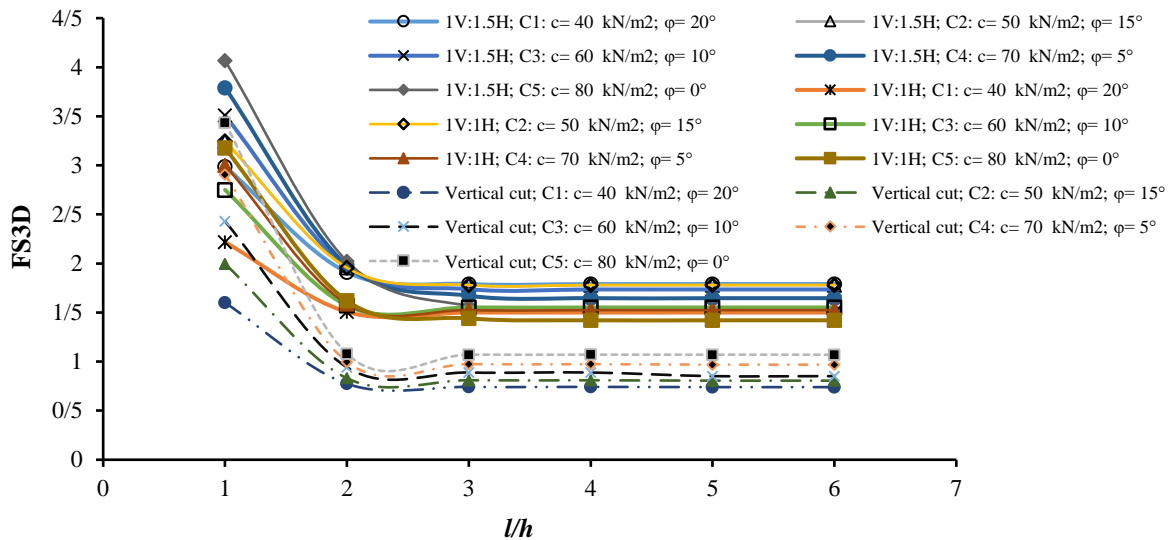
Fig. 13. Variation of FS3D with different *l/h* ratios having different soil properties (r_u = 0.0, k_{eq} = 0.0)
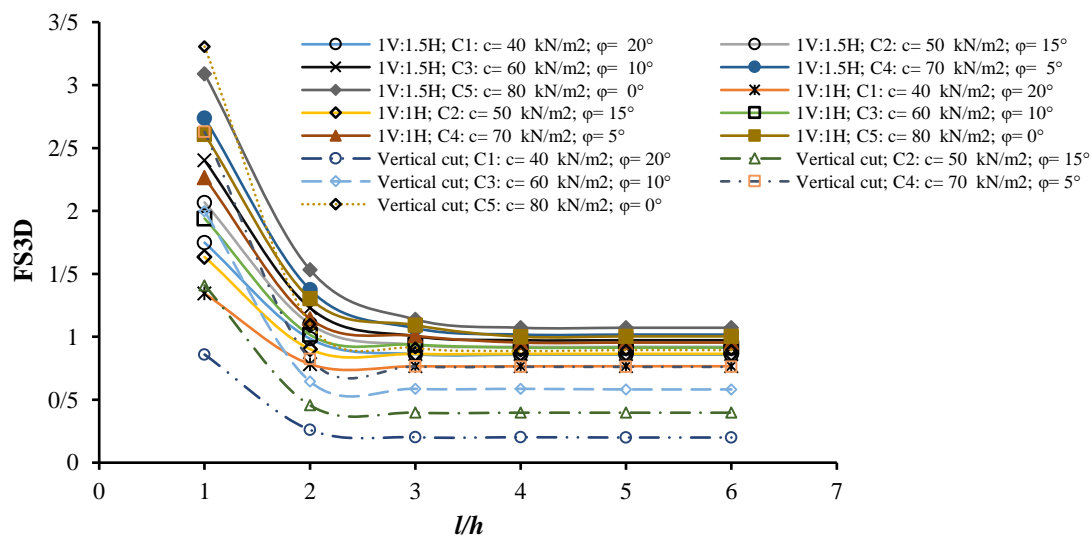
Fig. 14. Variation of FS3D with different *l/h* ratios having different soil properties (r_u = 0.50, k_{eq} = 0.20)
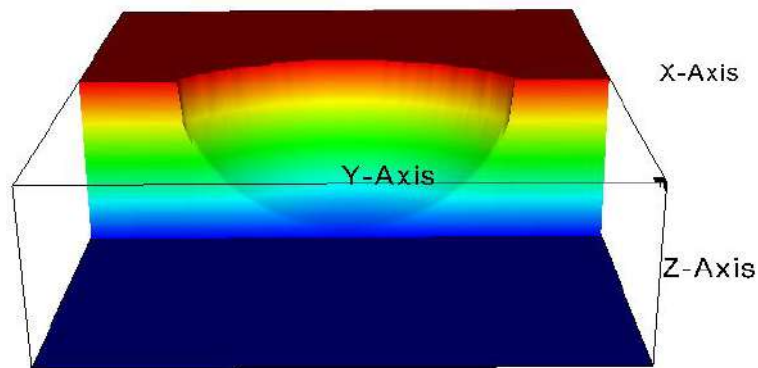
Fig. 15. 3D critical failure surface for Case 1 of vertical cut under gravity loading ($r_u = 0.0$, $k_{eq} = 0.0$)

6. Conclusions

During 3D slope stability analysis, fixing the longitudinal direction of the 3D slope model is a very important task. If the longitudinal dimension of the 3D slope model is selected incorrectly, the 3D slope stability analysis will produce the wrong results. The present paper recommended the longitudinal dimension of a 3D slope by observing the convergence behavior of the ratios FS3D and FS2D.

Based on Bishop's simplified analysis, the limit equilibrium technique was used to determine FS2D. On the other hand, FS3D was determined using a 3D extension of Bishop's simplified method through the Scoops-3D computer program of the USGS. The effects of pore pressure loading were incorporated by considering different pore pressure ratios ($r_u = 0.0$, 0.25, and 0.50, respectively).

The effects of seismic loading were simulated in the analysis by considering different values of horizontal seismic coefficients, i.e., $k_h = k_{eq} = 0.0$, 0.05, 0.10, 0.15, 0.20, etc.

Altogether, 15 loading combination cases were analyzed to study the variation of the ratio of $\eta = $ FS3D/FS2D concerning l/h values for slopes with different inclination angles (β). The above study yielded the following findings:
- It is observed that η converges satisfactorily for all loading combination cases at $l/h = 5.0$.
- The rate of convergence η is faster for steeper slopes and vice-versa.

- The third/longitudinal dimension of the 3D slope model should be considered equal to five times the height of the slope.
- The 2D and 3D safety factors decrease as the slope angle increases for a certain l/h ratio.
- Thus, decrease in the safety factor results from a reduction of the longitudinal extent of the sliding mass. Similarly, the volume of the failure mass from 3D slope analyses decreases simultaneously as the slope angle increases.
- As the resisting force develops along the entire failure mass, there is a corresponding decrease in the generated resisting moment, resulting in an overall decrease in the factor of safety against slope failure.
- For all analysis cases, the type of slope failure is also closely monitored. As the slope angle increases, the nature of the critical failure surface gradually transitions from base failure to toe failure.

7. Data Availability Statement

The authors state that all data related to the present work has been transparently provided in the manuscript. For any other queries, readers are requested to contact the corresponding author.

8. References

Arai, K. and Tagyo, K. (1985). "Determination of noncircular slip surface giving the minimum factor of safety in slope stability analysis", *Soils and Foundations*, 25(1), 43-51, https://doi.org/10.3208/sandf1972.25.43.

Arellano, D. and Stark, T.D. (2000). "Importance of

three-dimensional slope stability analyses in practice", In *Proceedings of Sessions of Geo-Denver 2000-Slope Stability 2000*, (Vol. 289, pp. 18-32), https://doi.org/10.1061/40512(289)2.

Baligh, M.M. and Azzouz, A.S. (1975). "End effects on stability of cohesive slopes", *ASCE Journal of the Geotechnical Engineering Division*, 101(11), 1105-1117, https://doi.org/10.3313/jls1964.23.16.

Bishop, A.W. (1955). "The use of the slip circle in the stability analysis of slopes", *Geotechnique*, 5(1), 7-17, https://doi.org/10.1680/geot.1955.5.1.7.

Cavounidis, S. (1988). "An extension of Bishop's simplified method of slope stability analysis to three dimensions", *Geotechnique*, 38(1), 155-156, https://doi.org/10.1680/geot.1988.38.1.155.

Chakraborty, A. and Goswami, D. (2021). "Three-dimensional (3D) slope stability analysis using stability charts", *International Journal of Geotechnical Engineering*, 15(5), 642-649, https://doi.org/10.1080/19386362.2018.145743.

Chugh, A.K. (2003). "On the boundary conditions in slope stability analysis", *International Journal for Numerical and Analytical Methods in Geomechanics*, 27(11), 905926, https://doi.org/10.1002/nag.305.

Cornforth, D.H. (2005). *Landslides in practice*, Jhon Wiley & Sons, New Jersey.

Dawson, E.M. and Roth, W.H. (1999). *Slope stability analysis with FLAC, In FLAC and Numerical Modeling in Geomechanics,* (pp. 3-9), CRC Press, https://doi.org/10.1201/9781003078531-2.

Deng, D., Zhao, L. and Li, L. (2015). "Limit equilibrium slope stability analysis using the nonlinear strength failure criterion", *Canadian Geotechnical Journal*, 52(5), 563-576, https://doi.org/10.1139/cgj-2014-0111.

Duncan, J.M. (1996). "State of the art: limit equilibrium and finite-element analysis of slopes", *Journal of Geotechnical Engineering*, 122(7), 577-596, https://doi.org/10.1061/(ASCE)0733-9410(1996)122:7(577).

He, Y., Liu, Y., Zhang, Y. and Yuan, R. (2019). "Stability assessment of three-dimensional slopes with cracks", *Engineering Geology*, 252, 136-144, https://doi.org/10.1016/j.enggeo.2019.03.001.

Huang, C.C., Tsai, C.C. and Chen, Y.H. (2002). "Generalized method for three-dimensional slope stability analysis", *Journal of Geotechnical and Geoenvironmental Engineering*, 128(10), 836-848, https://doi.org/10.1061/(asce)10900241(2002)128:10(836).

Janbu, N. (1973). *Slope stability computations*, Wiley (John) & Sons, Incorporated, https://doi.org/10.1016/0148-9062(75)90139-4.

Johari, A. and Mousavi, S. (2019). "An analytical probabilistic analysis of slopes based on limit equilibrium methods", *Bulletin of Engineering Geology and the Environment*, 78, 4333-4347, https://doi.org/10.1007/s10064-018-1408-1.

Kalantari, B. and Pourkhosravani, A. (2011). "A review of current methods for slope stability evaluation", *Electronic Journal of Geotechnical Engineering*, 16, 1245-1254.

Komasi, M. and Beiranvand, B. (2021). "Seepage and stability analysis of the Eyvashan Earth Dam under drawdown conditions", *Civil Engineering Infrastructures Journal*, 54(2), 205-223, https://doi.org/10.22059/ceij.2020.293429.1634.

Kumar, S., Choudhary, S.S. and Burman, A. (2023a). "Recent advances in 3D slope stability analysis: A detailed review", *Modeling Earth Systems and Environment*, 9(2), 14451462, https://doi.org/10.1007/s40808-022-01597-y.

Kumar, S., Choudhary, S.S. and Burman, A. (2023b). "The effect of slope height and angle on the safety factor and modes of failure of 3D slopes analysis using limit equilibrium method", *Beni-Suef University Journal of Basic and Applied Sciences*, 12(1), 84, https://doi.org/10.1186/s43088-023-00423-3.

Li, A.J., Merifield, R.S. and Lyamin, A.V. (2010). "Three-dimensional stability charts for slopes based on limit analysis methods", *Canadian Geotechnical Journal*, 47(12), 1316-1334. https://doi.org/10.1139/T10-030.

Lin, H.D., Wang, W.C. and Li, A.J. (2020). "Investigation of dilatancy angle effects on slope stability using the 3D finite element method strength reduction technique", *Computers and Geotechnics*, 118, 103295, https://doi.org/10.1016/j.compgeo.2019.103295.

Liu, X., Li, D.Q., Cao, Z.J. and Wang, Y. (2020). "Adaptive Monte Carlo simulation method for system reliability analysis of slope stability based on limit equilibrium methods", *Engineering Geology*, 264, 105384, https://doi.org/10.1016/j.enggeo.2019.105384.

Lorig, L. (1999). *Lessons learned from slope stability studies*, In *FLAC and Numerical Modeling in Geomechanics*, (pp.1722), CRC Press, https://doi.org/10.1201/9781003078531-4.

Loukidis, D., Bandini, P. and Salgado, R. (2003). "Comparative study of limit equilibrium, limit analysis and finite element analysis of the seismic stability of slopes", *Geotechnique*, 53(5), 463-479, https://doi.org/10.1007/s12040-019-1314-3.

Lyamin, A.V. and Sloan, S.W. (2002). "Lower bound limit analysis using non-linear programming", *International Journal for Numerical Methods in Engineering*, 55(5), 573-611, https://doi.org/10.1002/nme.511.

Michalowski, R.L. (2002). "Stability charts for

uniform slopes", *Journal of Geotechnical and Geoenvironmental Engineering*, 128(4), 351-355, https://doi.org/10.1061/(ASCE)1090-0241(2002)128:4(351).

Michalowski, R.L. (2010). "Limit analysis and stability charts for 3D slope failures", *Journal of Geotechnical and Geoenvironmental Engineering*, 136(4), 583593, https://doi.org/10.1061/(asce)gt.1943-5606.0000251.

Qi, S., Ling, D., Yao, Q., Lu, G., Yang, X. and Zhou, J.W. (2021). "Evaluating slope stability with 3D limit equilibrium technique and its application to landfill in China", *Engineering Geology*, 280, 105939, https://doi.org/10.1016/j.enggeo.2020.105939.

Qian, Z. G., Li, A.J., Chen, W.C., Lyamin, A.V. and Jiang, J.C. (2019). "An artificial neural network approach to inhomogeneous soil slope stability predictions based on limit analysis methods", *Soils and Foundations*, 59(2), 556-569, https://doi.org/10.1016/j.sandf.2018.10.008.

Qin, C.B., Chian, S.C. and Gazetas, G. (2019). "Kinematic analysis of seismic slope stability with discretisation technique and pseudo-dynamic approach: A new perspective", *Geotechnique*, 69(11), 1031-1033, https://doi.org/10.1680/jgeot.18.D.011.

Rao, B., Burman, A. and Roy, L.B. (2023). "An efficient box search method for limit equilibrium method-based 3D slope stability analysis", *Transportation Infrastructure Geotechnology*, 11(1), 327-358, https://doi.org/10.1007/s40515-023-00285-3.

Reid, M.E., Christian, S.B., Brien, D.L. and Henderson, S. (2015). *Scoops3D-software to analyze three-dimensional slope stability throughout a digital landscape*, (No. 14-A1), U.S. Geological Survey.

Soralump, S., Panthi, K. and Prempramote, S. (2021). "Assessment of the upstream slope failure of a dam due to repeated cyclic drawdown", *Soils and Foundations*, 61(5), 13861398, https://doi.org/10.1016/j.sandf.2021.08.006.

Su, Z. and Shao, L. (2021). "A three-dimensional slope stability analysis method based on finite element method stress analysis", *Engineering Geology*, 280, 105910, https://doi.org/10.1016/j.enggeo.2020.105910.

Tozato, K., Dolojan, N.L. J., Touge, Y., Kure, S., Moriguchi, S., Kawagoe, S., Terada, K. (2022). "Limit equilibrium method-based 3D slope stability analysis for wide area considering influence of rainfall", *Engineering Geology*, 308, 106808, https://doi.org/10.1016/j.enggeo.2022.106808.

Wang, L., Sun, D. and Li, L. (2019). "Three-dimensional, stability of compound slope using limit analysis method", *Canadian Geotechnical Journal*, 56(1), 116-125, https://doi.org/10.1139/cgj-2017-0345.

Wang, L., Sun, D., Yao, Y., Wu, L. and Xu, Y. (2020). "Kinematic limit analysis of three-dimensional unsaturated soil slopes reinforced with a row of piles", *Computers and Geotechnics*, 120, 103428, https://doi.org/10.1016/j.compgeo.2019.103428.

Xie, M., Esaki, T., Qiu, C. and Wang, C. (2006). Geographical information system-based computational implementation and application of spatial three-dimensional slope stability analysis", *Computers and Geotechnics*, 33(4-5), 260-274, https://doi.org/10.1016/j.compgeo.2006.07.003.

Xu, Y., Zhao, M. wei, Lu, J., Wang, C., Jiang, L., Yang, C. and Huang, X.l. (2022). "Methods for the construction of DEM is of artificial slopes considering morphological features and semantic information", *Journal of Mountain Science*, 19(2), 563-577, https://doi.org/10.1007/s11629-021-6831-2.

Yuan, W.H., Liu, K., Zhang, W., Dai, B. and Wang, Y. (2020). "Dynamic modeling of large deformation slope failure using smoothed particle finite element method", *Landslides*, 17(7), 1591-1603, https://doi.org/10.1007/s10346-020-01375-w.

Zheng, Y., Chen, C., Liu, T., Zhang, H., Xia, K. and Liu, F. (2018). "Study on the mechanisms of flexural toppling failure in anti-inclined rock slopes using numerical and limit equilibrium models", *Engineering Geology*, 237, 116-128, https://doi.org/10.1016/j.enggeo.2018.02.006.

Determination of Physical and Mechanical Properties of Fibre-Reinforced Coconut Shell Concrete

Odeyemi, S.O.[1]* , Durosinlorun, A.O.[2] and Wilson, U.N.[3]

[1] Associate Professor, Department of Civil and Environmental Engineering, Kwara State University Malete, Nigeria.

[2] B.Sc. Instructor, Department of Civil and Environmental Engineering, Kwara State University Malete, Nigeria.

[3] Assistant Professor, Department of Civil Engineering, Nigerian Defence Academy, Kaduna, Nigeria.

ABSTRACT: This study investigates the potential of using Elephant Grass Straw (EGS) as a reinforcing fibre in Coconut Shell Concrete (CSC) to enhance its mechanical properties. CSC, with a target compressive strength of 20 N/mm², was prepared using coconut shells as coarse aggregate. EGS was incorporated at varying percentages (1-5% by weight of cement). The coconut shell was tested for its properties while the fresh concrete was tested for its workability. The hardened concrete was tested for its density, water absorption capacity, compressive and split tensile strengths. The results indicate that the addition of EGS negatively impacts the workability, compressive and splitting tensile strengths of the concrete specimens. After 28 days of curing, the control sample (without EGS) exhibited the highest compressive strength at 23.1 N/mm² and splitting tensile strength at 1.74 N/mm². Furthermore, a decrease in compressive strength, workability and density was observed, while water absorption capacity increased with EGS inclusion. Overall, this study demonstrates that the incorporation of EGS does not improve the quality of CSC.

1. Introduction

Concrete is an essential construction material globally, with its utilization on the rise, driven by increased infrastructure and construction activities (Crow, 2008; Odeyemi et al., 2022a). Comprised of fine aggregate (sand), coarse aggregate (crushed stones), cement and water (Bamigboye et al., 2015) its production predominantly relies on traditional, heavy aggregates like gravel and granite, raising environmental concerns due to resource depletion (Kakade and Dhawale, 2015).

Surging construction costs are closely linked to escalating material expenses, with concrete a key concern for budget-conscious firms. Its robust properties, mirroring natural limestone, result from a mix of aggregates and cement. This study explores coconut shells, a lightweight aggregate often disregarded as agricultural waste, offering a potentially cost-effective alternative (Nunes et al., 2020).

---

* Corresponding author E-mail: samson.odeyemi@kwasu.edu.ng

Concrete fibres fall into two main types: steel and natural/synthetic options such as polypropylene, glass, and basalt. Adding these fibres boosts concrete's mechanical properties, notably increasing compressive, tensile and flexural strengths. Steel fibres, for example, enhance post-cracking behaviour, making concrete more ductile and less prone to brittle failure (Modarres and Ghalehnovi, 2023; Wang et al., 2021).

Additionally, polypropylene fibres have been shown to improve the properties of concrete structures and cement-stabilized sand, making them more suitable for harsh environmental conditions (Aisheh et al., 2022; Ghanbari and Bayat, 2022). Glass and basalt fibres, being inorganic materials, enhance the compressive strength of concrete, making it more resilient to heavy loads and impacts (Yahiaoui et al., 2022).

While effective, these options come with high costs, energy-intensive production processes and adverse environmental impacts. As a result, the pursuit of environmentally sustainable alternatives has gained momentum (Odeyemi et al., 2023). A growing body of research explores the feasibility of incorporating annually renewable, cost-effective crops and residues as viable fibre reinforcement in concrete (Adeniyi et al., 2022a,b).

Natural fibres, abundant and budget-friendly in many agricultural regions, are emerging as a promising option. Research indicates that the use of natural fibres in concrete can positively affect its tensile and flexural strength (Ayyappa et al., 2020; Chin et al., 2020; Micelli et al., 2020).

For instance, when coconut coir fibres are introduced into a concrete mix, they enhance its tensile strength while also providing crack control and durability (Yan et al., 2015). While prior studies have explored the use of agricultural waste in concrete as cement or aggregate replacements, there is a dearth of research on the impact of fibre reinforcement on coconut shell concrete. This study aims to address this gap by investigating the effects of fibre reinforcement on Coconut Shell Concrete (CSC).

2. Materials and Methods

The materials for this research are cement, fine aggregate (sand), coconut shell (coarse aggregate) and natural fibre (Elephant Grass straw). Dangote brand of Limestone Portland Cement (LPC), Grade 42.5 R, with a specific gravity of 3.13 was used for the concrete.

Natural sand passing through sieve 4.75 mm having a fine modulus of 2.27, specific gravity 2.63 and water absorption capacity of 2.54% meeting the standard specified in BS EN 12390-2 (2019) was used as fine aggregate. Potable water with a pH of 7 as recommended by Odeyemi (2022b) was used in mixing the concrete.

Coconut shells, sourced from Oja Oba in Ilorin, Kwara State, Nigeria, were manually crushed, water-rinsed, and air-dried for days to eliminate impurities potentially harmful to concrete. Figure 1 illustrates particle size distribution. Table 1 details other properties, determined following BS EN 12620: 2002 + A1: 2008 standards (2008).

The elephant grass straw fibre used for this study was obtained from Malete, Kwara State, Nigeria. The fibre was chopped into small, homogeneous strips and dried for 7 days. Coconut shells served as coarse aggregate, while fibre was added at 1%, 2%, 3%, 4%, and 5% of cement weight. Fresh concrete workability was assessed using the slump method. Cube moulds ($100 \times 100 \times 100$ mm) and cylindrical moulds (100×200 mm) were cleaned, oiled, and filled with well-compacted concrete. Labels indicated fibre content percentages (0%, 1%, 2%, 3%, 4%, and 5%). The mix ratio was 1:0.5:0.5 for cement, sand, and aggregate with a water-binder ratio (w/b) of 0.5 for CSC, targeting a compressive strength of 20 N/mm² (Grade 20).
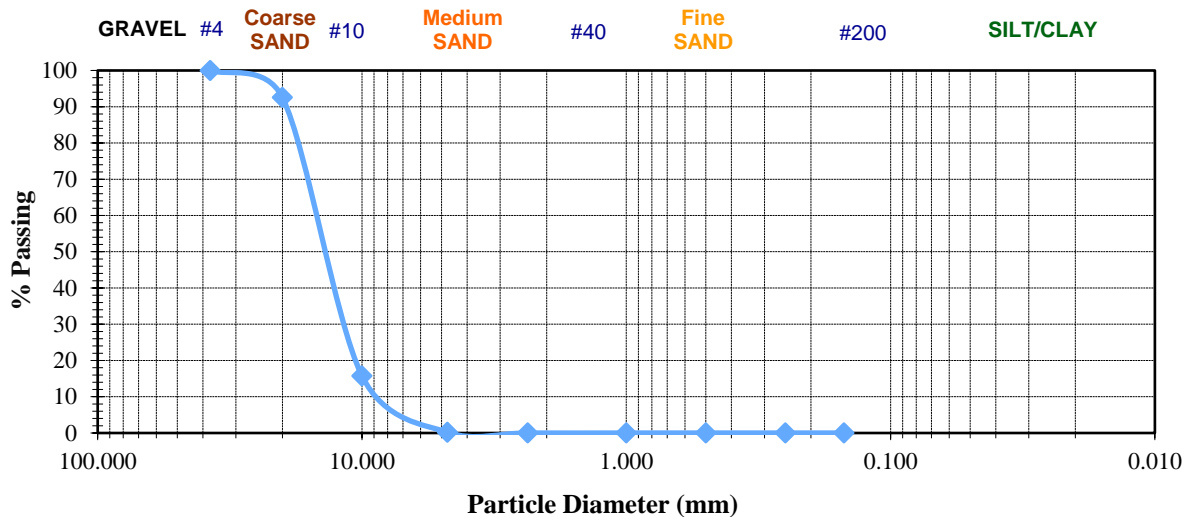
Fig. 1. Particle size distribution curve for coconut shell aggregate

Table 1. Physical properties of coconut shell

S/N	Description	Test value
1	Specific gravity	1.04
2	Water absorption	12%
3	Fineness modulus	6.9
4	Moisture content	15.2%
5	Aggregate impact value	2.56%
6	Abrasion	7.9%
7	Bulk density	717.6 kg/m^3
8	Surface texture	Smooth in inner surface and rough outer surface

After casting, the concrete samples were left to set for 24 hours, then demoulded and immersed in water at 21°C as prescribed by BS EN 12390-2 (2019) for thorough hydration. Before density and water adsorption testing at 28 days, excess moisture was removed by airing the samples for 30 minutes. Compressive and split tensile strengths were evaluated at 7, 28, and 56 days in the University of Ilorin Concrete Laboratory.

2.1. Workability

A slump test of the freshly prepared CSC was carried out to determine the effect of straw fibre on the workability of concrete at the University of Ilorin Concrete Laboratory. The test was conducted following BS EN 12350, 2 (2009) specifications.

2.2. Density

A set of three concrete specimen cylinders were removed from storage after 28 days of curing to undergo an ASTM C 642 density test. By wiping the surfaces dry, these specimens were brought into Saturated Surface Dry (SSD) condition.

The SSD specimen's weight in air (C) was then determined. The samples were then heated to between 100 °C and 110 °C for 24 hours in the oven. The specimen's weight was then determined. This is the samples air-filled oven dry weight (A).

The specimens were then submerged in water in a bucket to determine their weight underwater (D). Water density (ρ) for that temperature was determined using the water's test day temperature (T), which was also recorded. Concrete density was then determined using Eq. (1).

$$\text{Dry density} = \frac{A \times \rho}{(C - D)} \tag{1}$$

where A: is mass of oven-dried sample in the air (gr), C: is mass of saturated surface-dry sample in the air (gr), D: is mass of sample in water after immersion (gr), ρ: is density of water at T °C (kg/m^3).

2.3. Water Absorption

The fine aggregate, CSC and concrete specimens were weighed and given the designation (A) to calculate the aggregates water absorption. These samples were placed in an oven for 24 hours to dry before being removed and allowed to cool at room temperature. To achieve saturation, the aggregate samples were removed from the oven, placed in pans and left submerged in water for 24 hours. When the samples were completely soaked, they were surface-dried by rolling them in a towel until all observable water films were gone.

Surface-dry saturated sample weight was calculated and given the letter (B) designation. Eq. (2) was used to determine the aggregates water absorption capacity in percentage.

$$\text{Water absorption} = \frac{(A-B)}{B} \times 100\% \qquad (2)$$

2.4. Compressive and Split Tensile Strength

Similar to the density test, a set of three concrete specimens each was prepared for the compressive strength and split tensile test after 7, 28, and 56 days of curing following the procedure in BS EN 12390-3 (2019) and BS EN 12390-6 (BS EN 12390-6:2000, 2000).

According to standards, the cube's length and cylinder's diameters were measured and their cross-sectional areas were calculated. Compressive load was applied to specimens using a Universal Testing Machine (UTM) at the desired loading rate. The specimens' axis was correctly aligned, the specimens were positioned inside the bearing blocks and compression was then applied. By dividing the greatest force attained during the test by the specimen's cross-sectional area, the compressive strength and split tensile of the specimen were determined by the UTM.

3. Results and Discussion

3.1. Workability

The results of the slump test in this study, presented in Figure 2, show that as the quantity of straw increases, the workability of the concrete decreases which is evident with the reduction in the slump height. This result follows the same trend as the one reported by Olanipekun et al. (2006).
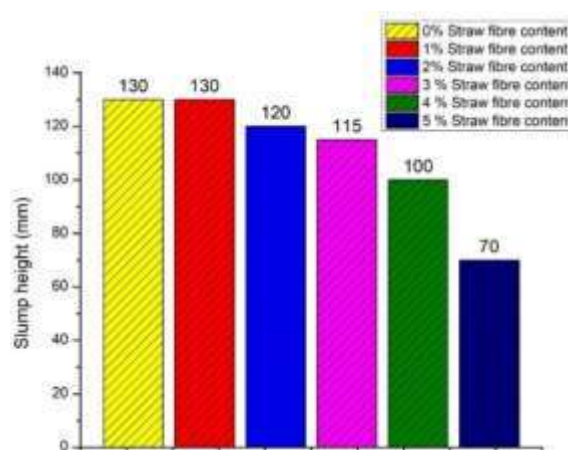
Fig. 2. Slump for CSC with different percentages of straw fibre

3.2. Density

Figure 3 shows the density of the concrete samples with varying percentages of straws. The density of the concrete specimen was found to range from 1989.7 to 2103.54 kg/m³ with different straw fibre

content.

The maximum density of 2103.54 kg/m³ was obtained at 0% replacement. The minimum density of 1989.7 kg/m³ was obtained at 5% replacement. It was observed that as the straw content

increased, the density of the concrete reduced.

3.3. Water Absorption Test

At 28 days after curing, the samples were tested for water absorption capacity.

Figure 4 shows how different percentages of straw fibre content affected water absorption. The percentage of water absorption increased as the percentage of straw fibre increased with CSC.
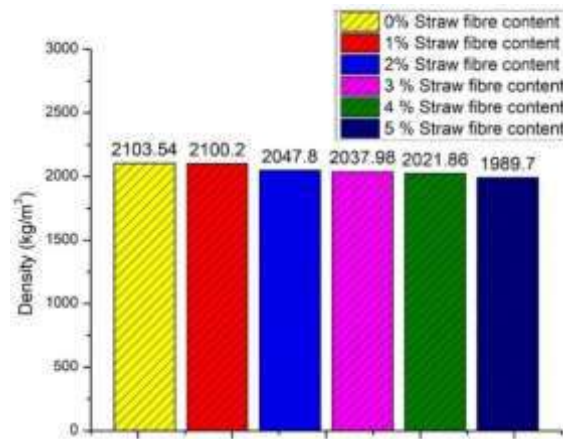
Fig. 3. Density of CSC with straw fibre content (%) at 28 days of curing
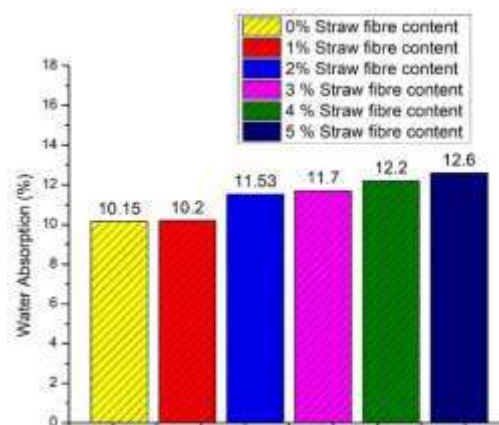
Fig. 4. Water Absorption Capacity of CSC with varying straw fibre content (%)

The highest water absorption was found in CSC with a straw fibre content of 5%, followed by 4%, 3%, 2%, 1% and 0%. The maximum absorption required for lightweight aggregate concrete is 45% (Domagała, 2015), indicating that the specimens meet the requirements.

3.4. Hardened Properties (Compressive Strength and Split Tensile Strength)

Figure 5 shows the compressive strength and split tensile strength of the CSC specimens at 7, 28, and 56 days of curing. In Figure 5a, the correlation between compressive strength and split tensile of CSC with straw fiber content at 7

days shows a consistent decline in strengths as straw content increases. The highest compressive strength (18.3 N/mm²) occurs at 0% straw, dropping to 6.27 N/mm² at 5% straw. Similar trends are observed in split tensile strength. Figure 5b at 28 days depicts a decline in compressive and split tensile strengths with increasing straw content, reaching 23.1 N/mm² and 1.74 N/mm², respectively, at 0% straw.

Figure 5c at 56 days shows the highest compressive strength (23.03 N/mm²) and splitting tensile strength (1.71 N/mm²) at 1% straw, decreasing to 10.53 N/mm² and 1.01 N/mm² at 5% straw. Results indicate that exceeding 1% straw adversely affects

compressive strength, while the water absorption capacity and straw fiber addition contribute to a sudden decrease in strength at 56 days. This study suggests that

maintaining straw fiber below 1% in the mix ratio can yield Grade 20 lightweight concretes, with compressive strength increasing with age.

(a)

(b)

(c)
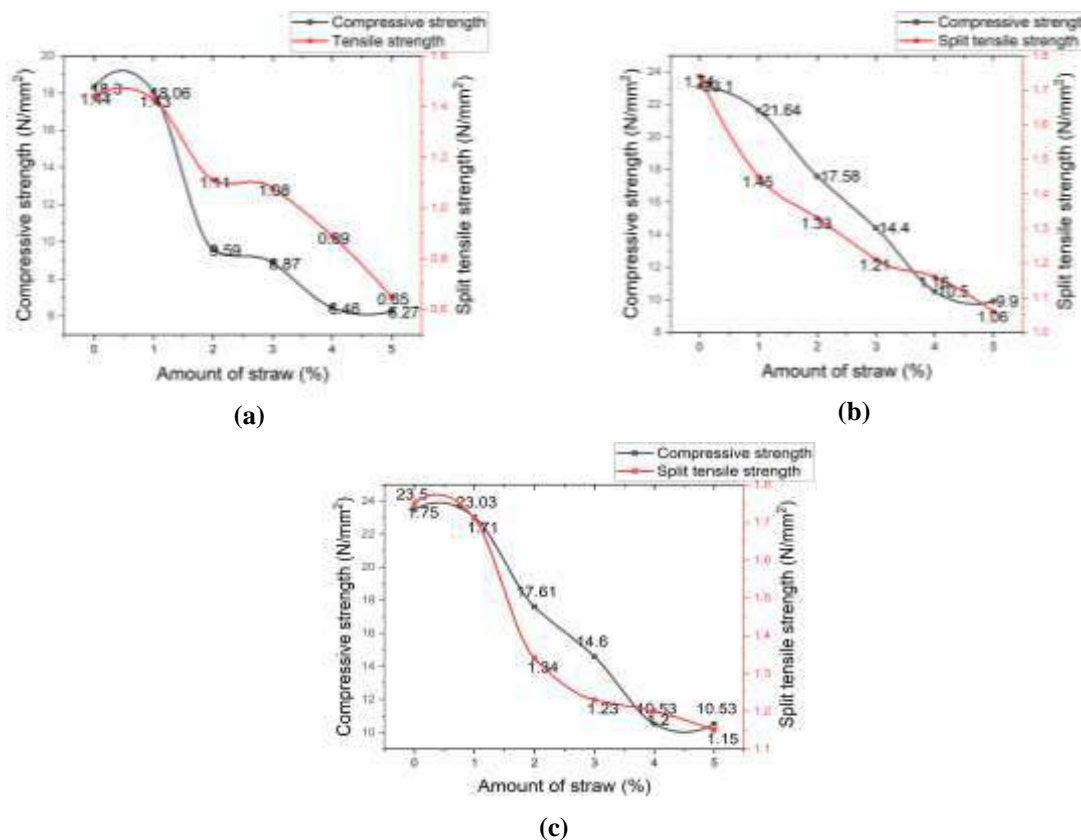
Fig. 5. Relationship between compressive strength and split tensile of CSC with straw fibre content (%) at: a) 7 days; b) 28 days; and c) 56 days of curing

4. Conclusions

From the findings of the study, the following conclusions were derived:
- The workability of Coconut Shell Concrete (CSC) displays a noticeable decline as the proportion of straw content increases. This inversely proportional relationship suggests that the incorporation of straw fibres comes at the expense of concrete workability, a crucial factor in construction.
- An obvious reduction in density was observed in CSC as the percentage of straw content increased. This trend underlines the impact of straw fibres on the structural characteristics of the concrete, potentially influencing its load-bearing capacity and overall performance.
- The study reveals a clear association

between the percentage of straw fibre content in CSC and increased water absorption. Notably, the highest water absorption was recorded in CSC samples with a 5% straw fibre content. This insight underscores the necessity for careful consideration of water resistance in concrete mixtures containing straw fibres.
- Analysis of the hardened concrete properties demonstrates a consistent reduction in both compressive and split tensile strengths with a rising percentage of straw fibre in the CSC mixture. Although it is important to note that strength improves with age, it becomes evident that the inclusion of 1% straw content in CSC yields concrete of Grade 20, implying a potential balance between sustainability and structural performance in specific applications. These findings provide

valuable insights into the effects of straw fibre reinforcement on the properties of Coconut Shell Concrete, offering practical guidance for engineering applications and sustainable construction practices. Further research may explore optimization techniques to harness the benefits of straw fibres in CSC while mitigating their adverse impacts on workability and strength.

5. References

Adeniyi, A.G., Abdulkareem, S.A., Ighalo, J.O., Abdulkareem, M.T., Iwuozor, K.O. and Emenike, E.C. (2022a). "A study on the hybrid polystyrene composite filled with elephant-grass-bio char and doped-aluminium-content", *Functional Composite Sand Structures*, 4(3), 035006, https://doi.org/10.1088/2631-6331/ac8ddf.

Adeniyi, A.G., Adeyanju, C.A., Iwuozor, K.O., Odeyemi, S.O., Emenike, E.C., Ogunniyi, S. and Te-Erebe, D.K. (2022b). "Retort carbonization of bamboo (Bambusa vulgaris) waste for thermal energy recovery", *Clean Technologies and Environmental Policy*, 25(3), 937-947, https://doi.org/10.1007/s10098-022-02415-w.

Aisheh, Y.I.A., Atrushi, D.S., Akeed, M.H., Qaidi, S. and Tayeh, B.A. (2022). "Influence of polypropylene and steel fibres on the mechanical properties of ultra-high-performance fibre-reinforced geopolymer concrete", *Case Studies in Construction Materials*, 17(April), 1-11, https://doi.org/10.1016/j.cscm.2022.e01234.

Ayyappa, R.A., Sandeep Reddy, B.G., Swamy Yadav, G. and Swetha Sudarshan, D. (2020). "Partial replacement of cement and coarse aggregate by egg shell powder and coconut shells", *International Journal of Innovative Technology and Exploring Engineering*, 4, 1242-1246, https://doi.org/https://doi.org/10.35940/ijitee.D1573.029420.

Bamigboye, G.O., Ede, A.N., Egwuatu, C., Jolayemi, J. and Olowu, O. (2015). "Assessment of compressive strength of concrete produced from different brands of Portland cement", *Civil and Environmental Research*, 7(8), 31-39.

BS EN 12350-2. (2009). *Testing fresh concrete-slump test*, British Standards, Standards Policy and Strategy Committee, BSI Group Headquarters, London, UK.

BS EN 12390-2. (2019). *Testing hardened concrete - Making and curing specimens for strength tests*, British Standards, Standards Policy and Strategy Committee, BSI Group Headquarters, London, UK.

BS EN 12390-3. (2019). *Testing hardened concrete,*

Compressive strength of test specimens, British Standards, Standards Policy and Strategy Committee, BSI Group Headquarters, London, UK.

BS EN 12390-6:2000. (2000). *Testing hardened concrete, tensile splitting strength of test specimens*, British Standards, Standards Policy and Strategy Committee, BSI Group Headquarters, London, UK.

BS EN 12620:2002 + A1:2008. (2008). *Specification for Aggregates from natural sources for concrete*, British Standards, Standards Policy and Strategy Committee, BSI Group Headquarters, London, UK.

Chin, S.C., Tee, K.F., Tong, F.S., Doh, S.I. and Gimbun, J. (2020). "External strengthening of reinforced concrete beam with opening by bamboo fibre reinforced composites", *Materials and Structures*, 53(6), 1-12, https://doi.org/10.1617/s11527-020-01572-y.

Crow, J.M. (2008). "The concrete conundrum", Chemistry World, Royal Society of Chemistry, https://www.chemistryworld.com/features/the-concrete-conundrum/3004823.article

Domagała, L. (2015). "The effect of lightweight aggregate water absorption on the reduction of water-cement ratio in fresh concrete", *Procedia Engineering*, 108, 206-213, https://doi.org/10.1016/j.proeng.2015.06.139.

Ghanbari, M. and Bayat, M. (2022). "Effectiveness of reusing steel slag powder and polypropylene fibre on the enhanced mechanical characteristics of cement-stabilized sand", *Civil Engineering Infrastructures Journal*, 55(2), 241-257, https://doi.org/10.22059/CEIJ.2021.319310.1742.

Kakade, S.A. and Dhawale, A.W. (2015). "Light weight aggregate concrete by using coconut shell", *International Journal of Technical Research and Applications*, 3(3), 127-129.

Micelli, F., Renni, A., Kandalaft, A.G. and Moro, S. (2020). "Fibre-reinforced concrete and ultrahigh-performance fibre-reinforced concrete materials", In *New Materials in Civil Engineering,* (pp. 273-314), Butterworth-Heinemann, https://doi.org/10.1016/B978-0-12-818961-0.00007-7.

Modarres, Y. and Ghalehnovi, M. (2023). "The effect of recycled steel fibres from waste tires on concrete properties", *Civil Engineering Infrastructures Journal*, 56(1), 1-18, https://doi.org/10.22059/CEIJ.2022.339592.1820.

Nunes, L.A., Silva, M.L., Gerber, J.Z. and Kalid, R.D.A. (2020). "Waste green coconut shells: Diagnosis of the disposal and applications for use in other products", *Journal of Cleaner Production*, 255(May 10), 120169, https://doi.org/10.1016/j.jclepro.2020.120169.

Odeyemi, S.O., Atoyebi, O.D., Kegbeyale, O.S.,

Anifowose, M.A., Odeyemi, O.T., Adeniyi, A. G. and Orisadare, O.A. (2022a). "Mechanical properties and microstructure of high-performance concrete with bamboo leaf ash as additive", *Cleaner Engineering and Technology*, *6*,1-6, https://doi.org/10.1016/j.clet.2021.100352

Odeyemi, S.O., Atoyebi, O.D., Odeyemi, O.T. and Ajamu, S.O. (2022b). "Investigating the optimal combination for gravel and granite in blended palm oil fuel ash concrete", *Innovative Infrastructure Solutions*, 7(6), 1-8, https://doi.org/10.1007/s41062-022-00950-5.

Odeyemi, S.O., Iwuozor, K.O., Emenike, E.C., Odeyemi, O.T. and Adeniyi, A.G. (2023). "Valorisation of waste cassava peel into biochar: An alternative to electrically-powered process", *Total Environment Research Themes*, 6 (December 2022), 100029, https://doi.org/10.1016/j.totert.2023.100029.

Olanipekun, E.A., Olusola, K.O. and Ata, O. (2006). "A comparative study of concrete properties using coconut shell and palm kernel shell as coarse aggregates", *Building and Environment*, 41(3), 297301, https://doi.org/10.1016/j.buildenv.2005.01.029.

Wang, X., Fan, F., Lai, J. and Xie, Y. (2021). "Steel fibre reinforced concrete: A review of its material properties and usage in tunnel lining", *Structures*, 34, (December 2021), 1080-1098, https://doi.org/10.1016/j.istruc.2021.07.086.

Yahiaoui, D., Saadi, M. and Bouzid, T. (2022). "Compressive behaviour of concrete containing glass fibres and confined with glass FRP composites", *International Journal of Concrete Structures and Materials*, 16(1), 2097, https://doi.org/10.1186/s40069-022-00525-9.

Yan, L., Su, S. and Chouw, N. (2015). "Microstructure, flexural properties and durability of coir fibre reinforced concrete beams externally strengthened with flax FRP composites", *Composites Part B, Engineering*, 80, 343354, https://doi.org/10.1016/j.compositesb.2015.06.011.

Reviewers

The Editorial Board of the Civil Engineering Infrastructures Journal (CEIJ) would like to express sincere thanks to all reviewers of papers submitted to CEIJ during years 2023 and 2024 for their time and efforts in evaluating papers for this journal.

Ghasemzadeh, S.H.
Gilan University
Gholhaki, M.
Semnan University
Golchin, B.
Mohaghegh Ardabili University
Guadouri, H.
University of Khemis Miliana
Haghighi, A.
Shahid Chamran University
Hakeem, B.
Higher Institute of Engineering and Technology
Hao, P.
Dalian University of Technology
Hassona, F.
El-Minia University
Hesami, Z.
Environment and Sustainable Development Department of Tehran Municipality
Hoseini Vaez, S.R.
University of Qom
Hristova, T.
University of Mining and Geology
Huang, W.
Wuhan University of Technology
Jahed Armaghani, D.
University of Technology Sydney
Jalali, M.
Shahrood University of Technology
Jalili, M.
Quchan University of Technology
Jalili, J.
International Institute of Earthquake Engineering and Seismology
Jamshidi, M.
Iran University of Science and Technology (IUST)
Johari, A.
Shiraz University of Technology
K, N.
National Institute of Technology Hamirpur
Kabir, M.Z.
Amirkabir University of Technology
Karumanchi, M.
Vignan's Foundation for Science, Technology and Research
Kavianpour, M.R.
K.N. Toosi University of Technology
khabiri, M.M.
Yazd University
Kolahdoozan, M.
Amirkabir University of Technology
Kumar, A.
National Institute of Technology Delhi
Kumar, M.
SRM Institute of Science and Technology

Kumar, V.
Central University of Haryana
Laknejadi, K.
Islamic Azad University, Science and Research Branch
Li, S.Q.
Heilongjiang University
Madani, S.H.
Graduate University of Advanced Technology
Maghsoudi, M.
University of Jiroft
Mahjuri, N.
K.N. Toosi University of Technology
Mahmoodian, M.
University of Tehran
Mahmoudi, M.
Shahid Rajaee Teacher Training University
Malathy, R.
Sona College of Technology (SCT)
Maleki, M.
Bu-Ali Sina University
Marchione, F.
Università Politecnica delle Marche
Marefat, M.S.
University of Tehran
Mazloom, M.
Shahid Rajaee Teacher Training University
Mirzabozorg, H.
K.N. Toosi University of Technology
Mohammadi, M.A.
Urmia University Faculty of Engineering
Mohammadi, Y.
University of Mohaghegh Ardabili
Moharrami, H.
Tarbiat Modares University
MolaAbasi, H.
Gonbad Kavous University
Moodi, F.
Amirkabir University of Technology
Moradi, M.
University of Tehran
Mostafaei, H.
University of Technology Sydney
Naeiji, A.
Florida International University
Navayi Neya, B.
Babol Noshirvani University of Technology
Nik Azizan, N.Z.
Universiti Malaysia Perlis (UniMAP)
Noormohammadi, N.
Isfahan University of Technology
Nourani, V.
Tabriz University
Ouhadi, V.R.
Bu-Ali Sina University

Oulapour, M.
Shahid Chamran University
Ozturk, B.
Hacettepe University
Revathi, P.
Puducherry Technological University
Padilha Thives, L.
Federal University of Santa Catarina
Panji, M.
Islamic Azad University, Zanjan Branch
Patel, N.K.
Navrachana University Vadodara Gujrat India
Pourdeilami, A.
Damghan University
Quadri, A.
The Federal University of Technology Akure
Rafiee, R.
University of Tehran
Rahnavard, R.
University of Coimbra
Ramezanianpour, A.M.
University of Tehran
Ranjbar Karkanaki, A.
Islamic Azad University, East Tehran Branch
Sadeghi, A.A.
Hakim Sabzevari University
Saeedmonir, S.
University of Tehran
Safari, S.
University of Maryland
Safarzadeh, A.
University of Mohaghegh Ardabili
Sahebkar, K.
Tarbiat Modares University
Sajadifar, S.H.
Islamic Azad University, Shahriar Branch
Salehi, A.M.
Kharazmi University
Salehi Neyshabouri, S.A.A.
Tarbiat Modares University
Sekhri, Kh.
University of BATNA 2
Shahbazbegian, M.R.
Tarbiat Modares University
Sharbatdar, M.K.
Semnan University
Sharma, V.
Government Engineering College, Rajkot
Sharma, A.
National Institute of Technology Patna
Shekarchi Zadeh, M.
University of Tehran
Shirkhani, A.
University of Tabriz
Siadatmousavi, S.M.
Iran University of Science and Technology

Singh, A.
Tongji University
Sobhani, J.
Road, Housing & Urban Development Research Center (BHRC)
Sohrabi, A.
University of Tehran
Suparp, S.
Srinakharinwirot University
Taghipour, A.A.
Damghan University
Talebbeydokhti, N.
Shiraz University
Tarighat, A.
Shahid Rajaee Teacher Training University
Tavakoli, H.R.
Babol Noshirvani University of Technology
Torabian, A.
University of Tehran
Usman, F.
Universiti Tenaga Nasional (UNITEN)
Valizadeh, H.
Özyeğin University
Vaseghi Amiri, J.
Babol Noshirvani University of Technology
Verma, A.K.
Indian Institute of Technology (BHU) Varanasi
Xu, Y.
Southeast University (China)
yahiaoui, D.
University of Batna 2
Yamin Rasa, A.
Atatürk University
Yousefi, H.
University of Tehran
Zahrai, S.M.
University of Tehran
Zakaria, Z.
University of Malta
Zammori, F.
University of Parma
Zapata Ferrero, I.
Universidad Tecnológica Nacional
Zarghami, M.
University of Tabriz
Zarrati, A.R.
Amirkabir University of Technology

AIMS AND SCOPE

Since the College of Engineering (Former Faculty of Engineering, FOE) of the University of Tehran has renewed its policy toward scientific publication, the Civil Engineering transaction of the well- built 45 years old Persian journal of *"Nashrieh Daneshkadeh Fanni"* is to be published in English and as separate independent journal with the name of ***Civil Engineering Infrastructures Journal***.

Civil Engineering Infrastructures Journal is an international journal which publishes high quality scientific papers in all areas of engineering and management of civil infrastructures. The civil infrastructures include, but are not limited to: buildings, bridges, dams, transportation systems, geotechnical structures, underground constructions, water distribution systems, offshore platforms, pipelines, ocean structures, airports and power plants.

The scope of this journal encompasses, but is not restricted to the following aspects of engineering and management of infrastructures:

- Mathematical modeling
- Computational and experimental methods
- Environmental Impact assessment
- Passive defense and security issues
- Monitoring and assessment
- Construction and design for durability
- Deterioration modeling and aging
- Failure analysis
- Field testing
- Financial planning
- Inspection and diagnostics
- Life-cycle analysis and prediction

- Maintenance, rehabilitation, repair and replacement strategies

- Non-destructive testing

- Optimization of maintenance and management

- Specifications and codes

- Reliability and risk management

- Supervisory Control and Data Assimilation (SCADA)

- Automation and Robotics in Construction

- Smart civil infrastructure Systems

- Sustainable civil infrastructure systems

- Case studies

Audiences of *Civil Engineering Infrastructures Journal* are researchers and practitioners as well as people working in infrastructure design, construction, maintenance and operation. Papers considered for publication must contain a clear and well-defined engineering component and make a significant contribution to the engineering and management of civil infrastructures. All articles submitted to this journal will undergo a rigorous peer review by anonymous independent experts.

Additional information can be obtained from:

Civil Engineering Infrastructures Journal

College of Engineering,

University of Tehran

P.O. Box: 11155- 4563

Tehran, Iran

Tel/ Fax: +98-21-88956097

Web Site: www.ceij.ir

Email: ceij@ut.ac.ir

University of Tehran
College of Engineering

Copyright Transfer Agreement

In order to protect the author(s), from the consequences of unauthorized use, the publisher requests that all author(s) sign the appropriate statement below:

Manuscript Title:

Corresponding Author

Author:
Date: Signature;

Author:
Date: Signature:

Author:
Date: Signature:

Author:
Date: Signature:

CIVIL ENGINEERING INFRASTRUCTURES JOURNAL (CEIJ)

is indexed and abstracted in the bibliographical databases including:

CONTENTS